DEVELOPMENT OF ZEOLITE Y AND ZSM5 COMPOSITE CATALYST FROM KANKARA KAOLIN

By

NURUDEEN SALAHUDEEN

DEPARTMENT OF CHEMICAL ENGINEERING

AHMADU BELLO UNIVERSITY, ZARIA

NIGERIA.

MARCH, 2015

DEVELOPMENT OF ZEOLITE Y AND ZSM5 COMPOSITE CATALYST FROM KANKARA KAOLIN

By

Nurudeen SALAHUDEEN, B. Eng, MSc. (ABU)
(Ph.D/ENG/9467/2011-2012)

A DISSERTATION SUBMITTED TO THE SCHOOL OF POSTGRADUATE STUDIES, AHMADU BELLO UNIVERSITY, ZARIA

IN PARTIAL FULFILLMENT OF THE REQUIREMENTS FOR THE AWARD OF A DOCTOR OF PHILOSOPHY IN CHEMICAL ENGINEERING

DEPARTMENT OF CHEMICAL ENGINEERING,
FACULTY OF ENGINEERING,
AHMADU BELLO UNIVERSITY, ZARIA,
NIGERIA.

MARCH, 2015

DECLARATION

I, Nurudeen Salahudeen hereby declare that the work in this dissertation entitled "Development of Zeolite Y and ZSM5 Composite Catalyst from Kankara kaolin" was performed by me in the Department of Chemical Engineering, Ahmadu Bello University, Zaria, under the supervision of Prof. A. S. Ahmed and Dr. S. M. Waziri of the Department of Chemical Engineering and Dr. Mohammed Dauda of the Department of Mechanical Engineering. Ahmadu Bello University, Zaria.

The information derived from the literature has been duly acknowledged in the text and a list of references provided. No part of this work has been presented for another degree or diploma at any institution.

_____ _____

Signature Date

CERTIFICATION

This dissertation entitled "Development of Zeolite Y and ZSM5 Composite Catalyst from Kankara kaolin" meets the regulations governing the award of the degree of Doctor of Philosophy of the Ahmadu Bello University, and is approved for its contribution to knowledge and literary presentation.

_____	_____
Chairman, Supervisory Committee Prof. A. S. Ahmed	Date
_____	_____
Member, Supervisory Committee Dr. Mohammed Dauda	Date
_____	_____
Member, Supervisory Committee Dr. S. M. Waziri	Date
_____	_____
Head, Dept. of Chemical Engineering Dr. S. M. Waziri	Date
_____	_____
Dean, School of Postgraduate Studies Prof. A. Z. Hassan	Date

DEDICATION

This project work is dedicated to my most beloved, my mentor, my role model, my leader and prophet, the best of mankind, son of Abdullah, Prophet Muhammad (S.A.W).

ACKNOWLEDGEMENTS

All praises and glorifications are due to Allah (S.W.T) the creator and sustainer of the universe. He created the man and taught him what he knew not. To Him alone belong all attributes of perfection.

I wish to acknowledge the financial support of the Petroleum Technology Development Fund (PTDF) Professorial Chair in Chemical Engineering, ABU, Zaria, for funding this research work.

My invaluable appreciation and acknowledgement goes to my learned Professor, my able supervisor, Prof. A. S. Ahmed, for his immeasurable courage and tireless supervision. Your magnanimous sea of knowledge has being the aid to the realization of this work.

In full measure, I also acknowledge the immense contribution of my other supervisors; Dr. Mohammed Dauda and Dr. S. M. Waziri. Your tireless contributions are fully appreciated. My acknowledgement cannot be complete without expressing my profound appreciation to Prof. B. Y. Jibril, who has supported this work immensely technical-wise and in kind, Dr. Ala'a Hamed Al-Muhtaseb and Prof. Joydeep Dutta of Sultan Qaboos University, Oman. Dr. Nagabhatla Viswanadham of Council of Scientific and Industrial Research (CSIR) India. My colleagues in the PTDF Professorial Chair in Department of Chemical Engineering ABU, Zaria and the entire academic and nonacademic staff of the Department of Chemical Engineering, Ahmadu Bello University, Zaria. Thank you all for your contributions to the success of this work.

I also wish to acknowledge the immense courage and invaluable support of my parents in making my pursuit of education a reality. Indeed, I will always live to remember and gratify your role in my life. I say, may Allah (S.W.T) reward you both with paradise. I cannot forget the rare supportive roles of my darling wife and my lovely kids, without your supports this noble course could not have been accomplished.

ABSTRACT

Zeolite Y was synthesized from Kankara kaolin using a novel split method. The zeolite Y synthesized was thermally stabilized by impregnating with rare earth metal. Catalytic cracking catalysts; catalyst Y zeolite and catalyst Y zeolite + ZSM5 blend were formulated. The physiochemical and thermal properties of the raw and intermediate materials, zeolite synthesized and catalyst formulated were characterized using XRD, XRF, BET, SEM, TEM, TGA/DTG, FTIR, UV/VIS spectrometry and Flame photometry. The acidity of the zeolite Y synthesized was determined using the pyridine probe acidity test. The catalytic performance of the catalysts formulated were determined using fixed bed catalytic cracking reactor. The BET specific surface area, pore volume, Si/Al, and average particle size of the Kankara kaolin used as raw material were 12.95 m^2/g, 0.0038 cm^3/g, 1.9 and 1.0 µm respectively. The BET specific surface area, pore volume, Si/Al, and average particle size of a typical zeolite Y synthesized from Kankara kaolin were 830.0 m^2/g, 0.2951 cm^3/g, 4.26 and 1.425 nm respectively. The crystallinity of the synthesized zeolite Y was 72.5% that of a commercial zeolite Y. The Lewis acidity, BrØnsted acidity, total acidic concentrations of the synthesized zeolite Y using the novel method were 69.82, 178.19 and 248.01 µmol/g respectively. The formulated catalyst Y prepared from the zeolite Y synthesized using the novel split method showed high catalytic performances. The activity and gasoline yield at reaction temperature of 500˚C were 70.89% and 17.92% respectively. The formulated composite catalyst Y zeolite + ZSM5 blend using the zeolite Y synthesized using the novel split method showed higher catalytic performances than their counterpart catalyst Y. The activity and gasoline yield at reaction temperature of 500˚C were 73.17% and 59.38% respectively. The synthesized zeolite Y also showed highly promising performance when used for adsorptive desulfurization of a model diesel oil using microwave assisted desulfurization method.

TABLE OF CONTENTS

Content		Page
Title Page		i
Declaration		ii
Certification		iii
Dedication		iv
Acknowledgements		v
Abstract		vi
Table of Contents		vii
List of Figures		xiii
List of Tables		xxi
List of Abbreviations and Symbols		xxiii
CHAPTER 1: INTRODUCTION		1
1.1	**Background**	1
1.2	**Research Problem**	4
1.3	**Research Aim**	4
1.4	**Specific Objectives**	4
1.5	**Scope of the Research**	5
1.6	**Research Justification**	6
CHAPTER 2: LITERATURE REVIEW		7
2.1	**Zeolite**	7
2.2	**Historical Background**	7
2.3	**Occurrence of Zeolites**	9
2.4	**Application of Zeolite**	10
	2.4.1 Commercial and domestic applications	11
	2.4.2 Petrochemical industry	11
	2.4.3 Nuclear industry	13
	2.4.4 Construction industry	13
	2.4.5 Heating and refrigeration	14

2.4.6 Detergents 14
2.4.7 Medical industry 14
2.4.8 Agricultural industry 15
2.4.9 Other uses of zeolite 16

2.5 Classification of Zeolites 16
2.5.1 Framework types 17

2.6 Zeolite Structure 18
2.6.1 Primary building units 19
2.6.2 Secondary building units 20
2.6.3 Characteristic cage-building units 21
2.6.4 Characteristic chain and layer-building units 22

2.7 Zeolite Production 23
2.7.1 Traditional production 23
2.7.2 Synthetic production 24

2.8 Methods of Synthesis of Zeolites 26
2.8.1 Hydrothermal method 27
2.8.2 Solvothermal method 27
2.8.3 Ionothermal method 28

2.9 Safety Considerations for Zeolite Synthesis 29
2.9.1 Source materials 28
2.9.2 Batch preparation 29
2.9.3 Crystallization 29
2.9.4 Product recovery 31

2.10 ZSM5 31

2.11 Zeolite Y 34

2.12 Catalysis Using Zeolites 36
2.12.1 Homogeneous catalysis 37
2.12.2 Heterogeneous catalysis 38

2.13 Catalytic Cracking 39
2.13.1 Mechanism of catalytic cracking 40

2.14 Fluidized Catalytic Cracking Unit 42

2.15 FCC Catalyst Formulation 44
2.15.1 Impregnation 45
2.15.2 Adsorption from solution 45
2.15.3 Co-precipitation 47
2.15.4 Deposition 47

2.16 Catalyst Design Parameters 48
2.16.1 Activity 49
2.16.2 Stability 49
2.16.3 Selectivity 51
2.16.4 Regenerability 51

2.17 Some Past Related Works on Zeolite Synthesis 51

CHAPTER 3: MATERIALS AND METHOD 53
3.1 Materials and Equipment 53
3.1.1 List of materials 53
3.1.2 List of apparatus 54
3.1.3 List of equipment 54

3.2 Experimental Procedure 55
3.2.1 Preparation of zeolite Y using high purity chemicals 56
3.2.2 Preparation of zeolite Y using Kankara kaolin 57

3.2.3 Protonation of the synthesized zeolite Y 63
3.2.4 Thermal stabilization of the synthesized zeolite Y 63
3.2.5 Catalyst formulation 63
3.2.6 X-ray diffraction (XRD) 64
3.2.7 X-ray fluorescence (XRF) 64
3.2.8 Brunauer-Emmett-Teller (BET) analysis 64
3.2.9 Fourier transform infrared (FTIR) spectroscopy 64
3.2.10 Thermo gravimetric/differential thermo gravimetric (TGA/DTG) 65
3.2.11 Scanning electron microscope (SEM) analysis 65
3.2.12 Transmission electron microscope (TEM) analysis 66
3.2.13 Characterization of sodium silicate 66
3.2.14 Acidity test 67
3.2.15 Catalytic performance test 68

CHAPTER 4: RESULTS AND DISCUSSION 70

4.1 Characteristics of Kaolin and Metakaolin 70

4.1.1 XRD characteristics of kaolin and metakaolin 70
4.1.2 XRF characteristics of kaolin and metakaolin 73
4.1.3 BET characteristics of kaolin and metakaolin 75
4.1.4 SEM micrographs of kaolin and metakaolin 76
4.1.5 TEM images of kaolin and metakaolin 78
4.1.6 Thermogravimetry characteristics of kaolin and metakaolin 80

4.2 Characterizationstics of Aluminium Hydroxide 83

4.2.1 XRD characteristics of the aluminium hydroxide 83
4.2.2 XRF characteristics of the aluminium hydroxide 91
4.2.3 BET characteristics of the aluminium hydroxide 96
4.2.4 SEM micrograph of the aluminium hydroxide 97
4.2.5 TEM image of the aluminium hydroxide 102
4.2.6 Thermogravimery characteristics of the aluminium hydroxide 104
4.2.7 FTIR spectrum of the aluminium hydroxide 108

4.3 Characteristics of Silica 109
4.3.1 XRD characteristics of the silica 109
4.3.2 FTIR spectrum of the silica 111
4.3.3 SEM micrograph of the silica 111

4.4 Characteristics of Sodium Silicate 112
4.4.1 Determination of SiO_2/Na_2O ratio of the sodium silicate 112
4.4.2 FTIR spectrum of the sodium silicate 115
4.4.3 Thermogravimetry characteristics of the sodium silicate 116

4.5 Characteristics of Zeolite 117
4.5.1 XRD characteristics of zeolite Y synthesized using HPC 117
4.5.2 XRF characteristics of zeolite Y synthesized using HPC 122
4.5.3 XRD characteristics of zeolite Y synthesized from kaolin 123
4.5.4 XRF characteristics of zeolite Y synthesized from kaolin 124
4.5.5 Study of the optimum synthesis conditions for zeolite Y from kaolin 126
4.5.6 Characteristics of the formulated catalysts 166
4.5.7 Catalytic cracking of model petroleum oil using the formulated catalyst 188

CHAPTER 5: CONCLUSIONS AND RECOMMENDATIONS 205

5.1 Conclusions 205

5.2 Recommendations 208

CONTRIBUTIONS TO KNOWLEDGE 209

PUBLICATIONS 210

REFERENCES 211

APPENDICES 218
Appendix A: Detail Calculations for the Dealumination of Metakaolin 218
Appendix B: GCMS Online-Gas and Liquid Analyses Data Obtained for the Cracking of Hexadecane 222

LIST OF FIGURES

Figure	Title	Page
2.1.	Zeolite unit structure (a) TO_4tetrahedron (b) TO_4 tetrahedron	18
2.2.	Zeolite unit structure illustration	19
2.3.	Unit secondary building unit (SBU) for zeolites	20
2.4.	Some of the cage-building units in zeolites	21
2.5.	Chart illustration world production of natural zeolites	23
2.6.	MFI membered ring structure (a) framework (b) channel system	32
2.7.	Structure of faujasite zeolite Y	35
3.1.	Flow diagram for synthesis of zeolite from kaolin	58
3.2	Flow diagram for the synthesis of zeolite Y from the reagents prepared	62
3.3.	Setup for the reactor used for catalytic cracking (source; Sandeep et al., 2013)	69
4.1.	XRD pattern of raw Kankara kaolin	71
4.2.	XRD pattern of beneficiated Kankara kaolin	71
4.3.	XRD pattern of metakaolin	72
4.4.	Comparison of the XRD patterns; raw kaolin, beneficiated and metakaolin	74
4.5.	TGA/DTG curves of raw Kankara kaolin	81
4.6.	TGA/DTG curves of beneficiated Kankara kaolin	81
4.7.	TGA/DTG curves of metakaolin	82
4.8.	XRD pattern of $Al(OH)_3$ 3 fold uncalcined	84
4.9.	XRD pattern of $Al(OH)_3$ 4 fold uncalcined	84
4.10.	XRD Pattern of $Al(OH)_3$ 5 fold uncalcined	85
4.11.	XRD pattern of $Al(OH)_3$ calcined at 300˚C	86
4.12.	XRD pattern of $Al(OH)_3$ calcined at 400°C	87
4.13.	XRD pattern of $Al(OH)_3$ calcined at 500°C	87
4.14.	XRD pattern of $Al(OH)_3$ calcined at 600°C	88
4.15.	XRD pattern of $Al(OH)_3$ calcined at 700°C	88
4.16.	XRD pattern of $Al(OH)_3$ calcined at 800°C	89
4.17.	XRD pattern of $Al(OH)_3$ calcined at 900°C	89
4.18.	XRD pattern of commercial gamma alumina	90

4.19.	Comparison of XRD patterns of aluminum hydroxide	90
4.20.	Trend of alumina and sulphur contents of the aluminum hydroxide	95
4.21.	TGA/DTG curves of uncalcined aluminum hydroxide	106
4.22.	TGA/DTG curves of aluminum hydroxide calcined at 400˚C	106
4.23.	TGA/DTG curves of aluminum hydroxide calcined at 800˚C	107
4.24.	TGA/DTG curves of aluminum hydroxide calcined at 900˚C	107
4.25.	FTIR spectra of aluminum hydroxide prepared	111
4.26.	XRD pattern of silica produced using variable dealumination folds	110
4.27.	FTIR spectrum of silica prepared from Kankara kaolin	111
4.28.	Calibration curve for silica using UV/VIS spectroscopy	113
4.29.	FTIR spectra of commercial and as-synthesized sodium silicate.	116
4.30.	TGA/DTG curves of the prepared sodium silicate	117
4.31.	XRD pattern of zeolite Y using HPC.	118
4.32.	XRD pattern of zeolite Y synthesized using alumina source from clay	119
4.33.	XRD pattern of zeolite Y synthesized from silica obtained from clay	119
4.34.	Comparison of XRD patterns for zeolite Y; partial substitution of clay	120
4.35.	Comparison of XRD patterns for zeolite Y: using HPC	121
4.36.	XRD patterns of zeolite Y synthesized from clay; variable dealumination	124
4.37.	XRD patterns of synthesized zeolite Y from clay using 5 fold dealumination	127
4.38.	XRD patterns of zeolite Y synthesized using $Al(OH)_3$ calcined at 400˚C	129
4.39.	XRD patterns of zeolite Y synthesized using variable product recovery	132
4.40.	XRD patterns of zeolite Y synthesized using variable degrees of dealumination	133
4.41.	XRD patterns of zeolite Y synthesized using variable dosage of silica	136
4.42.	Comparison of XRD patterns for zeolite Y; commercial, using HPC and clay	138
4.43.	Comparison of XRD patterns for zeolite Y; novel and conventional methods	138
4.44.	XRD pattern of zeolite Y synthesized using industrial grade acid and base	140
4.45.	XRD pattern of zeolite Y synthesized using analar grade acid and base	141
4.46.	Comparison of XRD patterns for the various batches of zeolite Y synthesized	141
4.47.	XRD pattern of bulk synthesized Zeo-BY at variable calcination treatment	154

4.48. TGA/DTG curves of Zeo-CY: NaY 156
4.49. TGA/DTG curves of Zeo-HPC: NaY 156
4.50. TGA/DTG curves of Zeo-AY: RE Y 157
4.51. TGA/DTG curves of Zeo-BY: RE Y 157
4.52. TGA/DTG curves of Zeo-CY: RE Y 158
4.53. TGA/DTG curves of Zeo-HPC: RE Y 158
4.54. FTIR spectra of the various zeolite NaY before pyridine adsorption 159
9.55. FTIR spectra of the various zeolite NaY after pyridine adsorption 160
4.56. FTIR spectra of the various zeolite RE Y before pyridine adsorption 160
4.57. FTIR spectra of the various zeolite RE Y after pyridine adsorption 161
4.58. Trend of microwave desulfurization at variable reaction times 163
4.59. Trend of microwave desulfurization at variable reaction temperatures 163
4.60. FTIR spectra of Zeo-AY used for desulfurization at variable temperatures 164
4.61. FTIR spectra of Zeo-AY used for desulfurization at variable temperatures 165
4.62. FTIR spectra of Zeo-HPC used for desulfurization at variable times 165
4.63. FTIR spectra of Zeo-HPC used for desulfurization at variable temperatures 166
4.64. XRD pattern of catalyst Y; Zeo-BY: RE Y, metakaolin and alumina support 167
4.65. XRD pattern of catalyst Y; Zeo-HPC: RE Y, metakaolin and alumina support 168
4.66. XRD Pattern of catalyst Y + ZSM; Zeo-BY: RE Y, ZSM5 and alumina support 168
4.67. FTIR spectra of the various as-synthesized zeolite NaY 172
4.68. FTIR spectra of commercial and the various as-synthesized zeolite HY 173
4.69. FTIR spectra of commercial and the various synthesized zeolite Y catalysts 173
4.70. FTIR spectra of as-synthesized zeolite Y + ZSM5 catalysts 174
4.71. TGA/DTG curves of Zeo-AY: catalyst Y 183
4.72. TGA/DTG curves of Zeo-BY: catalyst Y 183
4.73. TGA/DTG curves of Zeo-CY: catalyst Y 184
4.74. TGA/DTG curves of Zeo-HPC: catalyst Y 184
4.75. TGA/DTG curves of commercial catalyst Y 185
4.76. TGA/DTG curves of Zeo-BY: catalyst Y+ ZSM5 185

4.77. TGA/DTG curves of Zeo-CY: catalyst Y+ ZSM5 186
4.78. TGA/DTG curves of Zeo-HPC: catalyst Y+ ZSM5 186
4.79. Isothermal scan of the various catalyst Y at 750˚C for 1 h 187
4.80. Isothermal scan of the various catalyst Y + ZSM5 at 750˚C for 1 h 187
4.81. Product distribution for the various catalyst Y at 400˚C 189
4.82. Product distribution for the various catalyst Y + ZSM5 at 400˚C 189
4.83. Product distribution for the various catalyst Y at 500˚C 191
4.84. Product distribution for the various catalyst Y + ZSM5 at 500˚C 191
4.85. Product distribution for the various catalyst Y at 550˚C 192
4.86. Product distribution for the various catalyst Y + ZSM5 at 550˚C 193
4.87. Comparison of the gasoline yield; zeolite Y catalysts at 400 and 500˚C 194
4.88. Comparison of the gasoline yield; zeolite Y+ ZSM5 catalysts at 400 and 500˚C 195
4.89. Gasoline yield; variable zeolite percentage compositions 196
4.90. Gasoline yield; Y+ ZSM5 variable zeolite percentage compositions 196
4.91. Reaction conversion for Zeo-AY catalysts at various temperatures 197
4.92. Reaction conversion for Zeo-BY catalysts at various temperatures 198
4.93. Reaction conversion for Zeo-CY catalysts at various temperatures 198
4.94. Reaction conversion for Zeo-HPC catalysts at various temperatures 199
4.95. Comparison of the conversion of the various Y catalysts at 400 and 500˚C 200
4.96. Conversion of the various Y+ ZSM5 catalysts 200
4.97. Product selectivity for commercial catalyst at variable temperatures 202
4.98. Product selectivity for Zeo-AY catalysts at variable temperatures 202
4.99. Product selectivity for Zeo-BY catalysts at variable temperatures 203
4.100. Product selectivity for Zeo-CY catalysts at variable temperatures 203
4.101. Product selectivity for Zeo-HPC catalysts at variable temperatures 204

LIST OF TABLES

Table	Title	Page
2.1.	Major applications of zeolites in the petroleum industry	12
4.1.	XRF results for the Kankara kaolin and metakaolin	74
4.2.	BET surface area and pore volume for Kankara kaolin and metakaolin	75
4.3.	XRF results for $Al(OH)_3$ synthesized using variable extent of dealumination	92
4.4.	XRF results for $Al(OH)_3$ calcined at variable temperatures	94
4.5.	BET results for the aluminum hydroxide at variable calcination temperatures	96
4.6.	Concentration of silica (SiO_2) using UV/VIS spectroscopy analysis	113
4.7.	Concentration of Soda (Na_2O) using flame photometer analysis	114
4.8.	SiO_2/Na_2O ratio for the sodium silicate prepared	115
4.9.	XRF results of zeolite Y; HPC and partialy substituted from clay	122
4.10.	XRF results of zeolite Y; silica and alumina sources from clay	125
4.11.	XRF results of zeolite Y; 5 fold silica and alumina sources at variable calcination	128
4.12.	XRF results for zeolite Y; aluminum hydroxide calcined at 400˚C	130
4.13.	XRF results for zeolite Y; single and double dealumination	134
4.14.	XRF results for zeolite Y synthesized using different dosage of silica	137
4.15.	BET results for the various zeolite NaY synthesized	152
4.16.	BET results for the various thermally stabilized zeolite RE Y prepared	153
4.17.	Acidity analysis for the various NaY zeolites	162
4.18.	Acidity analysis for the various RE Y zeolite	162
4.19.	BET results for the various catalyst Y	169
4.20.	BET results for the various catalyst Y prepared using variable zeolite content	170

LIST OF PLATES

Plate	Title	Page
I.	Image of natural zeolite	10
II.	SEM images of raw Kankara kaolin at various magnifications	77
III.	SEM images of beneficiated Kankara kaolin at various magnifications	77
IV.	SEM images of metakaolin at various magnifications	78
V.	TEM images of Kankara kaolin at various magnifications	79
VI.	TEM images of metakaolin at various magnifications	80
VII.	SEM images of uncalcined aluminum hydroxide at various magnifications	99
VIII.	SEM images of aluminum hydroxide calcined at 400˚C	100
IX.	SEM images of aluminum hydroxide calcined at 600˚C	100
X.	SEM images of aluminum hydroxide calcined at 700˚C	101
XI.	SEM images of aluminum hydroxide calcined at 800˚C	101
XII.	SEM images of aluminum hydroxide calcined at 900˚C	102
XIII.	TEM images of aluminum hydroxide calcined at 400˚C	103
XIV.	TEM images of aluminum hydroxide calcined at 800˚C	103
XV.	TEM images of aluminum hydroxide calcined at 900˚C	104
XVI.	SEM images of silica prepared from Kankara kaolin at various magnifications	112
XVII.	SEM images of Zeo-AY: NaY at various magnifications	142
XVIII.	SEM images of Zeo-AY: RE Y at various magnifications	143
XIX.	SEM images of Zeo-BY: NaY at various magnifications	144
XX.	SEM images of Zeo-BY: RE Y at various magnifications	145
XXI.	SEM images of Zeo-CY: NaY at various magnifications	145
XXII.	SEM images of Zeo-HPC: NaY at various magnifications	146
XXIII.	SEM images of Zeo-HPC: RE Y at various magnifications	147
XXIV.	SEM images of commercial zeolite HY at various magnifications	148
XXV.	TEM images of Zeo-AY: NaY at various magnifications	149
XXVI.	TEM images of Zeo-AY: RE Y at various magnifications	150
XXVII.	TEM images of Zeo-BY: NaY at various magnifications	150
XXVIII.	TEM images of Zeo-HPC: NaY at various magnifications	151

XXIX. SEM images of Zeo-AY: catalyst Y at various magnifications 176
XXX. SEM images of Zeo-BY: catalyst Y at various magnifications 176
XXXI. SEM images of Zeo-CY: catalyst Y at various magnifications 177
XXXII SEM images of Zeo-HPC: catalyst Y at various magnifications 177
XXXIII. SEM images of commercial catalyst Y at various magnifications 178
XXXIV. SEM images of Zeo-AY: catalyst Y + ZSM5 at various magnifications 178
XXXV. SEM images of Zeo-BY: catalyst Y + ZSM5 at various magnifications 179
XXXVI. SEM images of Zeo-CY: catalyst Y + ZSM5 at various magnifications 179
XXXVII. SEM images for Zeo-HPC: catalyst Y + ZSM5 at various magnifications 180
XXXVIII. TEM images for Zeo-AY: catalyst Y at various magnifications 181
XXXIX. TEM images for Zeo-AY: catalyst Y + ZSM5 at various magnifications 181

LIST OF ABREVIATIONS AND SYMBOLS

Abbreviations/Symbol	Meaning
ε_b	Extinction coefficients for Brønsted site
ε_l	Extinction coefficients for Lewis site
ϴ	Angle, (˚)
atm	Atmosphere
B_C	Brønsted acid concentration, (µmol/g)
BET	Brunauer-Emmett-Teller
Conc.	Concentration
DTG	Differential Thermo Gravimetric
FTIR	Fourier Transformed Infrared Radiation
GCMS	Gas Chromatography Mass Spectroscopy
IR	Infrared
K	Kelvin
L.o.I	Loss on Ignition (wt%)
L_C	Lewis acid concentration, (µmol/g)
MFC	Mass flow controller
NA	Not Available
ND	Not determined
rpm	Revolution per minute
SEM	Scanning Electron Microscope
TEM	Transmission Electron Microscope
TGA	Thermogravimetry Analysis
UV	Ultra-Violent
VIS	Visible
WHSV	Weight Hourly Space Velocity (hr^{-1})
XRD	X-ray Diffraction
XRF	X-ray Fluorescence

CHAPTER 1

1.0 INTRODUCTION

1.1 Background

The global demand on energy is exponentially increasing on daily bases due to continuous advances in the global technology, especially mechanical, electrical, transportation and process technologies. Most of the machines, equipment or appliances invented as the products of these modern technologies are operated directly or indirectly by employing energy potent. Petroleum remains the major and primary global source of energy.

Petroleum occurs naturally as crude oil which is a complex mixture of hydrocarbons and some other sulfur, nitrogen and oxygen containing organic compounds. The treatment of this complex mixture to make it suitable for use as fuel requires extreme reaction conditions in the presence of an appropriate catalyst; a process referred to as refining. The refining process causes a variety of changes to occur simultaneously in the chemistry of the crude oil, producing a broad spectrum of commercially viable products. The industrial refining of crude oil entails atmospheric and vacuum distillation designed to achieve the maximum extraction of gasoline and other lighter fuels as much as possible during the refining process. The residual product, heavy bottom product, left of the crude oil after the atmospheric and vacuum distillation known as the gas oil can still produce a lot of useful petroleum products if it is properly processed. The profit maximization of a refinery depends on the extent it is able to recover the gasoline and other fuels in the gas oil. Hence, the gas oil produced is further sent to the cracking unit where the gasoline and other fuels are recovered from the gas oil.

Cracking means the breaking down of large hydrocarbon molecules into smaller and more valuable fractions. This can be done by the thermal or catalytic methods. The thermal method known as the thermal cracking was the earlier cracking method which is almost phased out in the modern petroleum technology practices. The method entails cracking of large hydrocarbon molecules, into smaller fractions by employing high reaction temperature up to 750 – 900°C and high pressure up to 70 atm (Gary and Handwerk, 2001). Under these extreme conditions the covalent bonds of the large hydrocarbon weakens and results into cracks or breakages along the hydrocarbon bonds giving rise to a number of lighter fraction hydrocarbons. The catalytic method known as the fluid catalytic cracking (FCC) is the state of the art in the modern petroleum technology pactices. This method entails cracking of large hydrocarbon molecules, majorly gas oil, charged in as feedstock, into a riser reactor in a fluidized stream of (high catalytic active solid acids) zeolite catalysts in a controlled catalyst-to-oil feed ratio, and reaction conditions of about 520 – 550°C and 1 atm (Gary and Handwerk, 2001). Today Fluid Catalytic Cracking Unit (FCCU) has become an indispensible profit booster of all modern refineries.

The catalysts used in the FCCU are zeolite catalysts. Zeolites are crystalline microporous, aluminosilicate minerals, with distinctive chemisorption and high selectivity property. They possess unique structural pattern of regular arrays of pores, cages, channels and cavities of molecular dimensional orders, hence, they are referred to as "molecular sieves". The term molecular sieve refers to a particular property of these materials which gives them ability to selectively sort molecules based primarily on a size exclusion process, as a result of this zeolite catalysts are known for their outstandingly high selectivity for gasoline yield when used in FCC

operation. Furthermore, their highly acidic nature and high hydrothermal stability has made them not just potent and indispensible but the best catalysts used in virtually all the modern FCCU.

Zeolites are produced both naturally and synthetically; however, those that find applications in the petroleum and petrochemical industries are mainly the synthetic ones. Zeolite Y is specifically used as the modern FCCU catalyst. However, recently research works are on-going in the area of looking for other zeolite catalysts which will compete well or out-perform the zeolite Y for FCC application, ZSM5 has been identified as a potential candidate for this feat. Zeolite Y can be synthesized from either natural minerals, such as clays, or from synthetic high purity chemicals. Most of the commercial zeolite Y catalysts used in the FCC unit today are produced from synthetic high purity chemicals, as such, they are very expensive because of the high technology involved in their production. Although, they have the advantage of possessing minimum impurities. Researchers in the past have investigated into the suitability of the various types of clays for zeolite Y synthesis, and it has been widely established that kaolin is the most suitable clay. Furthermore, many attempts were carried out in the past to synthesize pure zeolites Y from kaolin clay, but the success was limited due to production of products which possessed very low crystallinity and contaminated with high level of impurities.

This work is intended to research into the possibility of synthesizing pure and crystalline zeolite Y from Kankara kaolin using a different approach and using the zeolite obtained to formulate high performance zeolite Y catalyst and zeolite Y + ZSM5 composite catalyst targeted for FCC application.

1.2 Research Problem

The research problem of the work entails the following:

i. As a major producer of crude oil in the world/Africa, the total dependence of Nigeria on imported Zeolite Y catalyst used for refining of petroleum is not a sustainable economic/technological strategy.

ii. Nigerian kaolin deposit was estimated to be over 3 billion metric tons (Edomwonyi-Otu, *et al*. 2013). The need to harness this abundant mineral for synthesis of Zeolite Y catalyst which can serve as substitute for the imported ones cannot be over emphasized.

iii. Efforts to improve the purity of Zeolite Y catalysts from kaolin have yielded only little progress due to the inherent impurities in kaolin.

iv. Attempts to improve the performance of Zeolite Y catalyst for cracking by combining with ZSM5 as composite are yet to yield the desired results

1.3 Aim and Objectives

Aim

The aim of this work is to develop zeolite Y and ZSM5 composite catalyst from Kankara kaolin.

Objectives

The objectives of this work are:

i. To study synthesis of zeolites Y using high purity chemicals.

ii. To investigate the synthesis of zeolites Y from Kankara kaolin.

iii. To formulate zeolite Y catalyst and zeolite Y/ZSM5 composite catalyst.

iv. To characterize the zeolite catalysts formulated.

v. To test the catalytic performance of the catalysts formulated.

1.4 Scope of the Research

The scope of this research work was achieved as follows:

Synthesis technique of zeolite Y using high purity chemicals was studied. The chemicals were purchased from Fisher Chemical and Sigma-Aldrich Chemicals. The synthesis technique studied was modified and applied to synthesize zeolite Y using kaolin as the raw material instead of the high purity chemicals. The raw kaolin was collected from Kankara Local Government Area of Katsina State by representative mining. The kaolin collected was beneficiated and used to synthesize zeolite Y via a novel technique. The synthesized NaY zeolite was transformed to HY zeolite and was thermally stabilized by modification to RE Y zeolite.

The RE Y zeolite produced was used to formulate zeolite Y catalyst and zeolite Y + ZSM5 composite catalyst. The ZSM5 synthesized by another worker was used. The raw material, the synthesized zeolite Y and the catalysts formulated were characterized using X-ray diffraction technique (XRD), X-ray fluorescence technique (XRF), BET technique, Scanning electron microscopy (SEM), Transmission electron microscopy (TEM), and Thermogravimetry analysis (TGA). The acidity of the formulated catalysts were determined using pyridine probe acidity test. The catalytic performance of the catalysts was determined using fixed bed catalytic cracking reactor and n-hexadecane as the feed oil. The zeolite synthesized was also tested in microwave assisted desulfurization application of a model diesel. The results generated were analyzed using mathematical and graphical methods and conclusions were drawn.

1.5 Research Justifications

i. The huge kaolin deposits in Nigeria will be better harnessed economically.

ii. Production in the Nigerian refineries can be sustainably maintained as it will gradually reduce its dependence on imported catalyst.

iii. Huge job opportunities will be generated.

iv. This will contribute immensely to actualizing the Nigerian Content Initiative Policy.

CHAPTER 2

2.0 LITERATURE SURVEY

2.1 Zeolite

Zeolites are crystalline microporous, aluminosilicate minerals, with a unique three or two dimensional structural pattern of arrays of uniform pores, cavities and channels in molecular dimensional order. They are referred to as solid acids with fascinating chemisorptions, high selectivity and thermal stability properties (David, 2007). They are also referred to as "molecular sieves." due to their ability to selectively sort molecules based primarily on a size exclusion criterion, this is due to their possession of very regular pore structure of molecular dimensions. The pores are interlinked in a regular fashion to make channels and cavities. The maximum size of the molecular or ionic species that can enter the pores of a zeolite is controlled by the dimensions of the channels. These are conventionally defined by the ring size of the aperture, for example, the term "8-ring" refers to a closed loop that is built from 8 tetrahedrally coordinated silicon (or aluminium) atoms and 8 oxygen atoms. These rings are not always perfectly symmetrical due to a variety of effects, including strain induced by the bonding between units that are needed to produce the overall structure, or coordination of some of the oxygen atoms of the rings to cations within the structure. Therefore, the pores in many zeolites are not cylindrical.

2.2 Historical Background

Natural zeolites were first discovered in cavities and vugs of basalts. The term zeolite was originally coined in the 18^{th} century by Swedish mineralogist, Axel Fredrik Cronstedt, in1756, he observed that upon rapidly heating the material stilbite, the stone began to “dance about” and produced large amounts of steam from water that had been adsorbed by the material.

Based on this, he called the material *zeolite*, from the Greek word; ζέω (*zeō*), meaning "boil" and λίθος (*lithos*), meaning "stone". At the end of the 19th century, they were also found in sedimentary rocks. As a result of many geological explorations, zeolite formation was considered to include the following genetic types:

1. Crystals resulting from hydrothermal or hot-spring activity involving reaction between solutions and basaltic lava flows.
2. Deposits formed from volcanic sediments in closed alkaline and saline lake-systems.
3. Similar formations from open freshwater-lake or groundwater systems acting on volcanic sediments.
4. Deposits formed from volcanic materials in alkaline soils.
5. Deposits resulting from hydrothermal or low-temperature alteration of marine sediments.
6. Formations which are the result of low-grade burial metamorphism.

With geological exploration and study on minerals, more and more natural zeolites have been discovered. Up to now, over 40 types of natural zeolites have been found. Because natural zeolites could not meet the huge demands in industry, it became an urgent necessity to use synthesized zeolites besides the natural ones (Xu *et al.*, 2007).

The first attempt to synthesize zeolitic materials artificially was by St. Claire-Deville in 1862. He attempted by simulating the geological conditions under which zeolites were believed to form in nature. However, a major success was not recorded until in 1948 when Barrer reported the first definitive synthesis of an analogue of a natural zeolite via the hydrothermal synthetic method (Guisnet *et al.*, 2002). In 1949 researchers at Union Carbide, led by R.M. Milton developed the first reliable hydrothermal zeolite synthesis at low temperature (~100 $^{\circ}$C) and low pressure

(autogenous) using alkali metal aluminosilicate gels. They prepared a series of synthetic zeolites, including the zeolites A, X, and Y that the company commercialized in 1954 as a new class of industrial materials for separation and purification. In 1956, Linde Type A, the first commercial zeolite was synthesized (Dyer, 1988).

In the early 1960s, Barrer and Denny (1961) were the first to carry out synthesis of zeolites using organic alkylammonium cations instead of alkali metal cations. The organic cation acts as a structure directing template in the synthesis of the zeolites and also resulted in an increase in the Si/Al ratio (Guisnet *et al.*, 2002).

In 1962, Mobil Oil introduced the use of synthetic zeolite X as a cracking catalyst, followed by the synthesis of a more efficient, higher performance and more stable zeolite Y and later the high silica ZSM5 and zeolite beta which outperformed the earlier zeolites X and Y. At present, synthetic zeolites are used commercially more often than natural zeolites due to the purity of their crystals and their structural regularity and uniformity. However, the preparation of synthetic zeolites from chemical sources of silica and alumina is expensive. Such costs may be reduced by the use of geomaterials especially clays as supports in the fabrication of the final zeolite catalyst.

2.3 Occurrence of Zeolites

Zeolites occur naturally as low temperature, low pressure minerals formed where volcanic rocks and ash layers react with alkaline ground water at low temperature between 27°C to 55°C, and typical pH value between 9 and 10. Nature requires 50 to 50,000 years to complete the reaction.

Zeolites are usually white but sometimes may be coloured; pink, brown, red, yellow or green by inclusion (Oliver, 2000). The appearance of a natural zeolite is as shown in Plate I.



Plate I: Image of natural zeolite (http://en.wikipedia.org/wiki/zeolite, 2014)

Zeolites also crystallize in post-depositional environments over periods ranging from thousands to millions of years in shallow marine basins. Naturally occurring zeolites are rarely pure and are contaminated to varying degrees by other minerals, metals, quartz, or other zeolites. For this reason, naturally occurring zeolites are excluded from many important commercial applications where uniformity and purity are essential.

2.4 Application of Zeolite

Zeolites are used in wide range of commercial and domestic applications. Such applications include; usage as adsorbents for drying and purification of gases and for bulk separation of, for example, normal-/iso-paraffins, isomers of xylenes and olefins, and O_2 from air. They are used as catalysts for petroleum refining and petrochemical processes, as adsorbents and ion exchangers in water purification (Cejka *et al.*, 2010). They are also used as detergent builder and auxiliary agents in the soap and detergent industry. Also zeolites are used to trap harmful fission products in radioactive waste treatment and storage, and in the treatment of industrial liquid wastes. However, their biggest use is in the production of laundry detergents. They are

also used in medicine and in agriculture. Zeolites such as Y, ZSM5, Modernite and Zeolite beta, possess exclusive catalytic properties, such as high surface area, excellent pore volume, pore radius and pore distribution. Furthermore, they possess high acidity active sites and high thermal stability. These phase-pure microporous zeolites are widely used as acid catalysts in a diversity of commercial processes, especially in the petroleum and petrochemical industries. Therefore, Since 1950s, there have been three traditional fields of application for molecular sieves and porous materials: 1) separation, purification, drying and environment treatment process; 2) petroleum refining, petrochemical, coal and fine chemical industries; 3) ion- exchange, detergent industry, radioactive waste storage, and treatment of liquid waste (Cejka *et al.*, 2010). In addition to the traditional application fields, zeolites and related porous materials may also find applications in new areas such as microelectronics and molecular device manufacture. Applications of zeolites can be discussed under the following headings.

2.4.1 Commercial and domestic applications

Zeolites are widely used as ion-exchange beds in domestic and commercial water purification, softening, and other treatments. As molecular sieves, zeolites are used to separate molecules; only molecules of certain sizes and shapes can pass through. Zeolites have the potential of providing precise and specific separation of gases including the removal of H_2O, CO_2 and SO_2 from low-grade natural gas streams (Dyer, 1988).

2.4.2 Petrochemical industry

Synthetic zeolites are widely used as catalysts in the petrochemical industry, for instance in fluid catalytic cracking and hydro-cracking. Zeolites confine molecules in small spaces, which cause

changes in their structure and reactivity. The hydrogen form of zeolites (prepared by ion-exchange) are powerful solid-state acids, and can facilitate a host of acid-catalyzed reactions, such as isomerisation, alkylation, and cracking. The specific activation modality of most zeolitic catalysts used in petrochemical applications involves quantum-chemical Lewis acid site reactions (Mravec, *et al*., 2005). Zeolites are also employed in the drying and purification of natural gas, separation of paraffins and desulfurization processes. The main applications of zeolites in petroleum industry are summarized in Table 2.1 (Mravec, *et al*., 2005).

Table 2.1: Major applications of zeolites in the petroleum industry

Process	Catalyst	Products
Catalytic cracking	RE-Y, US-Y, ZSM5	Gasoline, fuels
Hydrocracking	Y, Mordenite + Mo, W, Ni	Y, Mordenite + Mo, W, Ni
Alkylation of aromatics	ZSM5, Mordenite	p-xylene, ethyl-benzene, styrene
Hydroisomerization	Mordenite + Pt, Pd	i-pentane, i-hexane
Xylene isomerization	ZSM5	p-xylene
Catalytic dewaxing	Mordenite, ZSM5 + Ni, noble metal	Improved cold flow properties
Transalkylation	Mordenite	Xylenes, cumene
Methyl Tertiary Butyl Ether (MTBE)	ZSM5	Aromatics, paraffins
Methanol-to-Gasoline (MTG)	Ga-ZSM5	Aromatics

Where; RE-Y means rare earth ion exchanged Y-type zeolite.
US-Y means ultra-stable zeolite Y and Ga-ZSM5 means gallium ion exchanged ZSM5.

2.4.3 Nuclear industry

Zeolites have uses in advanced reprocessing methods, where their micro-porous ability to capture some ions while allowing others to pass freely allow many fission products to be efficiently removed from nuclear waste and permanently trapped. Equally important are the mineral properties of zeolites. Their alumino-silicate construction is extremely durable and resistant to radiation even in porous form. Additionally, once they are loaded with trapped fission products, the zeolite-waste combination can be hot pressed into an extremely durable ceramic form, closing the pores and trapping the waste in a solid stone block. This is a waste form factor that greatly reduces its hazard compared to conventional reprocessing systems (New York Times, 2011).

2.4.4 Construction industry

Synthetic zeolite is also being used as an additive in the production process of warm mix asphalt concrete. The development of this application started in Germany in the 1990s. It helps by decreasing the temperature level during manufacture and laying of asphalt concrete, resulting in lower consumption of fossil fuels, thus releasing less carbon dioxide, aerosols, and vapours. Other than that, the use of synthetic zeolite in hot mixed asphalt leads to easier compaction and, to a certain degree, allows cold weather paving and longer hauls. When added to Portland cement as a pozzolan, it can reduce chloride permeability and improve workability. It reduces weight and helps moderate water content while allowing for slower drying which improves break strength (Andrejkovicova, 2012).

.

2.4.5 Heating and refrigeration

Zeolites can be used as solar thermal collectors and for adsorption refrigeration. In these applications, their high heat of adsorption and ability to hydrate and dehydrate while maintaining structural stability is exploited. This hygroscopic property coupled with an inherent exothermic (heat-producing) reaction when transitioning from a dehydrated to a hydrated form make natural zeolites useful in harvesting waste heat and solar heat energy **(**Guglielmo and Lara 2007).

2.4.6 Detergents

The largest single use for zeolite is the global laundry detergent market. This amounted to 1.44 million metric tons per year of anhydrous zeolite A in 1992. Zeolite A is used in a very large scale in the detergent industry as detergent builder, used for softening hard water (http://en.wikipedia.org/wiki/zeolite, 2014).

2.4.7 Medical industry

Over the last several decades, numerous scientists, medical professionals, fitness/wellness consultants and alternative healthcare providers around the world have supported Research & Development into the many biochemical and biomedical applications of zeolites, particularly the naturally occurring species heulandite, clinoptilolite and chabazite. These applications include detoxicants and decontaminants, vaccine adjuvants and antibacterial agents. They are also used for delayed release drug delivery, as antitumor adjuvants, as antidiarrheal agents, in hemodialysis, to improve bone formation, and in the treatment of diabetes mellitus. In 2009, James Flowers from North Carolina-based Eno Research, published the findings of a study in which volunteers consumed a suspension of clinoptilolite in water (or a placebo) for up to 30

days. All participants were monitored for clinically significant, deleterious changes in either of the urinary and serum electrolyte panel or the general metabolic panel. The zeolite group experienced a rapid and significant increase in the urinary excretion of one or more heavy metals being monitored for the study, while the placebo group was unchanged. Within a few days the measured levels had returned to, or nearly to baseline concentrations, but they then continued to drop until they levelled off and stabilized well below initial values. The investigators ultimately reasoned that the zeolite must be exerting an influence on urinary excretion of these toxicants. Ultimately, the result was attributed to the natural capacity of zeolite to exchange pre-loaded magnesium, potassium and calcium for heavy metals (Tatrai *et al*., 1992; Auerbach, *et al*. 2003).

2.4.8 Agricultural industry

In agriculture, clinoptilolite (a naturally occurring zeolite) is used as a soil treatment. It provides a source of slowly released potassium. If previously loaded with ammonium, the zeolite can serve a similar function in the slow release of nitrogen. Zeolites can also act as water moderators, in which they will adsorb up to 55% of their weight in water and slowly release it under planned demand. This property can prevent root rot and moderate drought cycles.

In animal husbandry, both natural and synthetic zeolites have been used in animal nutrition mainly to improve performance traits and, based on their fundamental physicochemical properties, they were also tested and found to be efficacious in the prevention of ammonia and heavy metal toxicities, poisonings as well as radioactive elements uptake and metabolic skeletal defects. It was also discovered to improve feed conversion, reduce airborne ammonia up to 80%, act as a mycotoxin binder, and improve bone density. It can also be used in general odour elimination for all animal odours. Zeolites are also used as nutritional supplement for humans.

Some clinoptilolite-based dietary supplements have demonstrated antioxidant activity in humans (Fukushima, 1980).

2.4.9 Other uses of zeolite

Being solid state acids zeolites keep the environment cleaner and safer in many ways. Several zeolites applications were initiated by environmental concerns, including reduction of toxic waste and energy consumption. Zeolites replaced harmful phosphate builders in powder detergents. Catalysts save energy and thereby reduce pollution. Moreover, processes require fewer steps, minimizing unnecessary waste and by-products. As solid acids, zeolites can remove atmospheric pollutants, such as engine exhaust gases and ozone-depleting CFCs. Zeolites can clean water by separating out harmful organics and removing heavy metal ions, including radioactive ones produced by nuclear fission (David, 2007).

2.5 Classification of Zeolites

Zeolites are generally classified according to their structural or acidic nature under the following headings:

1. Based on pore size (Ruren *et al*., 2007):

   Microporous; having pore diameter < 2 nm

   Mesoporous; having pore diameter 2 – 50 nm

   Macroporous; having pore diameter > 50 nm

2. Based on acidity (determined by silica (Si/Al) ratio): Low

   silica: Si/Al ratio of 1.0 - 1.5, e.g. Zeolite X Intermediate

   silica: Si/Al ratio of 2.0 - 3.0, e.g. Zeolite Y

   High silica: Si/Al ratio of 10 - 250, e.g. zeolite ZSM5.

In addition extreme case of pure-silica zeolites have also been discovered, e.g. Silicate-1 (Xu *et al.*, 2007).

There are more than 50 known different families of zeolites, among which are; Amicite, Analcime, Barrerite, Bellbergite, Bikitaite, Boggsite, Brewsterite, Chabazite, Clinoptilolite, Cowlesite, Dachiardite, Edingtonite, Epistilbite, Erionite, Faujasite, Ferrierite, Garronite, Gismondine, Gmelinite, Gobbinsite, Gonnardite, Goosecreekite, Harmotome, Herschelite, Heulandite, Laumontite, Levyne, Maricopaite, Mazzite, Merlinoite, Mesolite, Montesommaite, Mordenite, Natrolite, Offretite, Paranatrolite, Paulingite, Pentasil (also known as ZSM5), Perlialite, Phillipsite, Pollucite, Scolecite, Sodium Dachiardite, Stellerite, Stilbite, Tetranatrolite, Thomsonite, Tschernichite, Wairakite, Wellsite, Willhendersonite, and Yugawaralite (Ruren *et al*., 2007).

2.5.1 Framework types

As at 2014, 206 types of zeolites and related frameworks have been recognized by the International Zeolites Association (Baerlocher, and McCusker, 2014; Iyoki *et al*., 2014). Some of the earlier synthetic zeolites include zeolites A, X, Y, L, ZSM5 and omega (Vermeiren *et al.,* 2009). The framework classifications of zeolites are based on their structural topology, while their family classifications are based on their mineral composition. Each framework type is assigned a three-capital-letter code in alphabetical order. The codes are generally derived from the names of the type materials. They only describe and define the network of corner sharing tetrahedrally coordinated framework atoms. Framework types do not depend on composition, distribution of the T-atoms (Si, Al, P, Ga, Ge, B, Be, etc.), cell dimensions, or symmetry. Example

of the zeolite framework types include; FRA, PU, LTN, DFO, VNI, AET, LTL, CHI, SBS, EMT, FAU, SBT, MFI, LTA, TER, MTW, AET, AFS, OSI, and MWW among others (Treacy et al., 2002).

2.6 Zeolite Structure

Zeolite comprises of TO_4 tetrahedral Primary Building Units (PBU). Through corner sharing, the PBU give rise to a three- dimensional four-connected framework. T atoms in the framework generally refer to Si, Al, or P atoms. In some cases, other atoms such as B, Ga, Be, and Ge, etc., are also involved. The T atom is at the center of each tetrahedron, O atoms are at the vertices of the tetrahedron, the pictorial view the TO_4 tetrahedral is as shown in Figure 2.1a. "Vertex O atoms are each shared by two tetrahedrons so that every T atom within the tetrahedral cage is bound to four neighbouring caged atoms through an O atom, as shown in Figure 2.1b (Xu *et al.*, 2007).

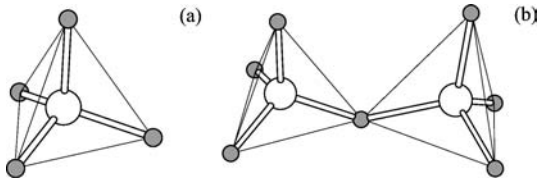


Figure 2.1: Zeolite unit structure (a) TO_4 tetrahedron (b) TO_4 tetrahedron sharing a common vertex oxygen (Ruren *et al*., 2007)

2.6.1 Primary building units

The TO_4 which are mostly SiO_4, AlO_4 or PO_4 tetrahedral are the basic structural building units of a zeolite framework also referred to as primary building units. In a zeolite, each T atom is coordinated to four oxygen atoms with each oxygen atom bridging two T atoms, so the structural type of a zeolite can be described as the (4; 2)-connection, a pictorial view of the

arrangement is shown in Figure 2.2. However some zeolites, such as $AlPO_4$-21 and VPI-5, contain five- or six-coordinated Al atoms with one or two extra-framework oxygen species (OH or H_2O), as well as four-coordinated Al atoms. By omitting the OH and H_2O species, these frameworks have a hypothetical (4; 2)-connected framework. The aluminosilicate zeolites constructed from SiO_4 tetrahedral and AlO_4 tetrahedral possess an anionic framework, the negative charge of which is compensated by extra-framework cations (Xu *et al.*, 2007).

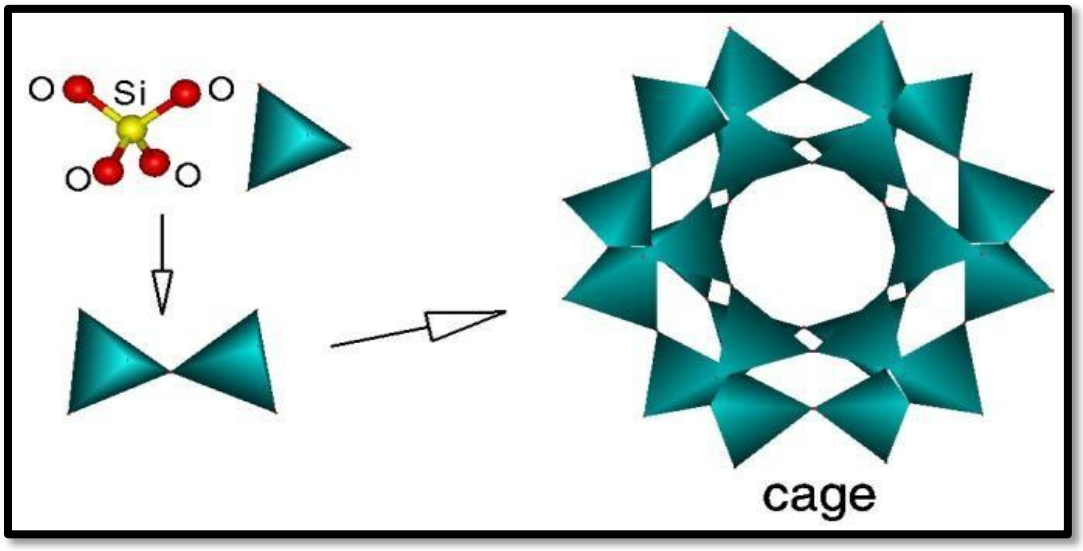


Figure 2.2: Zeolite unit structure illustration (Xu *et al.*, 2007)

2.6.2 Secondary building units (SBUs)

SBUs are theoretical topological building units. The framework of a zeolite can be thought of as being made of finite component units or infinite component unit-like chains and layers. 18 kinds of SBUs that have been found to occur in tetrahedral frameworks are shown in Figure 2.3. These SBUs, which contain up to 16 tetrahedrally coordinated atoms (T- atoms) are derived by assuming that the entire framework is made up of one type of SBU only. It should be noted that SBUs are invariably nonchiral. A unit cell always contains an integral number

of SBUs. One type of framework can comprise several SBUs. For example, the LTA framework contains five types of SBUs, including 4, 8, 4-2, 4-4, and 6-2 units, any of which can be used to describe its framework structure. In some instances, combinations of SBUs have been encountered, i.e., the framework cannot be generated by only one type of SBU. Examples include LOV, MEP, and other clathrasil- type frameworks.

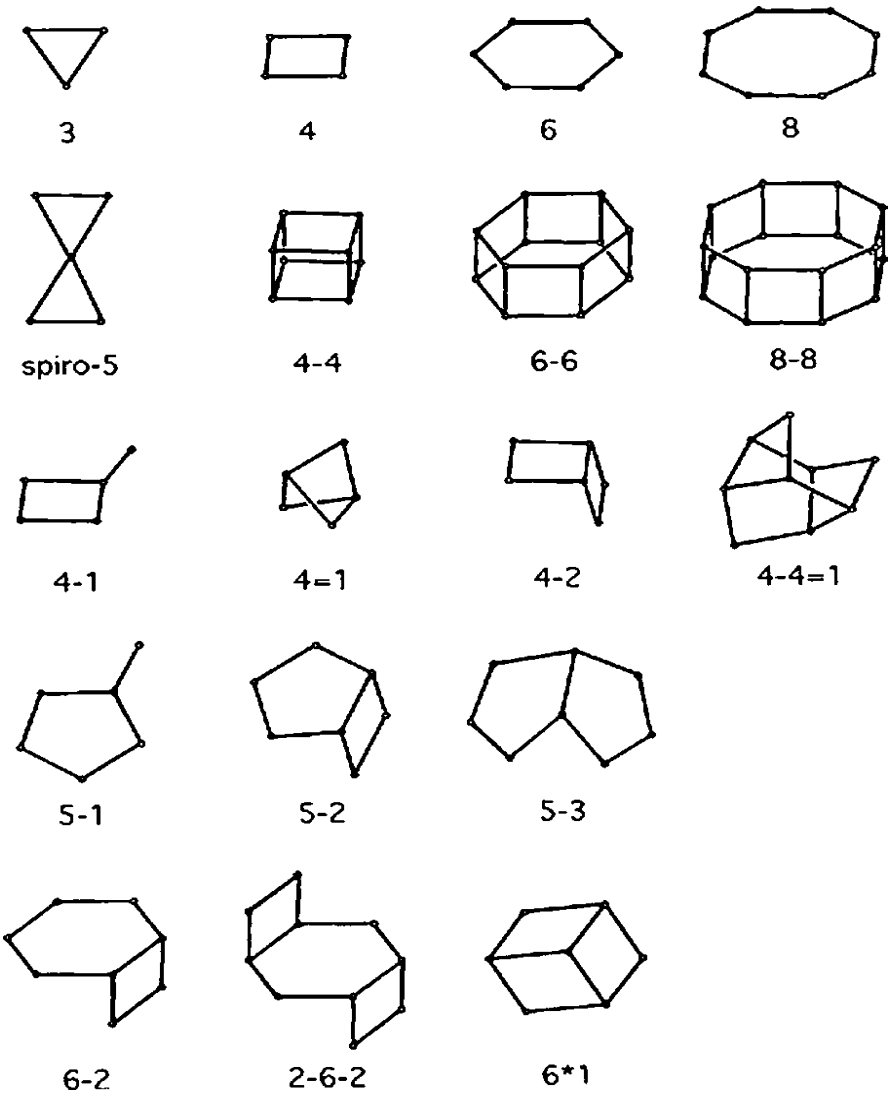


Figure 2.3: Unit secondary building unit (SBU) of zeolites (Xu *et al.*, 2007)

2.6.3 Characteristic cage-building units

There are some characteristic cage-building units in zeolite frameworks. Cages are generally described in terms of the n-rings defining their faces. For example, a truncated octahedron (sodalite unit), whose surface is defined by six 4-rings and eight 6-rings, would be designated a $[4^6 6^8]$ cage. Smith (1988), defined the names of parts of cages. It should be noted that a polyhedral pore, which has at least one face defined by a ring large enough to be penetrated by guest species, but which is not infinitely extended (i.e., not a channel), is called a cavity according to IUPAC recommendations. For example, the $[4^{12}6^8 8^6]$ polyhedron in zeolite LTA, traditionally called a cage, is actually a cavity. In this book the polyhedral are described in the traditional way. The cages occurring in the known zeolite frameworks are shown in Figure 2.4 (Ruren *et al*., 2007).

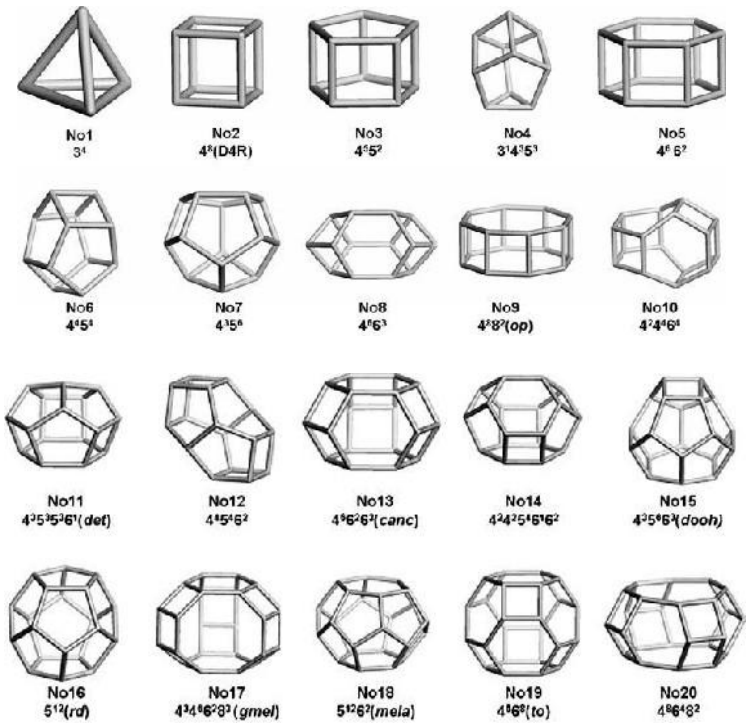


Figure 2.4: Some of the cage-building units in zeolites (Ruren *et al*., 2007)

Different zeolite frameworks may feature the same cage building unit, that is to say, the same cage-building unit may construct different framework types via different linkages. For example, starting from the SOD cage, the SOD structure is obtained when b-cages are linked by sharing 4-rings; the LTA structure is obtained when b-cages are linked through double 4-rings; FAU and EMT structures are obtained when b-cages are linked through double 6-rings (Ruren *et al*., 2007).

2.6.4 Characteristic chain and layer-building units

Some characteristic chain building units frequently occur in the zeolite frameworks. They are the double zig-zag chain, double sawtooth chain, double crankshaft chain, narsarsukite chain, and pentasil chain, respectively. The three double chains are all composed of edge-sharing 4-rings but with different orientations (up or down) of the fourth connection of a tetrahedron. The narsarsukite chain is found more often in AlPO4-based structures, whereas the pentasil chain, composed of edge-sharing [5^8] cages, is characteristic of the family of high-silica zeolites such as MFI and MEL. The zeolite structures may also be described by two dimensional (2-D) 3-connected nets. The most obvious way to generate the four-connected 3-D net from a 2-D three- connected net is to arrange one type of 2-D three-connected net into a parallel stack and to link each vertex to only one other vertex. To form a 3-D net, some of the new edges must point upward and some downward from each 2-D net. (Ruren *et al*., 2007).

2.7 Zeolite Production

As at the end of year 2011 the world‟ s annual production of natural zeolite was about 2.8 million tons. Of this quantity, 2.0 million tons were produced in China, 155,000 tons in Japan, 140,000 tons in Jordan, 240,000 tons in South Korea, 62,000 tons in USA, 235,000 in other countries. These statistics are illustrated in the pie chart shown in Figure 2.5 (Virta, 2012).

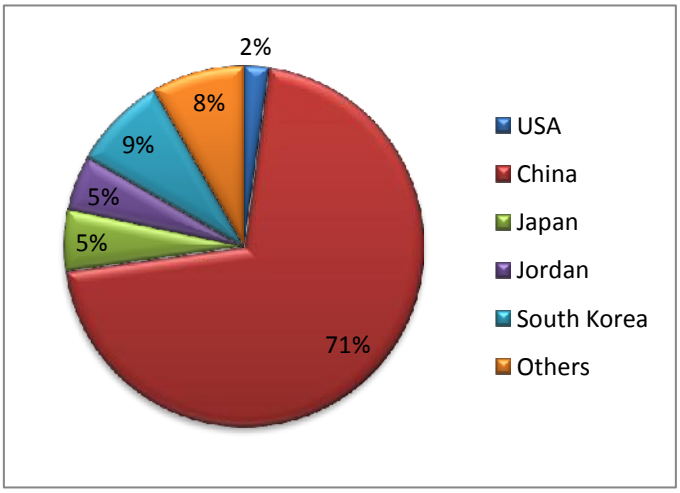


Figure 2.5: Chart illustration of world production of natural zeolites (Virta, 2012)

2.7.1 Traditional production

Conventional open pit mining techniques are used for mining natural zeolites. The overburden is removed to allow access to the ore. The ore may be blasted or stripped for processing by using tractors equipped with ripper blades and front-end loaders. In processing, the ore is crushed, dried, and milled. The milled ore may be air-classified as to particle size and shipped in bags or bulk. The crushed product may be screened to remove fine material when a granular product is required, and some pelletized products are produced from fine material.

2.7.2 Synthetic production

Since their successful introduction as commercial molecular sieves in 1954, synthetic zeolites production have grown to an estimate of $1.6 - 1.7 billion industrial consumption. Detergents represent the largest volume (Virta, 2012). LTA-type zeolites substitute phosphate compounds in the water softening process in laundry. There are several types of synthetic zeolites that are formed by a process of slow crystallization of a silica-alumina gel in the presence of alkalis and organic templates. One of the important processes used for carrying out zeolite synthesis is sol-gel processing. Zeolites can be synthesized hydrothermally starting from slow crystallization of a silica-alumina gel in alkaline environment using organic templates. The product properties depend on reaction mixture composition, pH of the system, operating temperature, pre-reaction 'seeding' time, reaction time as well as the templates used. In sol-gel process, other elements (metals, metal oxides) can be easily incorporated. The silicalite sol formed by the hydrothermal method is very stable. Also the ease of scaling up this process makes it a favourite route for zeolite synthesis.

Catalysts contain different components each of which is intended to affect the catalytic and/or physical properties in the catalytic applications the catalysts are intended for. In the case of FCC catalyst zeolite serves as the active ingredient for cracking higher molecular hydrocarbon feed to lighter petroleum fractions. More than 90% of catalytic cracking catalysts in the US are zeolite based (Oliver, 2000). The primary components of FCC catalyst are; zeolites, active alumina, binder, and fillers. The active alumina, binder and filler are often referred to as the support matrix. The relative percentages of each of these in the catalyst formulation will affect the

catalyst performance. In addition, each of these components may consist of one or more types and have been processed in one of several different ways.

Furthermore, the intrigue properties that are exploited in the catalysis of zeolites include:

i. Combines properties of excellent thermal stability even at 800°C, and above, and they are of pore size of molecular dimensions.

ii. Almost all reactive surface area and attendant acid sites of zeolite are located within the internal pore structure (>99%).

iii. Catalytic chemistries occur within the pores.

iv. A gram of zeolite has a surface area of 900 m^2 (Oliver, 2000).

v. High concentration of active acid sites, their high thermal stability, and high size selectivity make zeolites the catalyst of choice in refining operations.

vi. Zeolite catalysts have been the primary catalyst type used in refining in the last two decades. Zeolite catalysts can operate in the presence of substantial concentration of ammonia in marked contrast to other silica-alumina catalysts.

vii. Catalyst life of up to 7 years has been obtained commercially in processing heavy gas oils. Zeolites have up to 10,000 times the activity of so-called conventional catalysts in specific cracking tests.

viii. In the monomolecular mechanism, an alkane (paraffin) is protonated by a Brønsted acid site to form a five-coordinated carbon atom. The carbonium ion may undergo cracking to yield an alkane and an alkene, regenerating the acid site or it may dehydrogenate to yield H_2 and an alkoxide species. Desorption of the alkoxide yields an olefin and regenerates the acid site.

ix. Reactants are physico-absorbed in the pores of the zeolites (dominant interactions are the van der Waals interaction) and at high temperature are activated through proton transfer from the Brønsted acid sites. Because the rate-limiting step of monomolecular cracking is the protonation of the alkane, this reaction is an acid-base reaction between the zeolite and the alkane. Therefore, its intrinsic rate is a measure of zeolitic acidity (Oliver, 2000).

x. The better the fit between pore and reactant, the higher the observed rate per Brønsted acid site of the reaction (Xu *et al.*, 2007).

xi. Crystalline structure of zeolites provide higher activities and controlled selectivity compared to amorphous silica-aluminas.

2.8 Methods of Synthesis of Zeolites

Broadly speaking, synthesis of crystalline solid-state materials can be categorized into two major groups; those where the synthesis reaction takes place in the solid state and those where it takes place in solution. The solid-state method usually requires rather high temperatures above 300°C to overcome difficulties in transporting the reactants to the sites of the reaction. The other group are those carried out in liquid phase in the presence of a liquid solvent (Cejka *et al.*, 2010). Since molecular transport in the liquid phase is obviously much easier than in solids, syntheses in this category are carried out at a relatively lower temperature, lower than 300°C. Hence, the synthesis of zeolite falls under the latter category. There are three methods of synthesis of zeolite, they are as discussed in the following sections.

2.8.1 Hydrothermal method

Hydrothermal method is the earliest method of synthesis of zeolite in which synthesis is carried out in the presence of water as solvent, base solution as mineralizer and at temperature range of 90 – 180°C. The most common method of accomplishing hydrothermal synthesis is to seal the reactants inside Teflon-lined autoclaves so that there is also significant autogenous hydrothermal pressure produced, often up to 15 bar. The lower temperatures required for hydrothermal synthesis often lead to kinetic control of the products formed, and it is much easier to prepare metastable phases using this approach than it is using traditional solid-state approaches. The important reaction and crystallization processes in hydrothermal synthesis do not necessarily take place in solution (although, of course, they can) but can occur at the surfaces of gels present in the mixtures (Cejka *et al.,* 2010).

2.8.2 Solvothermal method

Solvothermal synthetic method refers to the general class of using a solvent in the synthesis of materials. Though hydrothermal will also fall as a member under this general classification, moreover, because water is by far the most important solvent, hence the special usage of the term hydrothermal to describe its use. Nevertheless, there are many other possible solvents such as alcohols, hydrocarbons, pyridine, and many others that have been used with proven successes for zeolite synthesis. The solvents used in solvothermal synthesis vary widely in their properties, from nonpolar and hydrophobic to polar and hydrophilic (Cejka *et al.,* 2010).

2.8.3 Ionothermal method

Ionothermal is another special category of solvothermal synthesis in which the solvent used are mainly ionic compounds and are not molecular in nature as in the case of the solvothermal solvents. The solvents used in the ionothermal method are referred to as ionic liquids (ILs). Their ionic nature imparts particular properties, including low vapour pressures (Cejka *et al.*, 2010).

2.9 Safety Considerations for Zeolite Synthesis

Zeolite synthesis like other laboratory experiments require the normal precautions which apply to any chemistry laboratory in order to protect both equipment and the investigator. In addition to these, extra safety measures are needed when the synthesis involves high pressure and/or use of templates. Therefore, certain precautions should be called to the attention of the inexperienced operator.

2.9.1 Source materials

Silica and alumina are inert in most forms, but ingestion of dust should be avoided. The alkoxides are skin irritants and should be handled with gloves and in a hood. Hydrofluoric acid (HF) is corrosive and skin contact or inhalation must be avoided. Likewise strong caustic is corrosive to skin and equipment. Gloves and a face mask are required, and the experiment should be done in a hood. In one case an "overflow" occurred when an inexperienced student put all the powdered aluminium required for a synthesis into a caustic solution. The exothermic dissolution heated the solution, accelerated the dissolution autocatalytically, and resulted in "boil over." Obviously, if hydrogen is given off, danger of explosion exists. The use of aluminium wire, which dissolves more slowly, is suggested. Organic templates cover a wide range of volatility

and toxicity. In many cases these materials are quite rare and their toxicity may not be well defined. Some are known to be biologically active; in all cases the investigator should avoid skin contact or inhalation by using gloves and working in a hood. In some cases, the potential exists for explosive decomposition of the template under crystallization condition. There is no good way to rule out this possibility, but a strong exotherm in the thermal analysis curve of the template indicates it should be treated with caution. No preparations in this book use beryllium (Be) or thallium (Tl), but reports can be found in the literature of zeolite syntheses using these materials. Be and Tl are extremely toxic and should be used only by experts who thoroughly understand the necessary precautions (Cejka *et al.*, 2010).

2.9.2 Batch preparation

The hazards of handling strongly caustic materials are increased when the solutions are hot. Gloves and face mask are still more important. Hydrolysis of the alkoxides produces heat; this may not be a problem in gram quantities but becomes so with scale-up. The alcohol produced is often removed by evaporation which can be a fire hazard. High-speed mixers can be splash hazards unless totally contained (Cejka *et al.*, 2010).

2.9.3 Crystallization

Zeolite crystallization is usually done at autogenous pressure at temperatures up to 200°C. With water present, this can mean pressure up to 15 atm. When organic templates are present, the pressure can be considerably higher. The manufacturer's specifications for the autoclave must be carefully considered. The liquid filling of the cold autoclave should not exceed 75%; the expansion of liquid water between 25 and 200°C is not negligible. Teflon loses its strength above

200˚C. Teflon gaskets and liners must be treated with caution at these temperatures. When working in metal autoclaves without liners, stainless steel exposed to caustic mixtures undergoes caustic embrittlement at temperatures above 200°C, which can quickly ruin an autoclave. To clean autoclave liners between experiments, strong, hot mineral acids are usually used, for example HNO_3. It takes copious amounts of rinse water to remove all the acid. Polypropylene jars may be used for crystallizations below 100°C. After extended use, they tend to spring a leak, as the bottom begins to separate. Although there is no danger of the jars bursting at this temperature, organic vapours are liberated, so that the oven or bath used for heating should be placed under a hood or have otherwise good ventilation. Sealed quartz tubes are often used as the crystallization container, especially for small quantities and high throughput. Also one can monitor progress of crystallization visually.

Quartz is a poor conductor of heat, but prolonged heating for sealing can heat the synthesis batch to boiling if the neck is too short. After crystallization, the quartz reactor should be opened behind a shield to protect the operator in case of residual gas pressure. Heat transfer by air, for example in an oven, is slow, and heating in a bath is preferred. As heating fluid, a polyglycol-type, which does not attack polypropylene, is recommended. Oil bath leaches plasticizer out of the polypropylene thus making the jar brittle and subject to cracking. Glycerol bath can be used, but has a relatively high vapour pressure (vapours condense on all surfaces in the lab making them sticky) and should be used under a hood. The temperature controls of a liquid bath should have a high-temperature shut-off to prevent overheating, in case the temperature controller fails. Combinations of organic templates and strong oxidizing agents such as chromate and permanganate are potential explosives, particularly in low-water conditions.

2.9.4 Product recovery

Opening the reaction vessel after crystallization should be treated with caution. Even when thoroughly cooled, residual gas pressure should be expected. Organic templates may degrade during the reaction; the products may be toxic and often cause a stench problem. The mother liquor after a templated synthesis may be a disposal problem. In most cases it should be collected for disposal as a hazardous chemical. The synthesis batch may crust over during crystallization and retain residual gas pressure. When the crust is penetrated, the contents may constitute a splash/missile hazard. A template not removed by washing is usually expelled by calcination. The template or its decomposition products are usually combustible and it is easy to start a fire. The heating equipment should be properly vented; if necessary nitrogen blanketed.

2.10 Zeolite ZSM5

ZSM5, which means Zeolite Sieve of Molecular porosity (or Zeolite Socony Mobil) – 5, (structure type MFI – mordenite framework inverted) is an aluminosilicate zeolite mineral belonging to the pentasil family of zeolites. Its chemical formula is $H_X\,[(AlO_2)_X\,(SiO_2)_{96-X}]\,.16H_2O$. ($0 < x < 27$). Patented by Mobil Oil Company in 1975, it is widely used in the petroleum industry as a heterogeneous catalyst for hydrocarbon isomerization reactions. ZSM5 is composed of several pentasil units linked together by oxygen bridges to form pentasil chains. A pentasil unit consists of eight five-membered rings as shown in Figure 2.6a. In these rings, the vertices are Al or Si and an O is assumed to be bonded between the vertices. The pentasil chains are interconnected by oxygen bridges to form corrugated sheets with 10-ring holes. Like the pentasil units, each 10-ring hole has Al or Si as vertex with an O assumed to be bonded between each vertex. Each corrugated sheet is connected by oxygen bridges to form a structure with straight

10-ring channels running parallel to the corrugations and sinusoidal 10-ring channels perpendicular to the sheets as shown in Figure 2.6b. Adjacent layers of the sheets are related by an inversion point. The estimated pore size of the channel running parallel with the corrugations is 5.4–5.6 Å (Mravec, *et al*., 2005; Ruren *et al*., 2007).

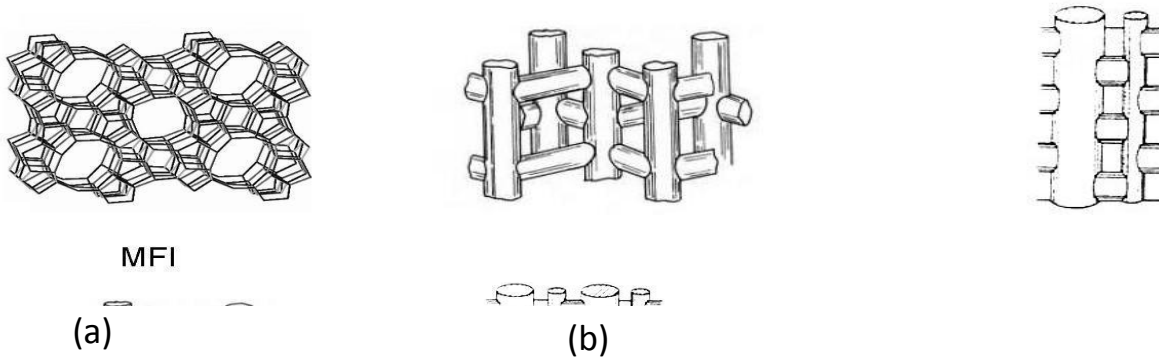


Figure 2.6: Pictorial illustration of MFI (a) eight membered ring framework (b) ten ring channel system (Ruren *et al*., 2007)

ZSM5 catalyst was first synthesized by Argauer and Landolt in 1972. It is a medium pore zeolite with channels defined by ten-membered rings. The synthesis involves three different solutions. The first solution is the source of alumina, sodium ions, and hydroxide ions; in the presence of excess base the alumina will form soluble $Al(OH)_4^-$ ions. The second solution has the tetrapropylammonium cation $N(C_3H_7)^+$, that acts as a templating agent. The third solution is the source of silica, one of the basic building blocks for the framework structure of a zeolite. Mixing the three solutions produces supersaturated tetrapropylammonium ZSM5, which can be heated to recrystallize and produce a solid.

As early as 1967, Argauer and Landolt worked out parameters for the synthesis of pentasil zeolites, particularly those relating to the following molar ratios: OH^-/SiO_2 = 0.07-10, SiO_2/Al_2O_3 = 5–100, H_2O/SiO_2 = 1–240. However, the Argauer and Landolt procedure

succeeded in synthesizing a reasonably pure phase ZSM5 zeolite only if organic amines with a structure-giving function (i.e. template function), such as tetrapropylammonium compounds were used. Subsequent publications have disclosed methods of conducting the synthesis of pentasil-zeolites without requiring the very expensive, toxic and easily inflammable organic amine templates. Still other subsequent publications have disclosed substitutes for these amines. In addition to their expense, toxicity and flammability, such amines are disfavored because they are subject to thermal decomposition which can destroy the zeolite structure. Further publications have disclosed modifications of the Argauer and Landolt process directed towards improving the reactivity of the SiO_2 and Al_2O_3 starting materials in the absence of organic template. The technique in this case involves; nucleation reaction with SiO_2 and Al_2O_3 starting materials at relatively high temperatures range of 180 - 210°C, followed by crystallization reaction at relatively low temperatures range of 130 - 170°C, until the crystallinity reaches substantially 100% with preference.

ZSM5 is a zeolite with a high silica and low aluminium content. Its structure is based on channels with intersecting tunnels. The aluminium sites are very acidic. The substitution of Al^{3+} in place of the tetrahedral Si^{4+} silica requires the presence of an added positive charge. When this is H^+, the acidity of the zeolite becomes very high. The reaction and catalysis chemistry of the ZSM5 is due to this acidity. The ZSM5 zeolite catalyst is used in the petroleum industry for hydrocarbon interconversion. An example of its usage is in the isomerization of xylene from meta to para-xylene. The acidic zeolite promotes carbocation isomerizations. And there are two suggested mechanisms for this type of isomerization. Firstly, the shape may play a role. Perhaps para-xylene has a shape which allows it to diffuse rapidly through the zeolite structure, whereas

as meta-xylene takes longer to pass through the zeolite and thus has more opportunity to be converted into the para-xylene.

Secondly, the orientation of reactive intermediates within the zeolite channels favours specifically para-xylene. In chemical processes, the progressive deactivation of solid catalysts is a major economic concern and mastering their stability has become as essential as controlling their activity and selectivity. For these reasons, there are strong motivations to understand the mechanisms leading to any loss in activity and/or selectivity and to find out the efficient preventive measures and regenerative solutions that open the way towards cheaper and cleaner processes.

2.11 Zeolite Y

Zeolite Y exhibits the FAU (faujasite) structure. It has a 3-dimensional pore structure with pores running perpendicular to each other in the x, y, and z planes similar to LTA, and is made of secondary building units 4, 6, and 6-6. The pore diameter is large at 7.4Å since the aperture is defined by a 12 member oxygen ring, and leads into a larger cavity of diameter 12Å. The cavity is surrounded by ten sodalite cages (truncated octahedral) connected on their hexagonal faces. Figure 2.7 shows a pictorial view of the FAU structure. The unit cell is cubic (a = 24.7Å). Zeolite Y has a void volume fraction of 0.48, with a Si/Al ratio > 1.5. It thermally decomposes at 793ºC. The chemical formula for NaY is $Na_7(AlO_2)_7(SiO_2)_{17}{:}32H_2O$. Zeolite Y, like zeolite A, is synthesized in a gelling process. Sources of alumina (sodium aluminate) and silica (sodium silicate) are mixed in alkaline (NaOH) aqueous solution to give a gel. The gel is then usually heated to 70-200ºC to crystallize the zeolite. The zeolite is present in Na^+ form and must be

converted to acid form. To prevent disintegration of the structure from acid attack, it is first converted to the NH_4^+ form before being converted to acidic form. If a hydrogenation metal such as platinum is needed, it is deposited via impregnation or ion exchange

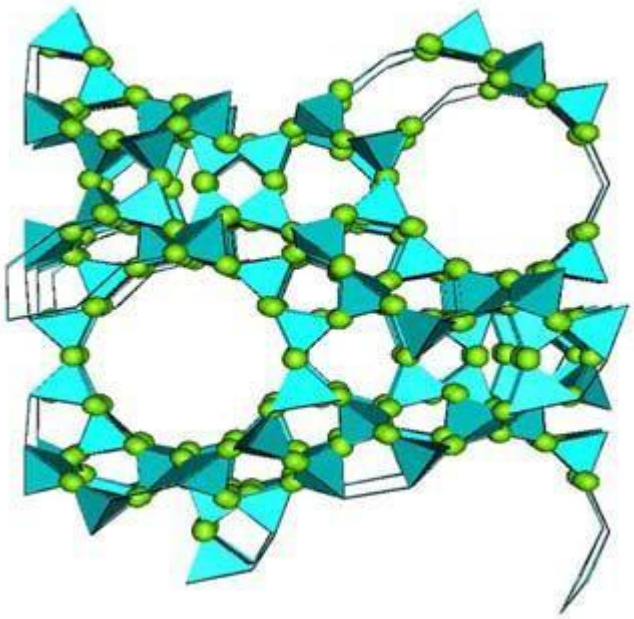


Figure 2.7: Structure of Faujasite Zeolite Y (David, 2007)

In the early 1950's it was recognized by Union Carbide Laboratories scientists that the tetrahedral aluminium positions in the zeolite frameworks provide a site of instability for attack by acid and water vapour of steam that make synthetic zeolites A and X less stable than their natural analogues. As a result of this, further research was embarked upon in the direction of making another zeolite of the same family as A and X which have superior stability characteristics reflecting higher Si/Al molar ratio > 1.5. Therefore, zeolites with higher content of silicon were needed, primarily to improve stability characteristics, both thermal and to acids. This lead to the discovery of third commercially important molecular sieve zeolites type Y, with an Si/Al ratio from 1.5 to 3.0, and a framework topology like that of zeolites X and the rare zeolites mineral faujasite, represented the first successful discovery in that row of compounds

made by D. W. Breck. Besides improvement in stability over the more aluminous X, the differences in composition and structures had a striking, unpredicted effect on properties making zeolites Y based catalysts valuable in many important catalytic applications involving hydrocarbon conversion since their initial commercial introduction in 1959 (Baerlocher *et al*., 2007). The most important use of zeolite Y is as a cracking catalyst. It is used in acidic form in petroleum refinery catalytic cracking units to increase the yield of gasoline and diesel fuel from crude oil feedstock by cracking heavy paraffins into gasoline grade naphtha. Zeolite Y has superseded zeolite X in this use because it is both more active and more stable at high temperatures due to the higher Si/Al ratio. It is also used in the hydrocracking units as a platinum/palladium support to increase aromatic content of reformulated refinery products (Bhatia, 1990).

2.12 Catalysis Using Zeolites

Eighty years ago it was the absorbability and the structure, particularly the subtlety of the structural changes that accompanied adsorption and desorption of gases and vapour on to and from zeolites that attracted the interest of many of the physico-chemical giants of the day, such as M. G. Evans and J. W. McBain (Auerbach *et al*., 2003). However, after the pioneer work on zeolite synthesis of R. M. Barrer, and later, D. W. Breck, W. and others, especially after the land mark paper of J. A. Rabo and C. L. Angell, it soon became apparent that zeolitic solids possessed enormous potential as heterogeneous catalysts, quite apart from their numerous advantageous properties as molecular sieves, ion-exchangers and membranes in separation science. The largest market value for zeolites is in refinery catalysis. Fluid Catalytic Cracking (FCC) catalysts account for more than 95% of zeolite catalyst consumption and consist of

various forms of zeolite Y. MFI-type zeolites are the second most used catalyst, primarily because they are added to FCC catalysts for octane number enhancement (Gary and Handwerk, 2001).

Most chemical transformations of petroleum hydrocarbons of a practical significance are carried out in the presence of catalysts. Catalysts lower the activation energy of chemical reactions and increase their rates appreciably. The catalysts perform this by reacting with the reactants only at the initial stage of the reaction and in the subsequent stages it is regenerated to regain its activeness to react with other fresh reactant molecules. Generally, any typical catalytic reaction will fall in either of the two broad classifications, which are homogeneous and heterogeneous catalysis.

2.12.1 Homogeneous catalysis

In homogeneous catalysis the catalyst and reactants form a homogeneous system, for example, gas mixtures, or liquid solutions. The mechanism of the reaction is explained quite well by the theory of intermediate chemical compounds. By this theory, a catalyst forms an unstable reactive intermediate with a reactant. The activation energy of this process is lower than that of non-catalytic basic reaction. Subsequently, the intermediate decomposes or reacts with a new molecule of a reactant, freeing the catalyst in an unchanged form. These transformations are characterized by comparatively low activation energy.

2.12.2 Heterogeneous catalysis

In heterogeneous catalysis, the catalyst is most frequently in the solid phase, while the reactants are in the gaseous or vapour state. Cases are possible where the reactants and catalysts are immiscible liquids. The most popular catalytic processes for producing fuel in the petroleum-refining industry are catalytic cracking, isomerization, reforming, alkylation, and hydrocracking.

In heterogeneous catalysis, all the changes and transformations of substances occur at the interface of the solid phase of the catalyst and the gas or vapour phase of the reactants and are associated considerably with the phenomenon of sorption. The process can be divided into the following five stages:

(1) Motion (diffusion) of the reacting molecules to the catalyst surface;

(2) Activated adsorption (chemisorption) of the reactant on the catalyst surface;

(3) A chemical reaction on the catalyst surface;

(4) Desorption (removal from the catalyst surface) of the reaction products;

(5) Diffusion of the products into the gaseous stage;

The rate of the whole process is determined by that of the slowest stage. Here two cases are distinguished. If diffusion of the reactants and products proceed more rapidly than the catalytic reaction itself, the rate of the process depends completely on the composition and properties of the catalyst surface. Such a process is said to be kinetically controlled. Conversely, if diffusion proceeds at a slower rate than all the transformations on the catalyst surface occur, the overall rate of the reaction will be determined by the rate of diffusion. Such a process is said to be diffusion-controlled. The activation energy in heterogeneous catalytic reaction is lowered as a result of involved physicochemical processes characterizing the stage of activated adsorption (chemisorption).

Chemisorption is the formation of a sufficiently strong mono-molecular layer of the reactants on the surface of a catalyst. It proceeds at the expense of the valence forces of the catalyst, is in essence close to a real chemical reaction, and therefore results in appreciable weakening of the bonds in the reacting molecules. The activated desorption of the reactant molecules occurs not on the entire free surface of a solid catalyst, but only on what are called active centers. Thus the mechanism of reaction of heterogeneous catalyst proceeds by collision of the reactant molecules with the active center of the catalyst. The collision leads to chemisorption which results into formation of various unstable intermediates (radical or ions). Both the rate of the reactions and the composition of their products depend on the reactivity and nature of these intermediates. When choosing and employing heterogeneous catalysts, one must take into account their selectivity, activity, and stability. The stability determines their service life.

2.13 Catalytic Cracking

Catalytic cracking is the process of breaking down the larger, heavier and more complex hydrocarbon molecules into simpler and lighter molecules to produce higher value products. It uses heat, pressure and a catalyst. The catalytic cracker consists of a furnace which preheats and vapourizes the feed oil, after which the riser transports the feed vapour into the reactor zone. Catalytic cracking was introduced to refining in the 30‟s in response to need for more gasoline and has superseded thermal cracking as it yields more of the desired high octane products. It can virtually double the yield of gasoline type products from a barrel of crude oil. There are two major types of catalytic cracking viz; fixed-bed catalytic cracking, and fluid bed catalytic cracking. In fixed-bed processes, the catalyst is in the form of small lumps or pellets in layers or beds in several (four or more) catalyst containing drums called converters.

Fluid catalytic cracking processes are the most widely used and are characterized by the use of finely powdered catalyst that is moved through the processing unit. The catalyst particles are of such a size that when aerated with air or hydrocarbon vapour, the catalyst behaves like a liquid and can be moved through pipes. The vaporized feedstock and fluidized catalyst flow together into a reaction chamber where the cracking reactions take place (Speight, 1999).

2.13.1 Mechanism of catalytic cracking

The major and the most widespread concept explaining the mechanism of catalytic cracking on zeolite catalyst is the carbonium-ion theory. It is based on the following notations expressed as in Equations 2.1 – 2.7.

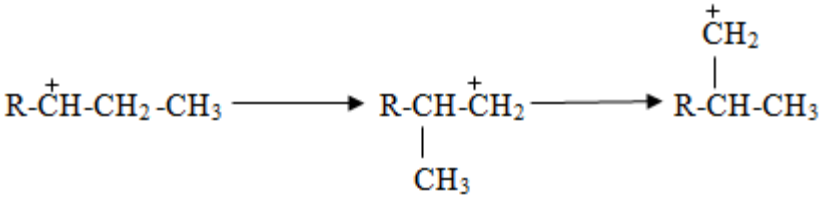
Carbonium ions are similar to their ammonium counterparts and contain a trivalent positively charged carbon atom. They form the easiest when a proton of the catalyst reacts with an alkene;

$$R\text{-}CH{=}CH_2 + H^+ \longrightarrow R\text{-}\overset{+}{C}H\text{-}CH_3 \qquad (2.1)$$

The participation of the catalyst hydrogen in the reaction has been proved by experiments with tracer atoms (deuterium). Carbonium ions form in the chemisorbed layer of molecules and are active intermediate of many reactions proceeding in catalytic cracking. The unstable carbonium ions tend to acquire more stable form by internal regrouping or reaction with other molecules. They are distinguished by a very high reactivity and can enter into the most diverse reaction.

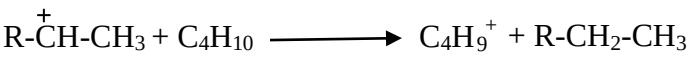
The following transformations are the most typical of carbonium ions (Erikh *et al.,* 1988).

1. Regrouping of the atoms in a molecule with the relocation of hydrogen or methyl groups, i.e. in other words, skeleton isomerization leading to the formation of an isomer ion:

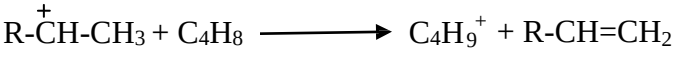


(2.2)

2. Reaction with neutral molecules with the formation of new carbonium ions and new saturated or unsaturated molecules:



(2.3)



(2.4)

Consequently, a carbonium ion can either detach a proton from other molecules or transfer its proton to alkenes and transform into a stable alkene.

3. A carbonium ion with a large number of carbon atoms generally decomposes at the β position (2nd bond), counting from the charged carbon atom. The decomposition products are alkene and a carbonium ion with a smaller number of carbon atoms:



(2.5)

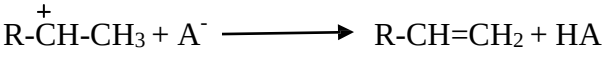
As a whole, by the carbonium ion theory, the mechanism of catalytic cracking is represented in the form of chain reactions. A chain is initiated under the action of a hydrogen ion of the catalyst:



(2.6)

Where HA signifies a silica-alumina catalyst in the form of an acid.

The chain propagates by diverse transformations of the carbonium ions and hydrogen exchange with neutral molecules. Finally, the chain terminates because of a reaction between a carbonium ion (cation) and an aluminosilicate anion:



(2.7)

The catalyst is regenerated as a result, and the process can begin again if the catalyst surface still retains its activity (Erikh *et al.,* 1988).

2.14 Fluidized Catalytic Cracking Unit

Fluid catalytic cracking (FCC) is the most important conversion process used in petroleum refineries. It is widely used to convert the high-boiling, high-molecular weight hydrocarbon fractions of petroleum crude oils to more valuable gasoline, olefinic gases, and other products. Cracking of petroleum hydrocarbons was originally done by thermal cracking, which has been almost completely replaced by catalytic cracking because it produces more gasoline with a higher octane rating. It also produces byproduct gases that are more olefinic, and hence more valuable, than those produced by thermal cracking. The feedstock to an FCC unit is usually that portion of the crude oil that has an initial boiling point of 340°C or higher at atmospheric pressure and an average molecular weight ranging from about 200 to 600 or higher. This portion of crude oil is often referred to as heavy gas oil. The FCC process vaporizes and breaks the long-chain molecules of the high-boiling hydrocarbon liquids into much shorter molecules by contacting the feedstock, at high temperature and moderate pressure, with a fluidized powdered catalyst (Wilson,1997). Basically, there are two different configurations for an FCC unit: the "stacked" type where the reactor and the catalyst regenerator are contained in a single vessel with the reactor above the catalyst regenerator and the "side-by-side" type where the reactor and catalyst regenerator are in two separate vessels. The preheated high-boiling petroleum feedstock (at about 315 to 430°C) consisting of long-chain hydrocarbon molecules is combined with recycle slurry oil from the bottom of the distillation column and injected into the catalyst riser where it is vaporized and cracked into smaller molecules of vapour by contact and mixing with

the very hot powdered catalyst from the regenerator. All of the cracking reactions take place in the catalyst riser. A typical riser has dimension of 5.7 m height and 0.102 m diameter. The hydrocarbon vapours "fluidize", the powdered catalyst and the mixture of hydrocarbon vapours and catalyst flow upward to enter the reactor at a temperature of about 535°C and a pressure of about 1.72 bar (Bose *et al.*, 2007). Since the cracking reactions produce some carbonaceous material (referred to as *coke*) that deposits on the catalyst and very quickly reduces the catalyst reactivity, the catalyst is regenerated by burning off the deposited coke with air blown into the regenerator. The regenerator operates at a temperature of about 715°C and pressure of about 2.41 bar (Bose *et al.*, 2007).

2.15 FCC Catalyst Formulation

Zeolite catalysts like other precious catalyst are not composed of the active ingredients only, but are composed of the active ingredients supported on a less active support material. The primary aim of applying a catalytically active component to a support is to obtain the catalyst in a highly dispersed form and hence in a highly active form when expressed as a function of the weight of the active component. This feature of supported catalysts is especially important with regard to precious material catalysts, because it allows more effective utilization of the material than can be achieved in its bulk systems. However, in the case of base-metal catalysts the use of the support is often primarily aimed at improving the catalyst stability. This can be achieved by suitable interaction between the active material and the support. For example: unsupported copper oxide is a very active oxidation catalyst but suffers from thermal instability at high temperatures. However, when copper oxide is supported on a high-surface-area alumina, its thermal stability is improved. A properly designed catalyst should have the essential attributes of

activity, stability, selectivity and regenerability. These can be related to the physical and chemical properties of the catalyst, which in turn can be related to the variable parameters inherent in the method used for the preparation of the catalyst. The principal catalyst-preparation technique involves two stages. First, rendering the catalytically active ingredient component into a finely dispersed form on a support and secondly; conversion of the supported active ingredient into a thermally stable state.

The first stage is known as dispersion and is achieved by impregnation, adsorption from solution, co-precipitation, or deposition, while the second stage is variously called calcination or reduction.[It is brought about by a thermal treatment in either an inert atmosphere or an active atmosphere of either oxygen or hydrogen depending on the type of catalyst in focus. When the active atmosphere is hydrogen the process is known as reduction. Although calcination/reduction can cause major problems in catalyst preparation on a large scale, it is a generalization to say that once the active species has been bound to the support surface its degree of dispersion and location will be retained during subsequent treatments. A wide range of techniques has been employed for the incorporation of a catalytically active species onto a support material. A summary of the most widely used techniques is given below (Kemball, 1981).

2.15.1 Impregnation

Impregnation as a means of supported catalyst preparation is achieved by filling the pores of a support with a solution of the metal salt from which the solvent is subsequently evaporated. The catalyst is prepared either by spraying the support with a solution of the metal compound or by adding the support material to a solution of a suitable metal salt, such that the required weight of

the active component is incorporated into the support without the use of excess of solution. This is then followed by drying and subsequent decomposition of the salt at an elevated temperature, either by thermal decomposition or reduction. With this method of preparation it is essential to have an understanding of both chemical and physical properties. This technique has been widely used for the preparation of small amounts of catalyst for basic studies,

2.15.2 Adsorption from solution

Adsorption is defined as the selective removal of metal salts or metal ion species from their solution by a process of either physio-sorption or chemical bonding with active sites on the support. Depending upon the strength of adsorption of the adsorbing species, the concentration of the active material through the catalyst particle may be varied and controlled. This technique is widely used in the preparation of industrial catalysts as it permits a greater degree of control over the dispersion and distribution of the active species on the support. In some systems, however, the weight of the active component that can be incorporated into the support is limited. Although multiple adsorption is often possible it is not recommended when close control of physical parameters is required.

2.15.2.1 Simple cation adsorption from solution

The equilibrium of the reaction involved is largely determined by the pK, of the surface acidic group and shifts to the right at a high solution pH. The affinity of the functional group for the metal ion determines the relative adsorption strength of the different metals and this is largely a function of the charge to radius ratio of the cation. Hence, the affinity of a given cation adsorber is generally in the same order as the cation charge $C^{4+} > C^{3+} > C^{2+} > C^{+}$ H^{+} and a high valent

cation, *e.g.* Cr^{3+}, would displace that of a lower valency, *e.g.* Cu^{2+}. A typical exchange reaction taking place is as expressed in Equation 2.8.

$$SOH^{+} + C^{+} \rightleftharpoons SOC^{+} + H^{+} \qquad (2.8)$$

Since zeolites are cation exchangers, this approach is most suitable for preparing their supported catalyst.

2.15.2.2 Simple anionic adsorption from solution

Here again the equilibrium would be pH dependent but in this case shifts to the left at a high pH. It is also dependent upon the ionic affinity which increases with anionic polarizability and ionic charge, ***e.g.*** , $I^{-} > Br^{-} > C1^{-} > F^{-}$ and $SO_4^{2-} > Cl^{-}$. A typical reaction taking place is as expressed in Equation 2.9.

$$S(OH)^{-} + A^{-} \rightleftharpoons SA^{-} + (OH)^{-} \qquad (2.9)$$

2.15.3 Co-precipitation

The preparation of supported catalysts by the co-precipitation of active ingredient ions with the support ions usually produces an intimate mixing of catalysts and support. An example of this technique is the co-precipitation of metal ions with aluminium ions to produce a precipitated alumina gel containing the metal hydroxide. This precipitate when calcined produces a refractory support with active component dispersed throughout the bulk as well as at the surface. However, in the preparation of multicomponent catalysts, it is possible under improper conditions to obtain a heterogeneous product because of the different solubility products of the constituents. Care should be taken therefore to avoid this undesirable situation by appropriate forethought (Kemball, 1981).

2.15.4 Deposition

Deposition, as used in preparing supported catalysts, is the laying down or placing of the active components on the exterior surface of a support. One means by which this may be achieved is the preparation of catalysts by sputtering, which involves condensing the active ingredient vapour onto an agitated finely dispersed support. However, as this process is performed under a high vacuum, the technique is probably only useful for the preparation of „model" catalysts. Alternatively, the process may be performed in the liquid phase by the deposition of a metal sol onto a suspended support.

The art of catalyst preparation is, has been, and probably always will be the art of preparing a material or suitable combination of materials in a highly dispersed form, and in maintaining that dispersion and combination against every natural thermodynamic tendency towards agglomeration. All the techniques of catalyst preparation discussed earlier reduce to two simple steps, dispersing the active material in a liquid or gaseous form and immobilizing this dispersed material as it is reconverted to an insoluble solid form. Broadly speaking there are two ways of doing this. Either one converts the material itself to an insoluble form or one allows it to react with an insoluble support surface. If one chooses the latter, it is necessary that the support surface should be reactive with the soluble or gaseous active material. The majority of commercial catalysts of interest are typified by this second approach for the reason that in this way an atomic dispersion is in principle possible and in practice more closely approached. For low-surface area generally unreactive supports, however, the former approach must necessarily be used. With many of the compounds used for catalyst impregnation hydrolysis giving colloidal solutions is always a possibility and may not always be recognized.

2.16 Catalyst Design Parameters

For catalyst design purposes it is first necessary to translate the catalyst performance parameters into a physical picture of catalyst structure. As we shall see, different performance parameters can give rise to different structural features and so a compromise is generally required. For example it is commonly found in industrial applications that initial catalyst activity may be sacrificed in favour of improved catalyst stability, since a lower activity and a prolonged operating catalyst life is in general preferable to a higher initial activity that decays rapidly. First, we should therefore discuss some of the relationships between the catalyst performance parameters and physical structure.

2.16.1 Activity

In general activity arises from maximizing both the dispersion and availability of the active catalytic material. Ideally, from an activity viewpoint, the catalyst material should be highly dispersed and concentrated on the external surface of the support. Already, however, there is an inherent conflict as high concentrations of active material become progressively more difficult to disperse.

2.16.2 Stability

By stability we refer to the loss in activity with time. This is due to one or several of four main causes; fouling of the active surface with non-volatile reaction by-products, sintering of crystal growth of the active material, poisoning of the active surface by feed impurities, and blockage of the support pore structure. Sintering during catalyst use is usually not a problem if catalysts are properly designed for their end use, although it is perhaps an important problem during catalyst

preparation, activation, and reduction if the impregnated metal is not bound to the support surface. It also becomes an important factor under the more severe conditions imposed during catalyst regeneration. Fouling of the active surface by reaction by-products is a real problem, which typically can be partially met by selective poisoning of the active ingredient. In a general sense the use of bimetallic supported catalysts would also commonly fall into this category, since selective poisoning implies a close control over the ratio of poison to active material. In this case a severe constraint is imposed upon catalyst design in that both active and moderating components should ideally be in a constant ratio throughout the catalyst support, that is to say, the placement of both should be the same. Poisoning of the catalyst by impurities introduced with the reactants can often be minimized by placing the active material deep within the catalyst support structure, and since most catalyst supports are also good absorbents, poisons frequently can be selectively removed by such absorption before reaching the active surface. An example would be the removal of traces of lead and phosphorous from a car exhaust by the surface of the catalyst support. A catalyst design modification of this same technique would be the deposition of a poison-resistant catalyst component close to the surface and a poison-sensitive component deep within the support. This technique can be taken even further; an inert material can be used as a poison trap close to the support‟ s external surface. In this way each catalyst support particle can be viewed as coming complete with its own catalyst guard bed. Once again for poison resistance the location of the active component becomes a critical factor in proper catalyst design. Finally, blockage of the support-pore structure is critically dependent upon the pore-size distribution of the support. Normally a correct balance of large and small pores is required; the former to aid reactant transport and the latter to provide the large surface necessary for the optimal dispersion of the active components. Whereas one might intuitively expect that small

pores would block more readily, an important exception has only recently been recognized in the case of ZSM 5 type zeolites; the structure is small enough to prevent the formation of the high molecular weight non-volatile by-products that normally are the pore blocking agents, and yet is still large enough to allow for the transport of reactants and products to and away from the catalytically active sites (Anderson *et al*., 1979).

.

2.16.3 Selectivity

Catalyst selectivity can change due either to physical or chemical reasons. For sequential reactions diffusivity and mass transport through the pore structure can lead to apparent loss in selectivity in the formation of intermediate products. Location of active ingredients and pore-size distributions are therefore of importance. Changes in selectivity can also arise from changes in intrinsic chemical activity of the active component. Typically this can be affected by use of multicomponent catalysts in which case, as was seen earlier for stability improvement, the location of the different components ideally should be the same. A specific example of this type of selectivity arises in the case of multifunctional catalysts in which a hydrogenation function is combined with an acid function. Since the latter is typically provided by the support and the former by the impregnated material, a uniform impregnation is required. The selectivity of a product in a chemical reaction is expressed as shown in Equation 2.10 (Taufiqurrahmi *et al*., 2010).

$$\text{Selectivity} = = \frac{\text{Product yield}}{\text{Reaction conversion}} \text{X}\,100\% \qquad (2.1)$$

(2.10)

2.16.4 Regenerability

Regenerability refers to the reactivation of a catalyst, which typically will involve an air calcination followed in some cases by a re-dispersion of the active components. From the catalyst design viewpoint, this will generally imply enhanced thermal-hydrothermal stability of the support itself, combined with stability of the active components under the high temperature oxidizing environments required for the oxidation of the deactivating carbonaceous deposits. It is now generally recognized that many metals sinter more readily under oxidizing conditions and in extreme cases may even dissolve in the underlying support and become effectively removed from the reaction system. A further complication arises with multicomponent catalysts in which the combination ratio is all important, since such combinations frequently are destroyed under oxidizing conditions. Summarizing this Section, the activity, stability, and selectivity are determined by the correct dispersion and location of the active ingredients. Dispersion, location, and regenerability are each in their turn determined by the interaction of the active components with the support surface and with each other during preparation, activation, use, and regeneration (Kemball, 1981).

2.17 Some Past Related Works on Zeolite Y Synthesis

Barth-Wirshing *et al*., (1993) synthesized zeolites from waste perlite at 100 – 140˚C in NaOH solutions with the addition of aluminium. They succeeded in obtaining hydroxysodalite as the synthesis product. Wajima *et al*., (2006) synthesized zeolite Na-P1 zeolite from mixture of paper sludge ash and diatomite. NaOH solution was used as the reaction medium and hydrothermal crystallization was carried out for 8 – 12 hr at 90˚C. Atta *et al*., (2007), synthesized faujasite zeolites from Kankara kaolin. Kaolin was fused in NaOH solution , aged for 3 days and

crystallized at 100˚C for 24 hr. Mixed phases of zeolite Y and X were obtained. Christidis, *et al.,* (2008) attempted synthesis of FAU type zeolite Y from SiO_2-sinter and perlite glass. The silica and perlite glass were fused in NaOH solution and was mixed with commercial aluminium hydroxide dissolved in NaOH to make the synthesis gel. Crystallization was carried out at 90˚C for 120 hr. Mixed phases of zeolite Y, P and gmelinite were obtained. Htay and Oo, (2008) attempted synthesis of zeolite Y from kaolin. They fused kaolin with NaOH at 850˚C for 3 hr. The fused clay was hydrothermally crystallized at 100˚C for 16 hr. Mixed phases of zeolite Y and P were obtained. Khabuanchalad *et al.*, (2008) attempted synthesis of zeolite Y using rice husk ash fused in NaOH solution. The fused ash was mixed with commercial sodium aluminate to make the synthesis gel. The synthesis gel was hydrothermally crystallized at 100˚C for 24 hr. Mixed phases of zeolite Y and P were obtained. Rahman *et al.*, (2009) attempted synthesis of FAU type zeolite Y from rice husk ash. They processed rice husk ash to silica and fused it in NaOH solution. The solution was used alongside commercial sodium aluminate to prepare synthesis gel which was aged for 24 hr and then crystallized at 90˚C for 22 hr. Zeolite Y was successfully synthesized. Mezni *et al*., (2011) synthesized mixed phases of zeolite X and RHA from Tunisian illite clay, by fusing the clay in NaOH solutions and subjecting the mixture to hydrothermal heating at 110˚C for 96 hr. Atta *et al.*, (2012) synthesized zeolite from mixture of Kankara kaolin and rice husk ash using the conventional hydrothermal method using NaOH solution, 72 hr aging and crystallization at 80˚C for 24 hr. They succeeded in synthesizing analcime and zeolite P. Saceda *et al.*, (2012) synthesized zeolite Y using partial substitution of rice husk ash with high purity chemicals and crystallization at 100˚C. Ma *et al*., (2014) synthesized zeolite 13X from kaolin clay by using the conventional method of fusing the kaolin in NaOH solution for 90˚C for 8 hr.

CHAPTER 3

3.0 MATERIALS AND METHOD

The materials and methodology employed for this work are presented in this chapter.

3.1 Materials, Apparatus and Equipment

3.1.1 List of materials

1. Kankara kaolin
2. Distilled water and deionized water
3. Concentrated sulfuric acid (Sigma-Aldrich, Lobal Chemie, 98%)
4. Sodium hydroxide pellets (Sigma-Aldrich, Lobal Chemie, ≥98%)
5. Sodium silicate solution (Fisher Chemical, wt. ratio SiO_2 : Na_2O; 2:1)
6. Sodium aluminate (Sigma-Aldrich)
7. Activated alumina (Sigma-Aldrich)
8. Barium chloride (Chemlight)
9. Ludox HS-30 colloidal silica (Sigma-Aldrich, 30 wt% suspension in water)
10. Lanthanum chloride and Ammonium chloride (Fisher Chemicals)
11. Silica standard solution (BDH chemicals)
12. Hydrochloric acid (BDH chemicals ≥98%)
13. Ammonium molybdate (Sigma-Aldrich)
14. Oxalic acid (BDH chemicals)
15. Commercial zeolite Y (Zeolyst international)
16. Filter paper
17. ZSM5 (synthesized and supplied by Yunusa, 2014: on-going PhD Dissertation)

3.1.2 List of apparatus

1. Beakers (250 – 2000 ml)
2. Measuring cylinders (50 – 250 ml)
3. Conical flasks (50 – 100 ml)
4. Polypropylene bottles (250 ml)
5. Spatula
6. Wash bottles and brushes (plastic types)
7. Petri dishes
8. Tyler mesh sieve (Mesh size 200)
9. Glass and plastic funnels
10. Ceramic Buckner funnel
11. Ceramic crucibles (25ml – 75ml)
12. Air tight desiccator
13. Ceramic mortar and pestle
14. Wooden mortar and pestle
15. Filter papers (Whatman, 1-541)
16. Full range pH paper (BDH, 1-14)

3.1.3 List of equipment

1. Electric furnace. (Nabertherm; 30 - 1400°C)

3. Electric oven (NYC – 101; 30 - 400°C, Nabertherm; 30 - 650°C)

4. Weighing balances (Weda, T18; 0 – 100kg, Metler Toledo; AB204; 0 - 210g)

5. High vacuum pump (Edwards, E2M5)

6. X-ray diffraction machine (Stchmabzu, 6000).
7. X-ray fluorescence machine (Pananalytical, Minipal 4).
8. High torque stirrer (Trieb, 73 – 660 rpm)
9. Heavy duty laboratory high shear mixer (Silverson, L2R)
10. Hot plate with magnetic stirrer (AMTAST, MS300)
11. Water Deionizer (LAB-IoN, 5R2)
12. Water distiller (Lasany, LPH-4)
13. Ball milling machine
14. Brunauer-Emmett-Teller (BET) machine (Quantachrome: Nova 2200e s/area and pore size analyzer)
15. Fourier Transformed Infrared Radiation (FTIR) spectrometer (Perkin Elmer Frontier FTIR Spectrometer)
16. Scanning Electron Microscope (JEOL SEM: JSM – 7600F)
17. Transmission Electron Microscope (JEOLTEM: JEM – 1230)
18. Thermogravimetric Analyzer (Perkin Elmer simultaneous thermal analyzer, STA 6000)
19. UV–VIS Spectrometer (Perkin Elmer Lambda 25)
20. Flame photometer (TIMPL TWF-45)
21. Gas Chromatography Mass Spectroscopy (GCMS) (Perkin Elmer Clarus 600C)

3.2 Experimental Procedure

Description of the experimental procedures employed in this work and the procedural steps of the instrumental technique analyses carried out are presented in this section.

3.2.1 Preparation of zeolite Y using high purity chemicals

Zeolite Y was synthesized by adapting and modifying the verified method of the Synthesis Commission of the International Zeolite Association using high purity reagents (Ginter *et al*., 1992; Robson, 2001). This process involved preparation of a seed gel, feedstock gel and the overall gel. Then the overall gel was crystallized using template-free low-temperature crystallization inside a polypropylene bottle.

3.2.1.1 *Seed gel preparation*

Seed gel was prepared by dissolving 4.07 g sodium hydroxide pellet in 19.95 g deionized water in a polypropylene beaker, then pouring 2.09 g sodium aluminate, and stirring the mixture with a magnetic stirrer until the sodium aluminate dissolved. The resulting solution was mixed with 22.72 g of sodium silicate solution, then stirred for 10 minutes, after which the mixture was capped in a polypropylene bottle and aged for 24 hr at room temperature (Ginter *et al*., 1992).

3.2.1.2 *Feedstock gel preparation*

The feedstock gel, was prepared by dissolving 0.14 g sodium hydroxide pellet in 130.97 g deionized water in a polypropylene beaker, then pouring 13.09 g sodium aluminate, and stirring the mixture with a magnetic stirrer until the sodium aluminate dissolved. The resulting solution was mixed with 142.43 g sodium silicate solution, and then stirred vigorously with a high-shear mixer until the gel appeared somewhat smooth. The resulting mixture was mixed with 16.5 g of the 24 hr aged seed gel and the resulting mixture mixed using the high-shear mixer for another 20 min after which the mixture was capped in a polypropylene bottle and aged for another 24 hr at room temperature (Ginter *et al*., 1992).

3.2.1.3 *Crystallization*

After 24 hr aging the feed gel was crystallized in electric oven maintained at 100°C for 7 hr (Ginter *et al*., 1992).

3.2.1.4 *Product recovery*

After the 7 hr crystallization, the reaction was quenched in deionized water and washed until the pH was below 9. The fine Zeolite Y crystals were separated and dried at 110°C for 8 hr

3.2.1.5 *Modification of the synthesis method*

The method used by Ginter *et al*., 1992 was modified by substituting aluminium hydroxide calcined at 400°C for sodium aluminate and the amount of the aluminium hydroxide used in the seed gel and feedstock gel preparation was 96% of the amount reported by Ginter *et al*., 1992. The aluminium hydroxide and sodium silicate used in the modified novel method were processed from Kankara kaolin.

3.2.2 Preparation of zeolite Y using kankara kaolin

Zeolite Y was prepared from Kankara clay by a novel method which entailed thorough purification of the clay by a clay-split method. The raw clay was wet beneficiated and calcined, and then split by dealumination. Then each of the split products were further processed to make them suitable for Zeolite Y preparation. Figure 3.1 shows the flow diagram of the processes involved in the synthesis of zeolite Y from kaolin.

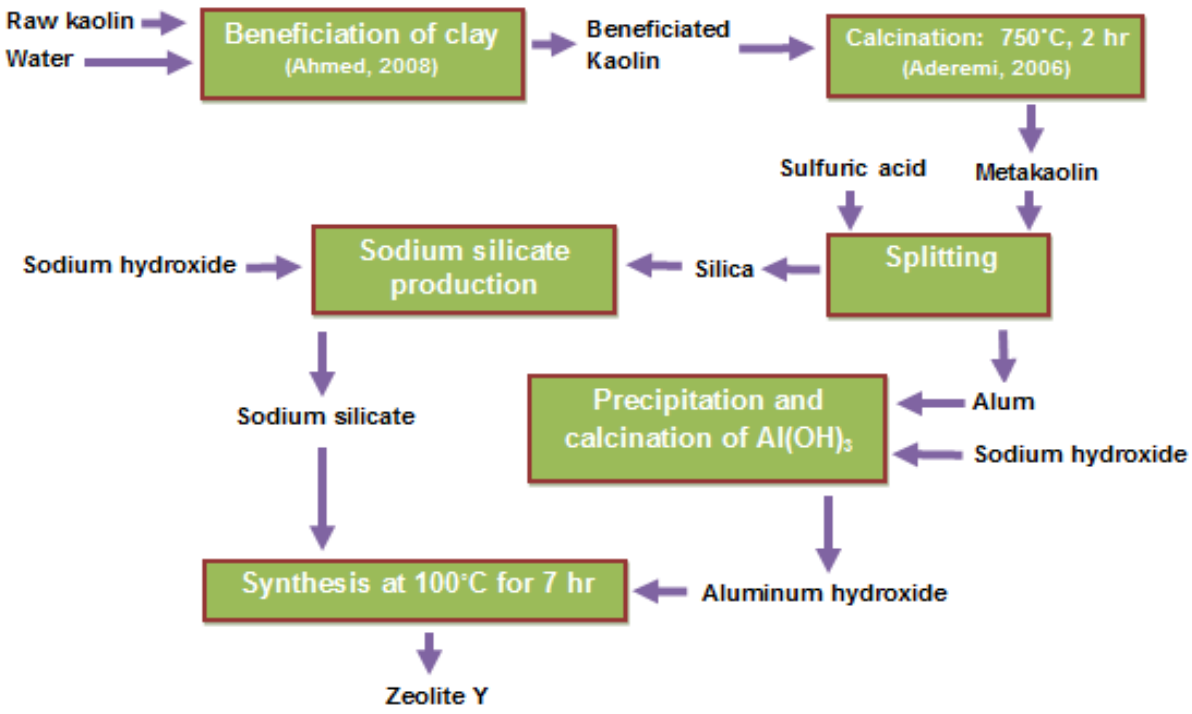


Figure 3.1: Flow diagram of synthesis of zeolite Y from kaolin using novel processing route

3.2.2.1 *Beneficiation*

The raw kaolin clay mined from Kankara Local Government Area of Katsina State was wet-beneficiated in order to purify it from physically and chemically combined impurities such as metallic oxide, soluble salts and grits such as; Fe_2O_3, FeO, MgO, CaO, MnO, Na_2O, K_2O, $MgSO_4$, $CaSO_4$, Na_2SO_4, K_2SO_4, Na_2CO_3, K_2CO_3, $MgCO_3$, $CaCO_3$, etc. The raw clay was crushed and ground using wooden mortar and pestle. Then, the ground clay was wet-beneficiated using an experimentally determined optimum mixing ratio of 0.1kg:1lt of clay to water, and optimum settling time of 24 hr. After allowing the clay to soak properly for 24 hr the mixture was blunged by vigorously stirring at 200 rpm for 3 hr so as to separate all the agglomerates of clay particles. Then the mixture was further allowed to settle overnight. The next day the blunged clay slurry settled into three clear layers; the bottom coarse particles; the middle fine clay particles and the

top supernatant water layer. The three layers were separated by decantation. The top supernatant water layer and the bottom coarse particles were discarded and the middle fine clay slurry layer was further processed. The fine clay slurry was sieved using Tyler mesh sieve of mesh size 200 (75 μm aperture opening) so as to further separate the fine grits present in the fraction. The resulting clay slurry was allowed to settle and the supernatant water layer was decanted in regular intervals until there was no reasonable quantity of supernatant water layer rising up. Then the thick slurry was poured into fabric sieve and the fabric was allowed in suspension for 4 hr to drain off all the water remaining in the slurry. Then the fabric was tied and pressed under heavy load overnight until the cake became very thick. Finally the solid cake was split into smaller sizes and open dried for 3 days after which it was ball milled (Ahmed, 2008).

3.2.2.2 *Metakaolinization*

The beneficiated and ground clay was calcined at 750°C for 2 hr in a chamber furnace for processing into metakaolin. Equation (3.1) expresses the chemical equation involved in the calcination process.

$$Al_2O_3{\bullet}2SiO_2{\bullet}2H_2O \xrightarrow{750^{\circ}C} Al_2O_3{\bullet}2SiO_2 + 2H_2O \qquad (3.1)$$

3.2.2.3 *Splitting*

The metakaolin was completely split into its silica and alumina components by complete dealumination involving double dealumination of metakaolin in excess acid. Variable stoichiometric ratio excess acid was used; details of reaction and calculations involved are presented in Appendix A. The dealumination process was carried out using 60 wt% concentrated sulfuric acid at room temperature which was reported as the optimum condition for sulfuric acid

dealumination of kaolin (Edomwonyi-Otu, 2008). Equation (3.2) expresses the chemical equation involved in the split process.

$$Al_2O_3 \bullet 2SiO_2 + 3H_2SO_4 \longrightarrow Al_2(SO_4)_3 + 2SiO_2 + 3H_2O \quad (3.2)$$

3.2.2.4 *First dealumiation*

The first dealumination was carried out using variable stoichiometric excess acid concentration: 100% - 500% excess acid (See details in Appendix A). The products of the first dealumination process were the filtrate-alum and the residue-silica. Each of these products was further processed so as to purify it to be suitable for zeolite synthesis.

3.2.2.5 *Second dealumination*

The silica obtained as the residue of the first dealumination was further purified by second dealumination of the silica. Then the silica obtained from the second dealumination was washed with distilled water until the absence of sulfate ion was confirmed with barium chloride test.

3.2.2.6 *Production of aluminium hydroxide*

The alum obtained during the dealumination process was further processed to obtain aluminium hydroxide $Al(OH)_3$ by titrating 50 wt% sodium hydroxide solution against the alum solution at room temperature with continuous stirring, until the pH of the solution rose to 7 – 9. The precipitated aluminium hydroxide was washed with distilled water until the absence of sulfate ion was confirmed. The aluminium hydroxide slurry was filtered using vacuum pump, then dried at 110°C for 7 hr, after which the dried aluminium hydroxide was ground using ceramic

mortal, then calcined at variable temperatures of 300, 400 and 500°C. Equation (3.3) expresses the chemical reaction involved in the production of aluminium hydroxide.

$$Al_2(SO_4)_3 + 6NaOH \longrightarrow 2Al(OH)_3 + 3Na_2SO_4 \quad (3.3)$$

3.2.2.7 *Production of sodium silicate*

The silica obtained as the residue of the second dealumination was processed to produce sodium silicate by leaching a specific weight of the silica in a 600 ml 2.5 M solution of sodium hydroxide such that the measured weight of the silica was varied between 11.26 wt% and 12.27 wt% of the resulting mixture. The mixture was maintained at 100°C for 3 hr with continuous stirring. The mixture was filtered after the 3 hr using vacuum pump and the filtrate was concentrated to produce the sodium silicate needed for synthesis of Zeolite Y.

3.2.2.8 *Synthesis of zeolite Y.*

Seed gel:

4.1 g sodium hydroxide was dissolved in 20 g deionized water, 2 g aluminium hydroxide was added and stirred in a polypropylene bottle until dissolved. 22.8 g of the prepared sodium silicate solution was added to the resulting solution and stirred for 10 min, then the bottle capped and allowed to age at room temperature for 24 hr (Robson, 2001).

Feed gel:

0.14 g sodium hydroxide was dissolved in 131 g deionized water, 12.6 g aluminium hydroxide was added and stirred in a polypropylene bottle until dissolved. 142.5 g of the prepared sodium

silicate solution was added to the resulting solution and stirred with a high-shear turbine mixer until the gel appears somewhat smooth.

Overall gel:

16.5 g of the aged seed gel was added to the feed gel and mixed vigorously, the resulting overall gel was capped in a polypropylene bottle and allowed to age at room temperature for 24 hr.

Crystallization/post treatment:

The aged overall gel was crystallized at 100°C for 7 hr. After the crystallization, the resulting zeolite Y crystal was filtered and washed with deionized water until the pH was less than 9. The resulting NaY (sodium base zeolite Y) was dried at 110°C over night (Robson, 2001). Figure 3.2 shows the flow diagram for the synthesis of zeolite Y using reagents prepared from the kaolin.

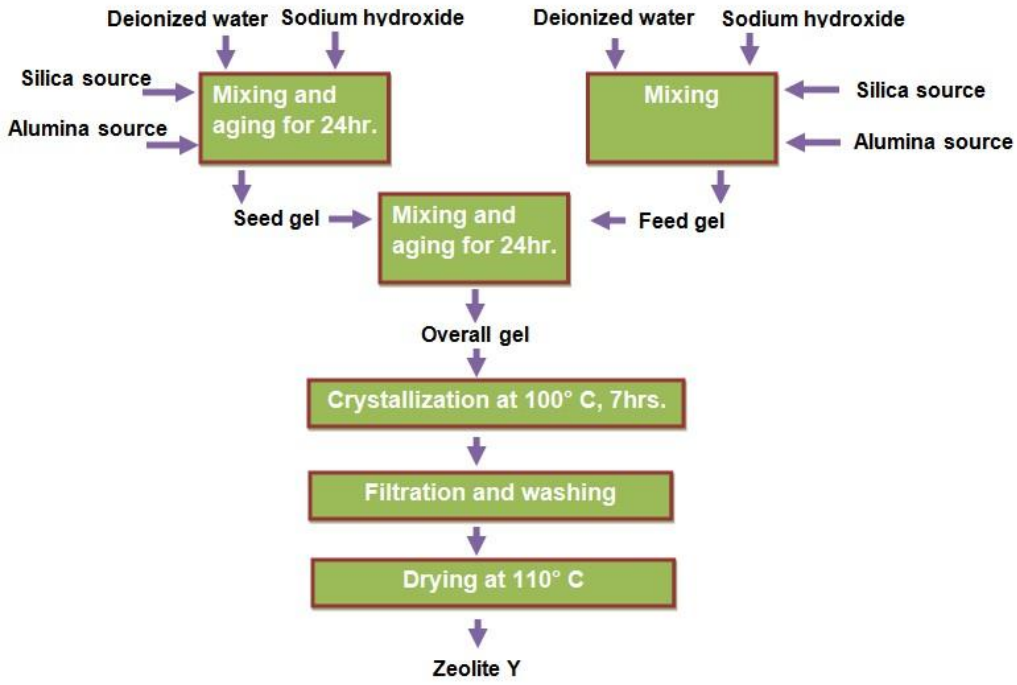


Figure 3.2: Flow diagram of the synthesis of zeolite Y from the reagents prepared

3.2.3 Protonation of the synthesized zeolite Y

The as-synthesized zeolite NaY was protonated by ion exchange reaction to make zeolite HY. 1.0 M solution of NH_4Cl was prepared and exchanged with zeolite NaY at 80°C using 10 ml solution to 1 g solid ratio and stirring the solution for 20 min (Gao *et al*., 2012; Du *et al*., 2013). After the exchange reaction the slurry was suction filtered using vacuum pump and washed thoroughly with distilled water and dried at 110°C for 6 hr. The resulting product was the NH_4Y zeolite. The NH_4Y was calcined at 650°C in air for 2 hr to form HY zeolite.

3.2.4 Thermal stabilization of the synthesized zeolite Y

The as-synthesized zeolite HY was thermally stabilized by impregnation of rare earth metal (La). The reaction was carried out using wet impregnation reaction to make zeolite RE Y. 0.5 M solution of $LaCl_3$ was prepared and mixed with the protonated zeolite (HY) at 80°C using 12.5 ml solution to 1 g solid ratio and stirring the solution for 1 hr (Gao *et al*., 2012; Du *et al*., 2013). After the reaction the product was filtered using a vacuum pump, washed thoroughly with distilled water. The wet cake of the zeolite was hydrothermally calcined at 650°C in air for 2 h.

3.2.5 Catalyst formulation

The FCC catalyst was formulated by employing wet granulation method. The RE Y zeolite was supported with silica-alumina matrix. The matrix was made of activated alumina and metakaolin. The silica sol was used as a binder. The percentage composition of the formulation was 30 wt% RE Y, 30 wt% metakaolin, 20 wt% activated alumina and 20 wt% silica sol (Al-Khattaf, 2003). After thorough mechanical agglomeration to ensure even dispersion, the mixture was dried at 110°C for 6 hr. In the case of the Zeolite Y + ZSM5 composite catalyst, the zeolite component

used for the formulation was made of zeolite RE Y and ZSM5 at a proportion of 75% and 25% respectively.

3.2.6 X-ray diffraction (XRD)

XRD patterns were recorded from Bragg‟s angle of 10° to 70° using Pananalytical X‟pert^3, operated at continuous scanning, scanning speed of 5°/min, generator settings of 10 mA and 40 kV, and CuKα node material.

3.2.7 X-ray fluorescence (XRF)

The chemical compositions of the materials used were determined using XRF machine; Minipal 4, Pananalytical X-ray fluorescence analyzer.

3.2.8 Brunauer-emmett-teller (BET) analysis

BET Nitrogen adsorption, surface area analysis was carried out using Autosorb Station1, Quantachrome. Outgassing was carried out at 300°C for 4 hr and N_2 absorption/desorption at 77.350K.

3.2.9 Fourier transform infrared spectroscopy (FTIR)

FTIR analysis was carried out using Perkin Elmer Frontier FTIR Spectrometer. In a typical analysis 0.07g wafer of the sample consisting of 1% of the sample and 99% KBr window was used. The mixture was pressed under pressure of about 12 MPa to produce a thin film wafer. The wafer was inserted in the sample holder of the FTIR equipment, then, FTIR spectra of the sample

was recorded from 400 to 4000 cm^{-1} with a 1 cm^{-1} resolution operated at scan speed of 0.125 $cm^{-1}s^{-1}$. Prior to the sample analysis background spectrum of air at ambient condition was ran.

3.2.10 Thermo gravimetric/differential thermo gravimetric (TG/DTG)

Thermogravimetric analyses were carried out using Perkin Elmer simultaneous thermal analyzer, STA 6000. The method used was thermal scanning from 30 to 900˚C at heating rate of 10˚C/min and cooling at 20˚C/ from 900 to 30˚C. Nitrogen was used as the purge gas at flow rate of 20 ml/min. In a typical run 10 – 30 mg sample was placed in the platinum crucible, then placed in the TGA furnace. The equipment was conditioned for about 30 min before the thermal scan was commenced.

3.2.11 Scanning electron microscope (SEM) analysis

SEM analysis was carried out using JEOL Field Emission Scanning Electron Microscope JSM – 7600F. In a typical run a very small amount of the sample; less than 1.0 mg was picked with a tweezer and placed on the sample stab. The sample was treated with acetone or methanol to wash off impurity and ensure particles dispersion. The stab containing the treated sample was placed in the sputter coater for surface polishing with gold or platinum film. After the sample preparation and sputtering the sample stab was placed in the analysis chamber of the SEM equipment, the vacuum was put on. When the vacuum was about 9.634×10^{-5} torr the scanning was commenced. The magnification and voltage were set and the focus of the microscope was manipulated until a sharp clear image was obtained and picture captured.

3.2.12 Transmission electron microscope (TEM) analysis

TEM analysis was carried out using JEOL JEM – 1230 TEM operated at vacuum of 9.634 x 10^{-5} torr. In a typical run a very small amount of the sample; less than 1.0 mg was picked with a tweezer and placed on the sample stab. The sample was treated with acetone or methanol to wash off impurity and ensure particles dispersion. The sample stab was placed in the analysis chamber of the TEM equipment, the vacuum was put on. When the vacuum was about 9.634 x 10^{-5} torr the beam gun was shot. The magnification and voltage were set and the focus of the microscope was manipulated until a sharp clear image was obtained and the picture captured.

3.2.13 Characterization of sodium silicate

3.2.13.1 Determination of concentration of SiO_2

The SiO_2 was characterized using the American Public Health Association (APHA) 4500-SiO_2 C Molybdosilicate Method (APHA, 1996). Standard solutions of silica of variable concentrations; 5 – 25 ppm were prepared from silica stock solution. UV–VIS Spectrometer scan of the standards were ran and the absorbance at wavelength of 410 nm were recorded (Perkin Elmer UV–VIS Spectrometer Lambda 25) for each standard. Calibration curve was plotted. The sodium silicate solution was diluted to 2.5 µl in 50 ml distilled water (2.5 mg in 50 g solution: dilution factor; 5 x 10^{-5}). 50 ml of the diluted solution was poured in a propylene tube. The pH of the solution was adjusted to 1.2 by adding 1 ml of 1 + 1 hydrochloric acid, 2.0 ml of ammonium molybdate was also added and mixed, the solution turned yellow. The mixture was allowed to stand for 10 min then 2.0 ml of oxalic acid was added. UV–VIS Spectrometer scan was ran and the absorbance at wavelength of 410 nm was recorded (Perkin Elmer UV–VIS Spectrometer

Lambda 25). The concentration of the sodium silicate was determined using the calibration curve as a reference scale.

3.2.13.2 Determination of concentration of Na_2O

The Na_2O was characterized using Flame Photometer analysis (TIMPL µp Flame Photometer TMF – 45). Firstly, variable concentrations of standard solutions of Na_2O were prepared; 5 – 25 ppm from Na_2O stock solution. The standard solutions were introduced into the flame photometer for inbuilt calibration. The sodium silicate solution was diluted to 2.5 µl in 100 ml distilled water (2.5 mg in 100 g solution: dilution factor; 2.5×10^{-5}). The diluted solution was introduced into the flame photometer and the concentration was digitally displayed on the equipment immediately after the analysis.

3.2.14 Acidity test

The surface acidity of the catalysts was tested by employing pyridine probe absorption using FTIR Spectrometer. Wafer of the catalyst was made containing KBr windows. Each wafer consisted of 1% catalyst and 99% KBr window. The wafer was heated at 473 K for 16 hr in vacuum then cooled to room 298 K, after cooling a base FTIR spectrum of the wafer was ran at 298 K. The wafer was exposed to pyridine absorption at 298 K for 30 min under vacuum condition such that the absorption was driven by the vapour pressure of the pyridine, then the wafer was heated to 473 K under vacuum for 16 hr and allowed to cool to 298 K, another FTIR spectrum was ran. Prior to these, background spectrum of air at ambient condition was ran. The FTIR spectra were recorded from 1600 to 1300 with a 0.5 cm^{-1} resolution operated at scan speed of 0.125 $cm^{-1}s^{-1}$.

The Lewis and BrØnsted acidic sites were identified by the spectra at 1450 and 1550 cm^{-1} bands respectively (Borade *et al*., 1990; Santi *et al*., 2013). And the Lewis and BrØnsted acid concentrations were evaluated using Equations (3.4) and (3.5) respectively (Akcay, 2005; Santi *et al*., 2013).

$$L_C = A_L/(m\varepsilon_l) \quad (3.4)$$

$$B_C = A_B/(m\varepsilon_b) \quad (3.5)$$

Where A_L and A_B are the integral areas covered by the Lewis and BrØnsted spectra respectively

m is the mass of the wafer (0.07g)

ε_l and ε_b are the extinction coefficients for the Lewis and BrØnsted sites respectively and their values were 2.23 and 1.67 respectively (Akcay, 2005).

3.2.15 Catalytic performance test

3.2.15.1 Desulfurization application

The RE Y form of the synthesized zeolite Y was used for desulfurization of a model petroleum oil using microwave assisted technique. The model oil used was made by dissolving 200 ppm thiophene in n-heptane. 10 g of the model oil was poured into a pressure vessel of a microwave reactor (Milestone Microwave Labstation) and 1 wt% of the RE Y zeolite was added. The pressure vessel was torqued and inserted in the workstation of the reactor, the reactor‟s thermocouple was inserted in the thermowell and the reactor was programed for variable time and temperature runs. After each reaction the reactor content was allowed to cool for 30 min after which the torque was loosened and the vessel content removed. The resulting mixture was centrifuged at 10,000 rpm for 10 min (Beckman Avanti^{TM} J – 251). The resulting liquid product was collected and GCMS analysis of it was carried out (Perkin Elmer Clarus 600C GCMS).

3.2.15.2 Catalytic cracking application

The commercial catalyst Y, the formulated catalyst Y and zeolite Y + ZSM5 blend were used for catalytic cracking of a model petroleum oil using a fixed bed reactor. The reaction was carried out at Catalysis & Conversion Processes Division, Council of Scientific and Industrial Research (CSIR) India. The reactor used had been used by other researchers (Sandeep *et al*., 2013), the setup is as shown in Figure 3.3. The reactor was equipped with an online GCMS for online analysis of the gaseous product which was connected via a gas meter for monitoring of the gas mass flow. The set-up also consisted of a condenser equipped with a high pressure liquid separator for collection of the liquid product for GCMS analysis. The carrier gas was nitrogen gas connected via a mass flow controller (MFC). The model oil used was n-hexadecane. The reaction conditions were 300 - 550^{0}C, 2 bar, weight hourly space velocity (WHSV); 3 hr^{-1}, N_2 gas flow; 50 l/hr. The reaction set-up is as shown in Figure 3.3.

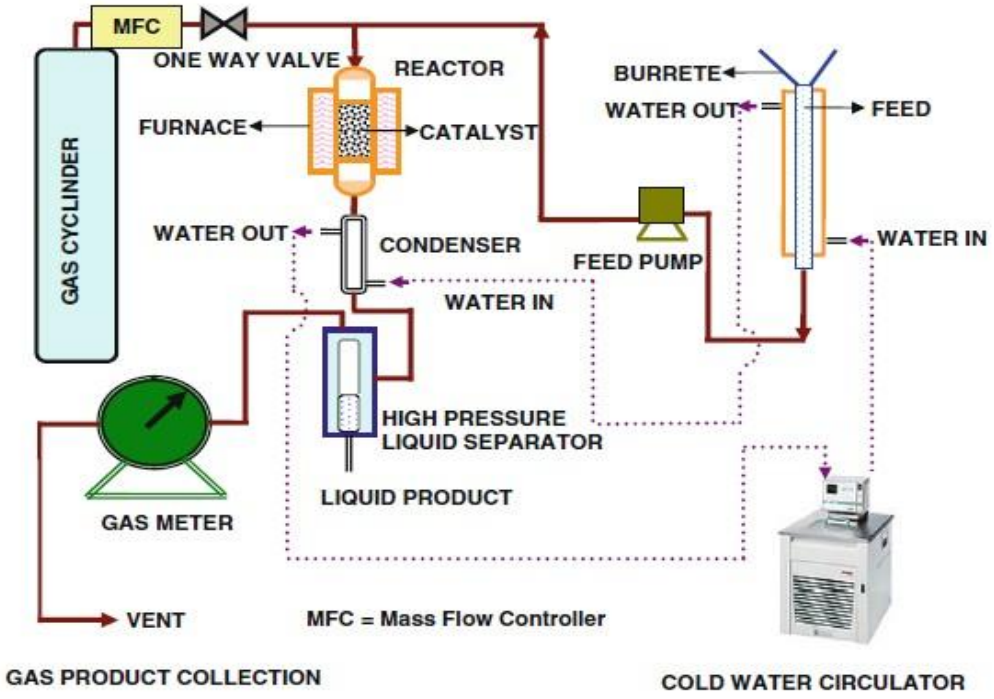


Figure 3.3: Setup for the reactor used for catalytic cracking (source; Sandeep *et al*., 2013)

CHAPTER 4

4.0 RESULTS AND DISCUSSION

4.1 Characteristics of Kaolin and Metakaolin

The physicochemical, morphological and thermogravimetrical characterizations of Kankara kaolin and the metakaolin produced from it are presented in this section.

4.1.1 XRD patterns of kaolin and metakaolin

Figure 4.1 presents the XRD pattern of the raw Kankara kaolin. It could be observed from the XRD pattern that the raw Kankara kaolin was amorphous. The characteristic peaks of kaolinite could be seen at Bragg‟s angles of 12.35, 19.89, 20.38, 24.88, 34.94, 35.95, 36.06, 38.35, 45.24,

54.88 and 62.37°. The peak at 26.65° was due to crystalline silica, also known as quartz (Chen, 1977; Ajayi *et al*., 2010; Panda, *et al*., 2010). Also, the peak at 17.4˚ was due to mica-montmorillonite (Chen, 1977). It could be observed that the peak for the quartz had the highest intensity of about 1000 counts. Whereas the other peaks which represent the kaolinite mineral were much lower; they generally had intensity of about 400 counts and even lower. Meaning that the quartz content was much higher in the clay.

Figure 4.2 shows the XRD pattern of the beneficiated Kankara kaolin. It could be seen from the XRD pattern that the peaks at Bragg‟s angles of 12.35, 19.89, 20.38, 24.88, 34.94, 35.95, 36.06,

38.35, 45.24, 54.88 and 62.37° responsible for the kaolinite mineral were more prominent after beneficiation. The XRD pattern was dominated by the kaolinite peaks after beneficiation of the kaolin, the main characteristic peaks of kaolinite (12.35 and 24.88°) had intensity of about 500 –

550 counts.

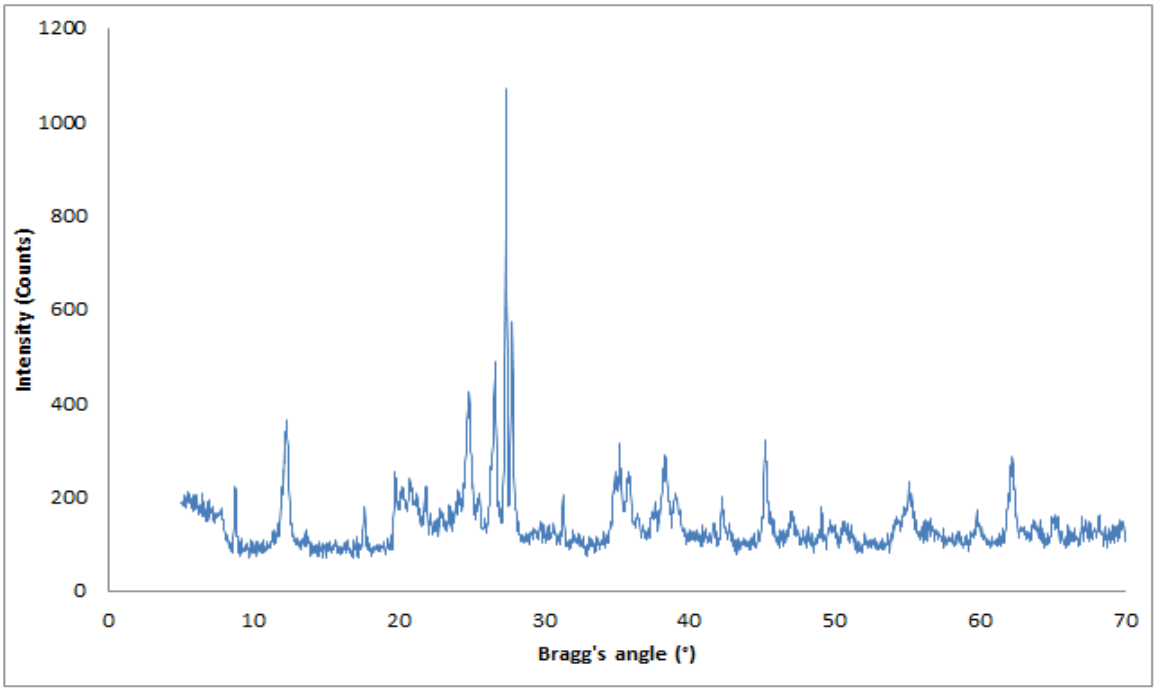


Figure 4.1: XRD pattern of raw Kankara kaolin

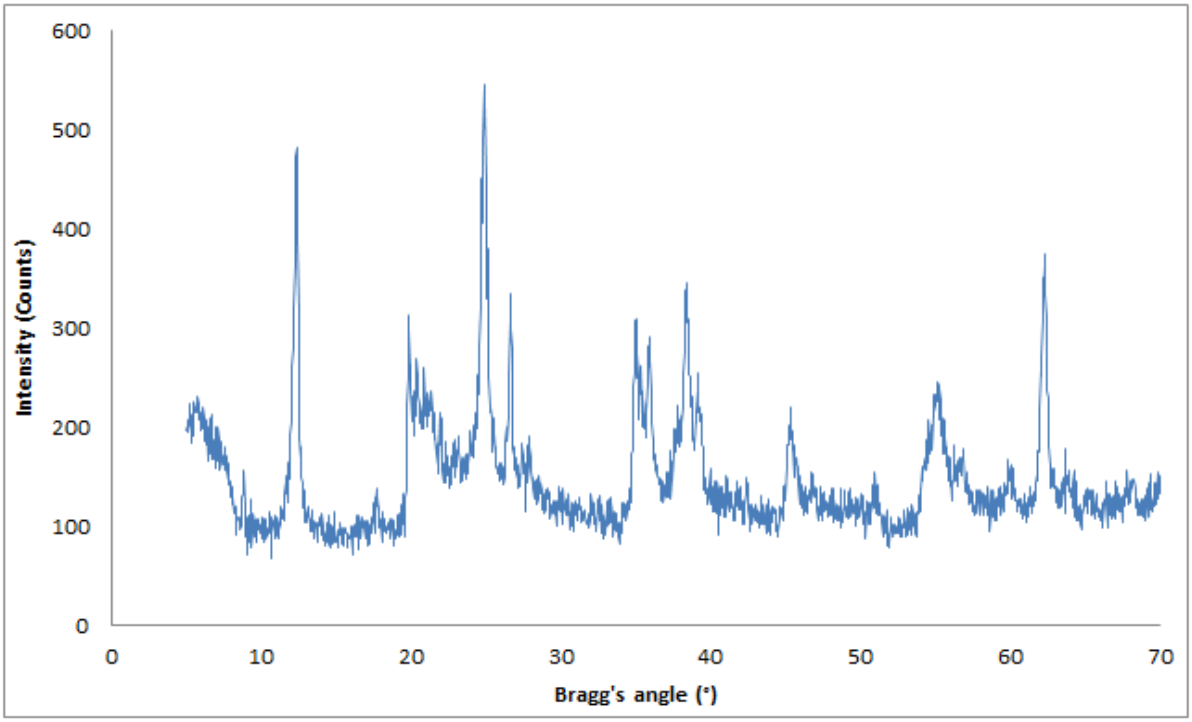


Figure 4.2: XRD pattern of beneficiated Kankara kaolin

It was also observed that the peak at 26.65° responsible for quartz became drastically reduces from its initial intensity of 1000 counts for the raw kaolin to about 300 counts after beneficiation. The mica peak‟s intensity also reduced from the initial 175 to 130 counts. Therefore, the reduction in the intensity of the quartz and mica could be attributed to reduction in the concentration of both due to washing away during the beneficiation process.

Figure 4.3 shows the XRD pattern of the metakaolin formed. It could be seen from the XRD pattern that the material became highly amorphous due to crumbling of the kaolinite structure as a result of calcination at 750°C. Even though the quartz component of the clay was earlier supressed as was shown by the relatively low of its peak after beneficiation, it became the only obvious mineral observable in the XRD of the metakaolin. Past works have shown that crystalline silica is inert to calcination treatment even at 1050°C (Edomwonyi-Otu, *et al.*, 2013).

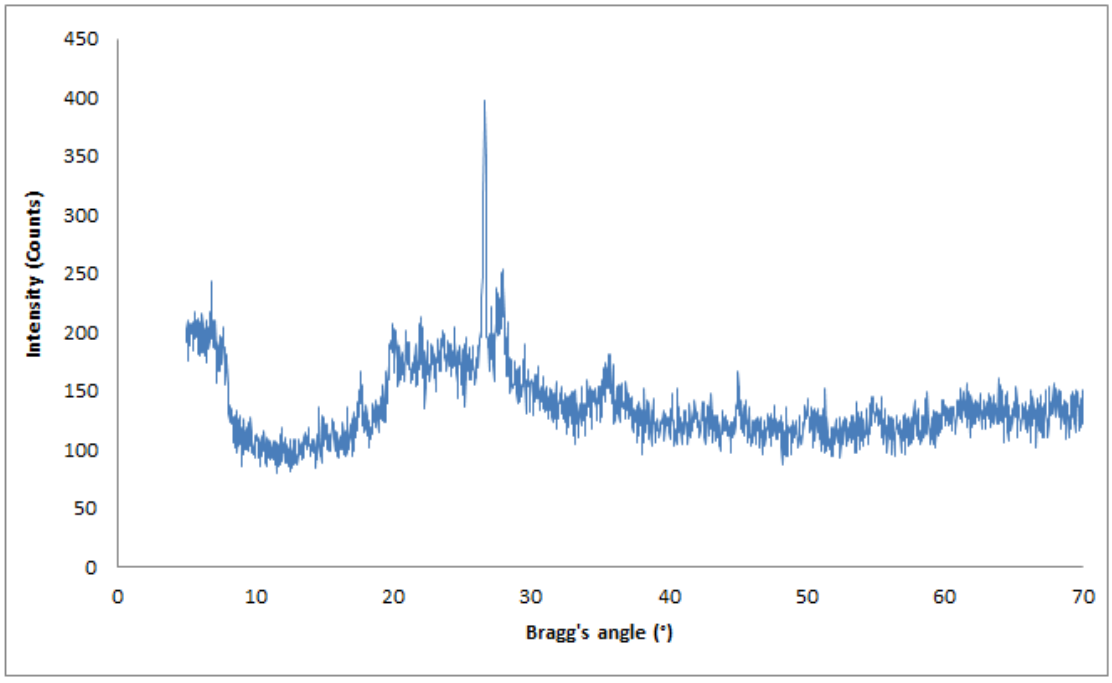


Figure 4.3: XRD pattern of the metakaolin produced

Hence, the XRD pattern of the metakaolin confirmed that the quartz content of kaolin was still inert after calcination at 750°C, showing that the temperature was not high enough to distort the structure of quartz.

Figure 4.4 shows the comparison of the XRD pattern of the raw kaolin, beneficiated kaolin and metakaolin; it further showed the relative intensities of the various peaks so as to give a clearer picture of the improvement of the kaolinite peaks and decrease of the quartz peak after beneficiation. Also, the amorphous nature of the XRD pattern of the material after metokaolinization could be clearly observed when compared to the XRD patterns before metakaolinization.

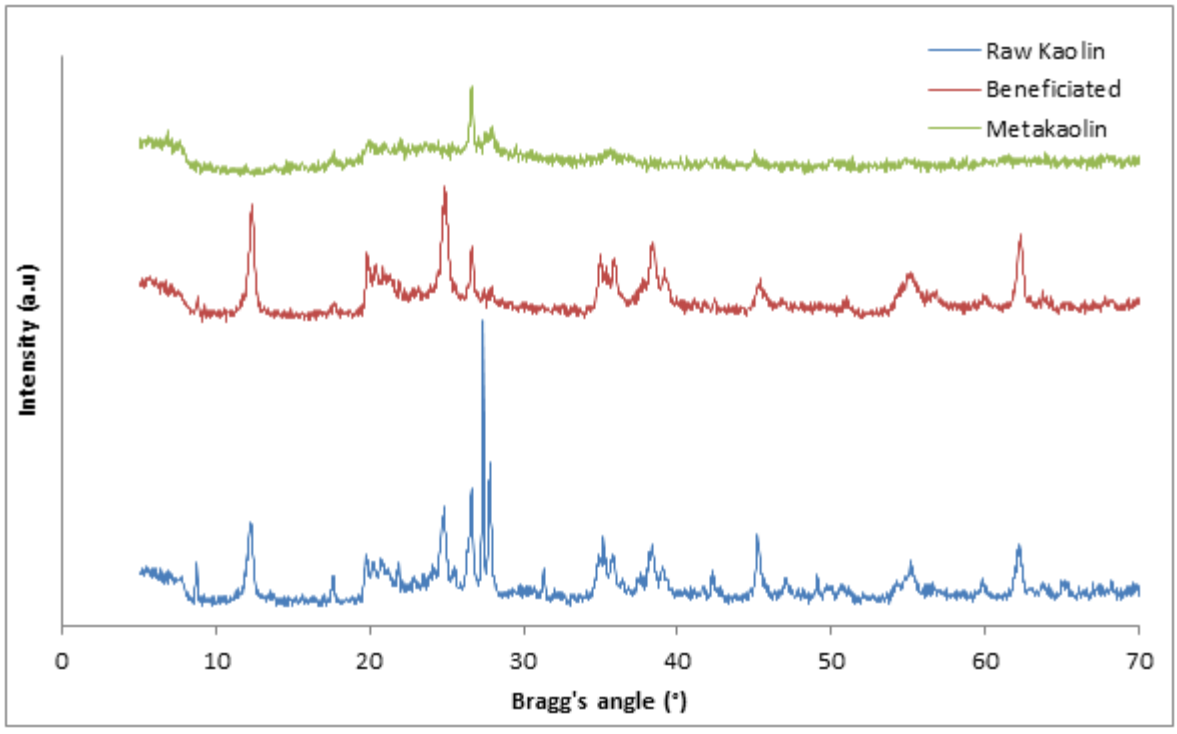


Figure 4.4: Comparison of the XRD patterns of raw kaolin, beneficiated kaolin and metakaolin

4.1.2 Chemical compositions of kaolin and metakaolin

Table 4.1 presents the chemical composition of the raw kaolin, beneficiated kaolin and the metakaolin produced. The Si/Al ratio of the raw clay which was initially 1.90 decreased slightly by 1.6% after beneficiation. The decrease in the Si/Al ratio could be attributed to washing away of silica during the beneficiation process, this fact was similarly buttressed in the interpretation of the XRD results of the kaolin before and after metakaolinazation as discussed earlier.

Table 4.1: Chemical compositions of the Kankara kaolin and metakaolin

Metallic Oxide	Sample/Composition (wt%)		
	Raw Kaolin	Beneficiated Kaolin	Metakaolin
Al_2O_3	28.43	27.81	32.94
SiO_2	54.21	52.04	59.16
Na_2O	0.22	0.57	0.26
K_2O	3.90	1.82	1.82
MgO	0.41	0.44	0.46
CaO	1.86	1.19	1.33
CuO	0.02	0.02	0.01
TiO_2	0.11	0.12	0.13
Fe_2O_3	0.80	0.93	1.82
LoI	9.74	14.70	1.66
Si/Al	1.90	1.87	1.80

There was no appreciable reduction in Na_2O, MgO, CuO and TiO. Nevertheless, some appreciable reductions were observed in the K_2O and CaO before and after beneficiation; K_2O reduced by 53% while CaO reduced by 36%. This is very important because K_2O has been identified by Ajayi, (2012) as the most problematic impurity which inhibits synthesis of pure phase zeolite Y. The reductions likely occurred as result of washing off of soluble salts of

potassium and calcium during the beneficiation process. It is worth noting that Na_2O and Fe_2O_3 had rather increased after the beneficiation; it was not clear what was responsible for the increment, however, the same trend have been reported for Kankara clay by other researchers (Edomwonyi-Otu, *et al*., 2013). The LoI of the raw kaolin was 9.74 wt%, it increased by 51% after beneficiation and decreased by 83% after metakaolinization. The increase after beneficiation could be attributed to increase in clay content of the kaolin resulting from washing away of impurities. The decrease in LoI after metakaolinization could be attributed to dehydroxylation of the clay during the calcination process; resulting into driving off of the chemically combined water in the clay.

4.1.3 BET results of kaolin and metakaolin

Table 4.2 presents the BET results of the raw Kankara kaolin and the metakaolin. The raw clay had a low specific surface area value of 12.95 m^2/g and pore volume of 0.0038 cm^3/g. The surface area of the clay increased by 49.7% on metakaolinization, while, the pore volume also increased exponentially by 1439% (14.39 times). The increase in the surface area may be attributed to the loss of crystallinity of the kaolinite mineral to the highly amorphous metakaolin as shown by the XRD patterns of the materials. The crumbling of the ordered platelet structure of kaolinite as a result of calcination had resulted into a higher surface area more amorphous structured metakaolin.

Table 4.2: BET specific surface area and pore volume of Kankara kaolin and metakaolin

Sample	Surface Area (m^2/g)	Pore Volume (cm^3/g)
Raw kaolin clay	12.95	0.0038
Metakaolin	19.38	0.0585

4.1.4 SEM micrographs of kaolin and metakaolin

Plates II and III show the SEM images of the raw and beneficiated Kankara kaolin respectively, scanned at various magnifications. The platelet structure of kaolinite clay reported in the literature (Abo-El-Enein, *et al*., 2013; Bergaya, 2013) which normally portrays booklets morphology could be clearly observed. Plates II A, B, C and D show the SEM scan at magnifications of 8000, 15000, 30000 and 45000 for the raw kaolin while Plates III A, B and C show the SEM scan at magnifications of 8000, 15000 and 30000 for the beneficiated kaolin. Each of the images showed a booklet morphology consisting of platelet sheets of kaolinite mineral as reported in the literature, the booklet morphology became clearer as the magnification increased. The average particle size was estimated as 1.0 μm for both the raw and beneficiated kaolin.

Plate IV A, B and C show the SEM images of the metakaolin scanned at magnifications of 8000, 15000 and 30000. It can be observed that the booklet morphology that was earlier obvious in the SEM image of the raw and beneficiated kaolin (Plates II and III) has been lost. Even though the metakaolin SEM image still possessed some relatively low platelet morphology, the morphology of the metakaolin was lump-like. The lump-like morphology could be attributed to the highly amorphous nature of the material as a result of the crumbling of the kaolinite structure as was already identified by the analysis of the XRD results. The relatively low platelet morphology observed in the material could be as a result of the crystalline silica contained in the clay even after the metakaolinization as the XRD results have earlier shown. The average particle size was estimated as 2.0 μm for the metakaolin.

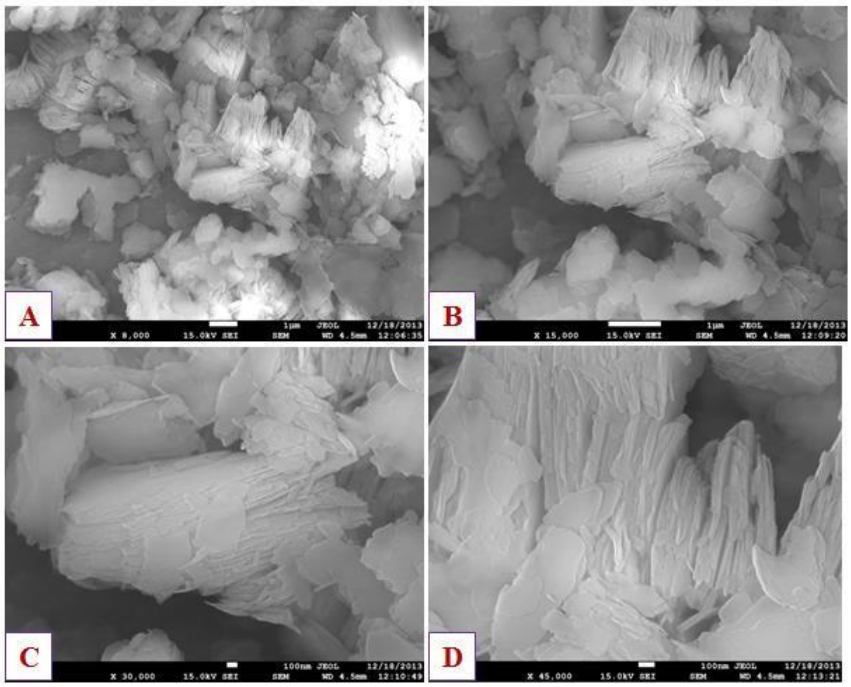


Plate II: SEM images of raw Kankara kaolin at magnifications of (A) 8000 (B) 15000 (C) 30000 (D) 45000

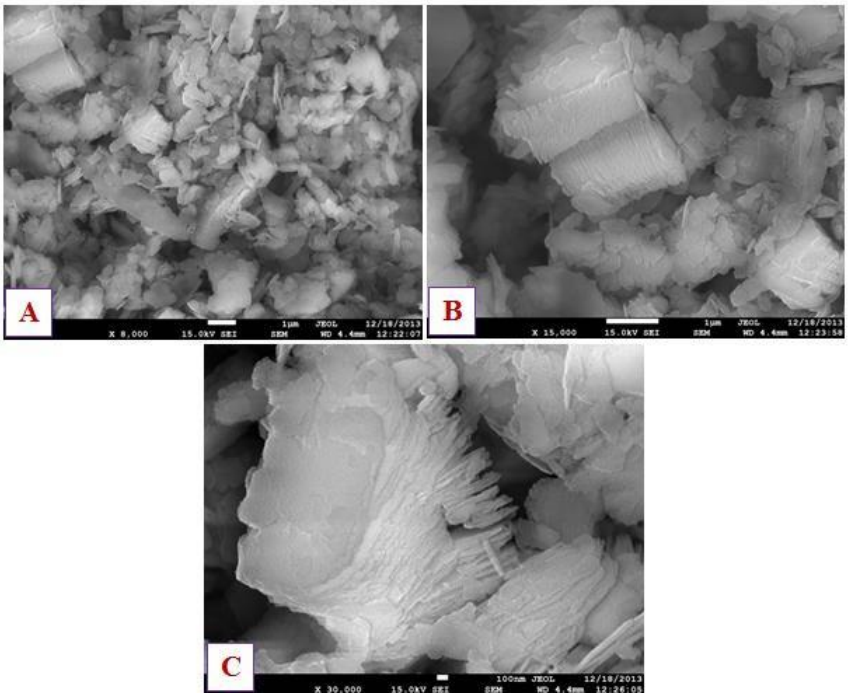


Plate III: SEM images of beneficiated Kankara kaolin at magnifications of (A) 8000 (B) 15000 (C) 30000

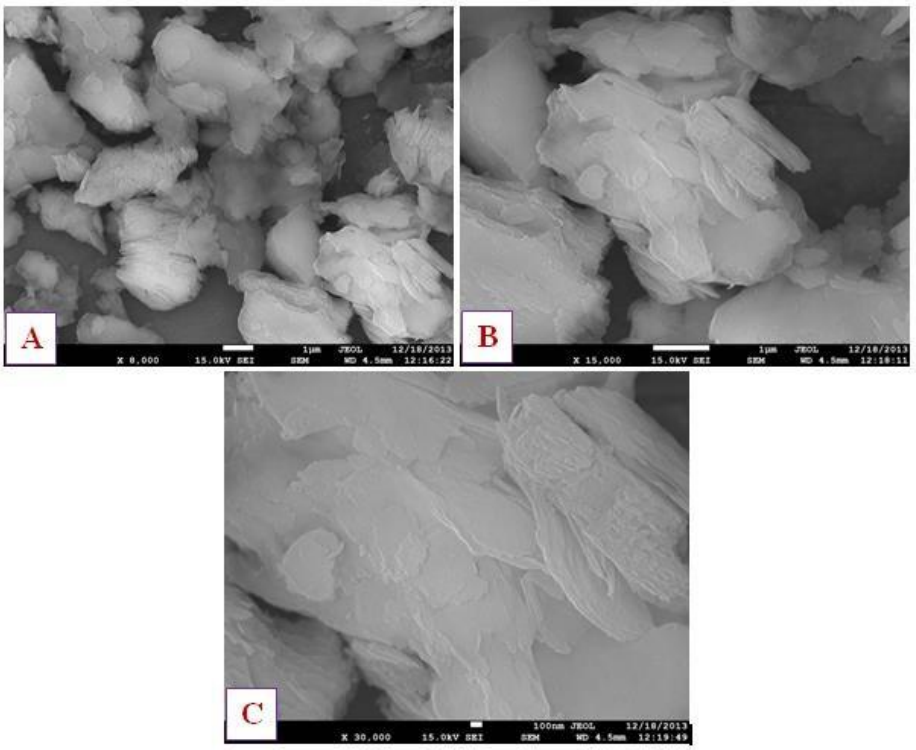


Plate IV: SEM images of metakaolin at magnifications of (A) 8000 (B) 15000 (C) 30000

4.1.5 TEM images of kaolin and metakaolin

Plates V A, B, C and D show the TEM images of the raw Kankara kaolin at magnifications of 15000, 25000, 50000 and 100000. The images at the lower magnifications; 15000 and 25000 appeared blurred due to the effect of overlapping of the clay particles. However, at the magnification of 50000 the TEM image appeared clearer revealing a definite shape of a unit clay particle. Different authors have commented on the diverse size and shape of kaolin particles (Ma and Eggleton, 1999). It has been reported that natural kaolins are often associated with high-defect structures. However, Plate V D, magnification of 100000 showed a clear structural shape of the Kankara kaolin crystals. Clear tetrahedral and hexagonal, euhedral morphology was very obvious despite overlapping of some of the particles. The average crystal size was estimated as 350 nm for the Kankara kaolin.

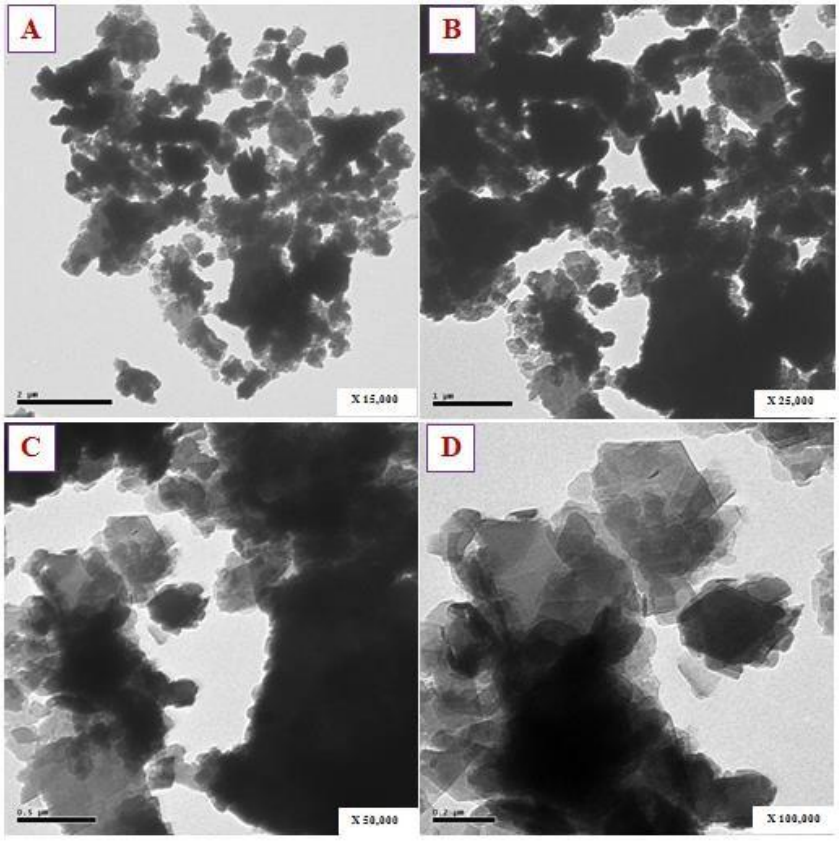


Plate V: TEM images of Kankara kaolin at magnifications of (A) 15000 (B) 25000 (C) 50000 (D) 100000

Plate VI A, B, C and D show the TEM images of the metakaolin at magnifications of 60000, 100000 and 150000. The image at the highest magnification appeared clearest because it shows the most details. The particle structure portrayed a hollow anhedral morphology showing irregular particle shapes. The irregularity of the particles could be as a result of the structural crumbling of the initial kaolinite structure experienced during the metakaolinization process as was already shown by the XRD and the SEM analyses. The average crystal size was estimated as 150 nm for the metakaolin.

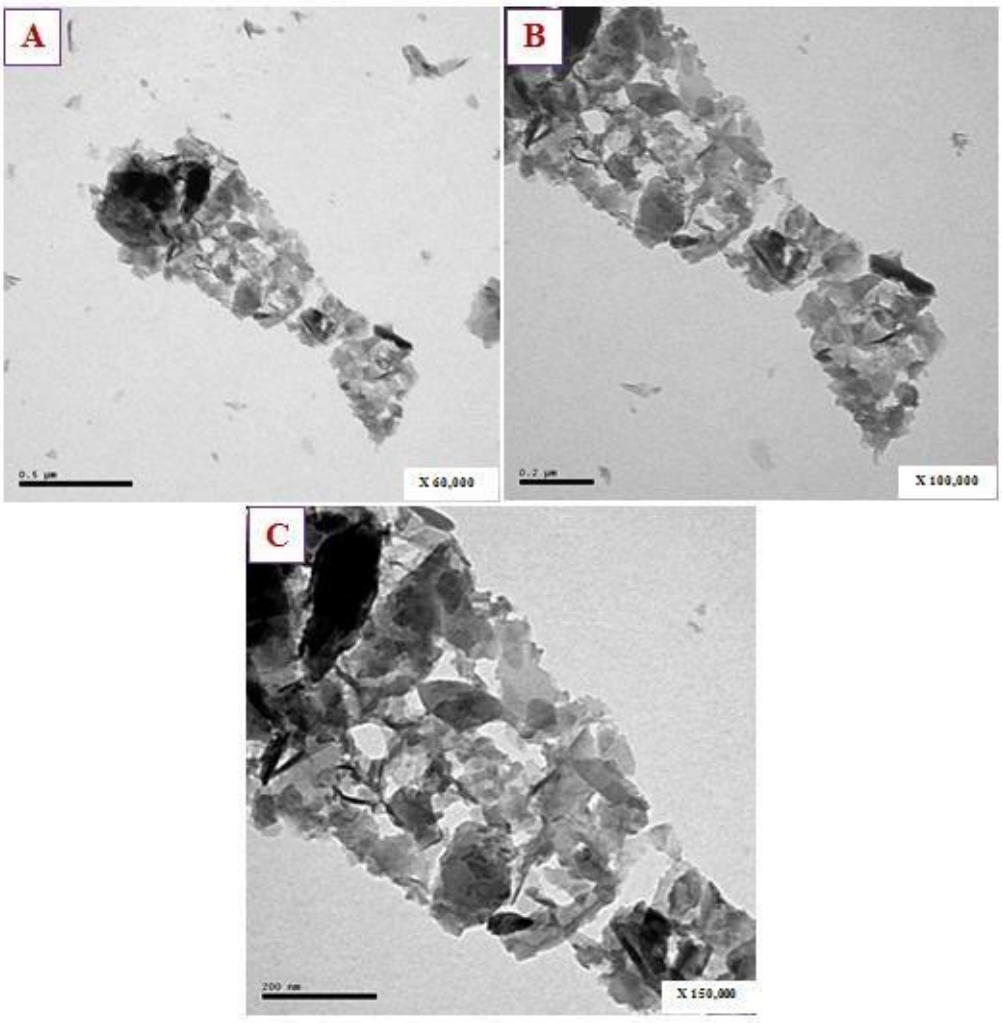


Plate VI: TEM images of metakaolin at magnifications of (A) 60000 (B) 100000 (C) 150000

4.1.6 Thermogravimetric properties of kaolin and metakaolin

Figures 4.5 and 4.6 show the TGA/DTG curves of the raw and beneficiated Kankara kaolin at thermal scan of 30 - 750˚C at heating rate of 10˚C/min. It could be observed that both materials possessed similar thermogravimetric curves. The total mass depletions resulting from the thermal treatment were 10 and 15 wt% for the raw and beneficiated kaolin respectively. These values were in a close proximity to the LoI values obtained for each of the samples in their chemical composition results presented in Table 4.1.

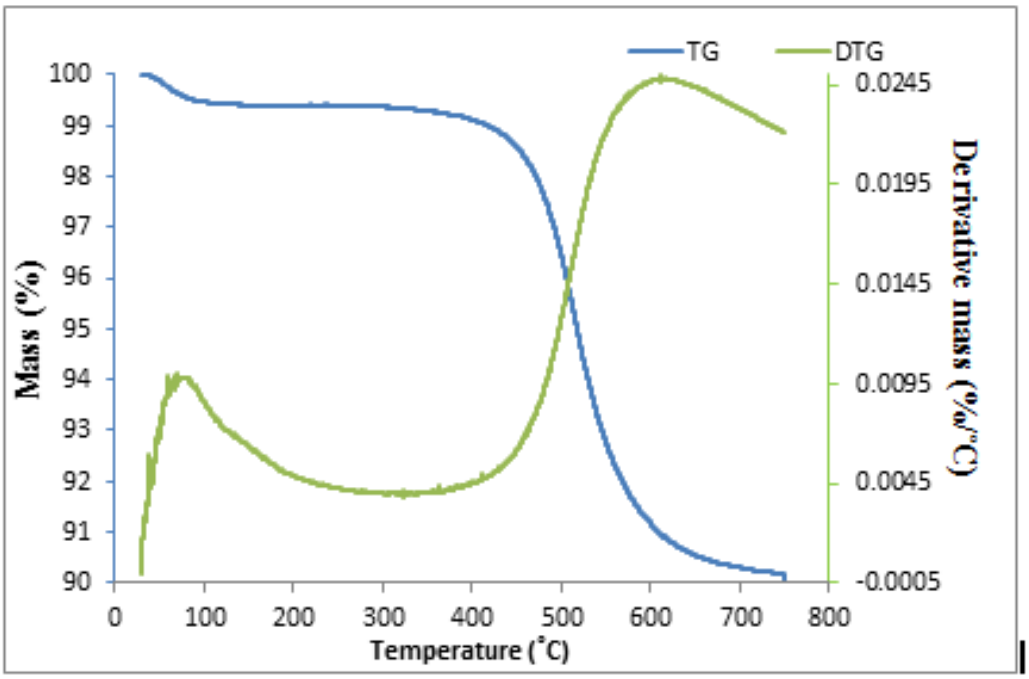


Figure 4.5: TGA/DTG curves of raw Kankara kaolin

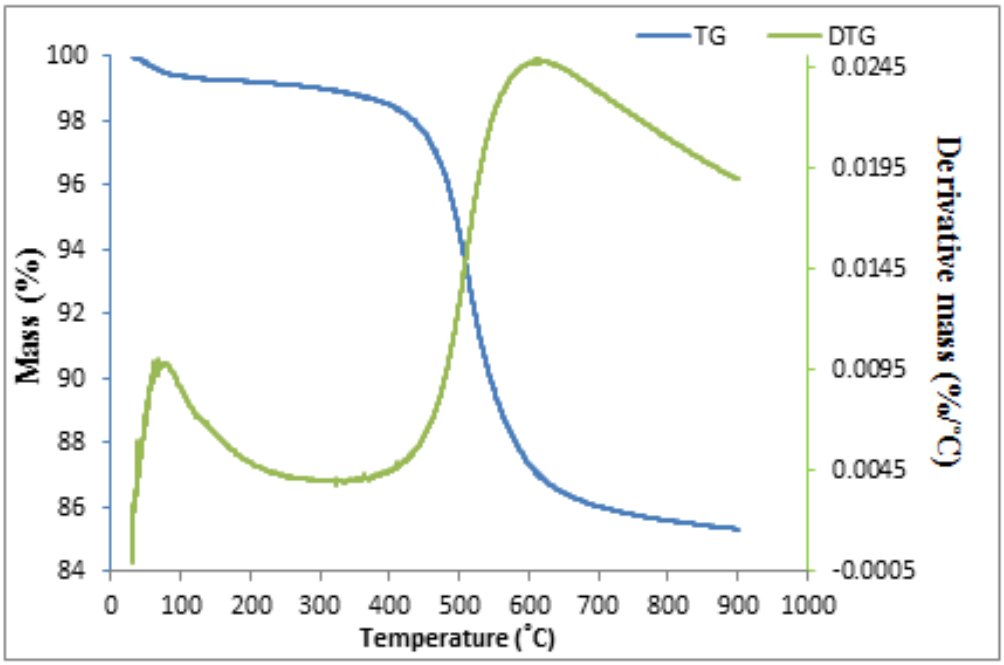


Figure 4.6: TGA/DTG curves of beneficiated Kankara kaolin

The DTG curve suggests the actual temperature responsible for the thermogravimetric mass depletion (Hatakeyama, *et al*., 1999; Konwar, *et al*., 2013). It could be seen from the DTG curves that the mass depletions occurred at temperatures of about 100 and 600˚C for both the raw and beneficiated Kankara kaolin. The loss at 100˚C could be attributed to the effect of dehydration due to physically adsorbed water while that of 600˚C was due to loss of chemically combined water on phase transformation of the kaolinite to metakaolin.

Figure 4.7 shows the TGA/DTG curves of the metakaolin at thermal scan of 30 - 900˚C at heating rate of 10˚C/min. It could be observed that the total mass depletion resulting from the thermal treatment was only about 2.7 wt%. The temperature responsible for the loss was not vividly identified like in the DTG curves of the raw and beneficiated clay, however, some faint thermal peak could be observed at about 500˚C.

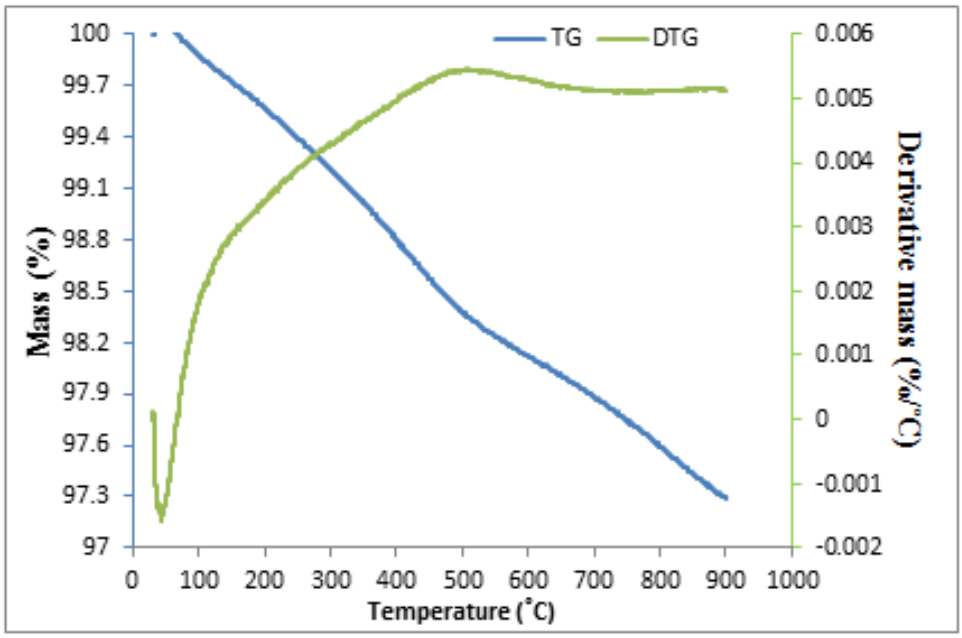


Figure 4.7: TGA/DTG curves of metakaolin

The low mass depletion observed for the metakaolin was likely because the material had already gone through phase transformation within the temperature range of the thermal treatment during metakaolinization, hence, further heating within the same temperature range would not likely result into any transformation or major mass depletion in the material. It is worth noting that since the metakaolinization was carried out in bulk it is likely that some little fraction of the material was not completely transformed. The slight DTG peak and the little mass depletion observed were likely due to complete phase transformation of such fractions to the metakaolin phase.

4.2 Characteristics of Aluminium hydroxide

The physicochemical, morphological and thermogravimetrical characterizations of the aluminium hydroxide produced are presented in this section.

4.2.1 XRD patterns of aluminium hydroxide

Figures 4.8, 4.9 and 4.10 show the XRD patterns of aluminium hydroxide synthesized from the aluminium sulfate produced from variable extents of dealumination; 3, 4 and 5 folds of dealumination of metakaolin respectively. It could be observed that irrespective of the extent of dealumination the XRD patterns of the products obtained were identical. It could be observed from the XRD that the products were amorphous. The characteristic XRD peaks of mixed phases of aluminium hydroxide could be observed at Bragg‟s angles of 20.4, 27.9, 38.0, 40.3, 48.7 and

64.8°, although the peaks were not clearly pronounced. The peaks at 27.9, 38.0, 48.7 and 64.8° were the characteristic peaks for the boehmite phase of aluminium hydroxide while peaks at 20.4, and 40.3° were due to the bayerite phase of aluminium hydroxide (Du *et al*., 2009; Lee *et*

al., 2009). It would be observed that the peaks were not clearly pronounced, implying that the materials were highly amorphous. It could also be due to the presence of some competing amorphous materials which are likely sulphate impurities such as aluminium sulphate precipitated alongside the aluminium hydroxide.

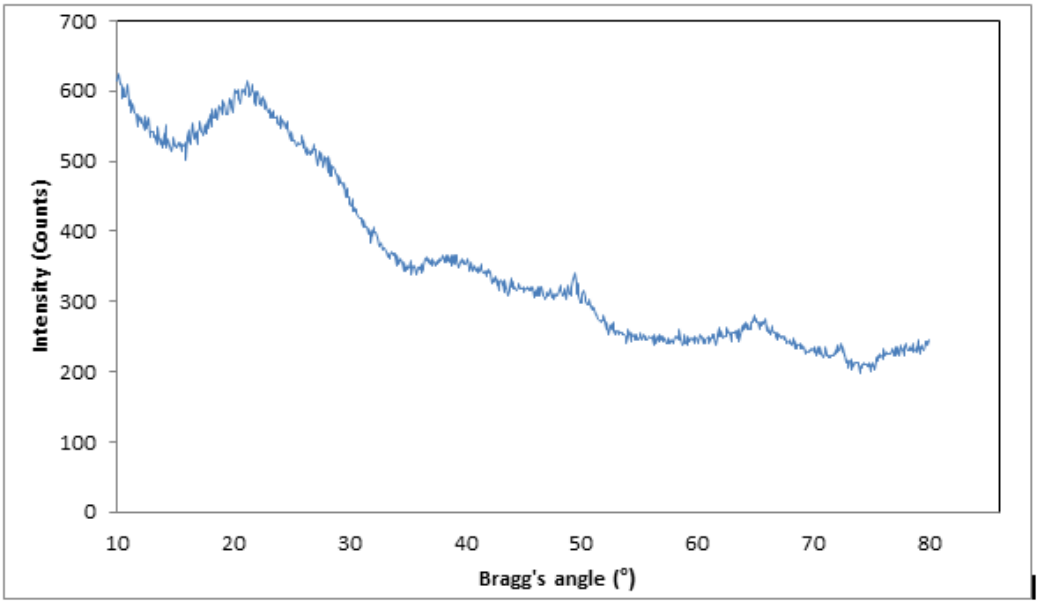


Figure 4.8: XRD pattern of $Al(OH)_3$ 3 fold uncalcined

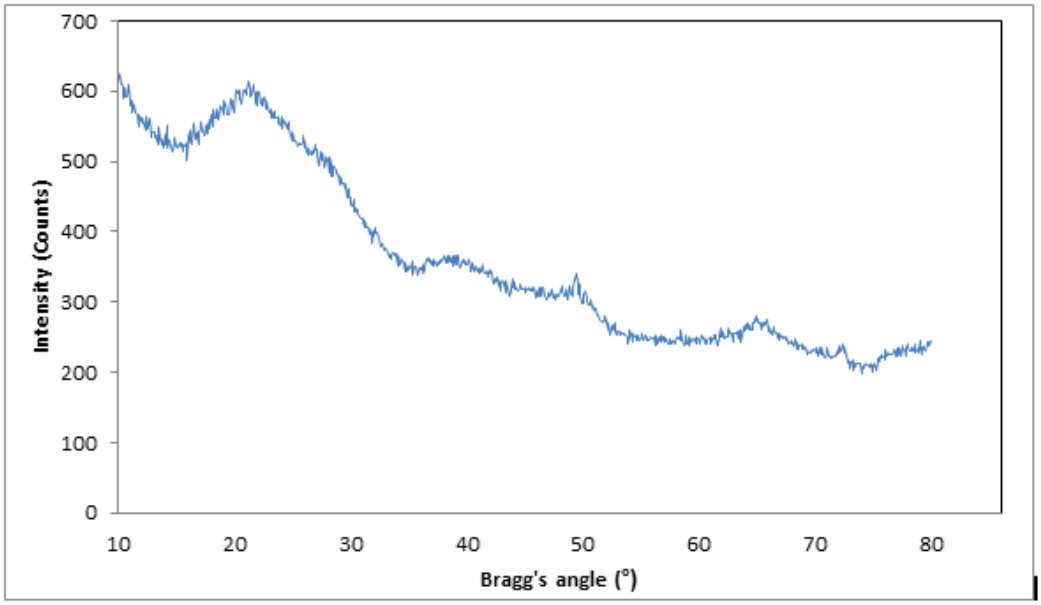


Figure 4.9: XRD pattern of $Al(OH)_3$ 4 fold uncalcined

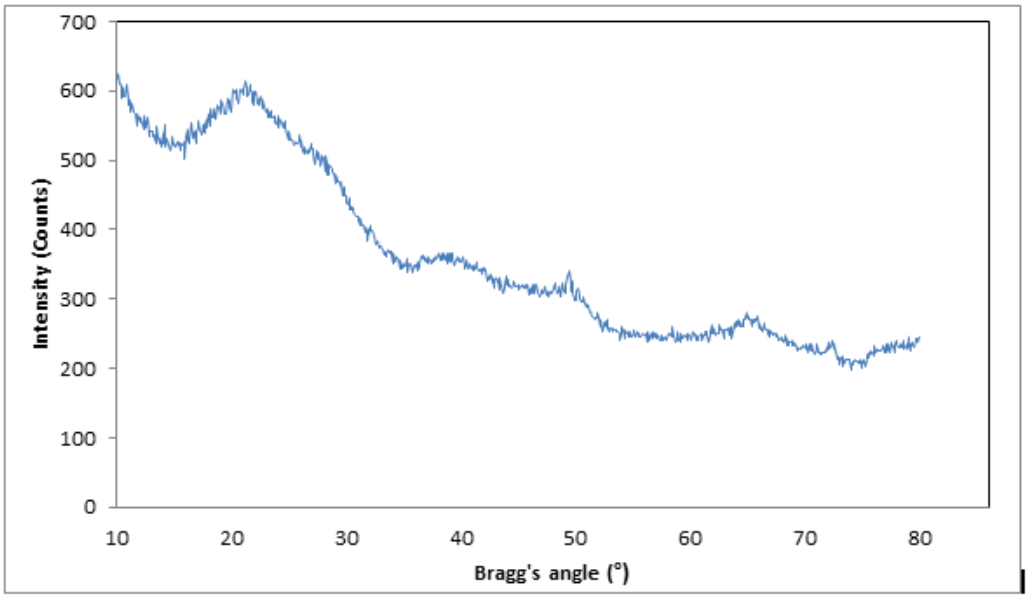


Figure 4.10: XRD pattern of $Al(OH)_3$ 5 fold uncalcined

Figures 4.11, 4.12 – 4.17 present the XRD patterns of the aluminium hydroxide produced and subjected to calcination at temperatures of 300, 400, 500, 600, 700, 800 and 900˚C respectively. It could be observed that at low temperatures calcination; 300 – 500°C the XRD patterns of the aluminium hydroxide produced was still largely indifferent as could be seen in Figures 4.11 – 4.13. However, at higher calcination temperatures of 600 and 700°C, clear difference could be observed in the XRD patterns, some tendency of phase transformation had begun to develop at these temperatures, some gamma – alumina peaks at Bragg‟s angles of 45.90 and 66.92° had started showing the tendency of becoming obvious as could be seen in Figures 4.14 and 4.15. At higher calcination temperatures 800 and 900°C the XRD pattern showed a complete phase transformation into the gamma alumina phase, all the characteristic peaks for gamma alumina at Bragg‟s angles of 39.52, 45.90 and 66.92° (Chen, 1977; Du *et al*., 2009) became obvious in the XRD pattern of the products as could be seen in Figures 4.16 and 4.17. Figure 4.18 shows the XRD pattern of the commercial gamma – alumina. It could be observed that the XRD patterns of

the aluminium hydroxide calcined at 800 and 900°C compared very closely with the XRD pattern of the commercial sample. The characteristic peaks of the gamma alumina at around 39.52, 45.90 and 66.92° had higher intensity in the aluminium hydroxide calcined at 900°C than the commercial alumina.

Figure 4.19 shows a clear comparison in the XRD patterns of the aluminium hydroxides calcined at the various temperatures and the commercial gamma alumina. It could be observed that before calcination; as shown in Figures 4.8 – 4.10 and even after calcination at low temperatures of 300 – 500°C the material produced was aluminium hydroxide as was already confirmed by the analysis of the XRD results of the products. It was confirmed that at calcination temperatures of 600 and 700˚C the material began to transform to gamma alumina phase. At 800˚C the phase transformation was completed and the XRD pattern compared closely with the commercial gamma alumina as could be seen in Figure 4.19.

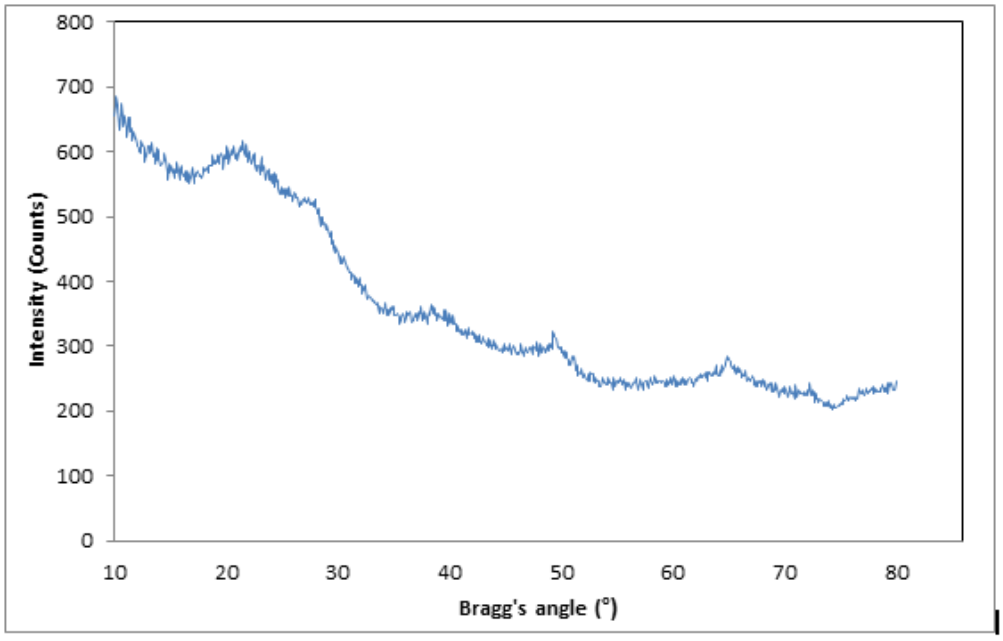


Figure 4.11: XRD pattern of $Al(OH)_3$ calcined at 300˚C

At calcination temperature of 900°C the XRD pattern of the product did not only compare well with the commercial gamma alumina but rather had higher intensities at all the characteristic peaks of gamma alumina. The intensities of the XRD pattern of the 900˚C calcination were 17%, 53% and 22% higher at the Bragg‟s angle of 39.52, 45.90 and 66.92° respectively.

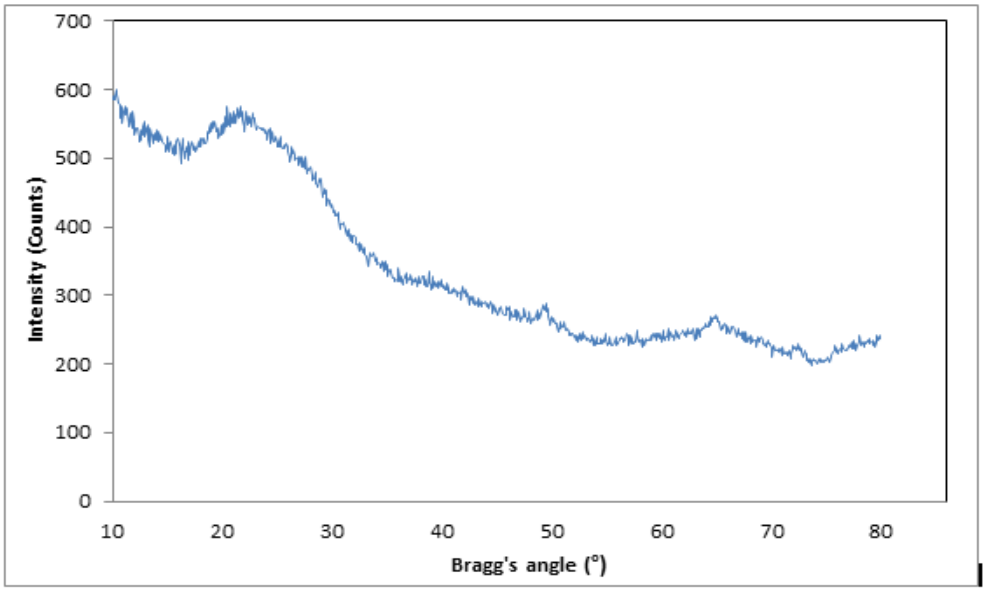


Figure 4.12: XRD pattern of $Al(OH)_3$ calcined at 400°C

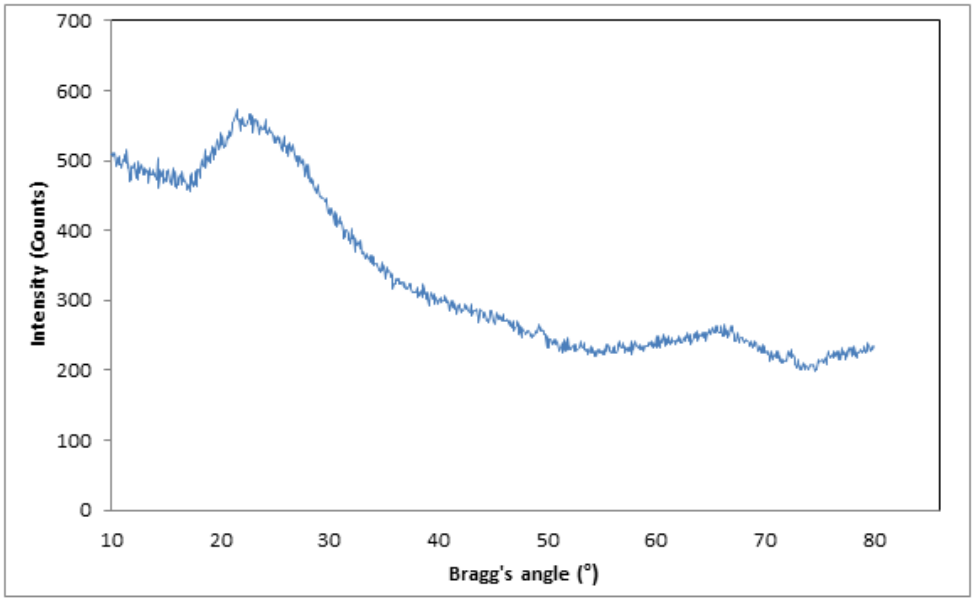


Figure 4.13: XRD pattern of $Al(OH)_3$ calcined at 500°C.

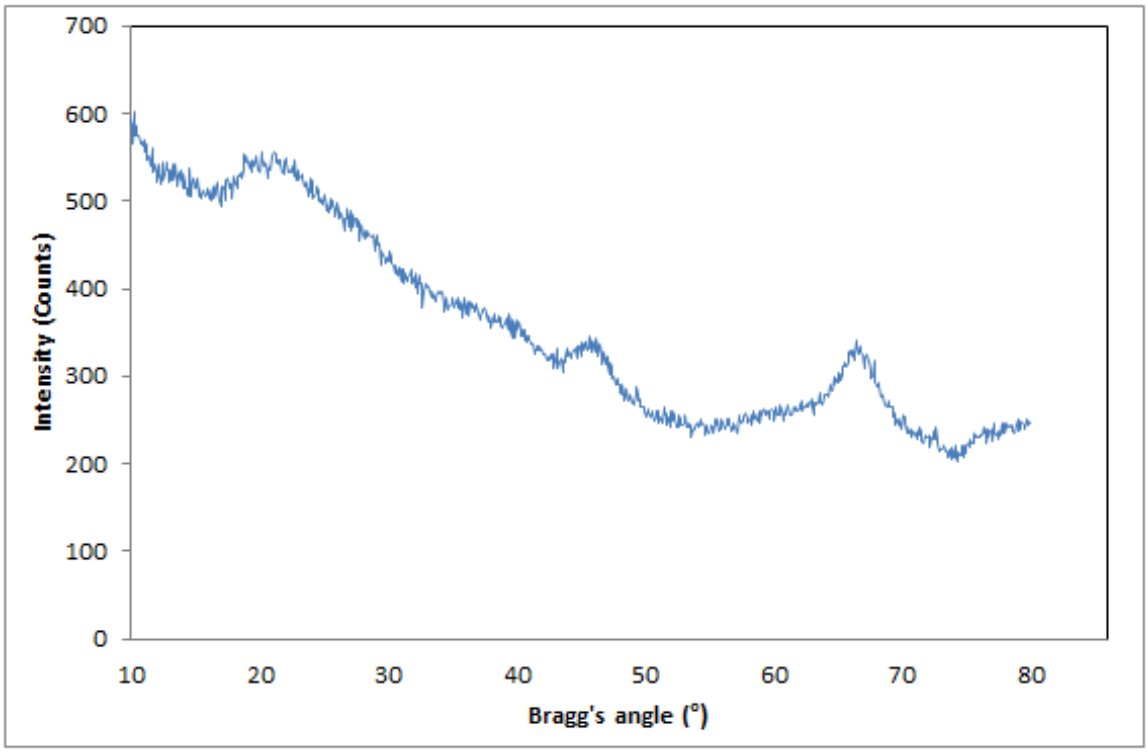


Figure 4.14: XRD pattern of $Al(OH)_3$ calcined at 600°C

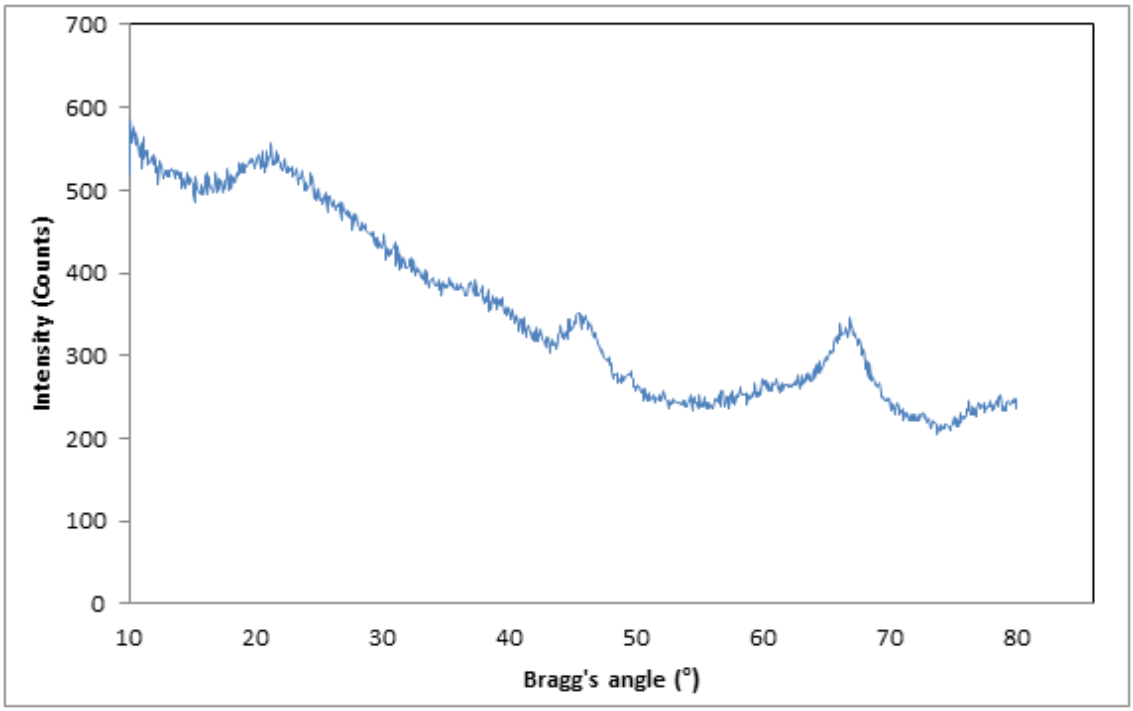


Figure 4.15: XRD pattern of $Al(OH)_3$ calcined at 700°C

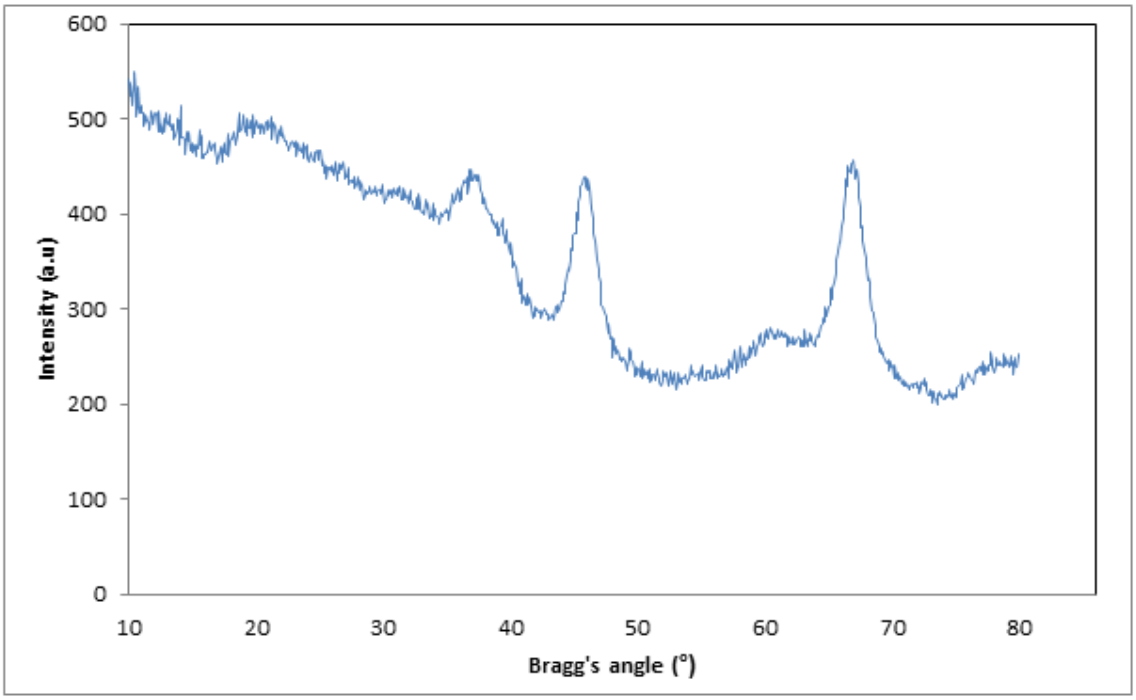


Figure 4.16: XRD pattern of $Al(OH)_3$ calcined at 800°C

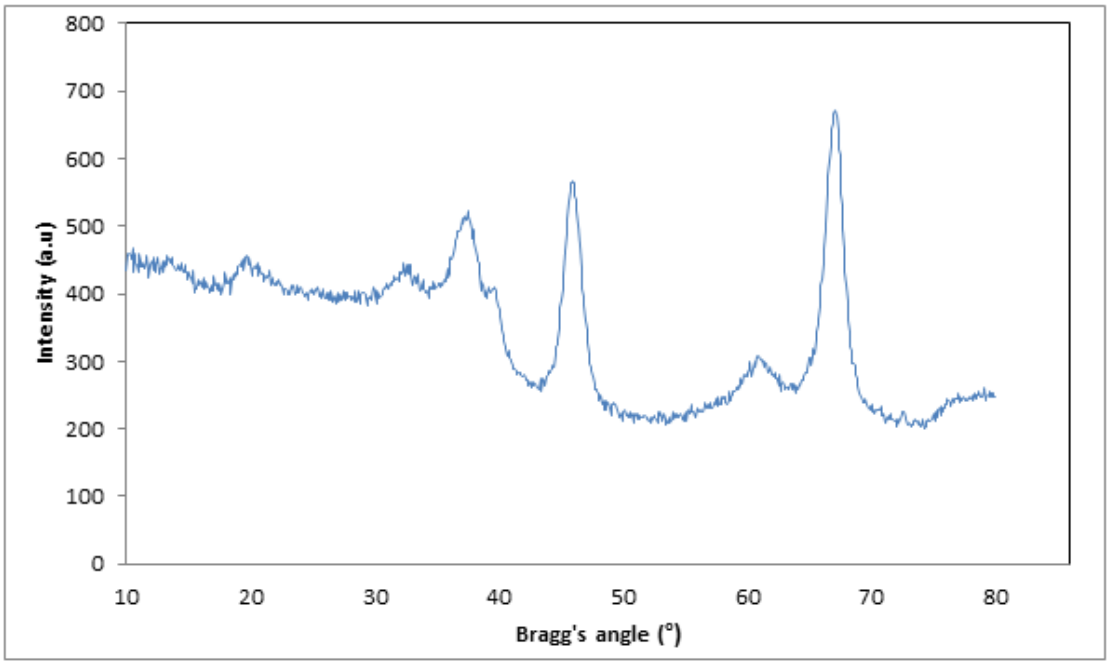


Figure 4.17: XRD pattern of $Al(OH)_3$ calcined at 900°C

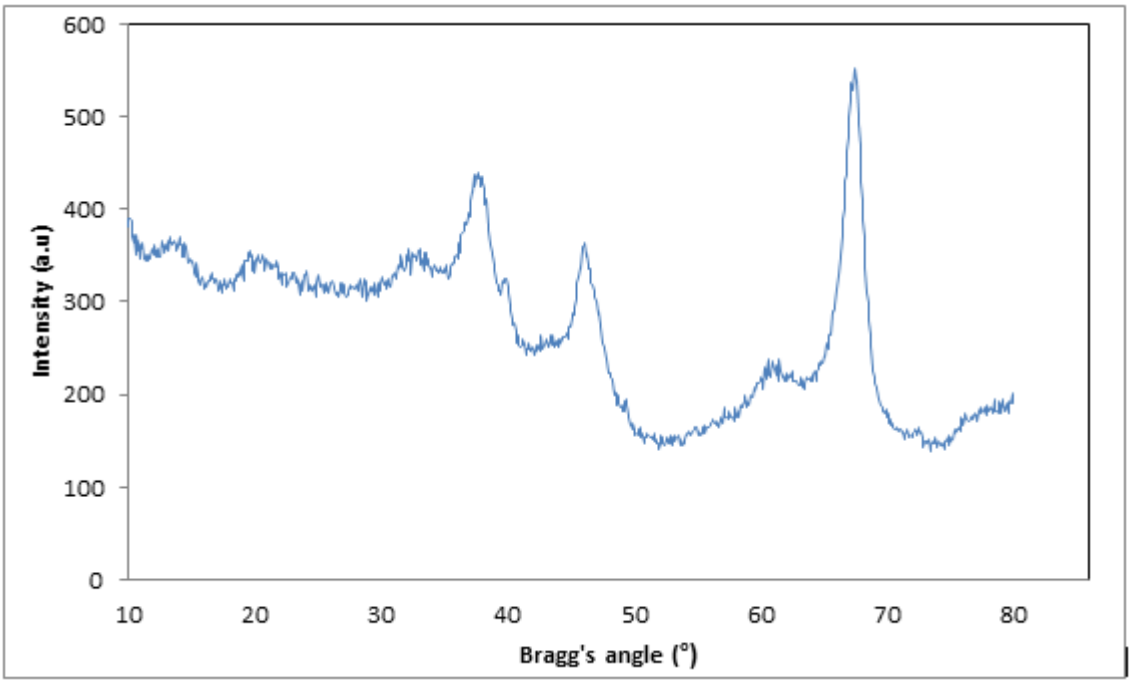


Figure 4.18: XRD pattern of commercial gamma alumina

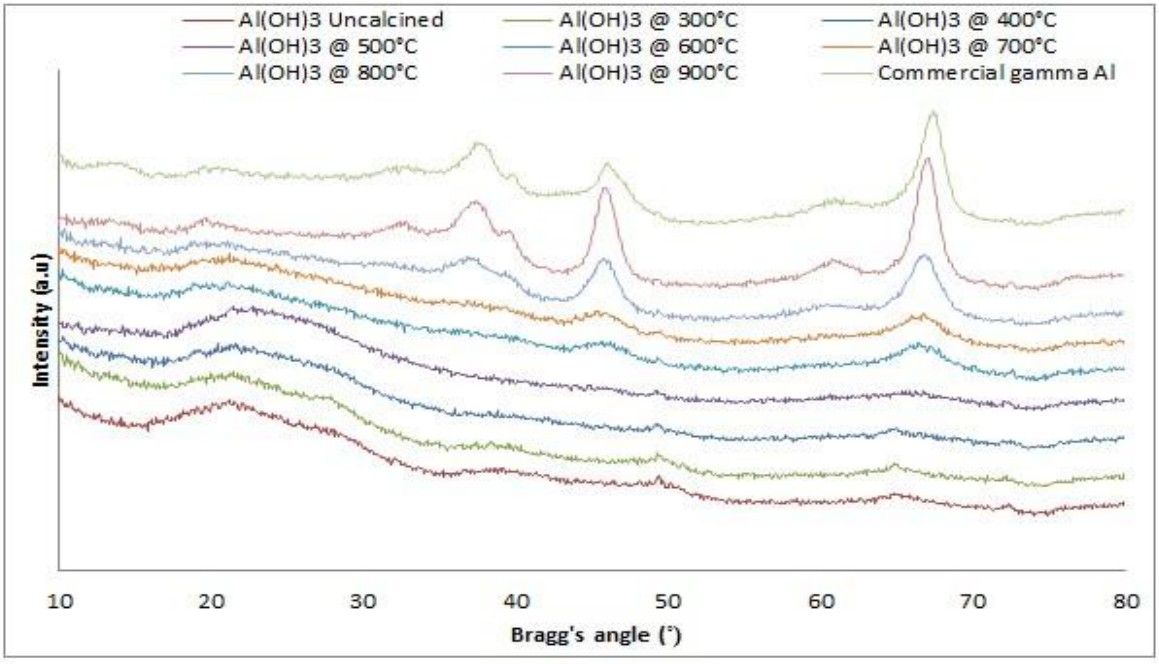


Figure 4.19: Comparison of XRD patterns of aluminium hydroxide at various calcination temperatures

4.2.2 Chemical compositions of the aluminium hydroxide

Table 4.3 presents the chemical composition results of the aluminium hydroxide produced at the various folds of dealumination. It could be observed that the Al_2O_3 content of the aluminium hydroxide produced with 3 fold dealumination was 58.92 wt% and the SiO_2 was 0.95 wt%. At 4 fold dealumination the alumina content increased slightly by 1.9% and the silica earlier observed in the 3 fold was completely absent. The sulfur content of the product was observed to be much; at 3 fold dealumination it was 13 wt%, this decreased by 11.5% at 4 fold dealumination. Other metallic oxides that decreased were MgO, Na_2O and TiO_2 they decreased by 40%, 61% and 29% respectively. Whereas CaO, Fe_2O_3 and CuO each increased to almost twice at 4 fold dealumination compared to the 3 fold dealumination, the reason for this was not understood. The Al_2O_3 content for the 5 fold dealumination was 52.2 wt%, which means 11.4% decrease from the value observed for the 3 fold dealumination. This was opposite to the trend observed between the 3 and 4 fold dealumination, also, the reason for this was not understood. Also, the sulfur content in the 5 fold dealumination product negates the trend observed between the 3 and 4 fold dealumination, instead of the earlier decrease it increased by 43.8%. This was likely as result of excessive use of sulfuric acid beyond the threshold needed for the dealumination. MgO, Na_2O and TiO_2 decreased following the same trend as observed between the 3 and 4 fold dealuminations, although the decrease in Na_2O did not streamline across; it could be seen that between 4 and 5 fold dealuminations Na_2O increased by 138%, although when compared with 3 fold dealumination the Na_2O for the 5 fold was 7.5% decrease of the value for 3 fold. Fe_2O_3 content of the 5 fold increased by 10.7% more than the 3 fold content. The absence of silica observed showed that the dealumination process had effectively split the clay into alumina filtrate and silica residue as predicted by Equation (3.2).

Table 4.3: Chemical compositions of $Al(OH)_3$ synthesized using variable extent of dealumination

Metallic Oxide	Sample/Composition (wt%)		
	$Al(OH)_3$ 3Fold	**$Al(OH)_3$ 4Fold**	**$Al(OH)_3$ 5Fold**
Al_2O_3	58.92	60.03	52.2
SiO_2	0.95	ND	ND
Na_2O	0.67	0.26	0.62
SO_3	13	11.5	18.7
MgO	1.63	0.98	0.33
CaO	0.436	0.852	0.369
TiO_2	0.058	0.041	0.02
Fe_2O_3	1.77	3.03	1.96
CuO	0.022	0.044	0.041
LoI	**22.5**	**23.26**	**25.76**

The presence of SO_3 in a relatively large quantity was traceable to the sulfuric acid used during the dealumination process. Although, ordinarily the sulfur content would be expected to be in traces amount since the precipitated aluminium hydroxide was thoroughly washed until the absence of sulfur was confirmed with barium chloride. Therefore, the high sulfur observed was likely due to the presence of aluminium sulphate precipitated alongside the aluminium hydroxide as was already suspected in the analysis of the XRD results of the products. Hence, it was likely that the sulphate contained in the product was not detected by the barium chloride probe because it was not in the free sulphate ion form.

Table 4.4 presents the chemical composition results of the aluminium hydroxide produced and calcined at variable temperatures. It could be observed that the alumina content of the aluminium hydroxide calcined at 300, 400 and 500˚C were relatively the same having average value of 60.30 wt%. This observation further buttressed the earlier deduction made from the XRD results that the material remained indifferently aluminium hydroxide within the calcination temperature range of $0 \leq T \leq 500$˚C. However, it could be observed that at calcination temperatures of 700˚C the alumina content of the product had increased by 29%, this further showed that at 700˚C the aluminium hydroxide was undergoing phase transformation to gamma alumina having alumina content value of 77.52%, an appreciably high value. At calcination temperatures of 800 and 900˚C the alumina content of the products were 38% and 51% higher than the values for the low temperature product. The alumina content at 800 and 900˚C calcination were 83.47 wt% and 91.02 wt% respectively, whereas that of the commercial alumina was 94.83 wt%. Hence, it could be seen that the products at 800 and 900˚C calcination temperatures compared closely with the commercial gamma alumina in terms of the alumina contents. The alumina content of the products at 800 and 900˚C calcination were 88% and 96% respectively of the alumina content in the commercial gamma alumina. This further showed that at 800 and 900˚C a fully developed gamma alumina phase was obtained as was already shown by the XRD results.

The aluminium hydroxide produced was free of silica impurity as could be seen from the chemical composition results, although the commercial gamma alumina had silica impurity of 0.01 wt% the Na_2O impurity content was low, especially that of the 800 and 900˚C calcination, the Na_2O contents were comparable to the content in the commercial gamma alumina. Other impurities observed in the produced samples such as MgO, CaO and CuO were in low

concentrations less than 1.0 wt%. Another noticeable impurity present in the aluminium hydroxide was Fe_2O_3, it was up to 2.13 wt% in the sample calcined at 300˚C, however, it reduced by 41% at calcination temperatures of 800 and 900˚C. It is worth noting that sulfur was present in the aluminium hydroxide produced in a very large quantity. In the sample calcined at temperatures between 300 and 500˚C the average sulfur content was 13.27 wt%, however, the sulfur content decreased with increasing calcination temperature. At 700˚C the sulfur content had decreased by 76%. At 800 and 900˚C the sulfur content decreased by 86% and 99% respectively. It could be seen that the sulfur content at 700˚C was negligible.

Table 4.4: Chemical compositions of $Al(OH)_3$ calcined at different temperatures

Metallic Oxide	Sample/Composition (wt%)						
	$Al(OH)_3$ @ 300˚C	**$Al(OH)_3$ @ 400˚C**	**$Al(OH)_3$ @ 500˚C**	**$Al(OH)_3$ @ 700˚C**	**$Al(OH)_3$ @ 800˚C**	**$Al(OH)_3$ @ 900˚C**	**Commercial Gamma Alumina**
Al_2O_3	60.03	60.09	60.78	77.52	83.47	91.02	94.83
SiO_2	ND	ND	ND	ND	ND	ND	0.01
Na_2O	0.56	0.21	0.43	0.29	0.27	ND	0.25
MgO	0.87	0.98	0.84	0.58	0.61	ND	ND
CaO	0.28	0.256	0.261	0.336	0.284	ND	ND
CuO	0.04	0.022	0.021	0.423	0.411	0.48	ND
Fe_2O_3	2.13	1.94	1.91	1.06	1.25	1.25	0.03
SO_3	13.40	13.30	13.10	3.21	1.52	0.11	ND
LoI	22.6	22.16	21.61	16.58	11.68	6.23	4.80

The LoI of the uncalcined aluminium hydroxide which was 22.6 wt% remained relatively unchanged within temperature range of 300 - 500˚C, nevertheless, at 700˚C the LoI had

decreased by 27% at 800 and 900˚C, the decrease observed were 48 and 72% respectively. The LoI value of the 900˚C product was 6.23 wt% which was close to the 4.80 wt% observed in the commercial gamma alumina.

Figure 4.20 shows the trend of alumina and sulfur contents in the aluminium hydroxide at the various calcination temperatures. It could be seen that the starting aluminium hydroxide contained high sulfur impurities which reduced continuously with calcination temperature. The sulfur content became minimal at 900˚C calcination, reducing to 0.6% of the sulfur content of the starting aluminium hydroxide. Conversely it could be seen that the alumina content increased continuously with increasing calcination temperature, the alumina content became very high at 900˚C calcination rising to 151% of the alumina content of the starting aluminium hydroxide.

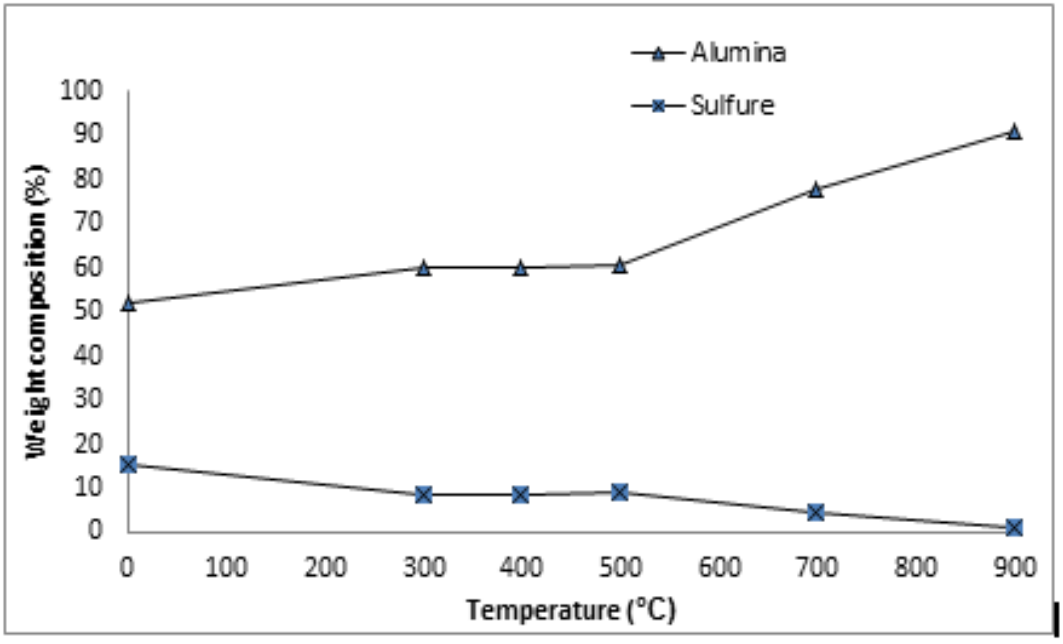


Figure 4.20: Trend of alumina and sulfur contents of the aluminium hydroxide produced under varying calcination temperatures

4.2.3 BET properties of aluminium hydroxide

Table 4.5 presents the BET results of the aluminium hydroxide; uncalcined and calcined at various temperatures and the BET result of the commercial gamma alumina. It could be seen that the BET surface area and the pore volume of the uncalcined aluminium hydroxide were 81.01 m^2/g and 0.0264 cm^3/g. After calcination at 400˚C both the surface area and the pore volume of the aluminium hydroxide reduced by 45%. The reason for this was not very clear; it could be as a result of structural rearrangement of the aluminium hydroxide in preparation for the transformation into the gamma alumina phase. It could also be as a result of decomposition of some of the sulphate impurities earlier identified by the XRF results to be present in the uncalcined aluminium hydroxide. However, it could be observed that at calcination temperature of 600˚C the surface area and pore volume of the product both increased by 60% more than the value at 400˚C calcination.

Table 4.5: BET results of the aluminium hydroxide at variable calcination temperatures

Sample	Surface Surface Area (m^2/g)	Pore Volume (cm^3/g)	Pore Diameter (Å)
$Al(OH)_3$ – Uncalcined	81.01	0.0264	ND
$Al(OH)_3$ @ 400C	44.32	0.0144	ND
$Al(OH)_3$ @ 600C	70.72	0.0230	ND
$Al(OH)_3$ @ 800C	202.3	0.0613	12.12
$Al(OH)_3$ @ 900C	102.6	0.0305	11.89
Commercial Gamma Al	123.4	0.0365	11.83

ND: Not determined

This was likely as a result of the transformation to the gamma alumina phase as was already identified by the XRD and XRF results that the transformation rarely started at 600˚C. At calcination of 800˚C the product developed an exponentially high surface area, the surface area and pore volume were 202.3 and 0.0613 cm^3/g respectively, which each was about 350% higher than the values obtained at 400˚C and the pore diameter was 1.212 nm. The material obtained at 800˚C was high surface area gamma alumina or activated alumina considering its high surface area and pore volume which fall within the value range reported for activated alumina in the literature (Bansiwal *et al*., 2010). The surface area and pore volume of the sample calcined at 900˚C also possessed high surface area and pore volume values of 102.6 m^2/g and 0.0305 cm^3/g respectively and the pore diameter was 1.189 nm. Although these values were high when compared to the values obtained for the uncalcined and the calcination at 400 and 600˚C, nevertheless the values were very low when compared to the values obtained at the 800˚C. The surface area and pore volume of 900˚C calcined sample were both 50% lower than the 800˚C sample. The reduction was likely because the structural morphology of the material developed into activated alumina at 800˚C and once the temperature is exceeded at 900˚C this peculiar structure begins to collapse resulting into a huge loss of surface area and pore volume, although the material retained its gamma alumina mineralogical phase as indicated by the XRD result.

4.2.4 SEM micrographs of aluminium hydroxide

Plates VII – XII show the SEM images of the uncalcined alumina hydroxide and aluminium hydroxide calcined at 400, 600, 700, 800 and 900˚C respectively, scanned at various magnifications. It could be observed from Plates VII A, B and C; irrespective of the magnification, each of the micrograph of the uncalcined aluminium hydroxide at magnifications

of 1200, 3000 and 4000 showed aggregated lumps. Each lump represented a macrostructure which consisted of agglomerated particles with irregular particle shapes. Therefore, it could be deduced from the images that the aluminium hydroxide possessed a lumpy anhedral morphology, this further showed the amorphous nature of the aluminium hydroxide produced as already shown by the XRD result. The average particle size of the aluminium hydroxide was estimated as 0.2 µm. Plates VIII A, B and C show the structural mophology of the 400˚C calcined aluminium hydroxide at magnifications of 4500, 5000 and 8000 respectively. The images show agglomerated particles which appeared hollow. It could be observed that some of the particles appeared in a regular shape which appeared to be octahedral, while others appeared to possess irregular shapes. Hence, the morphology of the aluminium hydroxide calcined at 400˚C was a hollow mixed-anhedral-euhedral structural morphology. The particle size of AL4 was estimated as 0.2 µm. Plates IX A, B, C and D show the structural mophology of the 600˚C calcined aluminium hydroaxide at magnifications of 1700, 13000, 20000 and 30000 respectively. The morphology of the material at 1700 magnification appeared fluffy and hollow, however, at other higher magnifications the structure of the morphology of the material was not clear enough. It could be seen from the 1700 magnification that the material appearance of the aluminium hydroxide calcined at 600˚C looked different from those of the uncalcined sample and the sample calcined at 400˚C. Looking at the morphology of the 600˚C calcination, it could be observed that the material possessed anhedral morphology, the average particle size was estimated as 0.2 µm. Plates X A, B, C and D show the structural mophology of the 700˚C calcined aluminium hydroxide at magnifications of 8000, 12000, 18000 and 43000 respectively. Each of the magnifications showed lumps of irregularly shaped agglomeration of particles. It could be observed that the material also possessed anhedral morphology and the average particle

size was estimated as 0.2 µm. Plates XI A, B, C and D show the structural mophology of the 800˚C calcined aluminium hydroxide at magnifications of 1000, 3000, 4000 and 5000 respectively. Aggregates of agglomerated particles forming a hollow structural arrangement could be observed. The agglomerated particles possessed a definite shape which appeared to be hexagonal, the shape was particularly obvious in Plate XI C. Therefore, the 800˚C calcination product possessed a hollow hexagonal euhedral morphology. The particle sizes were very diversed, however, the average size of the small particles observed was estimated as 0.2 µm. Plates XII A, B and C show the structural mophology of the 900˚C calcined aluminium hydroxide at magnifications of 1000, 2000 and 2500 respectively. The structural morphology showed flake-like densely agglomerated particles. The particles seem to possess a definite shape, although the shape was not clearly defined. The particle sizes were also diversed, however, the average size of the small particles observed was estimated as 0.12 µm. The structural morphology was a flake-like euhedral morphology.

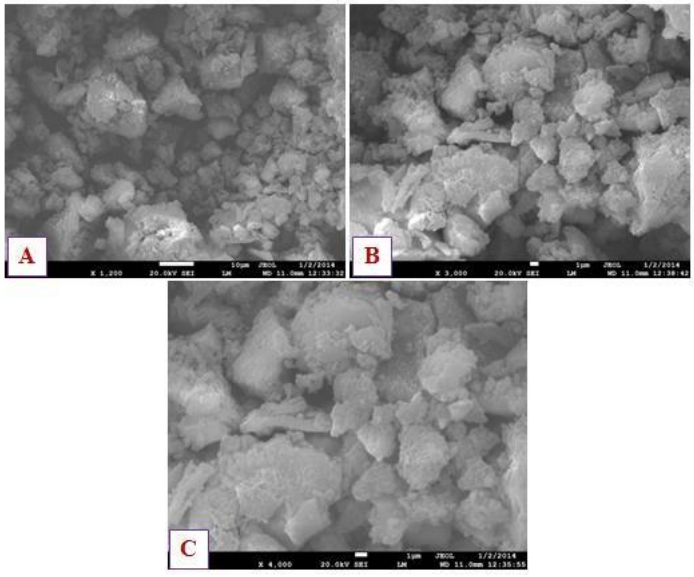


Plate VII: SEM images of uncalcined aluminium hydroxide at magnifications of (A) 1200 (B) 3000 (C) 4000

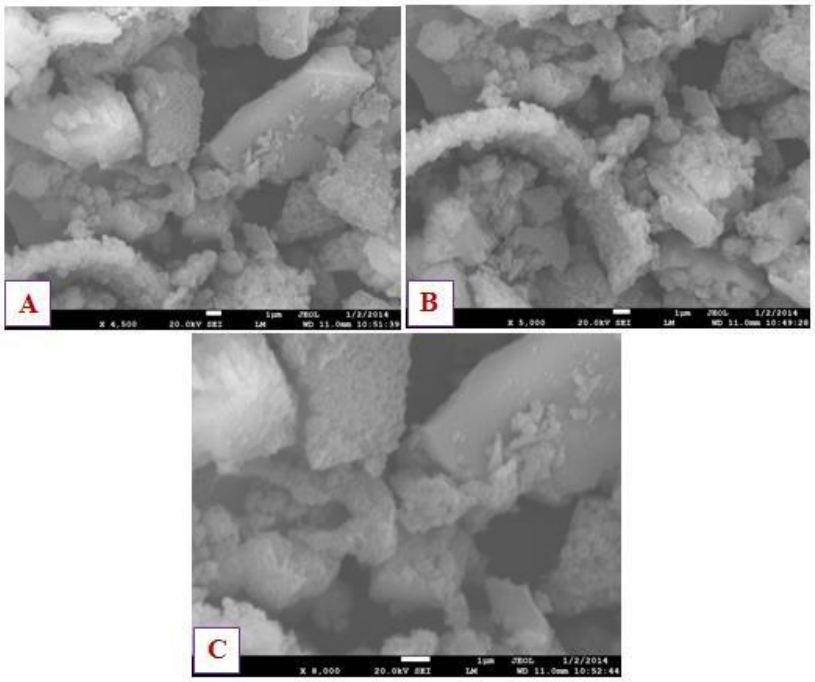


Plate VIII: SEM images of aluminium hydroxide calcined at 400˚C and magnifications of (A) 4500 (B) 5000 (C) 8000

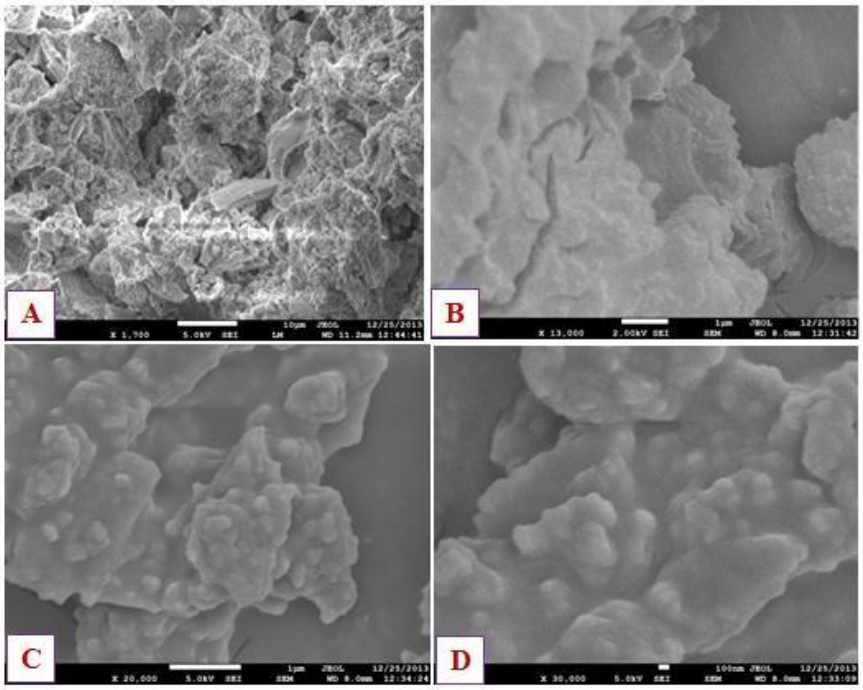


Plate IX: SEM images of aluminium hydroxide calcined at 600˚C and magnifications of (A) 1700 (B) 13000 (C) 20000 (D) 30000

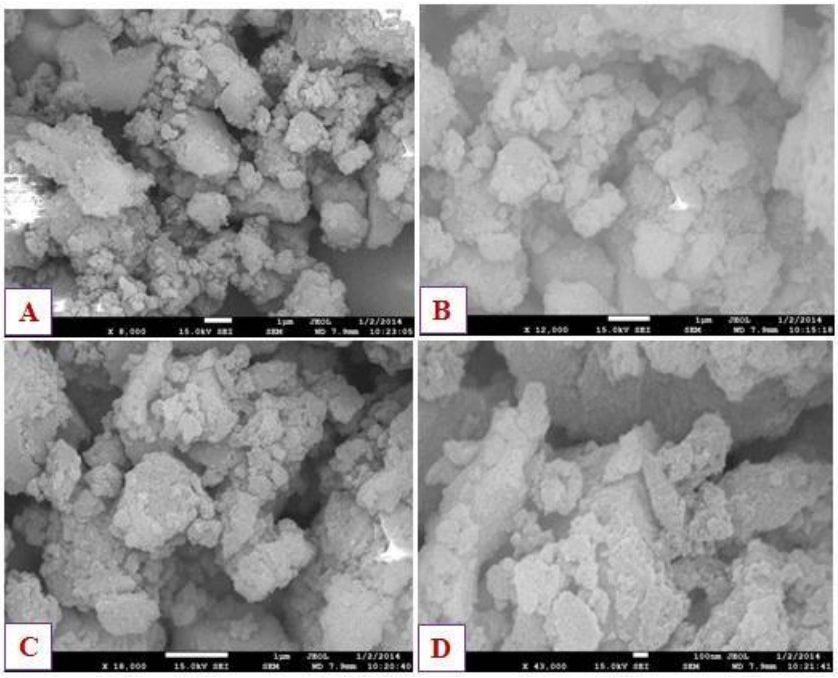


Plate X: SEM images of aluminium hydroxide calcined at 700˚C and magnifications of (A) 8000 (B) 12000 (C) 18000 (D) 43000

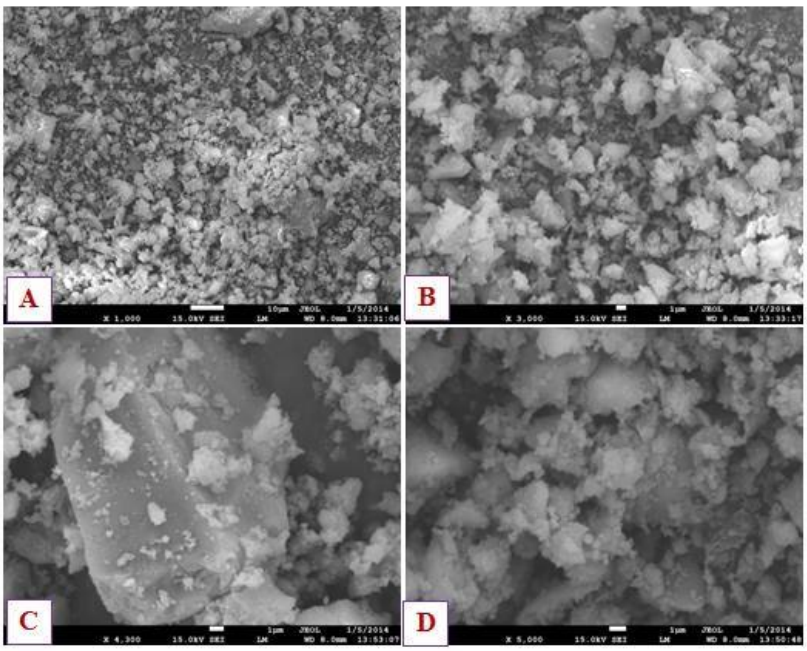


Plate XI: SEM images of aluminium hydroxide calcined at 800˚C and magnifications of (A) 1000 (B) 3000 (C) 4000 (D) 5000

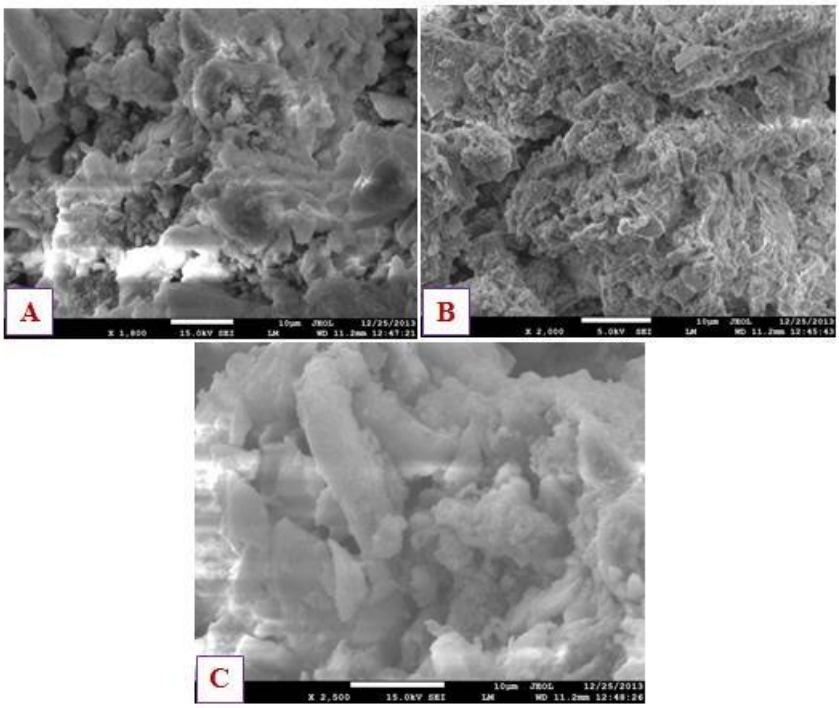


Plate XII: SEM images of aluminium hydroxide calcined at 900˚C and magnifications of (A) 1000 (B) 2000 (C) 2500

4.2.5 TEM images of aluminium hydroxide

Plates XIII A, B, C and D show the TEM images of the alumina hydroxide calcined at 400˚C, captured at magnifications of 100000, 200000, 300000 and 400000 respectively. Irrespective of the magnification, it could be observed that the structural images revealed by the TEM were blurred, this showed the amorphous nature of the material as already identified by the XRD and SEM results of the same sample. Plates XIV A, B, C and D show the TEM images of the alumina hydroxide calcined at 800˚C, captured at magnifications of 100000, 250000, 300000 and 400000 respectively. It could be observed from the images, especially at the higher magnifications, that unit crystal structures of the material were distinguishable. The actual crystal shape of the material could not be revealed even at the highest magnification.The average crystal size was estimated as 10 nm. Plates XV A, B, C and D show the TEM images of the alumina

hydroxide calcined at 900˚C, captured at magnifications of 120000, 200000, 300000 and 400000 respectively. It could be observed image of each unit crystal structures of the material appeared clearer. Image of most unit crystals were distinguishable.

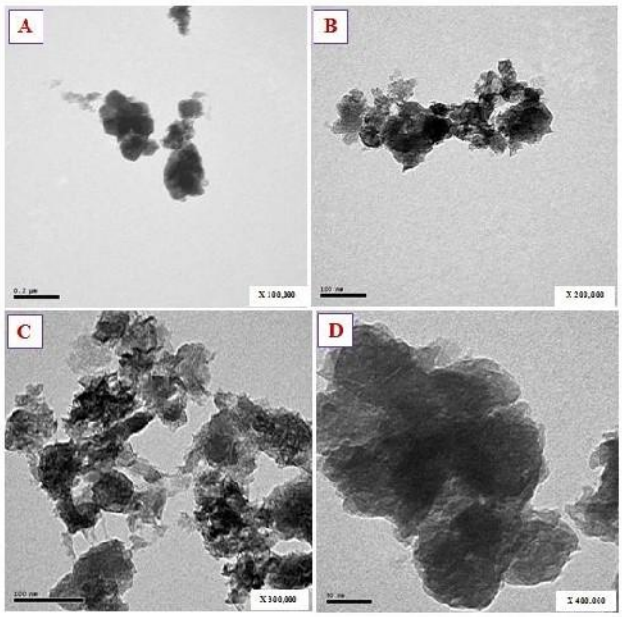


Plate XIII: TEM images of aluminium hydroxide calcined at 900˚C and magnifications of (A) 100000 (B) 200000 (C) 300000 (D) 400000

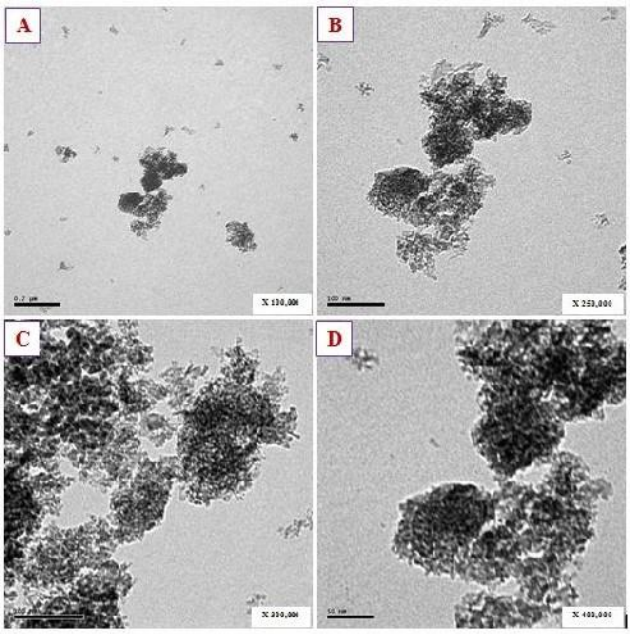


Plate XIV: TEM images of aluminium hydroxide calcined at 800˚C and magnifications of (A) 100000 (B) 250000 (C) 300000 (D) 400000

However, the actual crystal shape the unit crystals could not be revealed.The average crystal size was also estimated as 10 nm. Therefore, it could be seen that the product obtained at calcination temperatures of 800 and 900˚C were crystalline materials as already shown from the analyses of the XRD and SEM results. However, the TEM results further showed that the products were nano-sized.

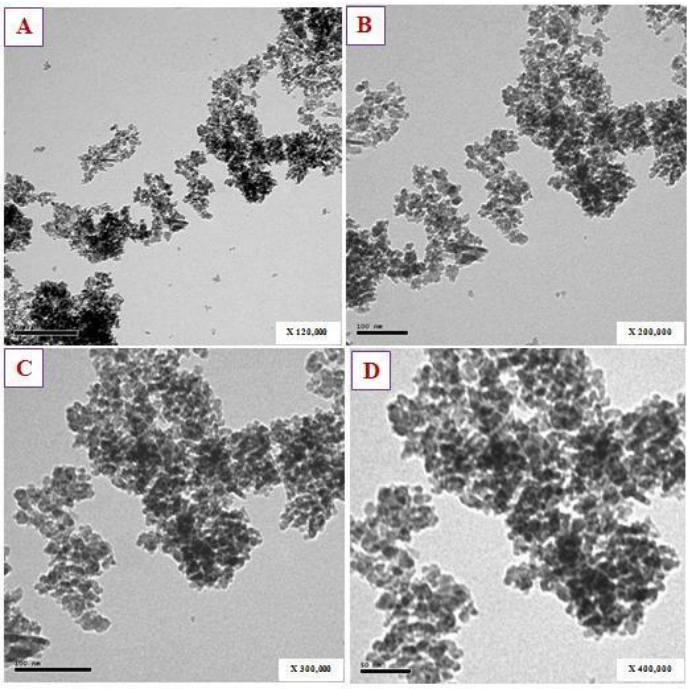


Plate XV: TEM images of aluminium hydroxide calcined at 900˚C and magnifications of (A) 120000 (B) 200000 (C) 300000 (D) 400000

4.2.6 Thermogravimery properties of aluminium hydroxide

Figures 4.21 – 4.24 show the TGA/DTG thermal scan curves within temperature range of 30 - 900˚C for uncalcined aluminium hydroxide and alumina hydroxide calcined at 400, 800 and 900˚C respectively. It could be observed that the total mass depletion as shown by the TGA curves of the uncalcined sample and samples calcined at 400, 800 and 900˚C were 40, 33, 18 and 7% respectively. It could also be observed from the DTG curve in Figure 4.21 that the actual

temperatures responsible for the mass loss in the uncalcined aluminium hydroxide were 100, 180 and 850˚C. The mass loss at 100˚C was likely due to dehydration of the physically adsorbed water. That of 180˚C was likely due to dehydroxylation of the chemically combined water and that of 850˚C was likely due to complete phase transformation to gamma alumina. It could be observed from the DTG curve in Figure 4.22 that the actual temperatures responsible for the mass loss in the aluminium hydroxide calcined at 400˚C were 250 and 850˚C. The mass loss at 250˚C was likely due to dehydroxylation of the chemically combined water since some of the chemically combined water were still expected to be present in this sample because its XRD and XRF results had shown that the material was still aluminium hydroxide, at 400˚C it had not lost all the chemically combined water as to satisfy the condition in Equation (3.1) for full transformation into gamma alumina phase. The mass loss at 850˚C was likely due to complete phase transformation to gamma alumina just as was shown earlier for the uncalcined sample.

The DTG curve in Figure 4.23 showed that the actual temperatures responsible for the mass loss in the aluminium hydroxide calcined at 800˚C were 180 and 800˚C. The mass loss at 180˚C was likely due to dehydroxylation of the chemically combined water, as it was likely that some little remnant of the chemically combined water were still in the sample. The mass loss at 800˚C was likely due to the indication that the material possessed some tendency of further transformation to the full gamma alumina phase when calcined further than 800˚C. Figure 4.24 showed that the actual temperature responsible for the mass loss in the aluminium hydroxide calcined at 900˚C only occurred at 100˚C. Hence, the mass in this sample was likely due to dehydration of the physically absorbed moisture, as it could also be observed that the total mass loss in this sample was relatively very small.

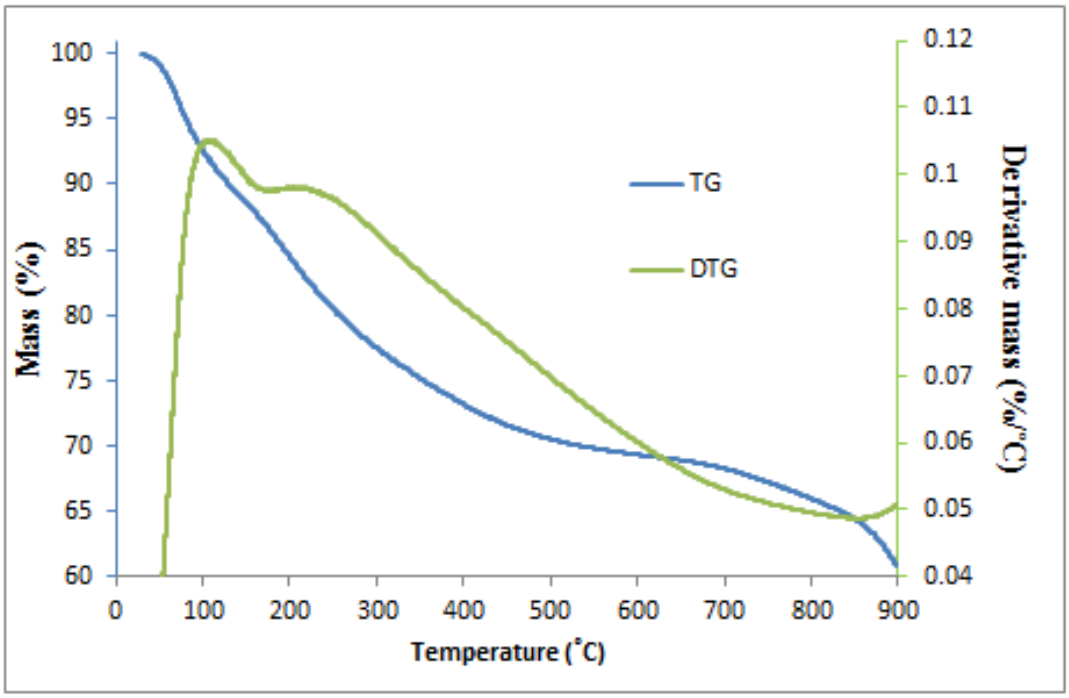


Figure 4.21: TGA/DTG curves of uncalcined aluminium hydroxide

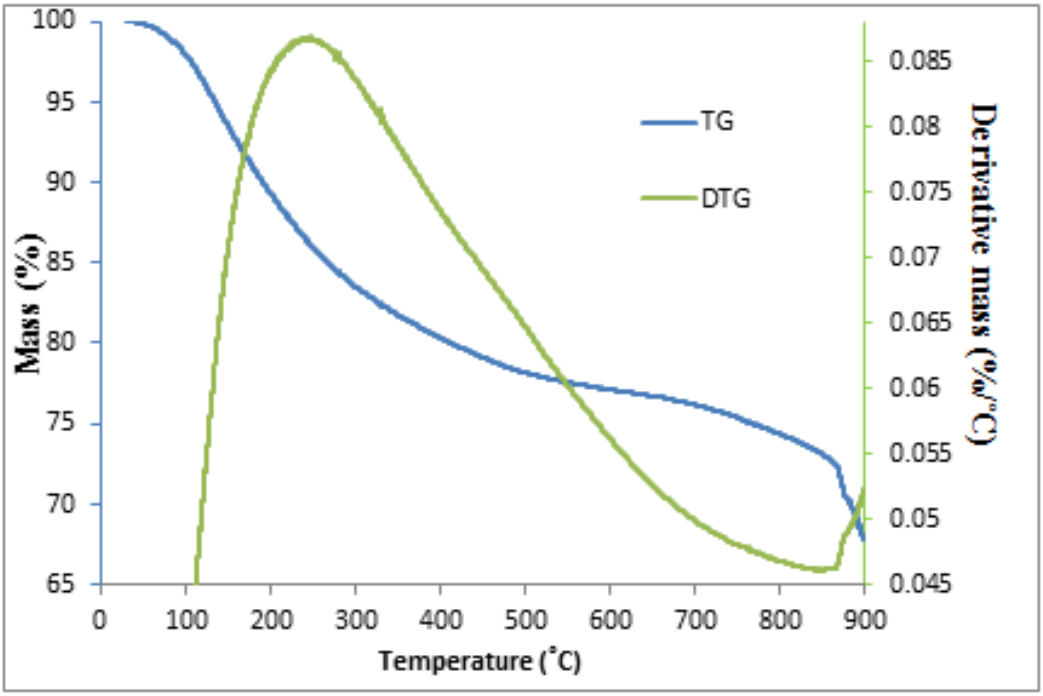


Figure 4.22: TGA/DTG curves of aluminium hydroxide calcined at 400˚C

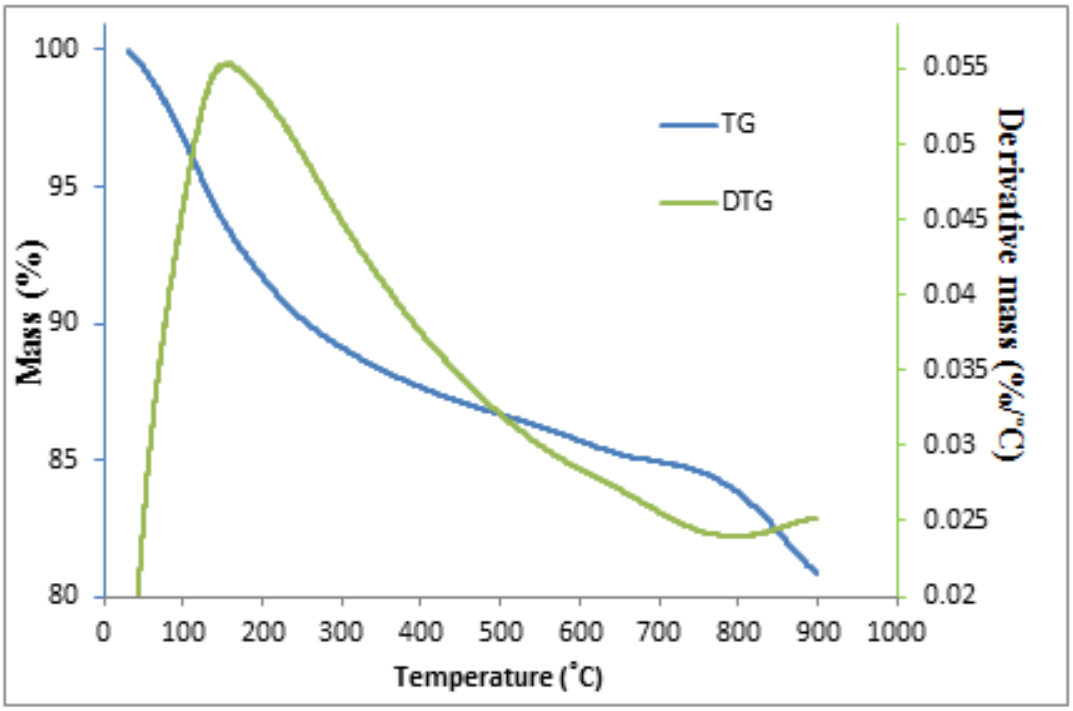


Figure 4.23: TGA/DTG curves of aluminium hydroxide calcined at 800˚C

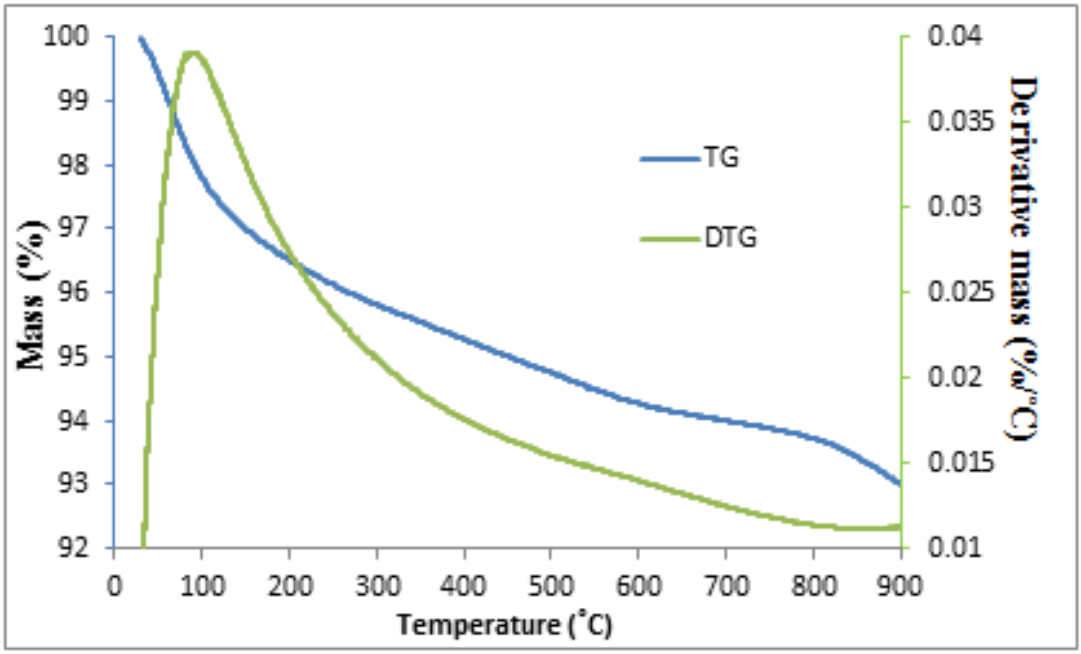


Figure 4.24: TGA/DTG curves of aluminium hydroxide calcined at 900˚C

4.2.7 FTIR spectra of aluminium hydroxide

Figure 4.25 shows the FTIR spectra of aluminium hydroxide uncalcined and aluminium hydroxide calcined at 300, 400, 800 and 900˚C and the commercial gamma aluminium. As it could be observed the uncalcined aluminium hydroxide, aluminium hydroxide calcined at 300 and 400˚C possessed steep bands at around 660 cm^{-1}, while the aluminium hydroxide calcined at 800 and 900˚C and the commercial gamma alumina possessed wide bands extending between 570 and 800 cm^{-1}, these bands were due to the symmetric bending of O–Al –O (El-Naggar, 2013). The similarity in the FTIR spectra of the uncalcined aluminium hydroxide, and aluminium hydroxide calcined at 300 and 400˚C further corroborate their similarity observed in the XRD, XRF and SEM results.

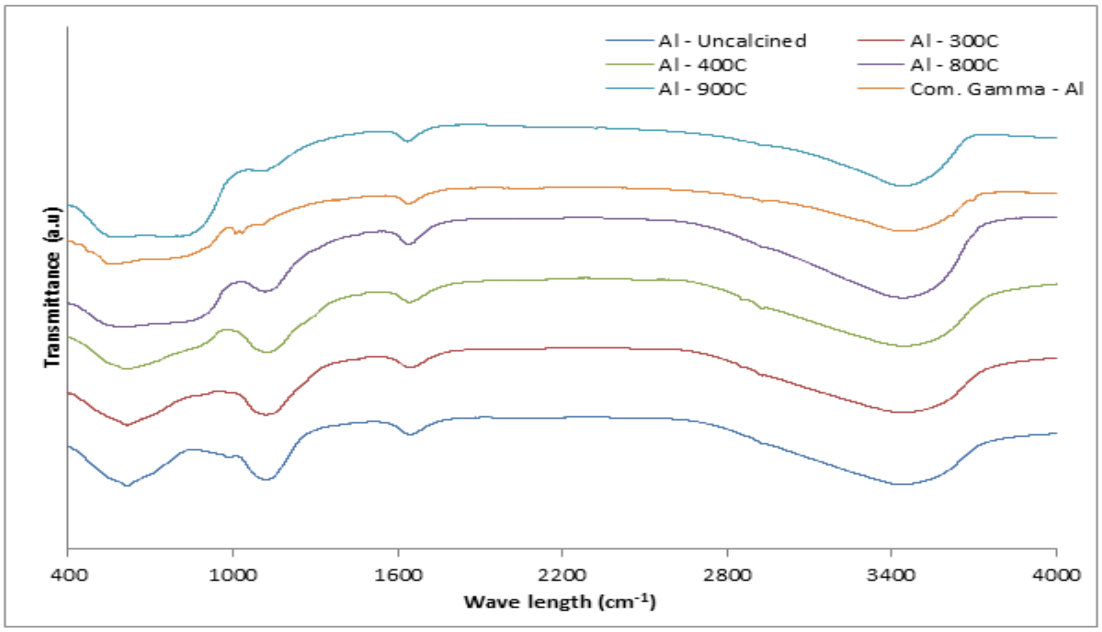


Figure 4.25: FTIR spectra of aluminium hydroxide prepared, the products when it was calcined at variable calcination temperatures and the commercial alumina

It was evident that these samples possessed similar pattern of O– Al–O vibration and this phase had been identified as aluminium hydroxide as evident from the XRD results. It could be seen

that the band had transformed from its earlier steep form to being wide band stretching across 570 and 800 cm^{-1} at the higher temperatures of calcination of 800 and 900˚C implying transformation into a new mineral phase; gamma alumina. The band around 1050 cm^{-1} was attributed to cluster of Al^{3+} and O^{2-} ions on the surface of Al–O vibration, this band was present in all the samples although it was more obvious in the uncalcined aluminium hydroxide and aluminium hydroxide calcined at 300 and 400˚C than in aluminium hydroxide calcined at 800 and 900˚C and the commercial gamma alumina. The band at 1650 cm^{-1} was attributed to bending of H–O–H bonds; it was experienced in all the samples. The band at around 3500 cm^{-1} was present similarly in all the samples and was attributed to the –OH stretching (Lee *et al*., 2013). When observed closely this band was relatively broader in the uncalcined aluminium hydroxide and aluminium hydroxide calcined at 300 and 400˚C than in aluminium hydroxide calcined at 800 and 900˚C and the commercial gamma alumina spectra, this was likely due to low hydroxylation content of the higher calcined samples as was already shown by the LoI of the materials.

4.3 Characteristics of Silica

The physicochemical, morphological and thermogravimetrical characterizations of the silica produced are presented in this section.

4.3.1 XRD patterns of silica

Figure 4.26 shows the XRD pattern of silica produced as the residual product of the dealumination at variable stiochiometric excess acid refered to as variable folds of dealumination. It could be observed that the XRD pattern of the 2 fold dealumination appeared

amorphous but it consisted of few crystaline peaks. The peaks at Bragg‟s angles of 12.4, 20.38,

24.8 and 34.94˚ represented the kaolinite peaks, indicating that the material still contained some residual kaolinite mineral. The peaks at 17.4 and 27.0˚ were characteristic peaks for mica. The peak at 26.4˚C was the silica peak.

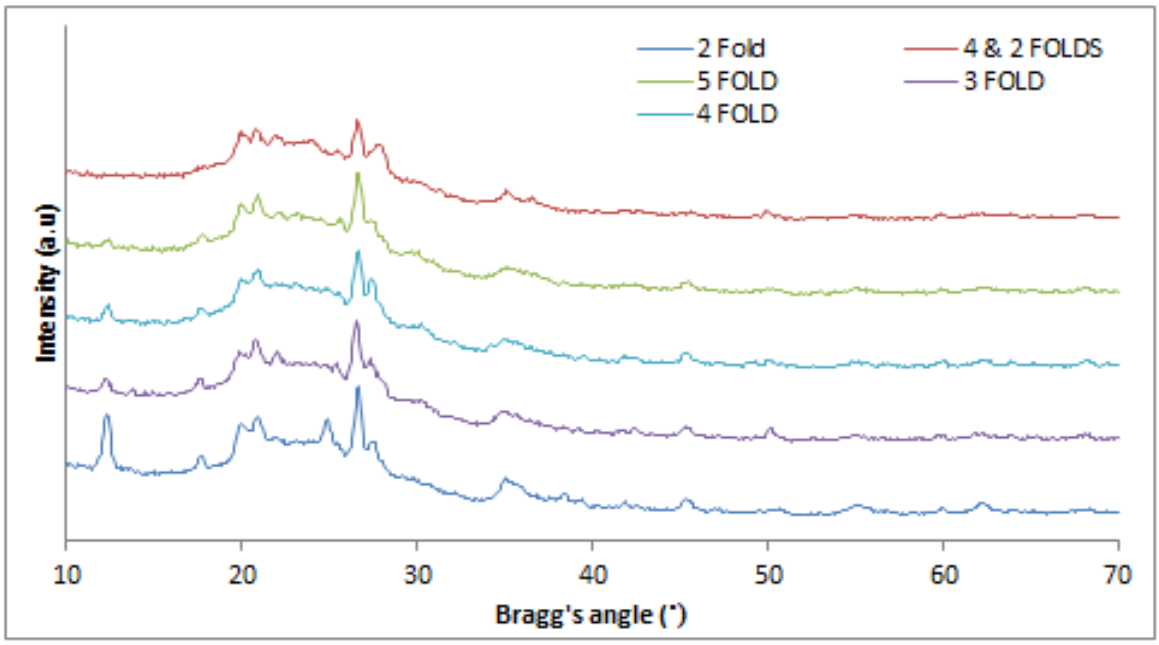


Figure 4.26: XRD pattern of silica produced using variable excess acid during dealumination

As it could be observed the silica peak was the most prominent of all the peaks, implying that the material was predominantly silica containing some impurities of mica and kaolinite. Hence it could be deduced that the kaolinite was not completely split to the expected pure silica and alumina using the 2 fold dealumination. The XRD pattern of the other folds of dealumination follow the same pattern as that of the 2 fold. However, it could be observed that the kaolinite peaks diminished as the fold of dealumination increased. At the 4 and 2 folds double dealumination the kaolinite peaks had disappeared, especially the peak at 12.4˚, at this extent of dealumination the material was obviously amorphous consisting majorly the silica peak. Even

though the kaolinite and the mica peaks had crumbled at the 4 and 2 folds double dealumination, it could still be observed that the product possessed a single noticeable peak at the Bragg‟s angle of 26.4˚; this was due to the crystalline silica present in the product.

4.3.2 FTIR spectra of silica

Figure 4.27 shows the FTIR spectrum of the silica produced using 4- and 2-folds double dealuminations. The spectrum possessed four major bands; at wavelengths of 800, 1100, 1600 and 3500 cm^{-1}. The band at 800 cm^{-1}, was due to the symmetric bending of O–Si–O (El-Naggar, 2013). The band at 1100 cm^{-1} was attributed to cluster of Si^{4+} and O^{2-} ions on the surface of Si–O vibration. The band at 1600 cm^{-1} was attributed to bending of H–O–H bonds. The band at around 3500 cm^{-1} was attributed to the –OH stretching (Lee *et al*., 2013).

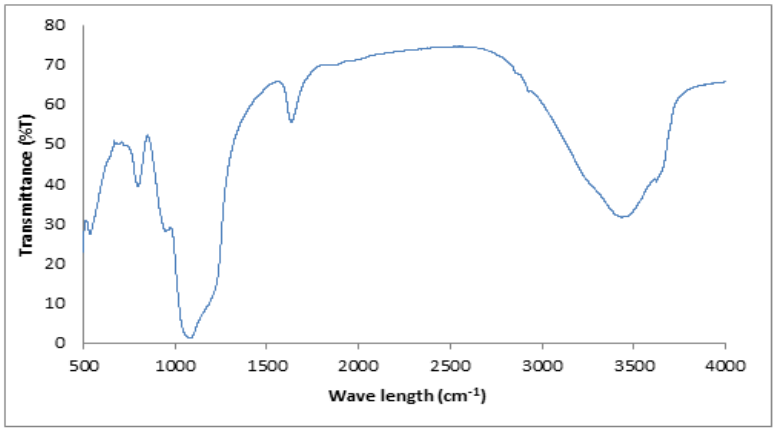


Figure 4.27: FTIR spectrum of silica prepared from Kankara kaolin

4.3.3 SEM micrographs of silica

Plates XVI A, B and C show the SEM images of the prepared silica scanned at magnifications of 950, 1700 and 5000. It could be observed from the highest magnification that the material possessed booklet structure containing sheets of silica. The lower magnifications revealed the

tetrahedral shape of the particles. Therefore, the morphology of the silica was tetrahedral euhedral morphology.

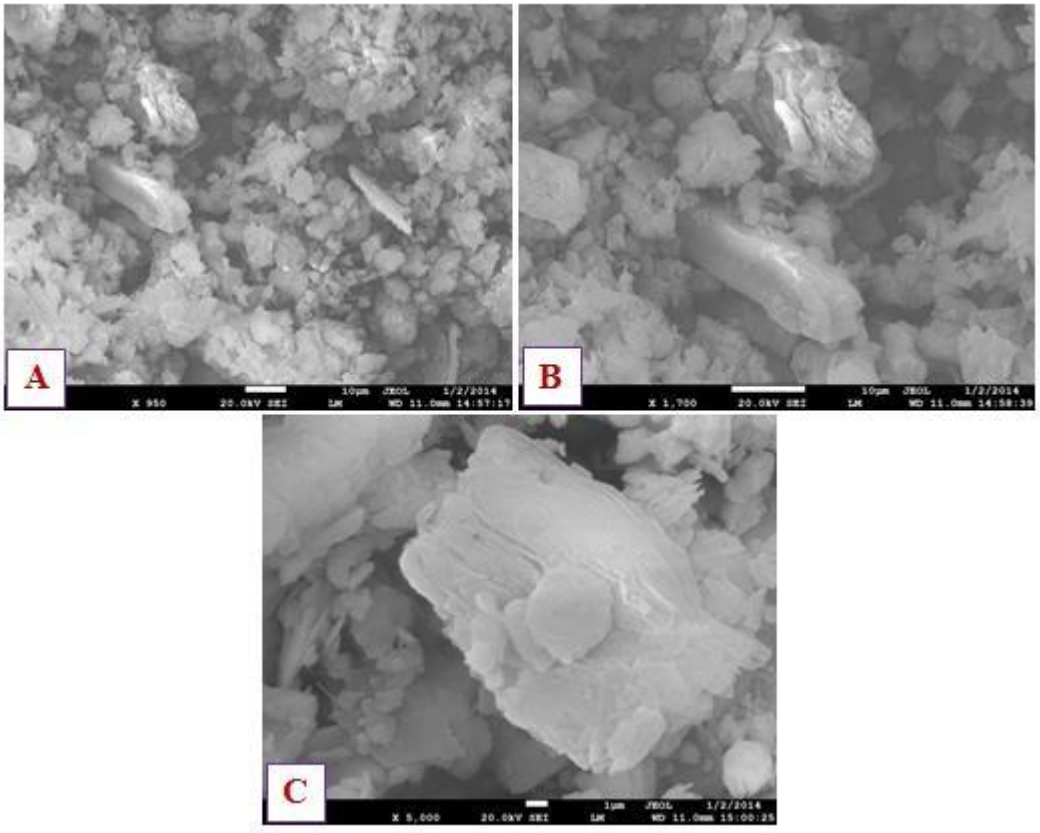


Plate XVI: SEM images of silica prepared from Kankara kaolin at magnifications of (A) 950 (B) 1700 (C) 5000

4.4 Characteristics of Sodium silicate

The physicochemical, morphological and thermogravimetrical characterizations of the sidium silicate produced are presented in this section.

4.4.1 Determination of SiO_2/Na_2O ratio of sodium silicate

The SiO_2 was characterized using the American Public Health Association (APHA) 4500-SiO_2 C. Molybdosilicate Method (APHA, 1996) as already discussed in Section 3.2.13. Figure 4.28

shows the silica calibration curve using different concentrations of standard silica solution. Table 4.6 presents the UV absorbance of the various samples of sodium silicate prepared at variable concentration temperatures and that of the commercial sodium silicate.

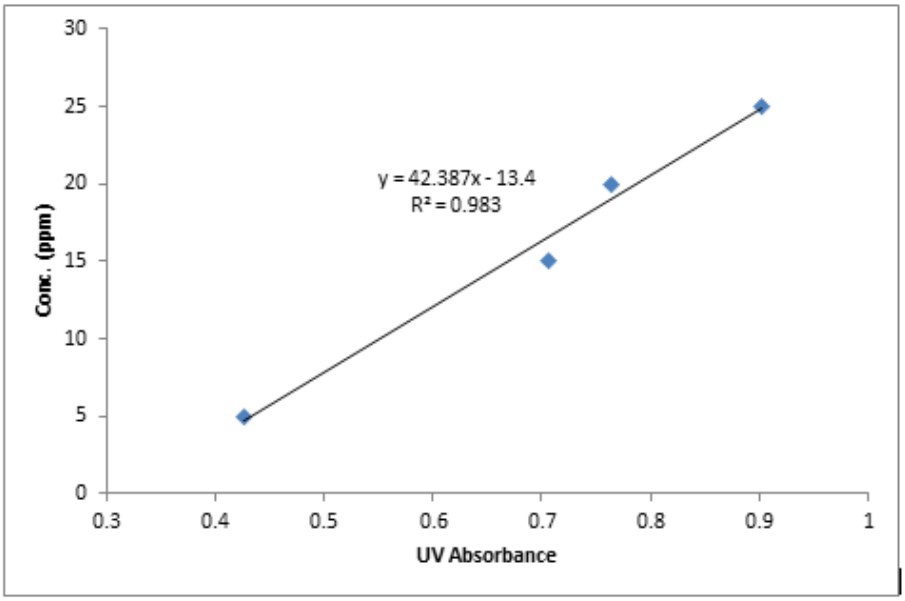


Figure 4.28: Calibration curve of silica using UV–VIS spectroscopy

Table 4.6: Concentration of silica (SiO_2) using UV–VIS spectroscopy analysis

Sample/Conc. Time (hr)	UV Absorbance	Conc. (ppm)	Actual wt%
0	1.281596	40.923	20.462
1	1.430816	47.248	23.624
2	1.635855	53.939	26.970
3	1.643098	56.246	28.123
Commercial	1.732442	60.033	30.016

The corresponding concentrations of the samples in ppm were determined using the calibration curve in Figure 4.28 and the actual concentrations of the samples, in wt%, were determined using Equation (4.1). It could be observed that the concentration of the initial sample (0 h) produced

after the caustic leaching of silica was 20.462 wt%, the concentration increased by 16%, 32% and 38% after 1, 2 and 3 hr concentration respectively. Although when compared with the commercial sample; the commercial sample had 47% higher concentration than the 0 hr sample.

$$\text{Actual conc. (wt)} = (\text{conc. (ppm)} \times \text{dilution factor}) / (1 \times 10^{-4}). \quad (4.1)$$

The Na_2O was characterized using Flame Photometer analysis as already discussed in Section 3.2.13. Table 4.7 presents the concentrations of the Na_2O in ppm for the various samples of sodium silicate prepared at variable concentration times and that of the commercial sodium silicate. The actual Na_2O concentrations of the samples in wt% were determined using Equation (4.2). It could be observed that the concentration of the 0 hr sample was 39.36 wt%, the concentration increased by 14%, 25% and 30% after 1, 2 and 3 hr concentration respectively. When compared with the commercial sample; the commercial sample had only 22% higher concentration than the 0 hr sample.

Table 4.7: Concentration of soda (Na_2O) using flame photometer analysis

Sample/Conc. Time (hr)	Conc. (ppm)	Actual wt%
0	39.36	9.840
1	44.928	11.232
2	49.248	12.312
3	50.976	12.744
Commercial	48.00	12.000

$$\text{Actual conc. (wt\%)} = (\text{conc. (ppm)} \times \text{dilution factor}) / (1 \times 10^{-4}). \quad (4.2)$$

Table 4.8 presents the SiO_2/Na_2O of each of the prepared and commercial sodium silicate. It could be observed that the 0 hr sample had SiO_2/Na_2O ratio of 2.08 which increased linearly with

the various concentration times. After 1, 2, and 3 hr the ratio increased by 1, 5 and 6% respectively. The 3 hr was observed as the optimum concentration time, although, the commercial sample had higher SiO_2/Na_2O ratio than the 3 hr concentrated sample; the commercial sample was 13% higher.

Table 4.8: SiO_2/Na_2O ratio of the sodium silicate prepared

Sample/Conc. Time (hr)	SiO_2/Na_2O
0	2.08
1	2.10
2	2.19
3	2.21
Commercial	2.50

4.4.2 FTIR spectra of sodium silicate

Figure 4.29 shows the FTIR spectra of the commercial and prepared sodium silicate. As could be seen from the figure, both spectra possessed similar pattern having infrared wave bands at 1000, 1500, 1700 and 3500 cm^{-1}. However, it could be observed that the commercial sample had relatively very low band intensity (high percentage transmittance) at wavelength of 1500 cm^{-1} while the prepared sample had relatively very high band intensity (low percentage transmittance) at the same wave, the intensity ratio was 1:7. Similarly the band at 1700 followed the same pattern and the intensity ratio was 1:3. However, for the commercial sample, the band at 3500 cm^{-1} was steep while for the prepared sample the band was broad extending between 2900 and 3500 cm^{-1}. Since the band at 3500 cm^{-1} was due to –OH stretching (Lee *et al*., 2013) it was likely

that the broadness of the band in the prepared sample indicated higher hydroxyl content which was suspected to have resulted from higher hydration content of the material.

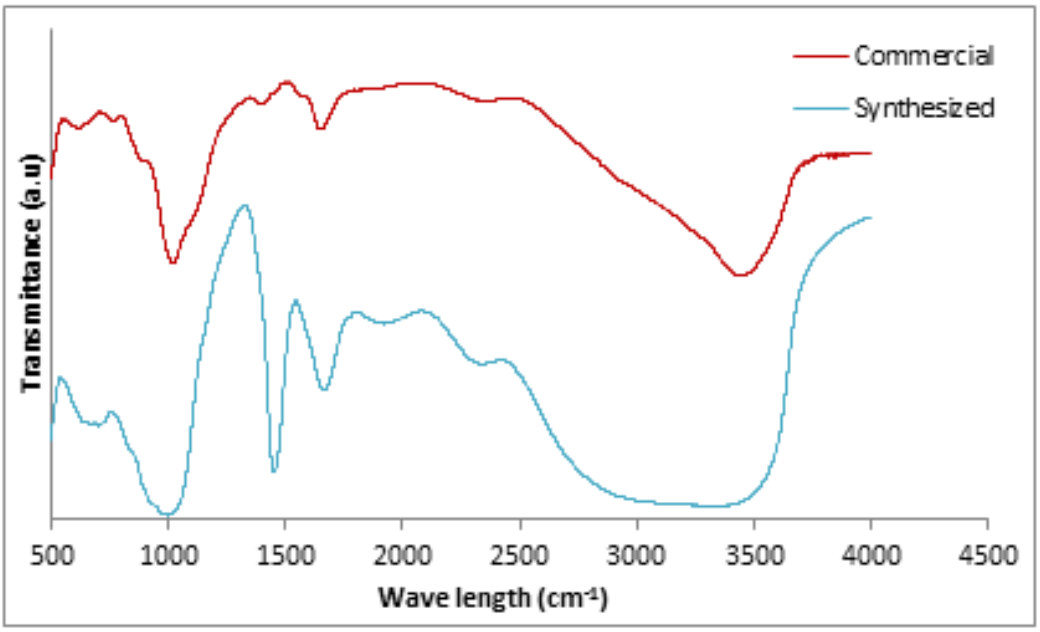


Figure 4.29: FTIR spectra of commercial and as-synthesized sodium silicate

4.4.3 Thermogravimetry properties of sodium silicate

Figure 4.30 shows the TGA/DTG curves of the prepared sodium silicate for thermal scan between 30 to 300˚C. It could be observed that total mass depletion resulting from the thermal treatment was about 53%. The DTG curve showed that the actual temperature responsible for the thermogravimetric mass depletion was around 200˚C. Therefore, it could be deduced that the sodium silicate was thermally stable up to temperature of about 200˚C, the DTG curve showed that further heating above 200˚C would dissociate the material.

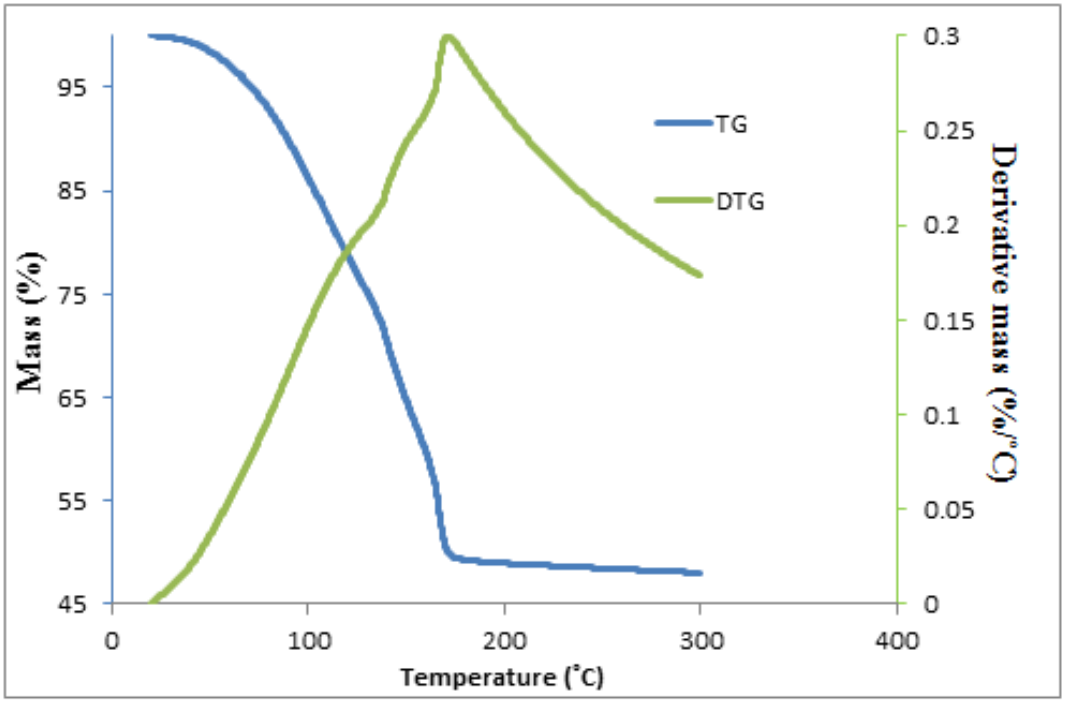


Figure 4.30: TGA/DTG curves of the prepared sodium silicate

4.5 Characteristics of Zeolite Y

The physicochemical, morphological and thermogravimetrical characterizations of zeolite Y synthesized from high purity chemicals (HPC) and those synthesized using the novel split mehod and the catalysts formulated from them were presented in this section. The catalytic cracking performance of the catalysts are also presented here.

4.5.1 XRD patterns of zeolite y synthesized using HPC

Figures 4.31 – 4.33 show the XRD patterns of zeolite Y synthesized using HPC, using clay partially substituted alumina source from clay, and using clay partially substituted silica source from clay. The zeolite Y peaks found at Bragg‟s angle of about 6, 10, 12, 16, 19, 20, 24, 27, 31 and 32˚ (Ginter *et al.*, 1992; Robson, 2001; Treacy and Higgins, 2001) could be observed in the

three XRD patterns. However, the intensity of the characteristic peak of zeolite Y at Bragg‟ s angle of 6.13 varied considerably among the samples. The sample prepared using HPC had intensity of 2170 counts, those of partially substituted alumina and silica were 620 and 540 counts respectively. The XRD intensity of the characteristic peak of a mineral indicates the extent of crystallinity and the concentration of the crystalline content of the material as expressed in Equation (4.3) (Bebon *et al*., 2002; Pal *et al*., 2013). Therefore it would be observed that the sample prepared from the HPC was relatively highly crystalline. Using Equation (4.3) and using the XRD of commercial zeolite Y shown in Figure 4.35 as the reference XRD pattern, the crystallinity of the HPC was calculated to be 88.4%. Whereas the crystallinity values of the

zeolite Y synthesized from partially substituted silica and partially substituted alumina were 29.4% and 28.0% respectively.

$$\text{Crystallinity} = \frac{\text{Intensity of the sample}}{\text{Intensity of the reference}} \quad (4.3)$$

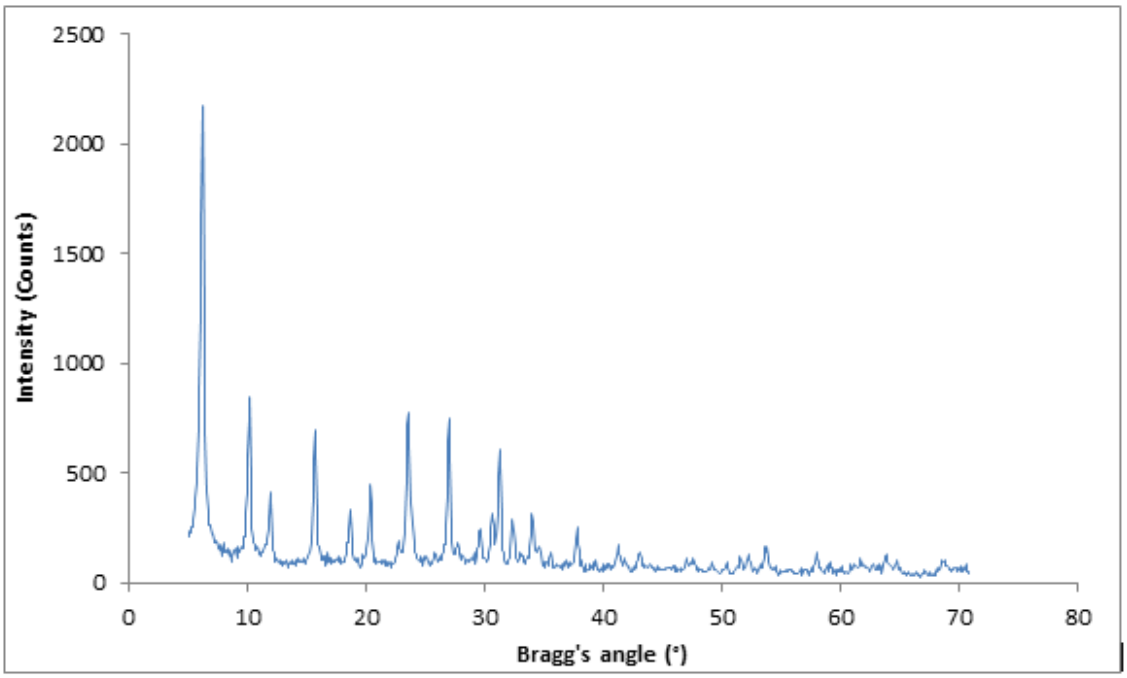


Figure 4.31: XRD pattern of zeolite Y synthesized from HPC

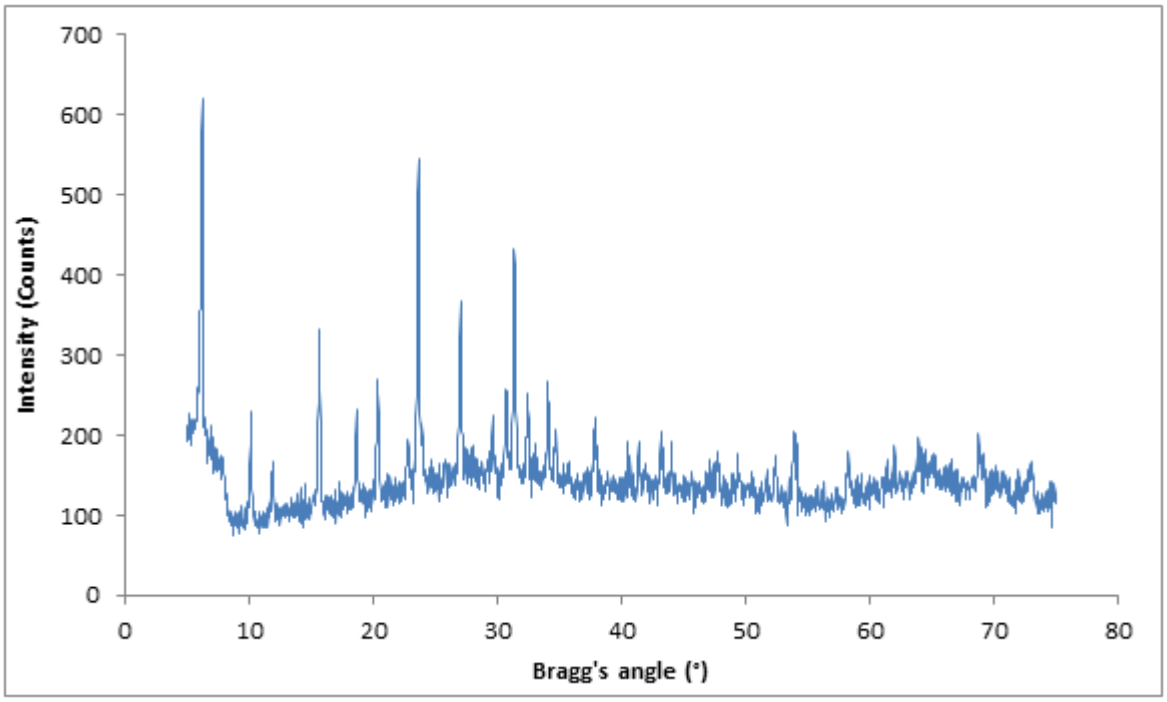


Figure 4.32: XRD pattern of zeolite Y synthesized using partial clay substitution; alumina source ($Al(OH)_3$) from clay

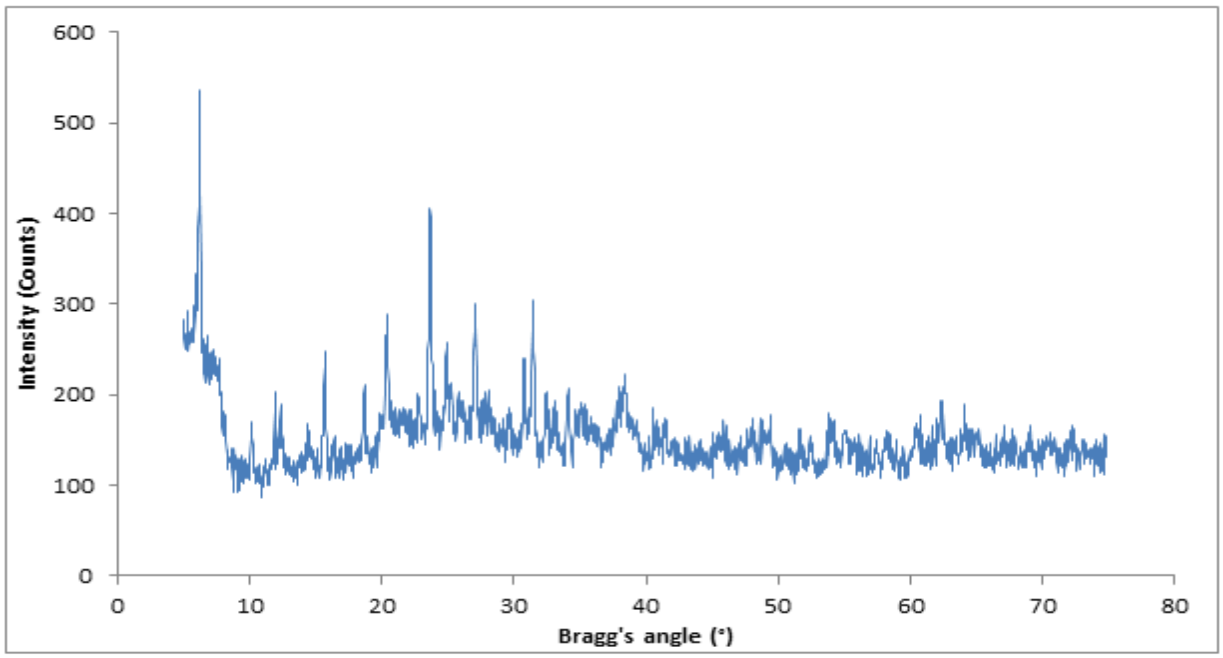


Figure 4.33: XRD pattern of zeolite Y synthesized using partial clay substitution; silica source (Na_2SiO_3) from clay

Figure 4.34 shows the comparison between the reference zeolite Y XRD pattern of the HPC synthesis method (Ginter *et al*., 1992; Robson, 2001), the zeolite Y synthesized using partially substituted alumina from clay and partially substituted silica from clay. The relative intensity of the characteristic peak at Bragg‟s angle of 6˚ to those of the next highest peak intensity; usually at 10 or 16˚ is a useful index indicating the purity of the material; high value indicates high competition of the characteristic mineral and other mineral impurities while low value indicates absence or low level of other mineral impurities. The intensity of the characteristic peak of the reference XRD pattern was 2000 counts and its relative competition index with the next highest peak was 23% while those of partially substituted alumina and silica were 92% and 70% respectively.

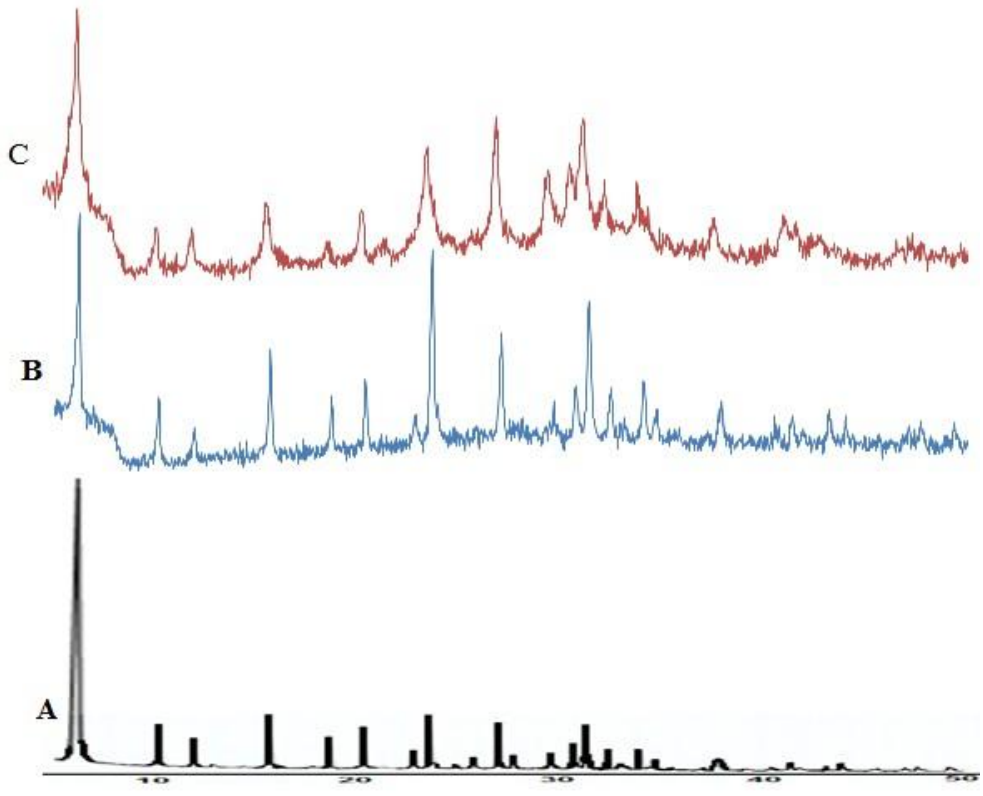


Figure 4.34: XRD patterns of zeolite Y: (A) NaY reference pattern [source; Ginter, 2001] (B) synthesized by partial substitution of alumina from clay (C) synthesized by partial substitution of silica from clay

Figure 4.35 shows the comparison between the reference zeolite Y XRD pattern, commercial zeolite Y and zeolite Y synthesized using high purity chemicals. It would also be observed that the three samples had similar XRD pattern, however, the synthesized zeolite Y using HPC had higher intensity at the Bragg‟s angle of 6˚; the characteristic peak of zeolite Y. The actual value of the intensity was 2170 counts as can be seen from Figure 4.36. The intensity of the reference zeolite Y at Bragg‟s angle of 6˚ was 2000 counts, while that of the commercial zeolite Y was

1860 counts. The relative competition index of the characteristic peak to the next highest peak was 39% for both the synthesized sample using HPC and the commercial sample, while that of the reference sample was 23%.

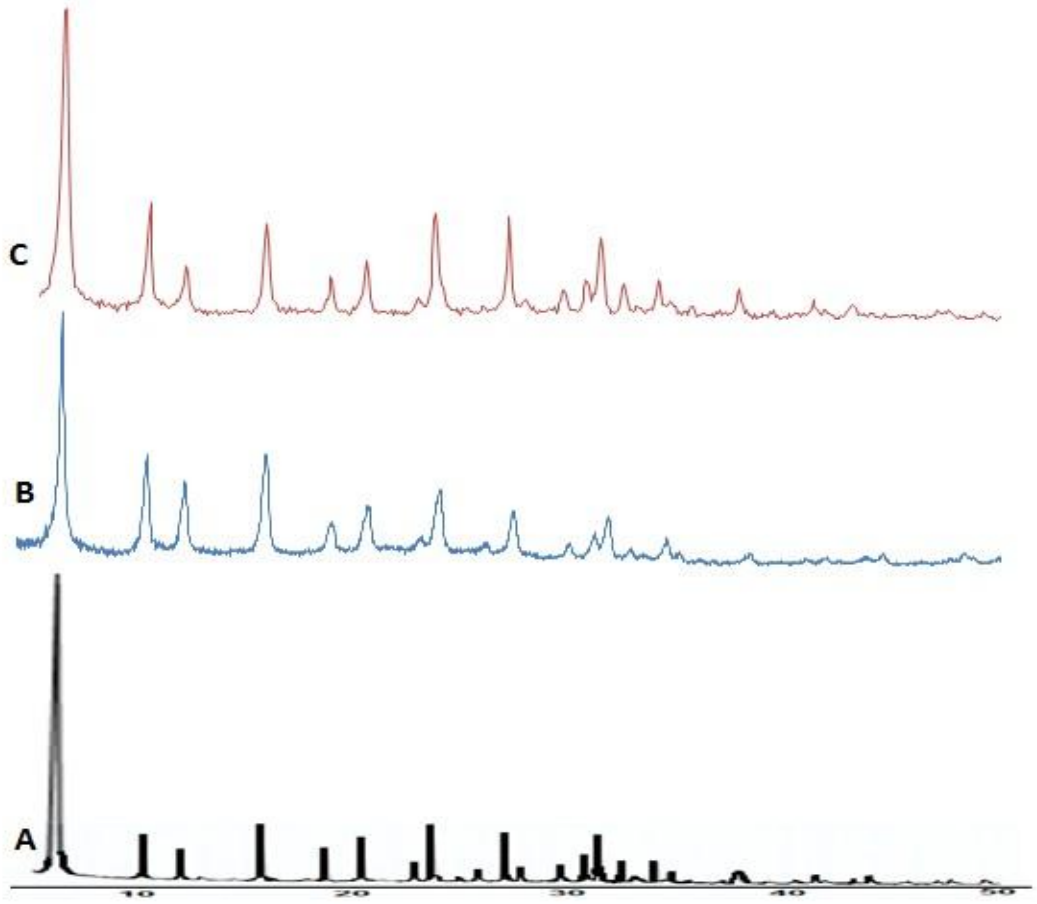


Figure 4.35: XRD patterns of zeolite Y: (A) NaY reference pattern [source; Ginter, 2001] (B) Commercial HY (C) NaY prepared using verified method and high purity chemicals

4.5.2 Chemical composition of zeolite Y synthesized using HPC

Table 4.9 presents the chemical composition results of the synthesized zeolite Y samples using HPC, using partially substituted alumina from clay and partially substituted silica from clay. The Si/Al ratios of the HPC, partially substituted silica and partially substituted alumina samples were 3.05, 2.30 and 1.41 respectively. The Si/Al ratio of a FAU zeolite is a major index used in differentiating zeolite Y and X since both zeolites have some common XRD peaks; zeolite X possesses Si/Al ratio value < 1.5 while zeolite Y possesses value ≥ 1.5 if used as mass ratio, whereas if used as molar ratio the bounds are Si/Al < 2.55 for zeolite X, while for zeolite Y; Si/Al ≥ 2.55 (Baerlocher *et al.*, 2007; Valtchev *et al*., 2011; Serrano *et al*., 2013).

Table 4.9: XRF results of zeolite Y synthesized using high purity reagents and partial substitution with reagents prepared from clay

Metallic Oxide	Sample/Composition (wt%)		
	High Purity Chemical	**Partially Substituted Silicate from Clay**	**Partially Substituted Alumina from Clay**
Al_2O_3	17.98	21.9	29.4
SiO_2	54.75	50.29	41.63
K_2O	0.04	ND	0.04
CaO	0.27	0.24	0.24
TiO_2	0.09	ND	0.05
Cr_2O_3	0.04	0.05	0.03
MnO	0.03	ND	0.01
Fe_2O_3	0.3	0.06	1.11
CuO	ND	0.01	0.03
LoI	26	26.5	26.5

Based on the Si/Al ratios, it could be observed that the HPC and the partially substituted silica synthesis produced zeolite Y while the partially substituted alumina synthesis produced zeolite X. The impurities in the HPC were generally very low, only CaO and Fe_2O_3 were up to 0.27% and 0.3 wt% respectively. Other impurities concentrations were very low in the range of 0.03 wt% – 0.09 wt%. Considering the partially substituted silica sample, apart from CaO which was 0.24 wt%, other impurities concentrations were generally low in the range of 0.01 wt% – 0.06 wt%, Fe_2O_3 was only 0.06 wt%, K_2O and MnO were absent. Similarly the partially substituted alumina sample also contained 0.24 wt% CaO, and other impurities were in low concentrations in the range of 0.01 wt% – 0.05 wt%. Although the Fe_2O_3 was relatively higher having concentration of 1.11 wt%.

4.5.3 XRD patterns of zeolite Y synthesized from kaolin

Figure 4.36 shows the XRD patterns of the zeolite Y synthesized using aluminium hydroxide and sodium silicate produced from 3, 4 and 5 fold dealuminations. It would be observed that the zeolite Y peaks were present in the XRD patterns of the three samples, however, the XRD patterns of the three samples were highly amorphous. The intensities of the characteristic peak for zeolite Y for the 3, 4 and 5 fold dealuminations samples were 358, 405 and 810 counts respectively. These values were very low compared with the reference or commercial sample‟s value. The relative competition index of the characteristic peak to the next highest peak for the 3, 4 and 5 fold dealuminations samples were 109%, 102% and 90% respectively, this indicated high level of impurities, the impurities were likely zeolite P and other GIS zeolites possessing peak at 12.5, 21.67 and 28.1˚.

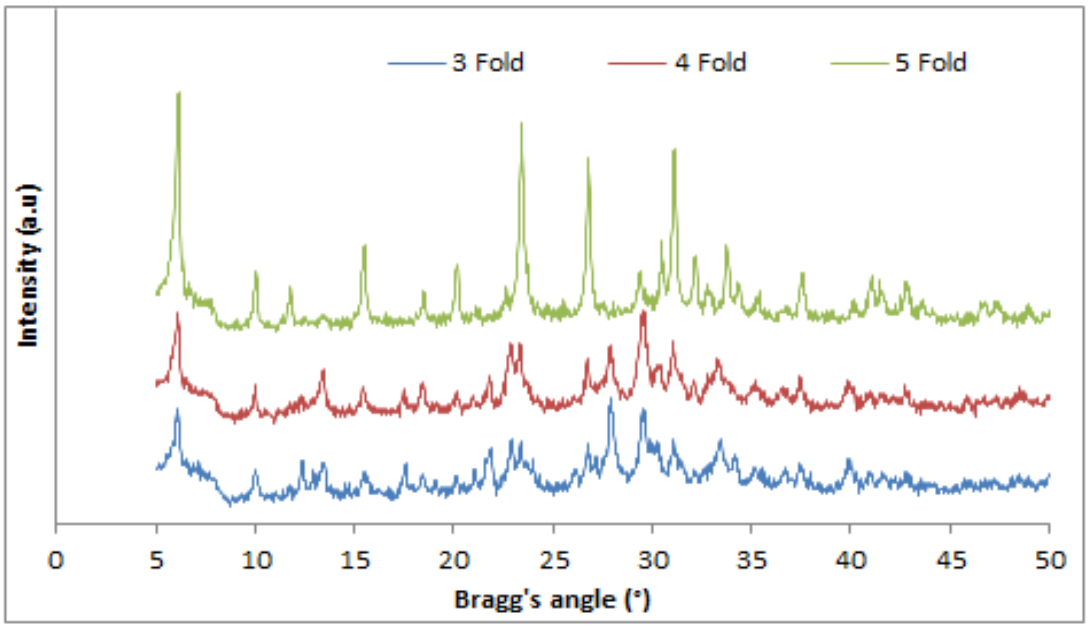


Figure 4.36: XRD patterns of zeolite Y synthesized using silica and aluminium sources from clay obtained from variable folds of dealumination

4.5.4 Chemical compositions of zeolite Y synthesized from kaolin

Table 4.10 presents the chemical composition results of the zeolite Y synthesized using 3, 4 and 5 folds dealumination, the Si/Al ratios were 2.20, 2.30 and 2.38 respectively. Hence, each of the synthesis produced zeolite Y. Considering the 3 fold dealumination sample; Fe_2O_3 at 1.98 wt% could be observed as the major impurity present. Other impurities present were in relatively low level, in the range of 0.03 wt% – 0.59 wt%.

The Fe_2O_3 level in the 4 fold dealumination sample was 1.82 wt% which was 8% reduction from the level in the 3 fold sample. Other impurities present in the 4 fold sample were relatively low, in the range of 0.02 wt% – 0.53 wt%. The 5 fold sample contained Fe_2O_3 impurity of just 0.53 wt% which was 73% reduction from the Fe_2O_3 level in the 3 fold sample. Other impurities present in the 5 fold sample were relatively low, in the range of 0.02 wt% – 0.1 wt%, except

Na_2O content which was the highest impurity; it was present to the level of 1.48 wt% which was 600% and 500% of its levels in the 3 and 4 fold dealumination samples respectively. It would be noted that the 5 fold dealumination product had the highest Si/Al ratio and the least Fe_2O_3, therefore it could be seen as the best of the three samples compared here just as was noted with the XRD analysis. The LoI values of the three samples were relatively the same, having average value of 25.27 wt%.

Table 4.10: XRF results of zeolite Y synthesized using silica and alumina sourced from clay; varying extent of dealumination

Metallic Oxide	Sample/Composition (wt%)		
	3 fold Dealumination	4 fold Dealumination	5 fold Dealumination
Al_2O_3	22.05	21.3	20.93
SiO_2	48.46	49.05	49.85
SO_3	0.59	0.53	0.10
CaO	0.35	0.45	0.29
TiO_2	0.05	0.05	0.02
Cr_2O_3	0.04	0.03	0.03
MnO	ND	0.02	0.02
Fe_2O_3	1.98	1.82	0.53
CuO	0.03	0.26	0.18
MgO	0.45	0.53	0.21
K_2O	0.38	0.38	0.16
Na_2O	0.23	0.3	1.48
LoI	25.00	25.00	25.82

4.5.5 Study of the optimum conditions for zeolite Y synthesis from kaolin

Deeper investigation into the optimum synthesis parameters for the synthesis of zeolite Y from clay using the novel split method is presented in this sub-section. The parameter considered included the calcination of aluminium hydroxide used, the extent and degree of dealumination, the dosage of silica in preparation of sodium silicate used, the product recovery technique and the grade of acid and base used in the synthesis process. The physicochemical and thermogravimetrical characterization of the products obtained are also presented.

4.5.5.1 Effect of calcination temperature of aluminium hydroxide used for the synthesis

Figure 4.37 shows the XRD patterns of the zeolite Y synthesized using 5 fold dealumination and aluminium hydroxide calcined at 300, 400 and 500˚C. It could be observed that in each case zeolite Y was produced as indicated by the presence of the zeolite Y peaks at Bragg‟s angle of about 6, 10, 12, 16, 19, 20, 24, 27, 31 and 32˚ although the XRD pattern could be seen to be amorphous. The intensity of the characteristic peak of zeolite Y at around 6˚ was 522, 495 and 523 counts for the 300, 400 and 500˚C calcination respectively. The relative competition index of the characteristic peak to the next highest peak for the 300, 400 and 500˚C calcinations were 83%, 75% and 73% respectively. It would be noted that the relative competition index had reduced as a result of calcination of the aluminium hydroxide implying improvement in the products crystallinity and reduction of impurity phases compared to when the aluminium hydroxide was not calcined. It would also be noted that the difference relative competition index was improving by showing a constant trend of decreasing as the calcination temperature increased. At 300˚C calcination the value was 83%, this value decreased by 10% and 12% at 400 and 500˚C respectively. Therefore, it could be observed that the improvement from 400 to 500˚C

was minimal, it did not commensurate the high energy cost gap between operation at 400 and 500˚C, as such, the 400˚C could be seen as the best calcination temperature for the aluminium hydroxide.

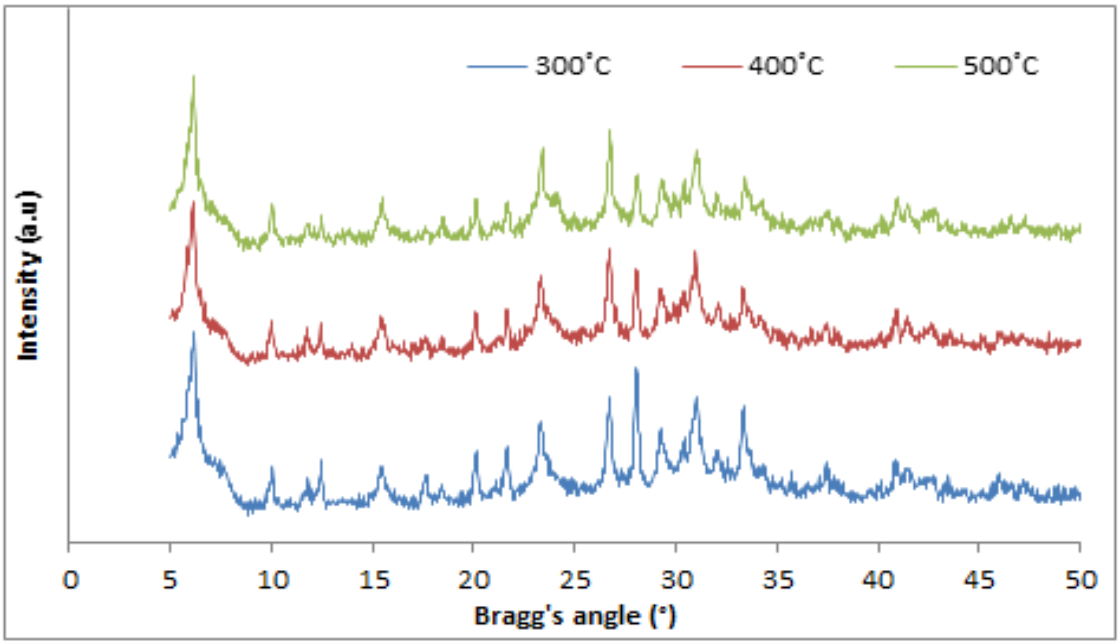


Figure 4.37: XRD patterns of zeolite Y synthesized using 5 fold dealumination and aluminium hydroxide calcined at variable temperatures

Table 4.11 presents the chemical composition results of the zeolite Y synthesized using 5 fold dealumination and aluminium hydroxide calcined at variable temperatures. The Si/Al ratios of the products obtained using 300, 400 and 500˚C calcination temperatures were 2.09, 2.06 and 2.02 respectively. The Fe_2O_3 content in the 300, 400 and 500˚C calcination temperatures were 1.25, 1.42 and 1.39 respectively. Other impurities were generally in the range of 0.01 – 0.15 for the three products. There was no clear-cut trend in the elemental analysis of the products; the chemical composition results did not show a noticeable improvement in the elemental composition of the products as shown by the XRF results. The LoI of the three products were relatively similar having average value of 25.33 wt%.

Table 4.11: XRF results of zeolite Y synthesized using 5 fold dealumination and aluminium hydroxide at variable calcination temperatures

	Sample/Composition (wt%)		
Metallic Oxide	**5 fold Calcined at 300˚C**	**5 fold Calcined at 400˚C**	**5 fold Calcined at 500˚C**
Al_2O_3	23.43	23.63	23.78
SiO_2	49.13	48.75	48.1
SO_3	0.10	0.15	0.15
CaO	0.28	0.34	0.34
TiO_2	0.04	0.05	0.06
Cr_2O_3	0.05	0.08	0.05
MnO	0.03	0.03	0.03
Fe_2O_3	1.25	1.42	1.39
CuO	0.01	0.02	0.03
LoI	**25**	**25**	**26**

Figure 4.384 shows the XRD patterns of the zeolite Y synthesized using 3, 4 and 5 folds of dealumination respectively, in each case aluminium hydroxide was calcined at 400˚C. It could be observed that the XRD pattern of each of the products showed that zeolite Y was produced as indicated by the presence of the zeolite Y peaks at Bragg‟s angle of about 6, 10, 12, 16, 19, 20,

24, 27, 31 and 32˚. The intensities of the characteristic peak of zeolite Y at around 6˚ were 608, 785 and 495 counts for the 3, 4 and 5 fold dealumination respectively. The relative competition indexes of the characteristic peak to the next highest peak for the 3, 4 and 5 fold dealumination were 76%, 63% and 75% respectively. It would be noted that the product obtained using 4 fold

dealumination and aluminium hydroxide calcined at 400˚C had the highest characteristic peak

intensity and the lowest relative competition index. Its characteristic peak intensity was 29% higher than the 3 fold dealumination and 56% higher than the 5 fold dealumination. The relative competition index for the 4 fold dealumination was about 18% lower than each of the 3 and 5 fold dealumination. These imply improvement in the 4 fold dealumination product crystallinity and reduction of impurity phases compared to the 3 and 5 fold products.

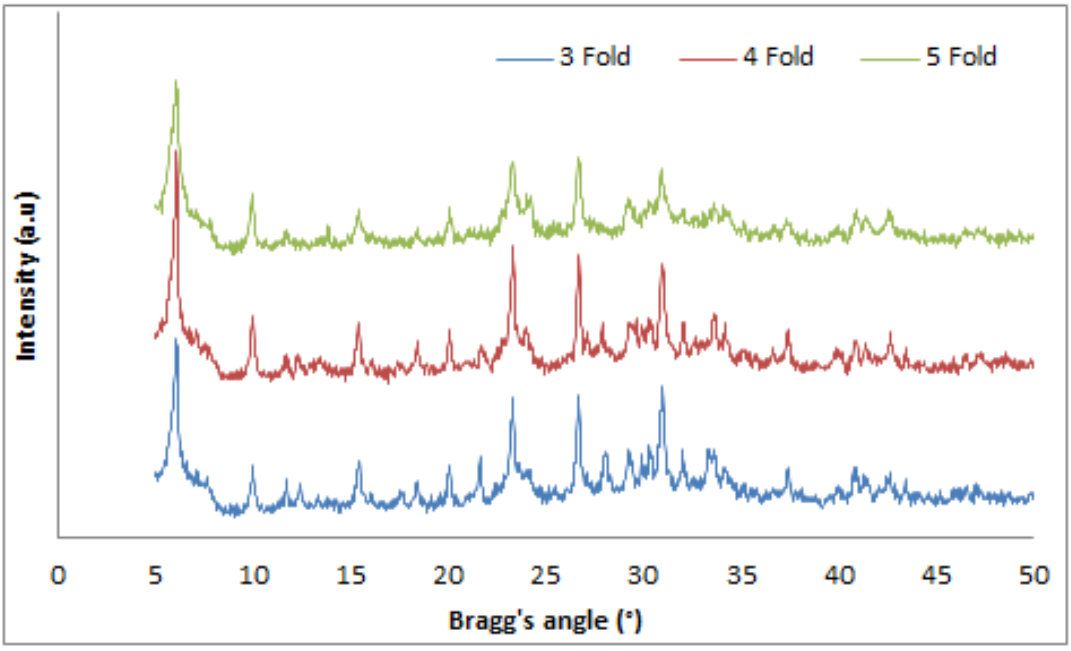


Figure 4.38: XRD patterns of zeolite Y synthesized using aluminium hydroxide calcined at 400˚C and variable folds of dealumination

Table 4.12 presents the chemical composition results of the zeolite Y synthesized using 3 and 4 fold of dealuminations and aluminium hydroxide calcined at 400˚C. The Si/Al ratios of the products obtained at the 3 and 4 fold dealuminations were 2.20 and 2.11 respectively. The 3 fold dealumination product contained 0.59 wt% sulphate ion (SO_3) and 1.98 wt% Fe_2O_3, other impurities were low, in the range of 0.03wt% – 0.45 wt%. The 4 fold dealumination product had the lower sulfur content, just 0.35 wt% and Fe_2O_3 of 1.04 wt%, other impurities were in the

range of 0.04 wt% – 0.35 wt%. It would be noted that K_2O, Na_2O, CuO and MgO were completely absent in the product of the 4 fold dealumination.

Table 4.12: XRF results of zeolite Y synthesized using silica and alumina sources from clay; aluminium hydroxide calcined at 400˚C and dealumination of 3 and 4 folds

Metallic Oxide	Sample/Composition (wt%)	
	3 fold $Al(OH)_3$ at 400˚C	4 fold $Al(OH)_3$ at 400˚C
Al_2O_3	22.05	23.48
SiO_2	48.46	49.43
SO_3	0.59	0.35
CaO	0.35	0.27
TiO_2	0.05	0.04
K_2O	0.38	ND
Na_2O	0.23	ND
CuO	0.03	ND
MgO	0.45	ND
Cr_2O_3	0.04	0.05
Fe_2O_3	1.98	1.04
MnO	ND	ND
LoI	25	25

The LoI of the 3 and 5 folds products were both 20 wt% while that of the 5 fold dealumination was 16% higher. Therefore it could be observed that the 4 fold dealumination and aluminium hydroxide calcined at 400˚C gave a better product compared with the 3 and 5 fold

dealuminations, this further buttressed the assertion arrived by the analysis of the XRD results of the three products. There was no clear-cut trend in the elemental analysis of the products; the chemical composition results did not show a noticeable improvement in the elemental composition of the products. The LoI of the three products were relatively similar having average value of 25.33 wt%.

4.5.5.2 Effect of products recovery on the product quality

Going by the XRD and XRF results analyses made in the preceding sections and the observations made therein, 4 fold dealumination and aluminium hydroxide calcined at 400˚C was chosen as the best condition so far for the synthesis of good zeolite Y. Therefore, Figure 4.39 shows the XRD patterns of zeolite Y synthesized using 4 fold dealumination and aluminium hydroxide calcined at 400˚C but using variable product recovery technique. It would be observed that in both cases zeolite Y was successfully synthesized as indicated by the presence of the zeolite Y peaks at Bragg‟s angle of about 6, 10, 12, 16, 19, 20, 24, 27, 31 and 32˚.

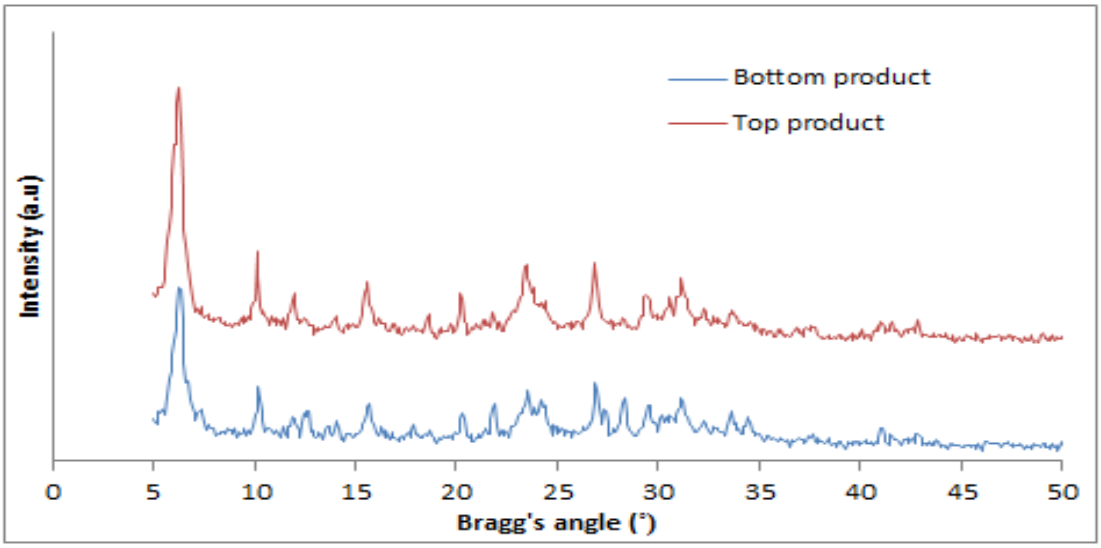


Figure 4.39: XRD patterns of zeolite Y synthesized using 4 fold dealumination, aluminium hydroxide calcined at 400˚C and variable product recovery

The intensities of the characteristic peak of zeolite Y at around 6˚ were 1245 and 785 counts for the top and the bottom recovery product respectively. The relative competition index of the characteristic peak to the next highest peak for the top and bottom recovery products were 38 and 63% respectively. Therefore, the top recovery product was 59% better than the bottom recovery in terms of characteristic peak intensity and it was 40% better than the bottom recovery product in terms of the relative competition index with the characteristic peak.

4.5.5.3 Effect of single and double dealumination on product quality

It would be recalled that the XRD and XRF results analyses made in the preceding sections have shown that the top product recovery method and 4 fold dealumination using aluminium hydroxide calcined at 400˚C was chosen as the best condition so far for the synthesis of good zeolite Y. Hence, Figure 4.40 shows the XRD patterns of zeolite Y synthesized using top product recovery, variable degrees of dealumination; single and double dealuminations and aluminium hydroxide calcined at 400˚C. The single dealumination was done using 4 fold while the double dealumination was done using 4- and 2-folds double dealuminations. It would be observed that in both cases zeolite Y was successfully synthesized as indicated by the presence of the zeolite Y peaks at Bragg‟s angle of about 6, 10, 12, 16, 19, 20, 24, 27, 31 and 32˚. The intensities of the characteristic peak of zeolite Y at around 6˚ were 1245 and 1550 counts for the 4 fold single dealumination and the 4- and 2-folds double dealuminations respectively. The relative competition indexes of the characteristic peak to the next highest peak of the 4 fold single dealumination and the 4- and 2-folds double dealuminations were 38 and 28% respectively. Therefore, the 4- and 2-folds double dealuminations was 25% better than the 4 fold single

dealumination in terms of characteristic peak intensity and it was 26% better than the 4 fold single dealumination in terms of the relative competition index with the characteristic peak.

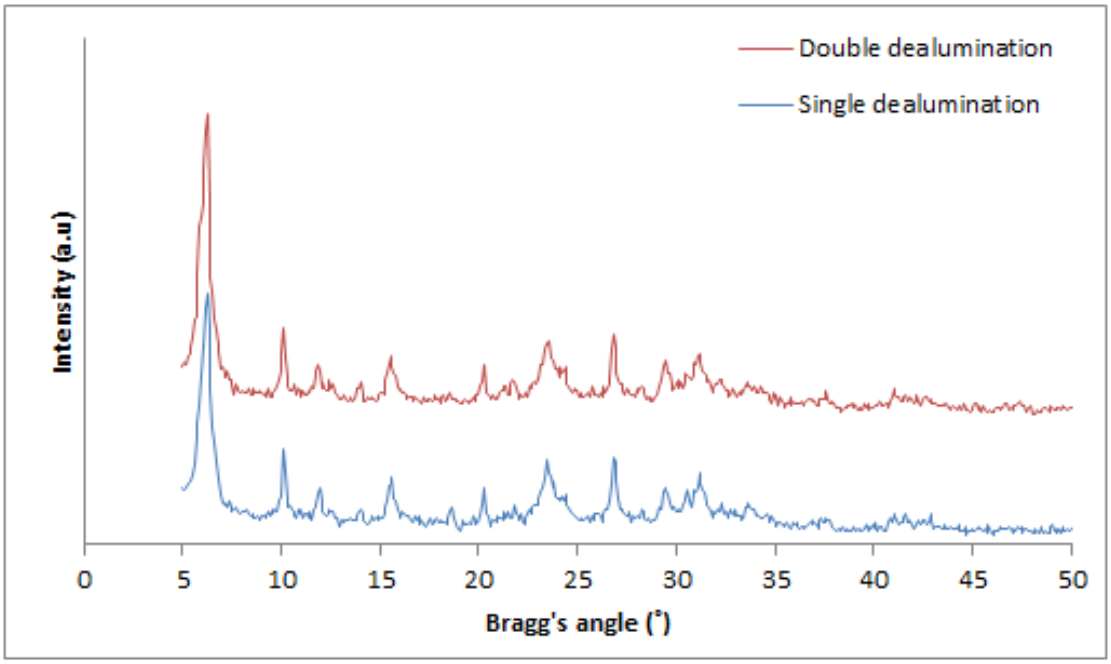


Figure 4.40: XRD patterns of zeolite Y synthesized using aluminium hydroxide calcined at 400˚C and variable degrees of dealumination

Table 4.13 presents the chemical composition results of the products of the synthesis carried out using top product recovery, aluminium hydroxide calcined at 400˚C using variable degrees of dealumination; single and double dealuminations. It is important to note that the dealumination referred to throughout the discussion is the dealumination carried out on the metakaolin as mentioned in Sections 3.2.2.4 and 3.2.2.5. It can be seen that Fe_2O_3 content in the single dealumination which was 2.54 wt% reduced by 80% in the double dealumination product. Other impurities in the single dealumination were low in the range of 0.03 – 0.45 wt%, however, they were relatively lower in the double dealumination than in the single dealumination product; they were in the range of 0.03 wt% – 0.32 wt% for the double dealuminations. Moreover, CuO, MgO, K_2O and Na_2O were completely undetected in the double dealumination sample, whereas they

were detected to the levels of 0.03 wt%, 0.45 wt% , 0.38 wt% and 0.23 wt% respectively in the single dealumination. The Si/Al ratios of the single and double dealumination were 2.1 and 2.15 respectively. Even though, the double dealuminations had higher silica it also had higher alumina, these translated to its higher Si/Al ratio compared to the single dealumination. Both the single and the double dealumination products possessed similar LoI values, the average value being 25.4 wt%.

Table 4.13: XRF results of zeolite Y synthesized using silica and alumina sources from clay; using single and double dealumination

Metallic Oxide	Sample/Composition (wt%)	
	4 fold Single Dealumination	4 and 2 folds Double Dealuminations
Al_2O_3	22.50	23.25
SiO_2	47.03	49.95
SO_3	0.38	0.23
CaO	0.30	0.32
TiO_2	0.07	0.08
Cr_2O_3	0.04	0.03
MnO	0.03	0.02
Fe_2O_3	2.54	0.53
CuO	0.03	ND
MgO	0.45	ND
K_2O	0.38	ND
Na_2O	0.23	ND
LoI	25.8	25

ND: Not determined

4.5.5.4 Effect of silica dosage on the sodium silicate produced

Figure 4.41 shows the XRD patterns of zeolite Y synthesized using the optimum conditions arrived at from the preceding sections, however, in the preparation of the sodium silicate used, different dosage of silica were used. It is important to note here that in developing the sodium silicate preparation method many preliminary runs of silica dosage was carried out which are not reported in this report. However the best range was obtained between 11 wt% – 12 wt%. Considering the XRD pattern of the synthesis carried out using sodium silicate prepared from 11.3 wt% silica dosage. It was observed that the product was not a pure phase of zeolite Y, the product was majorly sodalite mineral mixed with some zeolite Y minerals as could be seen that the XRD pattern was mainly dominated by the characteristic peak of sodalite at Bragg‟s angle of

24.6˚ having intensity of 780 counts and the zeolite Y characteristic peak could also be noted having lower peak intensities of 640 counts. For the sample synthesized using sodium silicate prepared from 11.4 wt% silica dosage, the XRD pattern showed that a good zeolite Y was synthesized, no other impurity phases was observed. The intensity of the characteristic peak of zeolite Y was 1550 counts. Similarly, the XRD pattern of the synthesis carried out using sodium silicate prepared from 11.5 wt% silica dosage showed that a good zeolite Y was synthesized, no other impurity phases was observed. Although, the intensity of the characteristic peak of zeolite Y was 1130 counts, which was 27% lower than that of the sample prepared from 11.4 wt% silica dosage. Also, the XRD pattern of the synthesis carried out using sodium silicate prepared from 12.0 wt% silica dosage showed that a good zeolite Y was synthesized, no other impurity phases was observed. However, the intensity of the characteristic peak of zeolite Y was 900 counts, which was 42% lower than that of the sample prepared from 11.4 wt% silica dosage. The relative competition indexes of the characteristic peak zeolite Y to other peaks, for the samples prepared

using silica dosages of 11.3 wt%, 11.4 wt%, 11.5 wt% and 12.0 wt% were 121%, 28%, 31% and 48% respectively. Therefore, 11.4% could be seen as the optimum silica dosage for synthesis of a good zeolite Y. The 11.4 wt% dosage was 77%, 10%, and 42% better than the 11.3 wt%, 11.5 wt% and 12.0 wt% silica dosages respectively, in terms of the relative competition indexes of the characteristic peak. It was also 142%, 37% and 72% respectively, better in terms of characteristic peak intensity and it was 40% better than the bottom recovery product.

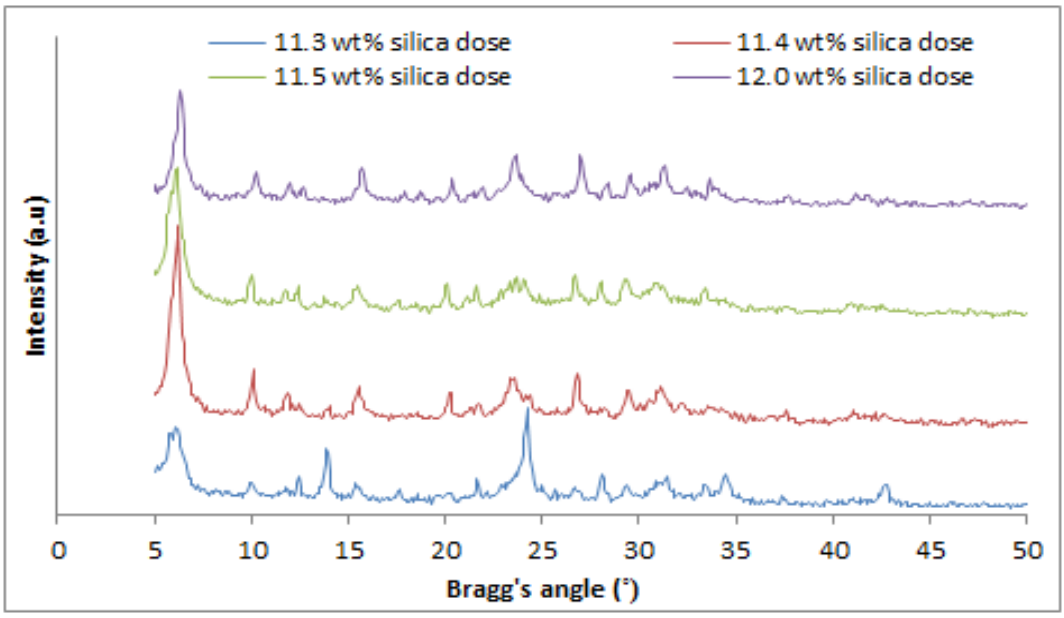


Figure 4.41: XRD patterns of zeolite Y synthesized using sodium silicate prepared at variable dosage of silica

Table 4.14 presents the chemical composition results of the products obtained using variable silica dosage in the synthesis of zeolite Y. The Si/Al ratios of the 11.43, 11.53 and 12.0 wt% silica dosages were 2.51, 2.43 and 2.27 respectively. The Fe_2O_3 content in the 11.43 wt% dosage of silica was 0.71 wt%. Other impurities were in the range of 0.04 wt% – 0.30 wt%, sulfur was not detected. The Fe_2O_3 content in the 11.53 wt% dosage of silica was 1.27 wt%, sulfur content was 0.65 wt%. Other impurities were in the range of 0.05 wt% – 0.28 wt%. The Fe_2O_3 content in

the 12.0 wt% dosage of silica was 0.73 wt%, sulfur content was 0.08 wt%. Other impurities were low in the range of 0.04 wt% – 0.31 wt%. The LoI values of the three samples were relatively in the same range having average value of 25.77 wt%.

Table 4.14: XRF results of zeolite Y synthesized using different dosage of silica

Metallic Oxide	Sample/Composition (wt%)		
	11.43 wt% Silica Dosage	**11.53 wt% Silica Dosage**	**12.0 wt% Silica Dosage**
Al_2O_3	20.48	20.55	22.58
SiO_2	51.32	50.02	51.3
CaO	0.3	0.28	0.31
TiO_2	0.04	0.05	0.05
Cr_2O_3	0.04	0.05	0.04
Fe_2O_3	0.71	1.27	0.73
SO_3	ND	0.65	0.08
LoI	26.5	25.82	25

Figure 4.42 shows the comparison between the reference zeolite Y XRD pattern, commercial zeolite Y, zeolite Y synthesized using high purity chemicals and zeolite Y synthesized using clay applying the optimum synthesis conditions arrived from the preceding sections. It would also be observed that the four XRD pattern were relatively similar, although the XRD pattern of the sample synthesized from clay appeared more fuzzy than the others. However, each of the XRD patterns possessed the zeolite Y peaks at Bragg‟s angles of about 6, 10, 12, 16, 19, 20, 24, 27, 31 and 32˚. The intensities of the characteristic peak of the reference, commercial, as-synthesized

sample using HPC and the as-synthesized sample using clay were 2000, 1860, 2170 and 1550 counts respectively. The relative competition indexes of the characteristic peak to the next

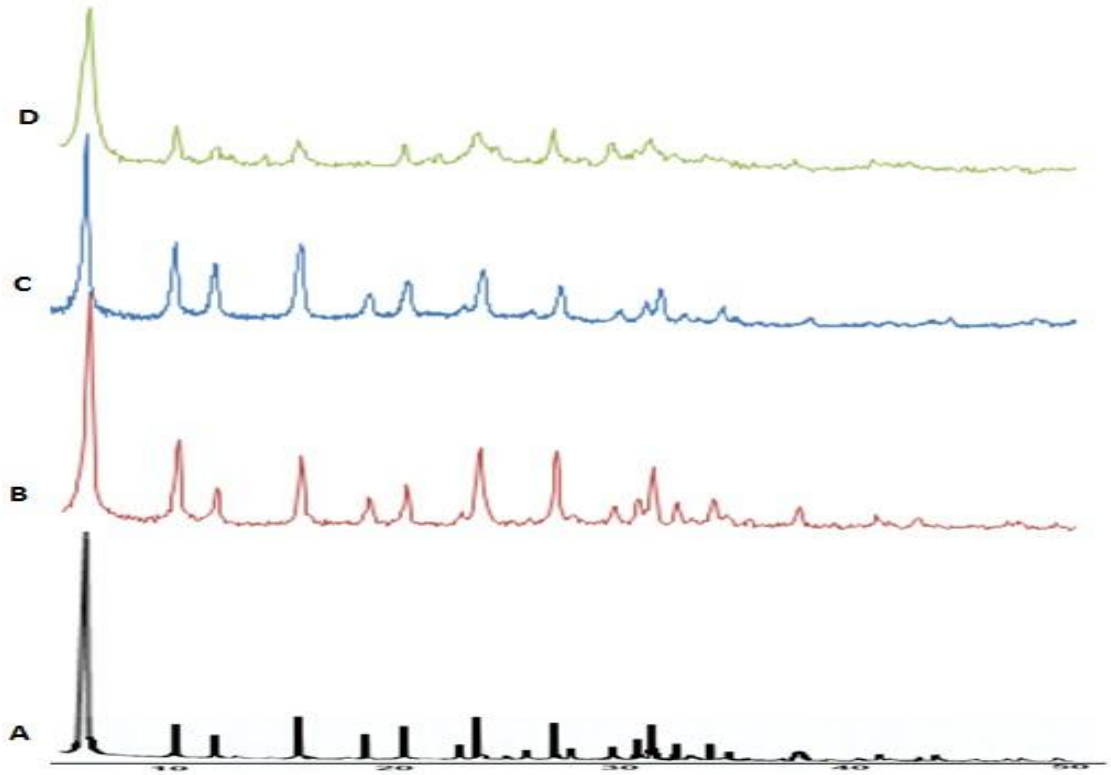


Figure 4.42: Comparison of XRD patterns for Zeolite Y (A) NaY Reference Pattern (B) as-synthesized; HPC (C) Commercial zeolite Y (D) as-synthesized; clay

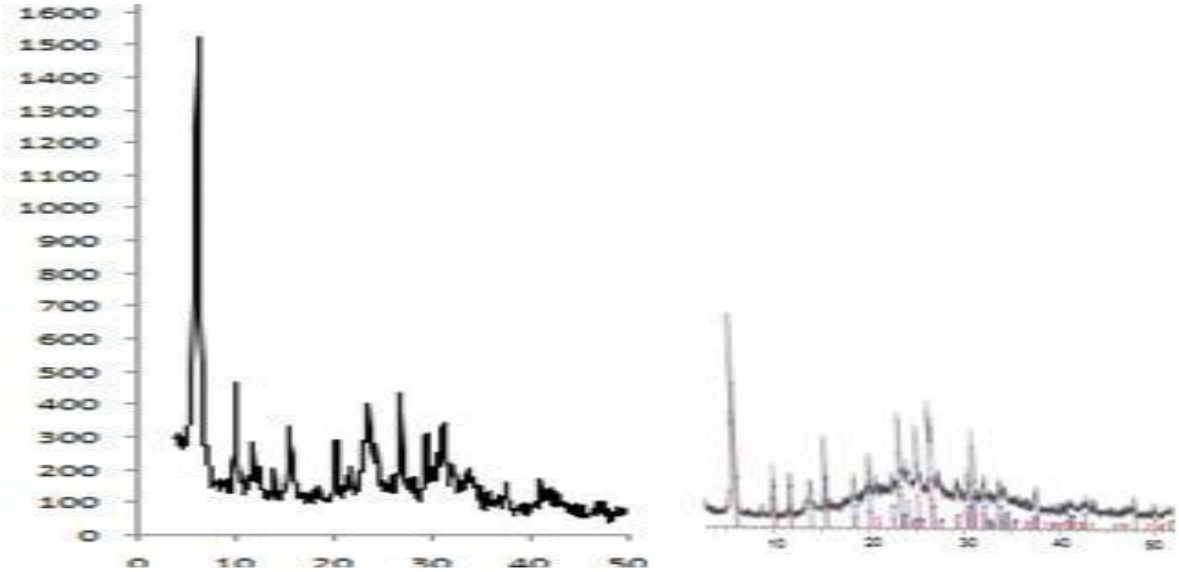


Figure 4.43: Comparison of XRD patterns for zeolite Y synthesized from clay (A) using novel method: Zeo-AY (B) conventional method: (Ajayi, 2012)

highest peak for the reference, commercial, as-synthesized sample using HPC and the as-synthesized sample using clay were 23%, 39%, 39% and 28% respectively. Figure 4.43 compared the XRD pattern of the zeolite Y synthesized using the split method with the one synthesized by other researchers (Ajayi, 2012). The crystallinity of the zeolite Y sample reported by Ajayi, 2012 was calculated to be 29.2% whereas that of the zeolite Y using the novel split method from clay was 72.5%.

4.5.5.5 Different batches of zeolite synthesized using different grades of acid and base

The zeolite Y synthesized using 11.4 wt% silica dosage which its XRD pattern was shown in Figure 4.41 was synthesized from Kankara kaolin using the optimum conditions arrived at in the preceding sections; in its synthesis analar grade sodium hydroxide and industrial grade sulfuric acid were used. This sample will henceforth be referred to as Zeo-AY in the subsequent discussions. Figure 4.44 shows the XRD pattern of zeolite Y synthesized from Kankara kaolin using the optimum conditions arrived at in the preceding sections; in its synthesis industrial grade sodium hydroxide and sulfuric acid were used. This sample will henceforth be referred to as Zeo-BY in the subsequent discussions. Figure 4.45 shows the XRD pattern of zeolite Y synthesized from Kankara kaolin using the optimum conditions arrived at in the preceding sections; in its synthesis analar grade sodium hydroxide and sulfuric acid were used. This sample will henceforth be referred to as Zeo-CY in the subsequent discussions. The zeolite Y represented by the XRD pattern shown in Figure 4.31 was synthesized from high purity chemicals (HPC). This sample will henceforth be referred to as Zeo-HPC in the subsequent discussions. Figure 4.46 is a cascade comparison of the four batches of synthesized zeolite Y. It could be observed that the intensities of the characteristic peak of the Zeo-AY, Zeo-BY, Zeo-CY

and Zeo-HPC were 1550, 1389, 1765 and 2170 counts respectively. The relative competition indexes of the characteristic peak to the next highest peak of the Zeo-AY, Zeo-BY, Zeo-CY and Zeo-HPC were 28%, 31%, 26% and 39% respectively. Based on the foregoing analysis it could be observed the order of the quality of the various batches of zeolite Y in terms of the intensity at the characteristic peak was Zeo-HPC > Zeo-CY > Zeo-AY > Zeo-BY. While the order of the quality of the various batches of zeolite Y in terms of the relative competition index of the characteristic peak to the next highest peak was Zeo-CY > Zeo-AY > Zeo-BY > Zeo-HPC. Using Equation (4.3) and taking the XRD pattern of the commercial zeolite Y as the reference Figure 4.35B the crystallinity of Zeo-HPC, Zeo-CY, Zeo-AY and Zeo-BY were evaluated as 88.4%, 72.5%, 66.5% and 58.6%.

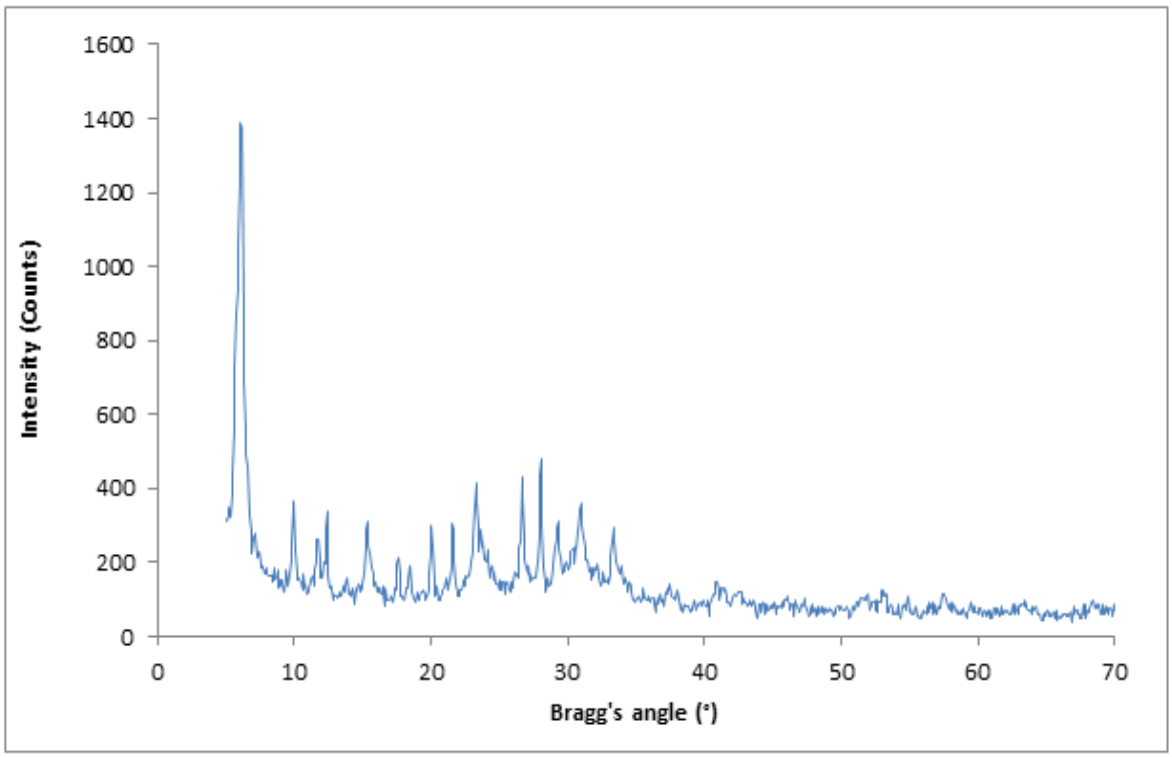


Figure 4.44: XRD pattern of zeolite Y synthesized from kaolin using industrial grade acid and base

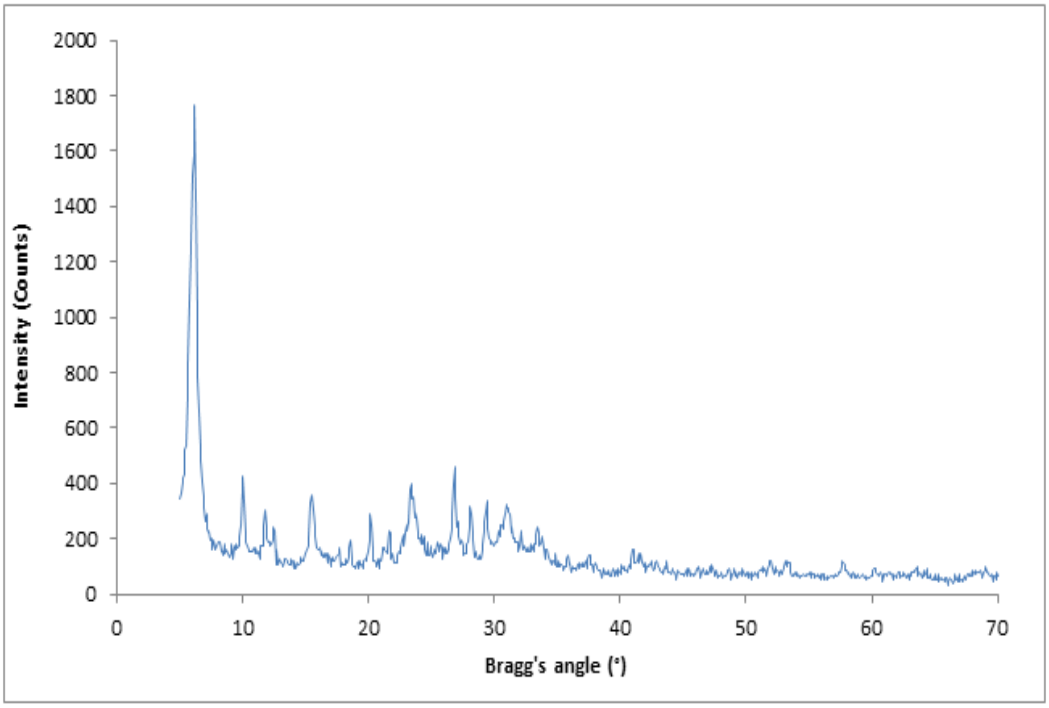


Figure 4.45: XRD pattern of zeolite Y synthesized from kaolin using analar grade acid and base

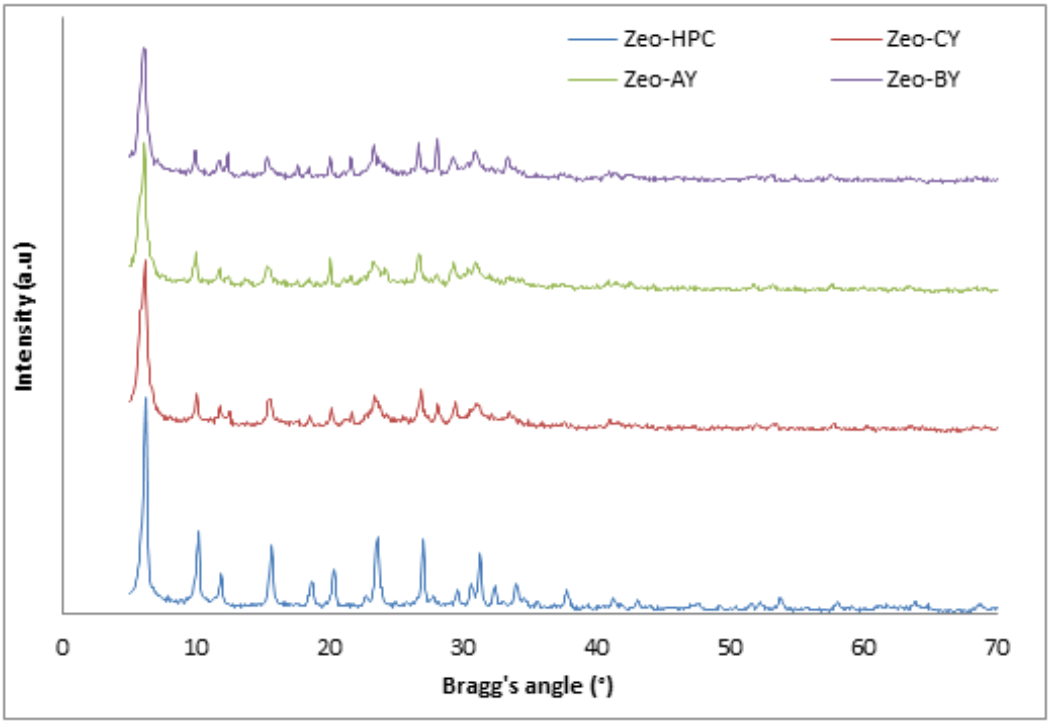


Figure 4.46: Comparison XRD patterns for the various batches of the synthesized zeolite Y

4.5.5.6 SEM micrographs of the synthesized zeolite Y

Plates XVII - XXIV show the SEM micrograph scanned at various magnifications of the NaY and RE Y forms of the various synthesized zeolite Y. Plates XVII A, B, C and D show the structural mophology of the Zeo-AY: NaY at magnifications of 8000, 15000, 30000 and 45000 respectively. At the lower magnifications the zeolite Y particles appeared densely agglomearted. However, at the highest magnification clear pictures of evenly distributed individual particles having regular tetrahedral shapes could be observed. Therefore, it could be deduced from the images that the Zeo-AY: NaY possessed an agglomerated tetrahedral euhedral morphology. The average particle size of the Zeo-AY: NaY was estimated as 200 nm. Plates XVIII A, B, C and D show the structural mophology of the Zeo-AY: RE Y at the same magnifications as the Zeo-AY: NaY. The micrograph of the Zeo-AY: RE Y was similar to that of the Zeo-AY: NaY except that the boundaries of the individual crystals were not as clearly obvious as in the micrograph of Zeo-AY: NaY.

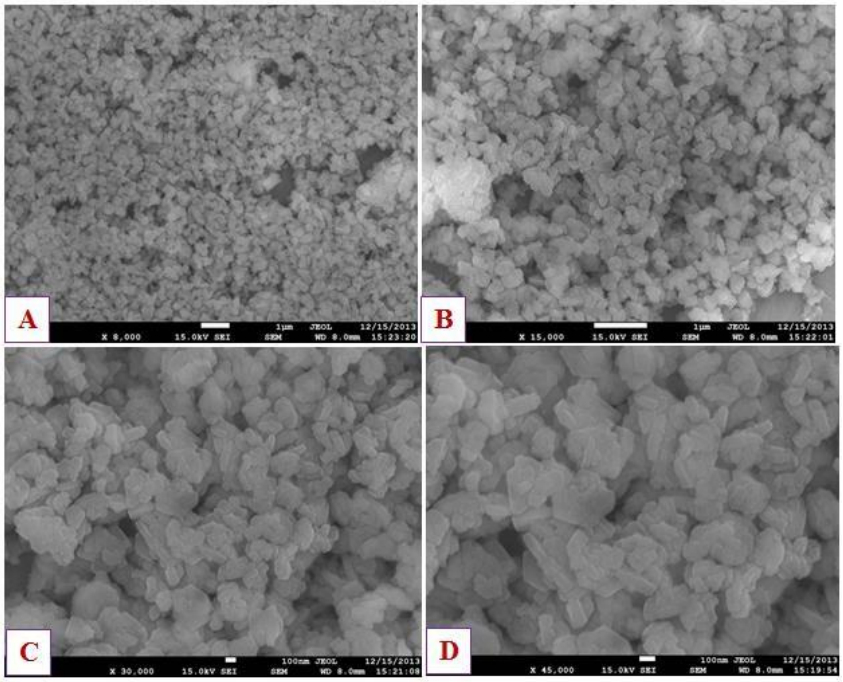


Plate XVII: SEM images of Zeo-AY: NaY at magnifications of (A) 8000 (B) 15000 (C) 30000 (D) 45000

This implies loss of crystalinity after converting to the Zeo-AY: RE Y form; this further confirmed the observation made in the analysis of the XRD of these samples that after conversion to the Zeo-AY: RE Y a reduction in crystallinity was observed. Plates XIX A, B, C and D show the structural mophology of the Zeo-BY: NaY at magnifications of 8000, 15000, 30000 and 45000 respectively. Irrespective of the magnification, the zeolite Y particles appeared densely agglomerated. Even at the highest magnification the micrograph appeared densly agglomerated revealing the porous nature of the agglomerated particles. The particles appeared to possess no definite shape. Therefore it could be deduced from the images that the Zeo-BY: NaY possessed an agglomerated anhedral morphology. The average particle size of the Zeo-BY: NaY was estimated as 200 nm.

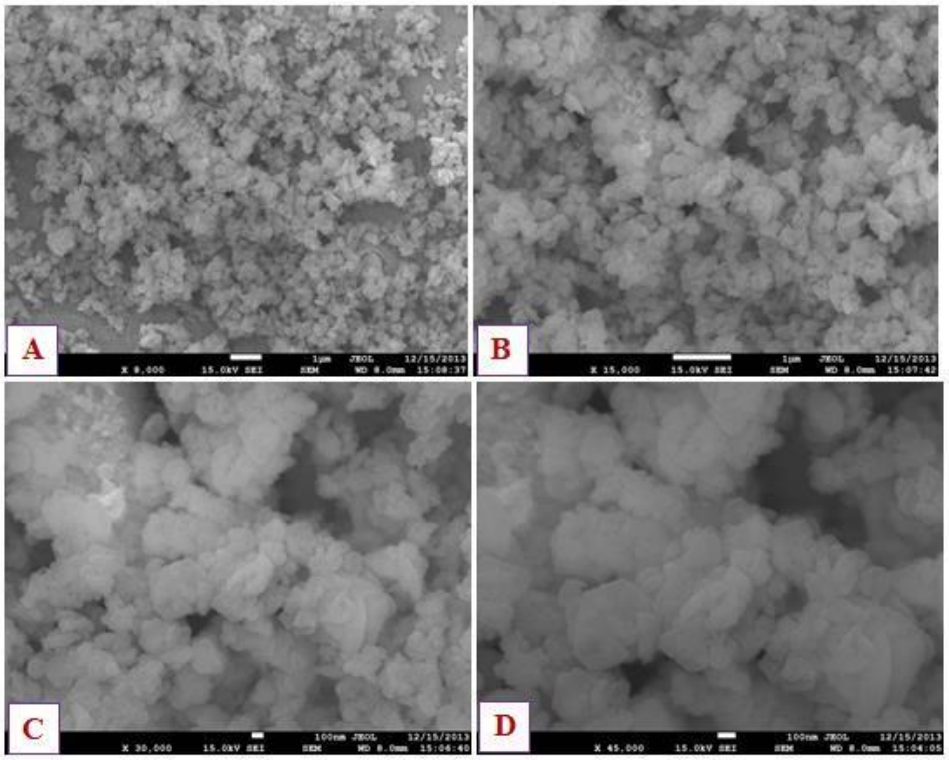


Plate XVIII: SEM images of Zeo-AY: RE Y at magnifications of (A) 8000 (B) 15000 (C) 30000 (D) 45000

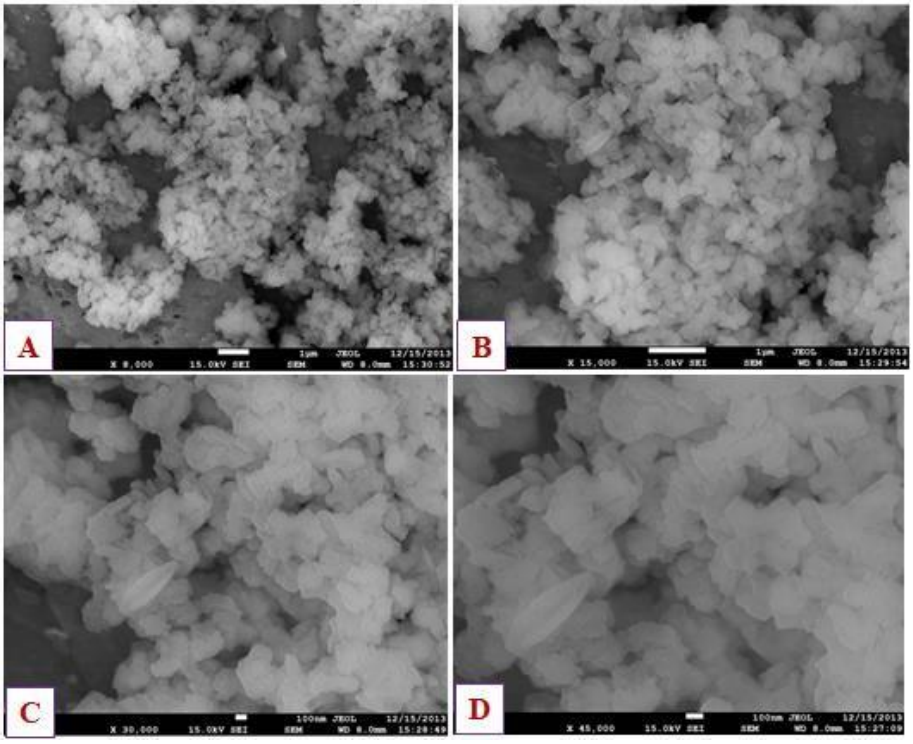


Plate XIX: SEM images of Zeo-BY: NaY at magnifications of (A) 8000 (B) 15000 (C) 30000 (D) 45000

Plates XX A, B, and C show the structural mophology of the Zeo-BY: RE Y at magnifications of 6000, 12000 and 25000 respectively. The micrograph of the Zeo-BY: RE Y was similar to that of the Zeo-BY: NaY except that the boundaries of the individual crystals were not as clearly obvious as in the micrograph of Zeo-BY: NaY implying loss of crystalinity after converting to the Zeo-BY: RE Y form; this further confirmed the observation made in the analysis of the XRD of these samples that after conversion to the Zeo-BY: RE Y a reduction in crystallinity was observed. Plates XXI A, B, C and D show the structural mophology of the Zeo-CY: NaY at magnifications of 8000, 14000, 27000 and 30000 respectively. Irrespective of the magnification, the zeolite Y particles appeared densely agglomearted. At the high magnification the micrograph appeared densly agglomerated revealing the definite shape of the particles, although the micrograph was not clear enough to reveal the actual shape clearly. Therefore it could be

deduced from the images that the Zeo-CY: NaY possessed an agglomerated euhedral morphology. The average particle size of the Zeo-CY: NaY was estimated as 200 nm.

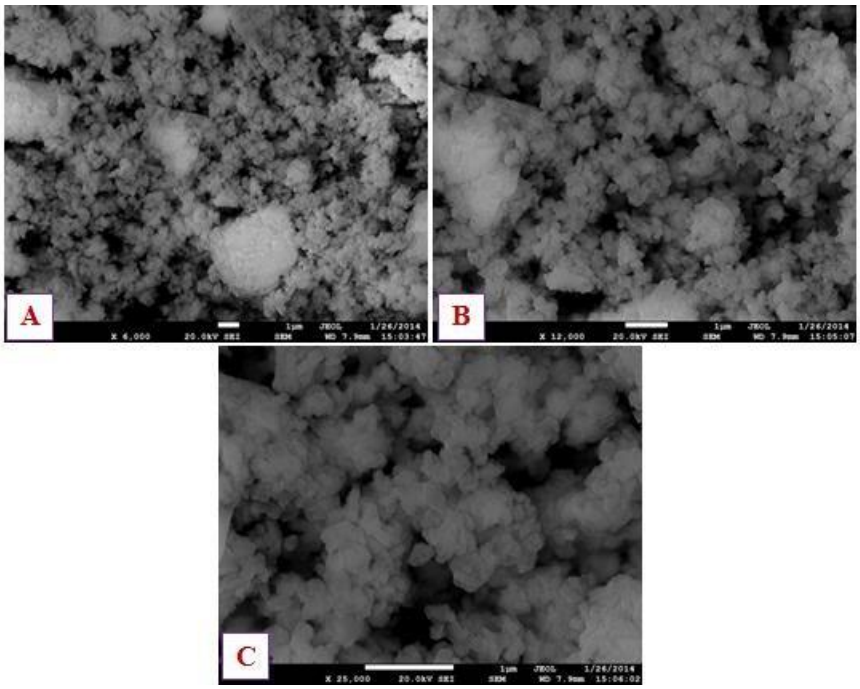


Plate XX: SEM images of Zeo-BY: RE Y at magnifications of (A) 6000 (B) 12000 (C) 25000

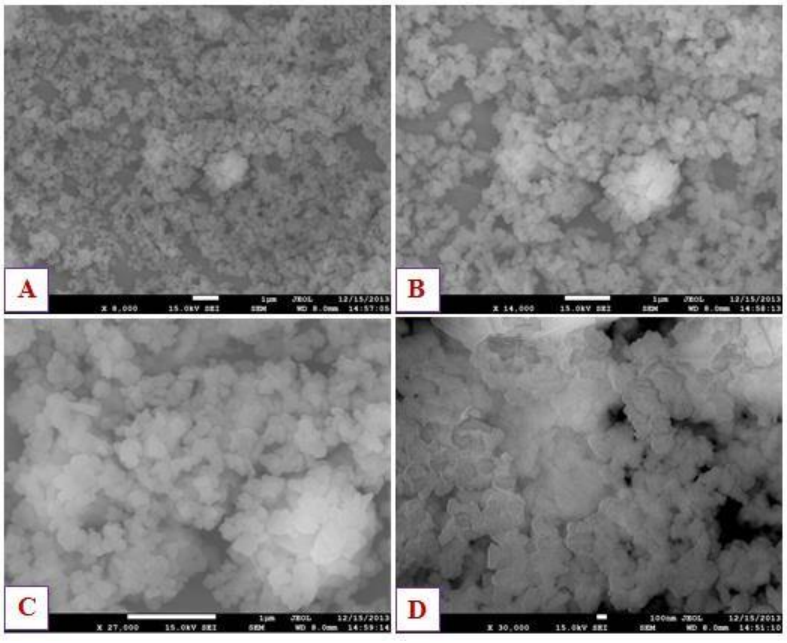


Plate XXI: SEM images of Zeo-CY: NaY at magnifications of (A) 8000 (B) 14000 (C) 27000 (D) 30000

Plates XXII A, B, C and D show the structural mophology of the Zeo-HPC: NaY at magnifications of 8000, 14000, 27000 and 30000 respectively. Irrespective of the magnification, the zeolite Y particles appeared densely agglomearted. At the high magnification the micrograph appeared densly agglomerated revealing the definite shape of the particles, although the micrograph was not clear enough to reveal the actual shape clearly. Therefore it could be deduced from the images that the Zeo-HPC: NaY possessed an agglomerated euhedral morphology. The average particle size of the Zeo-HPC: NaY was estimated as 200 nm.

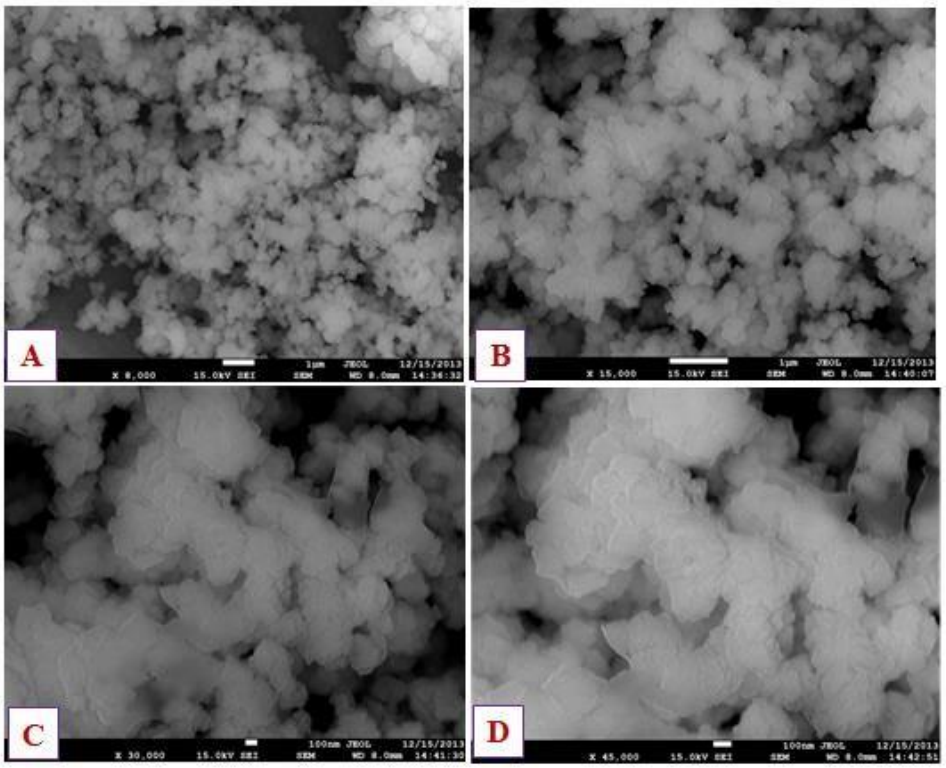


Plate XXII: SEM images of Zeo-HPC: NaY at magnifications of (A) 8000 (B) 14000 (C) 27000 (D) 30000

Plates XXIII A, B, C and D show the structural mophology of the Zeo-AY: RE Y at magnifications of 5000, 8000, 15000 and 30000 respectively, the micrograph of the Zeo-HPC: RE Y was similar to that of the Zeo-HPC: NaY except that the boundaries of the individual crystals were not as clearly obvious as in the micrograph of Zeo-AY: NaY implying loss of

crystalinity after converting to the Zeo-HPC: RE Y form; this further confirmed the observation made in the analysis of the XRD of these samples that after conversion to the Zeo-HPC: RE Y a reduction in crystallinity was observed.

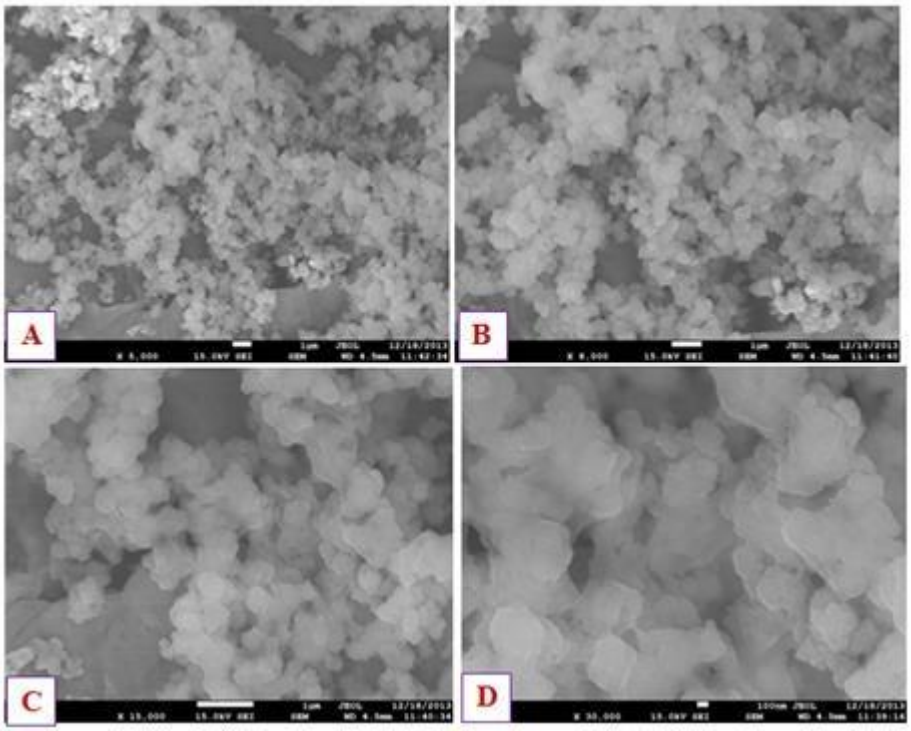


Plate XXIII: SEM images of Zeo-HPC: RE Y at magnifications of (A) 5000 (B) 8000 (C) 15000 (D) 30000

Plate XXIV A, B, and C show the structural mophology of the commercial zeolite HY at magnifications of 1200, 2500, and 5000 respectively, the micrograph of the commercial zeolite HY was similar to those of the synthesized zeolites shown in Plates XVII - XXIV having densely agglomerated crystal particles. It was also observed that the boundaries of the individual crystals were not clearly defined, however, the particles appear to possess a definite shape which seemed to be tetrahedral shape. However, it was noted that the the particles appeared relatively bigger at a relatively smaller magnifications compared to the synthesized samples. This was likely because the commercial zeolite possessed larger particle sizes than the synthesized zeolite Y. The average

particle size was estimated as 500 nm, this was 2.5 times the average particle size of the synthesized zeolite Y.

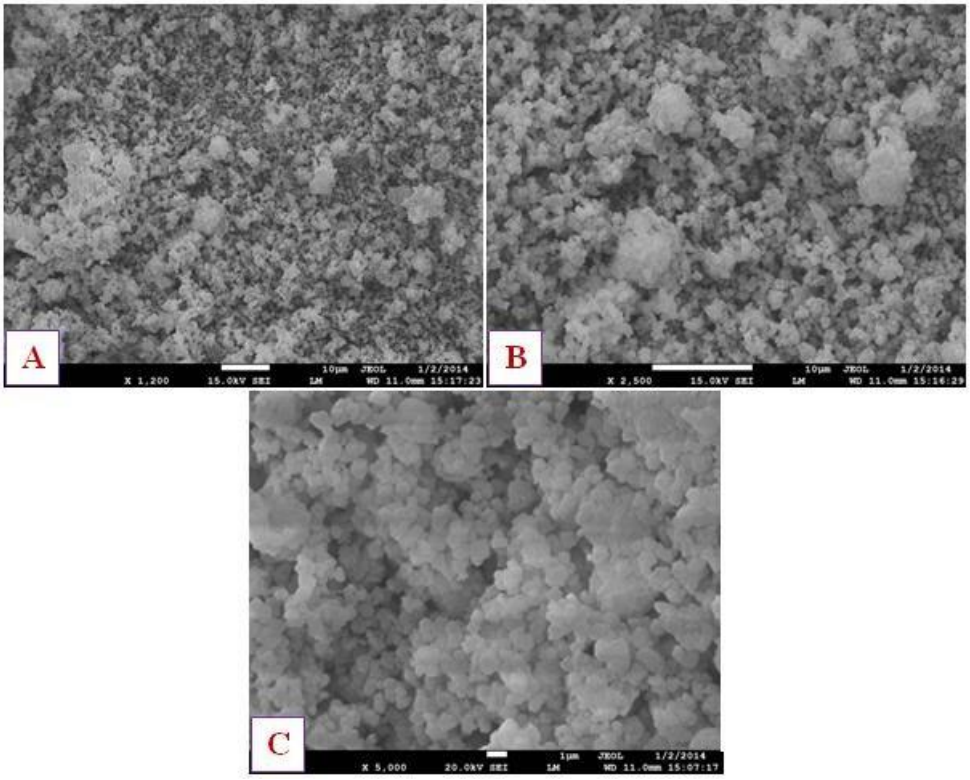


Plate XXIV: SEM images of commercial zeolite HY at magnifications of (A) 1200 (B) 2500 (C) 5000

4.5.5.7 TEM images of the synthesized zeolite Y

Plates XXV A, B, C and D show the TEM images of the Zeo-AY: NaY at magnifications of 100000, 200000, 400000 and 500000 respectively. The clear boundary shapes of the crystals could be seen at 100000 and 200000 magnification. The crystal shape appeared to be hexagonal although the crystals images overlapped each other, as a result, the crystal shapes were not clearly revealed. At higher magnifications 400000 and 500000 clearer boundary shapes were noticeable, although the crystals still appeared in overlap. The average crystal size was estimated as 200 nm.

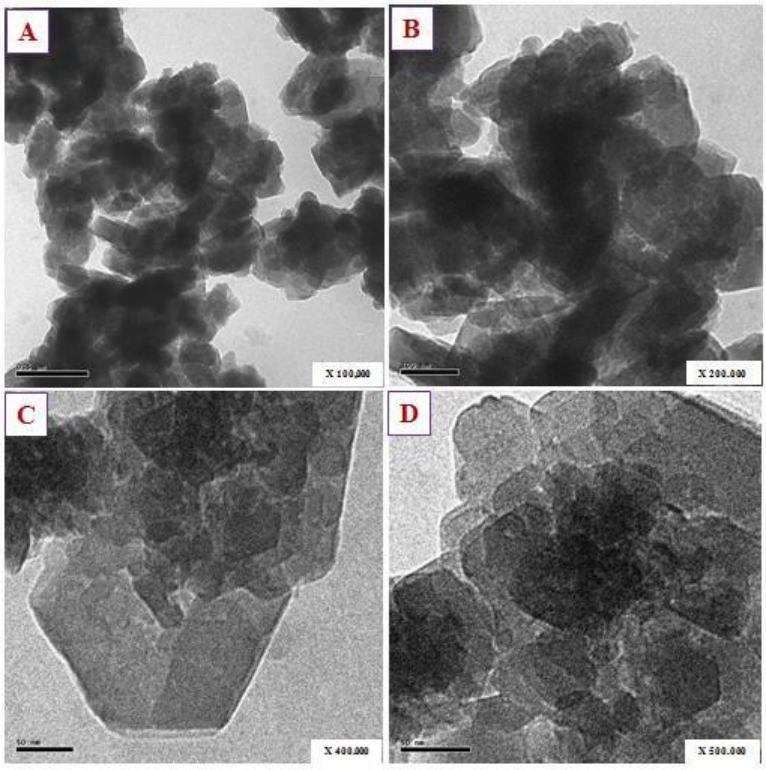


Plate XXV: TEM images of Zeo-AY: NaY at magnifications of (A) 100000 (B) 200000 (C) 400000 (D) 500000

Plates XXVI A, B, C and D show the TEM images of the Zeo-AY: RE Y at magnifications of 100000, 200000, 300000 and 500000 respectively. The clear boundary shapes of the crystals were very obvious at all magnifications, especially at the higher magnification. The crystal shape was hexagonal. The average crystal size was estimated as 100 nm. Plates XXVII A, B, C and D show the TEM images of the Zeo-BY: NaY at magnifications of 100000, 200000, 300000 and 400000 respectively. The clear boundary shapes of the crystals could be observed, although there was overlap of crystals. The crystal shape was hexagonal. The average crystal size was estimated as 300 nm.

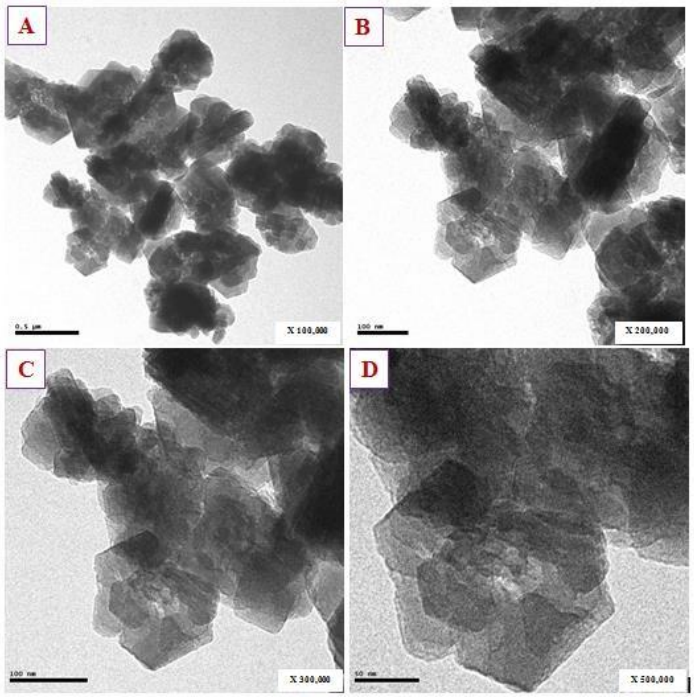


Plate XXVI: TEM images of Zeo-AY: RE Y at magnifications of (A) 100000 (B) 200000 (C) 300000 (D) 500000

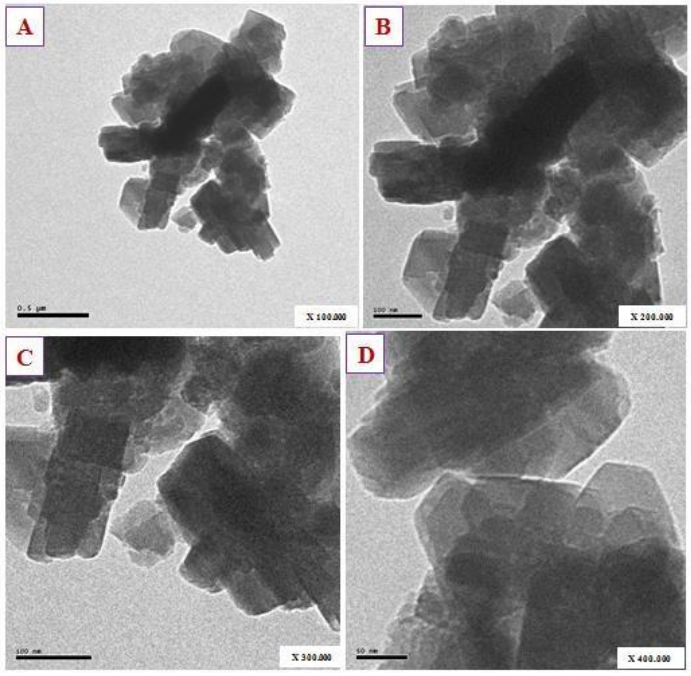


Plate XXVII: TEM images of Zeo-BY: NaY at magnifications of (A) 100000 (B) 200000 (C) 300000 (D) 400000

Plates XXVIII A, B, C and D show the TEM images of the Zeo-HPC: NaY at magnifications of 100000, 200000, 300000 and 400000 respectively. The clear boundary shapes of the crystals were very obvious. The crystal images were highly overlapping a clear distinction could not be made between tetrahedral and hexagonal crystal shape. The average crystal size was estimated as 200 nm.

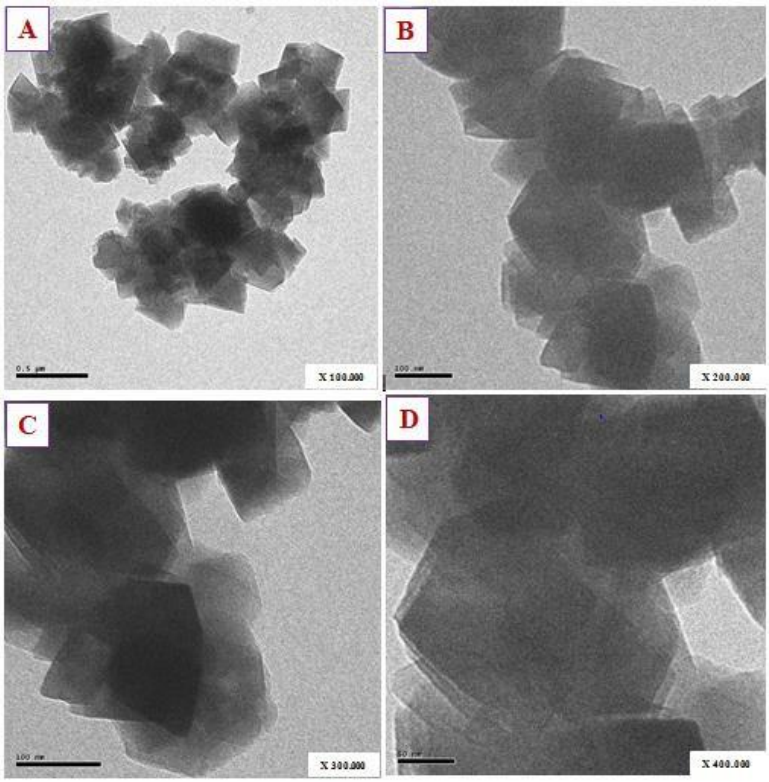


Plate XXVIII: TEM images of Zeo-HPC: NaY at magnifications of (A) 100000 (B) 200000 (C) 300000 (D) 400000

4.5.5.8 BET results of the synthesized zeolite Y

Table 4.15 presents the BET results of the various batches of the synthesized NaY zeolite. It could be observed that the specific surface areas of the sodium base Zeo-AY, Zeo-BY, Zeo-CY and Zeo-HPC were 732.0, 717.2, 830.0 and 980.9 m^2/g respectively. While that of the commercial zeolite HY was 601.8 m^2/g. It would be observed that the Zeo-HPC had the highest

surface area; it was 63% higher than the commercial zeolite HY and 34%, 37% and 18% higher than Zeo-AY, Zeo-BY and Zeo-CY respectively. The next highest surface area was Zeo-CY, it was 38% higher than the commercial sample it was also 13% and 16% greater than Zeo-AY, and Zeo-BY respectively. Followed by Zeo-AY which its surface area was 22% higher than the commercial zeolite Y and only 2% higher than the Zeo-BY. Zeo-BY was also higher than the commercial zeolite Y by 19%. The pore volume of the Zeo-AY, Zeo-BY, Zeo-CY and Zeo-HPC was 0.2611, 0.2553, 0.291 and 0.3494 cm^3/g respectively, while that of the commercial zeolite HY was 0.2500 cm^3/g. Similarly, the Zeo-HPC had the highest pore volume which was 40% higher than the commercial zeolite Y, it was also 34%, 37% and 18% higher than Zeo-AY, Zeo-BY and Zeo-CY respectively. Zeo-CY had the next highest pore volume; 18% higher than the commercial zeolite Y, it was also 13% and 16% greater than Zeo-AY, and Zeo-BY respectively. The next highest pore volume was Zeo-AY; its pore volume was 4% higher than the commercial zeolite Y and only 2% higher than the Zeo-BY. Zeo-BY also had pore volume 2% higher than the commercial zeolite Y. The pore diameter of Zeo-AY, Zeo-BY, Zeo-CY and Zeo-HPC was 14.26, 14.24, 14.22 and 14.25 Å respectively. That of the commercial zeolite Y was 16.4 Å. It could be observed that the commercial zeolite Y had the highest pore diameter of 1.64 nm.

Table 4.15: BET results of the various synthesized zeolite NaY

Sample	Specific Surface Area (m^2/g)	Pore Volume (cm^3/g)	Pore Diameter (Å)
Zeo-AY: NaY	732.0	0.2611	14.26
Zeo-BY: NaY	717.2	0.2553	14.24
Zeo-CY: NaY	830.0	0.2951	14.22
Zeo- HPC: NaY	980.9	0.3494	14.25
Commercial HY	601.8	0.2500	16.4

The other samples had relatively the same pore diameter of average value; 1.42 nm. The pore diameter of the commercial zeolite Y was 15% higher than those of the other samples. Nevertheless, all the samples including the commercial zeolite Y were microporous.

Table 4.16 presents the BET results of the various batches of thermally stabilized zeolite RE Y prepared. It could be observed that the specific surface areas of the Zeo-AY: RE Y, Zeo-BY: RE Y, Zeo-CY: RE Y and Zeo-HPC: RE Y were 456.0, 464.9, 482.7 and 764.8 m^2/g respectively. It would be observed that each of the thermally stabilized catalyst had reduced in surface area compared to the surface area values of their respective NaY form. The reductions were 38%, 35%, 42% and 22% for the Zeo-AY: RE Y, Zeo-BY: RE Y, Zeo-CY: RE Y and Zeo-HPC: RE Y respectively. The pore volumes of Zeo-CY: RE Y and Zeo-HPC: RE Y remained relatively unchanged while that of Zeo-AY: RE Y and Zeo-BY: RE Y reduced by 39% and 36% respectively. The pore diameter of Zeo-AY: R EY, Zeo-BY: RE Y and Zeo-CY: RE Y reduced by 2% each, while that of Zeo-HPC: RE Y changed by 1%. Hence, each of the thermally stabilized zeolites produced had very excellent BET properties, generally having typically high surface areas higher than the products reported by many other researchers (Ng *et al*., 2006; Ding *et al*., 2007; Li *et al*., 2007). All the thermally stabilized zeolites produced were microporous.

Table 4.16: BET results of the various thermally stabilized zeolite RE Y prepared

Sample	Specific Surface Area (m^2/g)	Pore Volume (cm^3/g)	Pore Diameter (Å)
Zeo- HPC: RE Y	764.8	0.2706	14.15
Zeo-CY: RE Y	482.7	0.1684	13.95
Zeo-BY: RE Y	464.9	0.1627	14.00
Zeo-AY: RE Y	456.0	0.1591	13.95

4.5.5.9 Effect of thermal treatment on the crystallinity of the synthesized zeolite Y

Figure 4.47 shows the XRD patterns of the bulk production of Zeo-BY; the uncalcined NaY form, HY form calcined at 450, 550 and 650˚C, and RE Y form calcined at 650˚C. All calcination was done in air for 2 hr. The intensity of the characteristic peak of zeolite Y in the NaY form was 1040 counts. At each of the calcination temperatures it was observed that the intensity of the characteristic peak of zeolite Y had reduced drastically. The reduction at 450˚C was 67%, that at 550˚C was 70%. However, calcination at 650˚C brought about total collapse of the zeolite Y structure as could be observed that the material became completely amorphous. These have shown that the zeolite HY was thermally unstable so much that it began to lose its crystallinity and quality as from calcination temperature of 450˚C and at 650˚C the material lost its mineral property completely, the zeolite Y was structurally destroyed making the material completely amorphous.

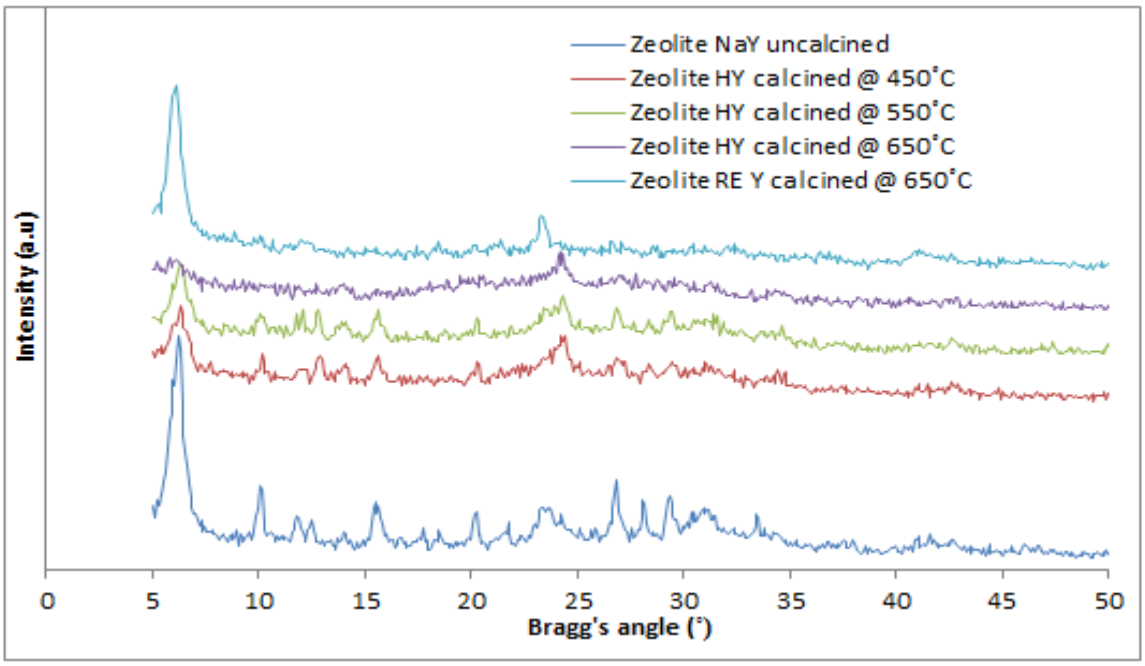


Figure 4.47: XRD pattern of bulk synthesized Zeo-BY uncalcined and calcined at variable temperatures

Considering the XRD pattern of the thermally stabilized zeolite RE Y which was prepared by protonation of the Zeo-BY: NaY and impregnation of rare earth metal as described in Section 3.2.4. It could be observed that the Zeo-BY: RE Y had been highly improved having high thermal stability compared to the earlier Zeo-BY: HY as it can be observed that the Zeo-BY: RE Y still retained its crystallinity and mineral form as shown by the XRD result even after calcination at 650˚C.

4.5.5.10 Thermogravimetric properties of the synthesized zeolite Y

Figures 4.48 – 4.53 show the TGA/DTG thermal scan curves within temperature range of 30 - 750˚C for the various synthesized zeolite Y. It could be observed that the total mass depletions of the synthesized NaY zeolites, as shown by the TGA curves of Figures 4.48 and 4.53 were relatively the same for the various synthesized zeolites having average value of 25 wt%. This value was relatively the same as the value obtained for the LoI of the samples presented earlier in Table 4.13. The DTG curves of the NaY zeolites suggested that the actual temperature responsible for the temperature loss was about 170˚C, hence, the mass loss was likely due to effect of dehydration of the physically and chemically combined water molecules. It would also be observed that the total mass depletions of the RE Y zeolites, as shown by the TGA curves of Figures 4.50 and 4.53 were relatively the same for the various synthesized zeolites having average value of 20 wt%. The DTG curves of the RE Y zeolites suggested that the actual temperature responsible for the temperature loss was about 140˚C, hence, the mass loss was likely due to effect of dehydration of the physically and chemically combined water molecules. It would be observed that no other DTG peaks were present in the RE Y zeollites showing that the materials were thermally stabilized.

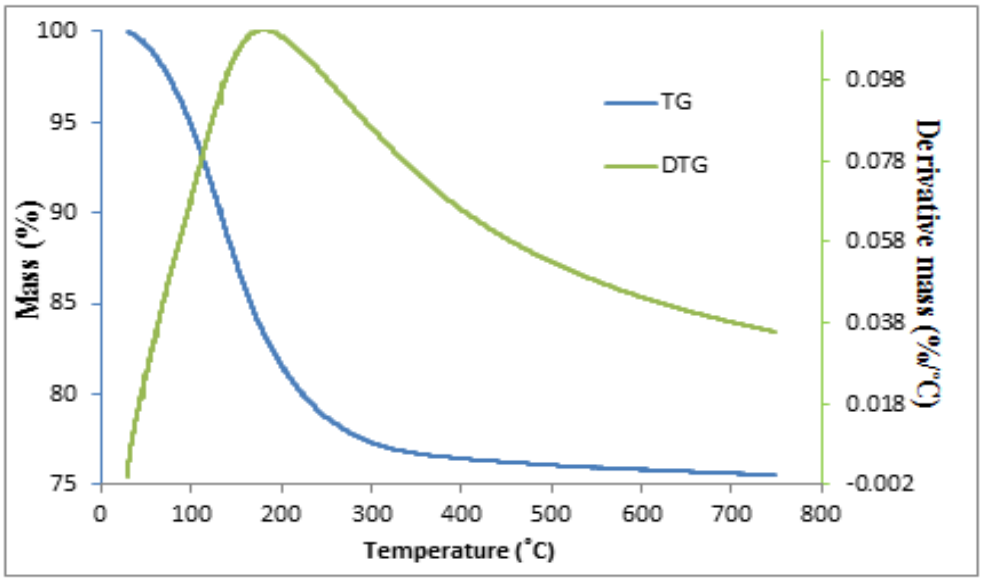


Figure 4.48: TGA/DTG curves of Zeo-CY: NaY

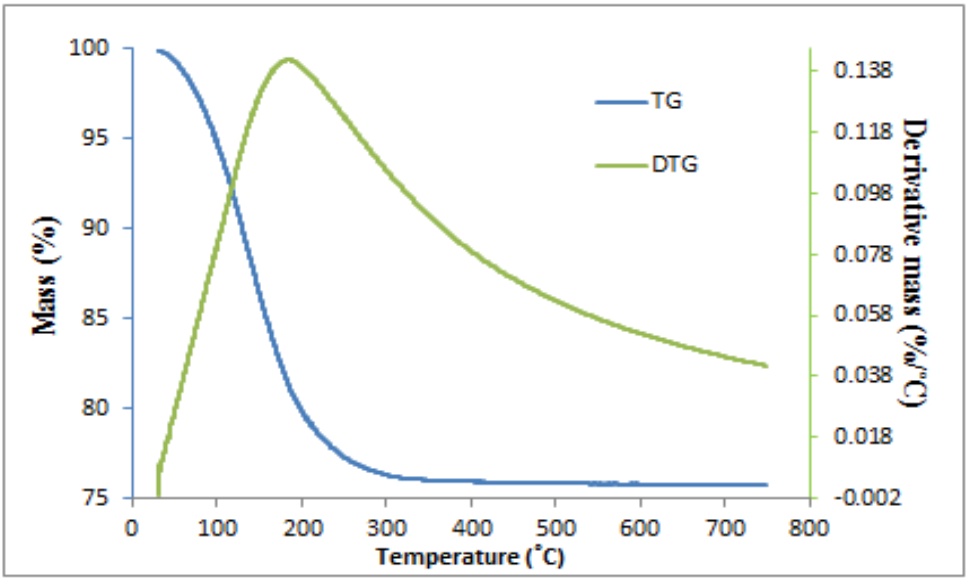


Figure 4.49: TGA/DTG curves of Zeo-HPC: NaY

Although it was expected that the DTG curves of the NaY zeolites would show some other peaks at higher temperatures; around 650˚C to buttress the observation made when the thermal stability was studied using the XRD analysis of the NaY zeolites. The absence of the expected peaks was

likely due to the inert atmosphere of the thermogravimetric analysis created by the nitrogen purge gas, whereas the thermal stability study using XRD was carried out in air.

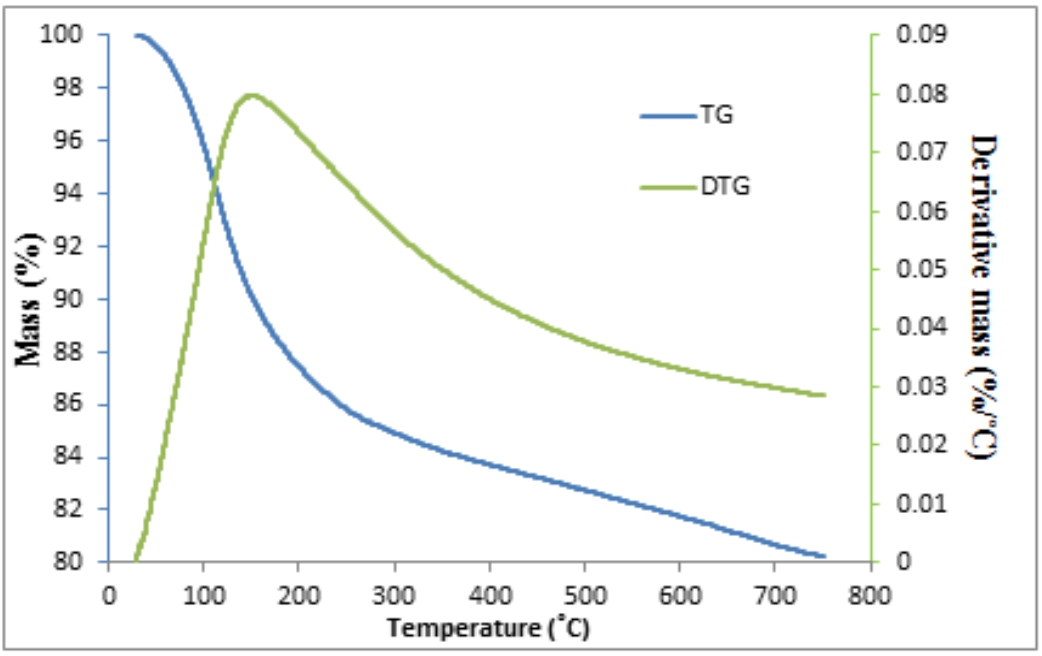


Figure 4.50: TGA/DTG curves of Zeo-AY: RE Y

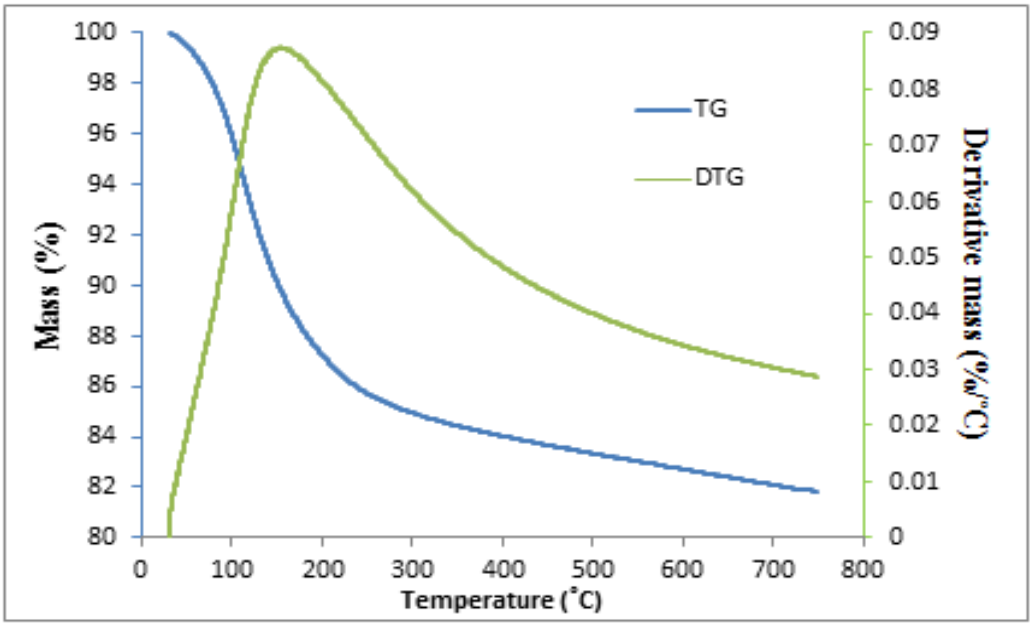


Figure 4.51: TGA/DTG curves of Zeo-BY: RE Y

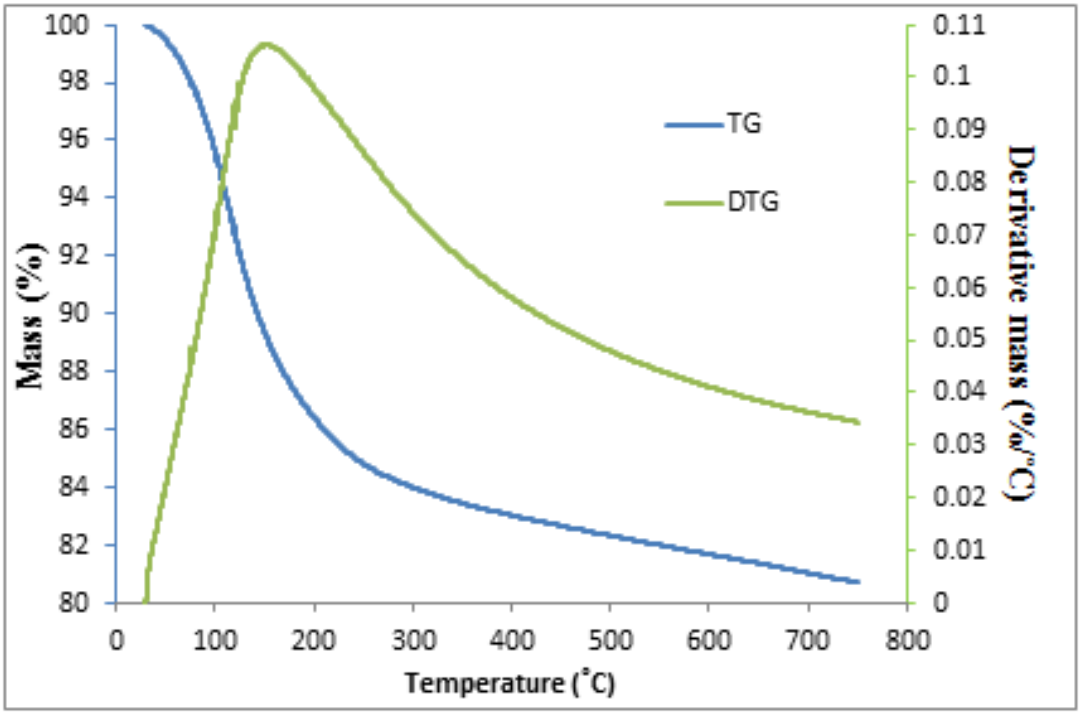


Figure 4.52: TGA/DTG curves of Zeo-CY: RE Y

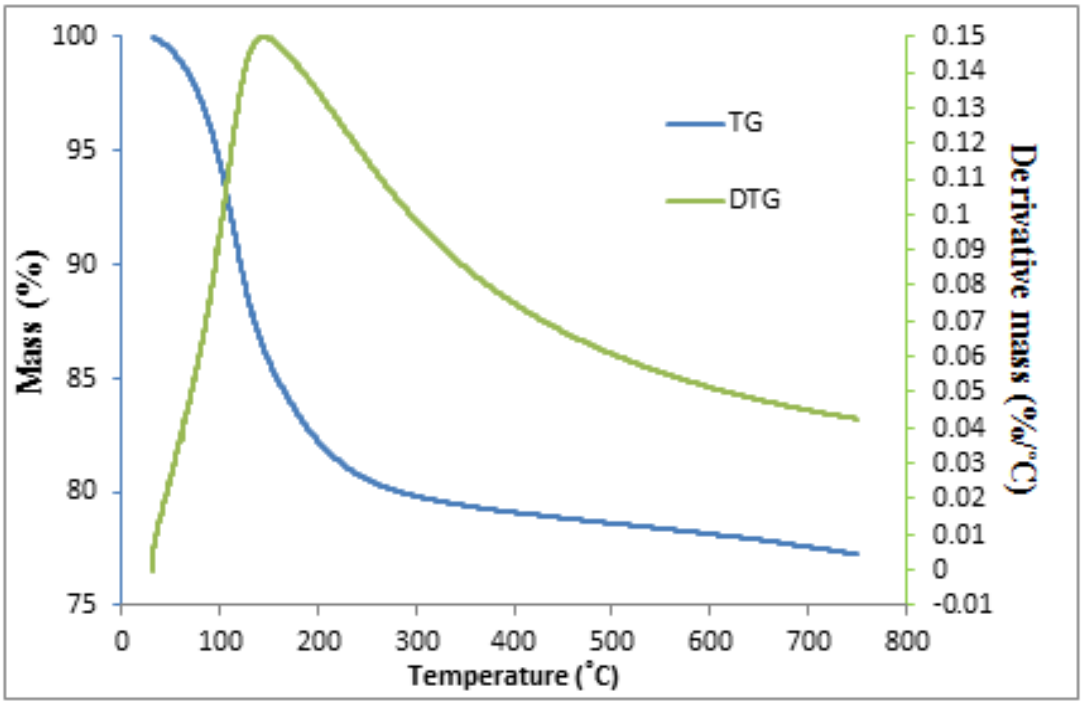


Figure 4.53: TGA/DTG curves of Zeo-HPC: RE Y

4.5.5.11 Acidity of the synthesized zeolites

Figures 4.54 and 4.55 show the FTIR spectra of the base and pyridine probed wafers of the various zeolite NaY respectively. It could be observed that the base spectra appeared as relatively smooth curves having no noticeable bands for FTIR scan within wavelength range of 1420 – 1600 cm^{-1}. However, each of the pyridine probed spectra showed appearance of well pronounced bands at wavelength of 1450 cm^{-1}. The integrated area of this band is directly proportional to the Lewis acid concentration (Barzetti *et al.*, 1996; Akcay, 2005) which was calculated using Equation (3.4). In addition some other low bands could be observed at 1600 cm^{-1} indicating presence of little BrØnsted acidity. Figures 4.56 and 4.57 show the FTIR spectra of the base and the pyridine probed wafers of the various zeolite RE Y. It could be similarly observed that the base spectra were relatively smooth showing no major band for FTIR scan within wavelength range of 1420 – 1600 cm^{-1}. As earlier observed in the case of zeolite NaY, each of the pyridine probed spectra of the various zeolite RE Y showed appearance of well pronounced bands at wavelengths of 1450 and 1550 cm^{-1}.

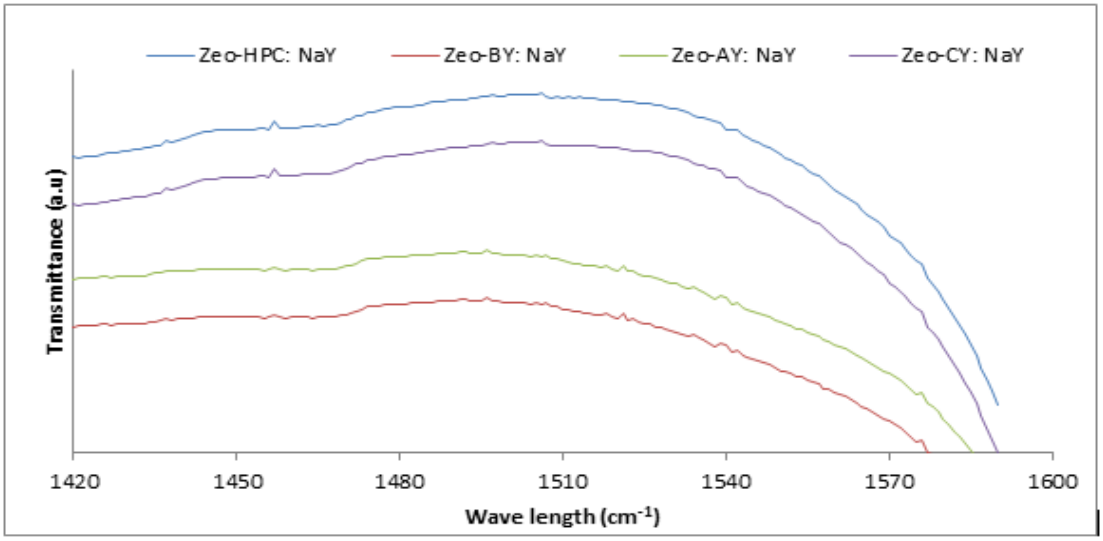


Figure 4.54: FTIR spectra of the various zeolite NaY before pyridine adsorption

The integrated areas of these bands are directly proportional to the Lewis and BrØnsted acid concentrations respectively, (Borade *et al.*, 1990; Santi, 2013) which were calculated using Equations (3.4) and (3.5) respectively.

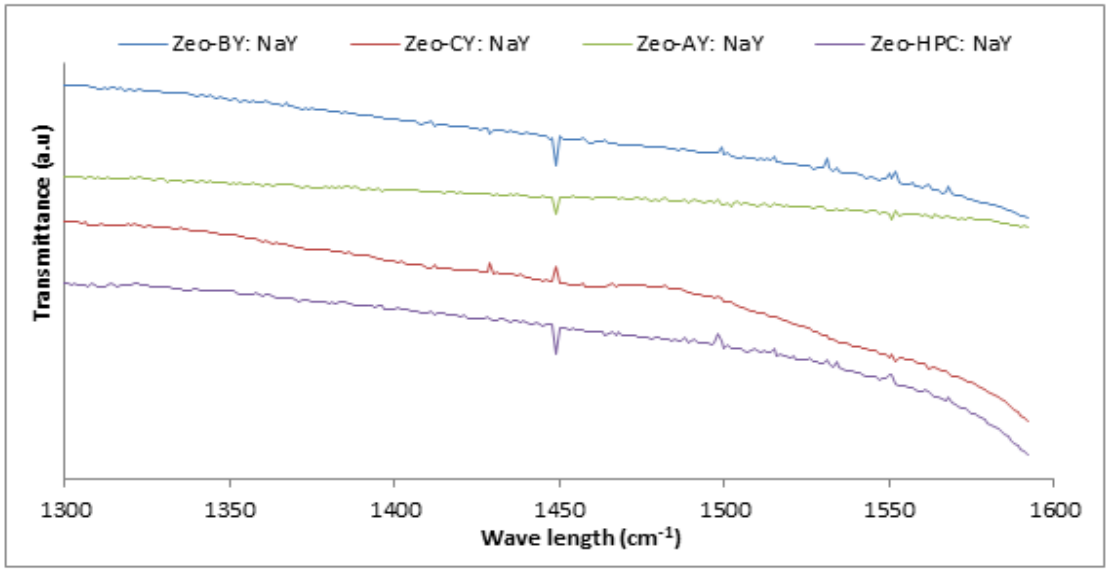


Figure 4.55: FTIR spectra of the various zeolite NaY after pyridine adsorption

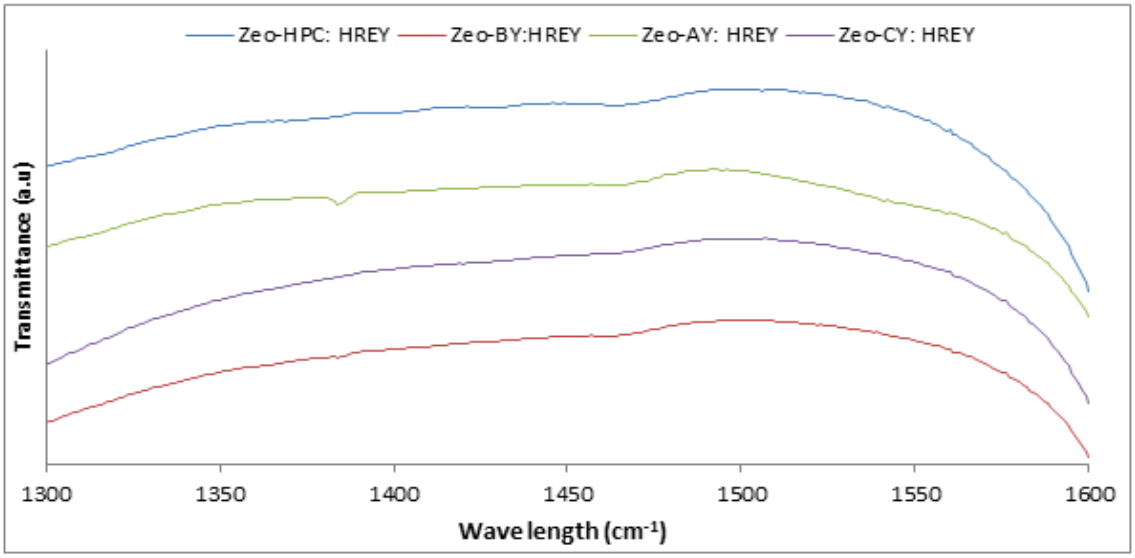


Figure 4.56: FTIR spectra of the various zeolite RE Y before pyridine adsorption

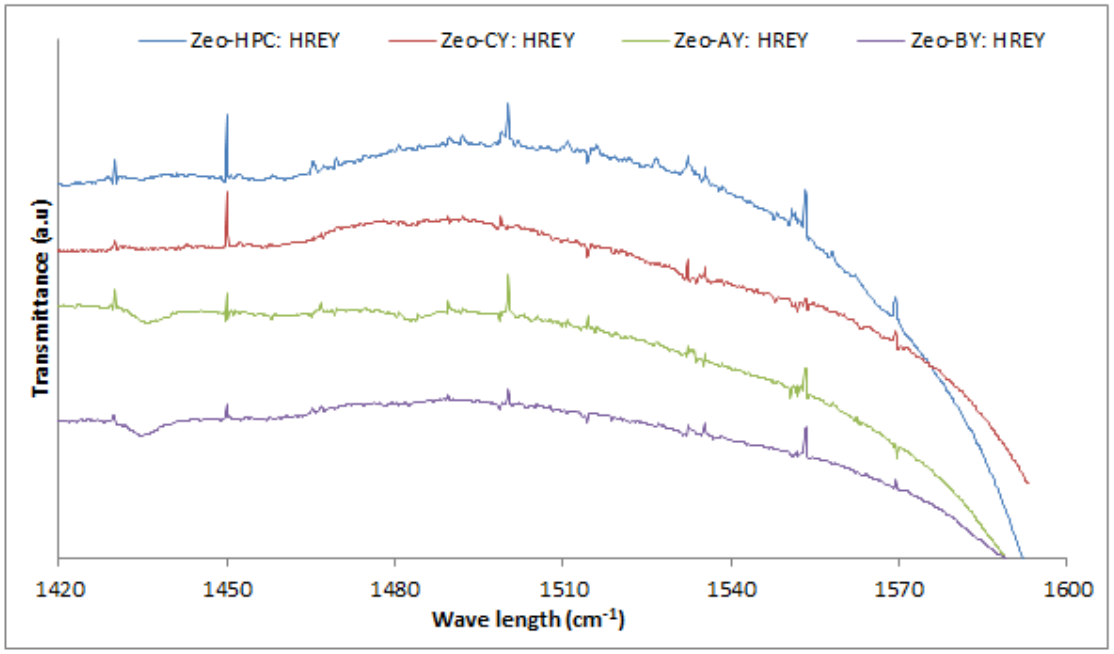


Figure 4.57: FTIR spectra of the various zeolite RE Y after pyridine adsorption

Tables 4.17 and 4.18 present the acidity analysis of the various zeolite NaY and RE Y zeolite respectively. It could be observed that the NaY zeolites generally possessed low values of the BrØnsted acidity and relatively high Lewis acidity thereby making the BrØnsted/Lewis acidity (B_C/L_C) ratio very low. It will be observed that the RE Y zeolites possessed relatively higher BrØnsted acidity compared to the NaY, this showed the effect of protonation. It could be observed that protonation had impacted higher BrØnsted acidity on the zeolites although not by the same proportion. As it could be observed the B_C/L_C ratio of the zeolites improved by 2388%, 538%, 35% and 169% for the Zeo-AY, Zeo-BY, Zeo-CY and Zeo-HPC respectively after protonation. When compared with the acidity of zeolite HY reported in the literature, it would be observed that the acidity properties of the Zeo-CY compared closely with the literature values (Jia *et al*., 2013).

Table 4.17: Acidity analysis of the various NaY zeolites

Sample (NaY)	Lewis Band (cm^{-1})	Area (µmol)	BrØnsted Band (cm^{-1})	Area (µmol)	L_C (µmol/g)	B_C (µmol/g)	Total (µmol/g)	B_C/L_C
Zeo-BY	1450	37.02	1550	6.57	238.22	56.20	294.42	0.24
Zeo-AY	1450	20.36	1550	6.14	131.02	52.52	183.54	0.40
Zeo-CY	1450	19.87	1550	2.03	127.86	17.37	145.23	0.14
Zeo-HPC	1450	36.31	1550	10.73	233.66	91.79	325.45	0.39

Table 4.18: Acidity analysis of the various RE Y zeolite

Sample (RE Y)	Lewis Band (cm^{-1})	Area (µmol)	BrØnsted Band (cm^{-1})	Area (µmol)	L_C (µmol/g)	B_C (µmol/g)	Total (µmol/g)	B_C/L_C
Zeo-BY	1450	6.87	1550	30.85	44.21	263.90	308.11	5.97
Zeo-AY	1450	10.85	1550	20.83	69.82	178.19	248.01	2.55
Zeo-CY	1450	41.5	1550	5.90	267.05	50.47	317.52	0.19
Zeo-HPC	1450	52.84	1550	41.65	340.03	356.29	696.31	1.05
Literature Value (Jia *et al*., 2013)			NA		233	53	286	0.23

NA: Not available

4.5.5.12 Catalytic properties of the synthesized zeolite Y: Desulfurization of model petroleum oil

Figures 4.58 and 4.59 show the trends of sulfur reduction at variable times and temperatures respectively of a microwave assisted desulfurization of a model petroleum oil using the protonated zeolites; Zeo-AY: RE Y and Zeo-HPC: RE Y as catalysts. Figure 4.58 shows the sulfur reduction for reactions carried out at 100˚C for variable times. It would be observed that a relatively similar sulfur reduction trend was observed for both the Zeo-AY: RE Y and Zeo-HPC: RE Y. The maximum sulfur reduction was observed at 15 min for both zeolites. At the 15 min

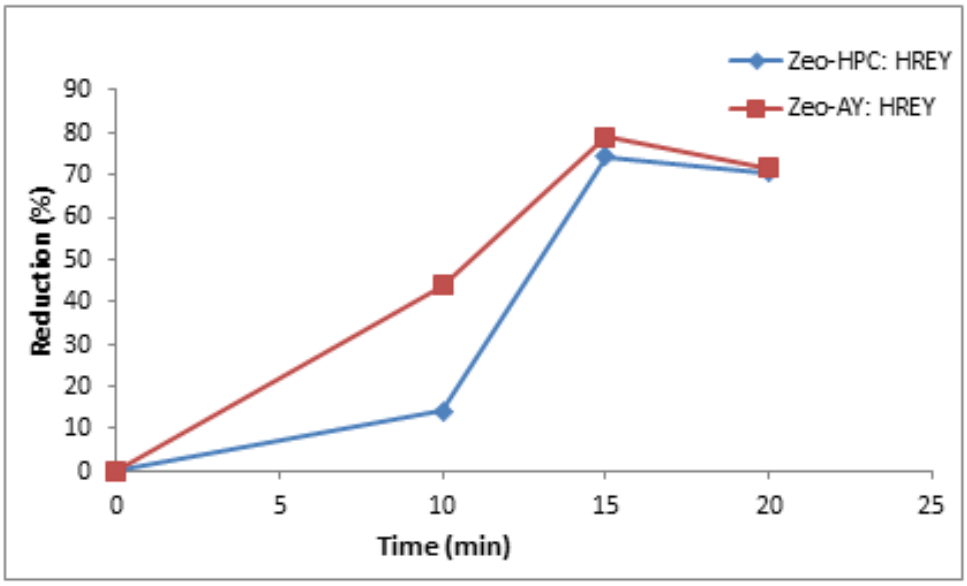


Figure 4.58: Trend of microwave desulfurization of model petroleum oil at variable reaction times

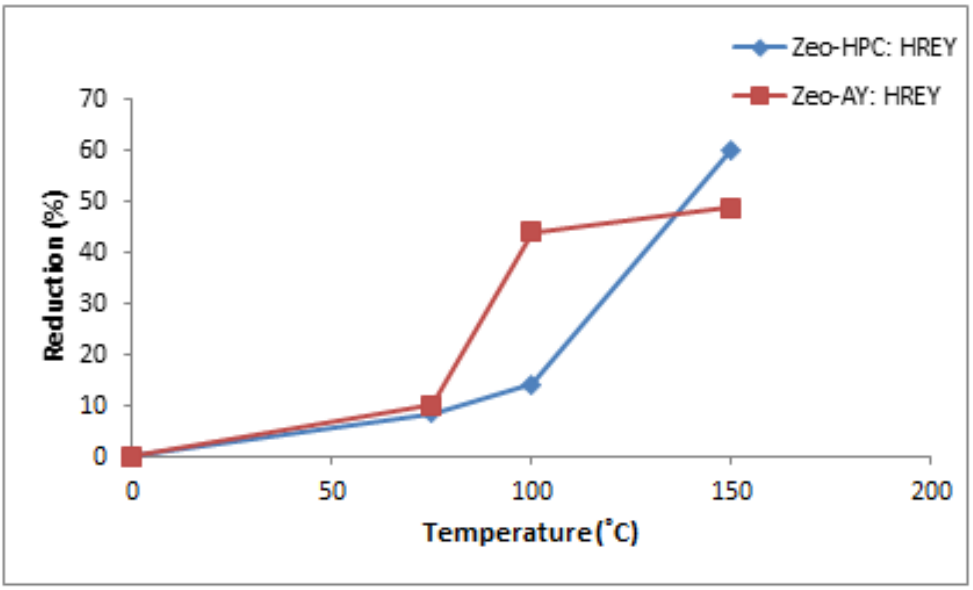


Figure 4.59: Trend of microwave desulfurization of model petroleum oil at variable reaction temperatures

reaction time the sulfur reduction observed for the Zeo-AY: RE Y and Zeo-HPC: RE Y were 79% and 74% respectively. Figure 4.59 shows the sulfur reduction for the reactions carried out for 10 min at variable temperatures. It would be observed that both zeolites attained the

maximum sulfur reduction at 150˚C, the maximum temperature considered in the study. It could be observed that the curve for Zeo-HPC: RE Y showed continuous progressive increase in sulfur reduction throughout the runs whereas curve for Zeo-AY: RE Y a progressively rapid increase in sulfur reduction from 0 - 100˚C but at higher temperatures above 100˚C it was observed that the increase was relatively very gradual. The reductions observed for the Zeo-AY: RE Y and Zeo-HPC: RE Y at 150˚C were 49% and 60% respectively.

Figures 4.60 and 4.61 show the FTIR spectra of the Zeo-AY: RE Y used for the microwave assisted desulfurization of model petroleum oil at variable times and temperatures respectively: before and after the reactions. It would be observed that the FTIR spectra of the zeolite before and after the reactions were similar except that the used zeolite showed presence of strange bands at wavelength range of 1350 – 1450 cm^{-1} and 2860 – 2930 cm^{-1} for both the variable temperatures and variable times curves. These band ranges are due to C=S functional group (Reusch, 2013; Song *et al*., 2013; Uddin, 2012); they are indication to adsorption of sulfur.

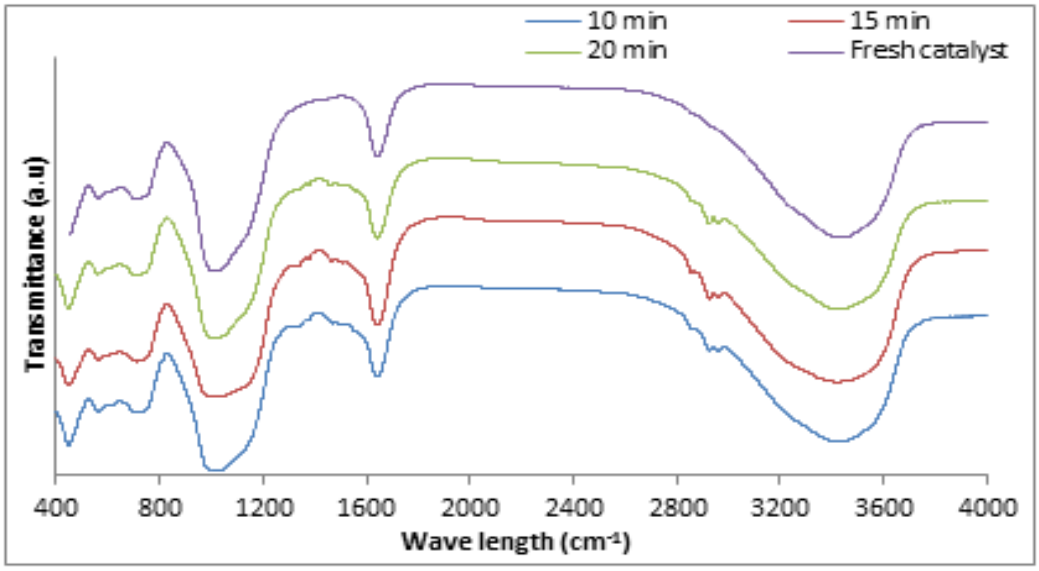


Figure 4.60: FTIR spectra of fresh and used Zeo-AY: RE Y used as catalyst for microwave assisted desulfurization of model petroleum oil at variable times

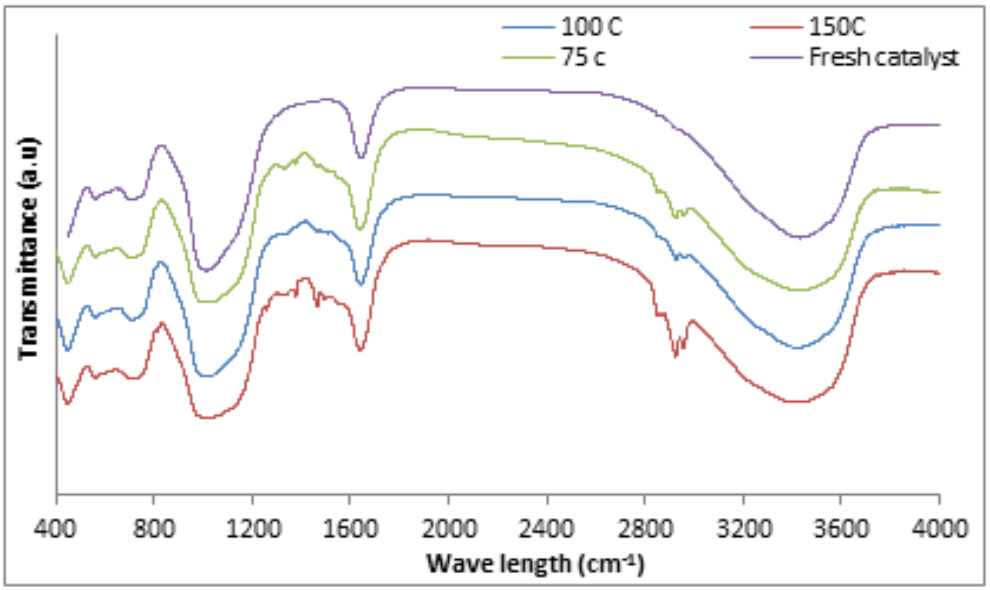


Figure 4.61: FTIR spectra of fresh and used Zeo-AY: RE Y used as catalyst for microwave assisted desulfurization of model petroleum oil at variable temperatures

Similarly Figures 4.62 and 4.63 show the FTIR spectra of the Zeo-HPC: RE Y used for the microwave assisted desulfurization of model petroleum oil at variable times and temperatures respectively: before and after the reactions.

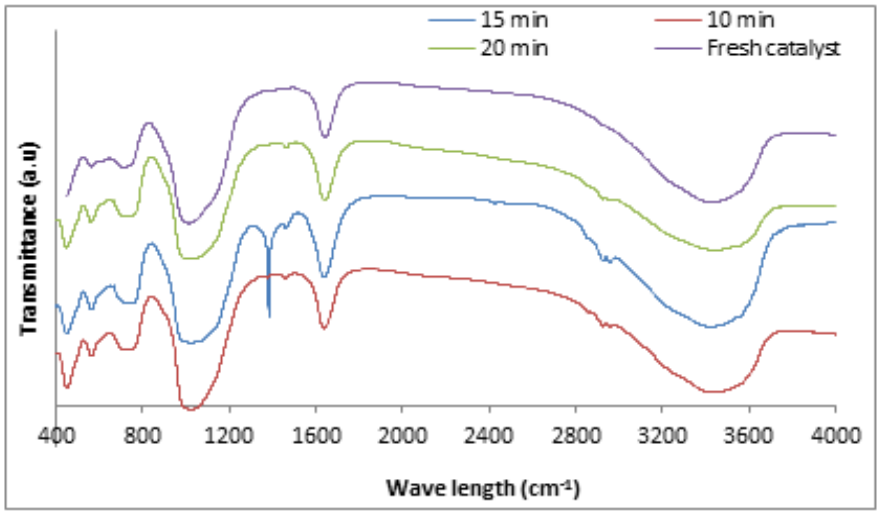


Figure 4.62: FTIR spectra of fresh and used Zeo-HPC: RE Y used as catalyst for microwave assisted desulfurization of model petroleum oil at variable times

It would be observed that the Zeo-HPC: RE Y showed the same behaviour as was observed in the Zeo-AY: RE Y. Hence, both zeolites had shown potent effect in desulfurization of the model petroleum oil, the FTIR analysis of the catalyst before and after the reactions suggested that the mechanism of desulfurization observed by the zeolites was adsorptive desulfurization. Although it could be observed that the spectra for the 15 min and 150˚C in Figures 4.62 and 4.63 respectively showed a strange band at 1386 cm^{-1}, this was due to C=O functional group (Reusch, 2013; Uddin, 2012). The presence of C=O in these samples was likely because oxygen or water vapour was present in the FTIR system during these scans as a result of inadequate purging of the system before the scans.

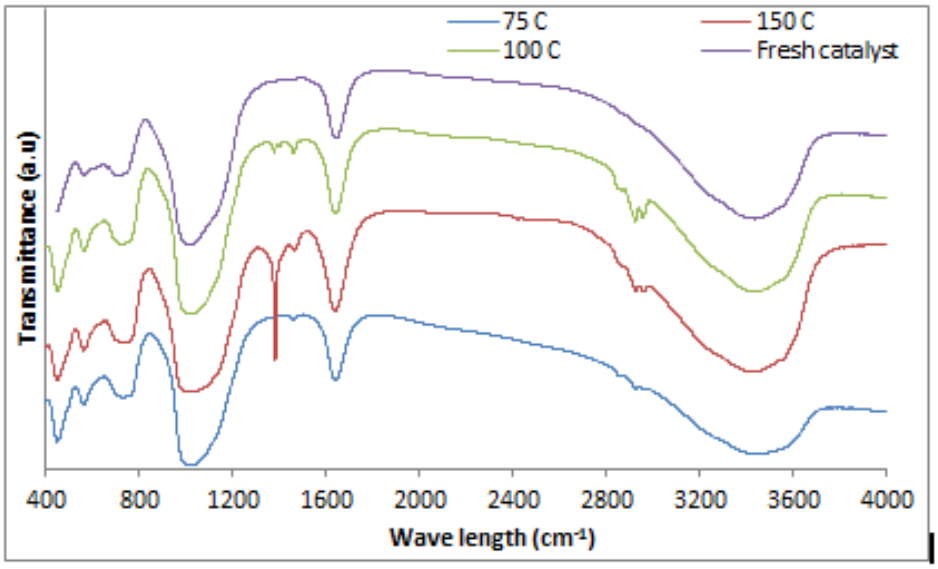


Figure 4.63: FTIR spectra of fresh and used Zeo-HPC: RE Y used as catalyst for microwave assisted desulfurization of model petroleum oil at variable temperatures

4.5.6 Characteristics of the formulated catalysts

4.5.6.1 XRD patterns of the formulated catalysts

Figures 4.64 – 4.65 show the XRD patterns of the various zeolite Y and zeolite Y + ZSM5 composite catalysts formulated as described in Section 3.2.5. Figure 4.80 shows the XRD pattern

of the zeolite Y catalyst formulate from zeolite RE Y prepared from clay. It could be observed that the intensity of the characteristic peak of zeolite Y of the catalyst was 622 counts, the reduction in the intensity was due to the incorporation of the matrix material onto the zeolite, therefore suppressing the concentration of the zeolite Y. Figure 4.81 shows the XRD pattern of the zeolite Y catalyst formulated from zeolite RE Y prepared from HPC. It could be observed that the intensity of the characteristic peak of zeolite Y of the catalyst was 1600 counts, the reduction in the intensity was due to the incorporation of the matrix material onto the zeolite, therefore suppressing the concentration of the zeolite Y. Figure 4.82 shows the XRD pattern of the zeolite Y +ZSM5 catalyst composite formulate from ZSM5 and zeolite RE Y prepared from clay. It could be observed that the intensity of the characteristic peak of the catalyst was 513 counts, the reduction in the intensity was due to the incorporation of ZSM5 and the matrix material onto the zeolites, therefore suppressing the concentration of the zeolite Y. Other new peaks at Bragg‟s angle of 7.9 and 8.7° could be observed in the XRD pattern of the composite catalyst, these were due to the characteristic peaks of ZSM5 (Jiang *et al*., 2014).

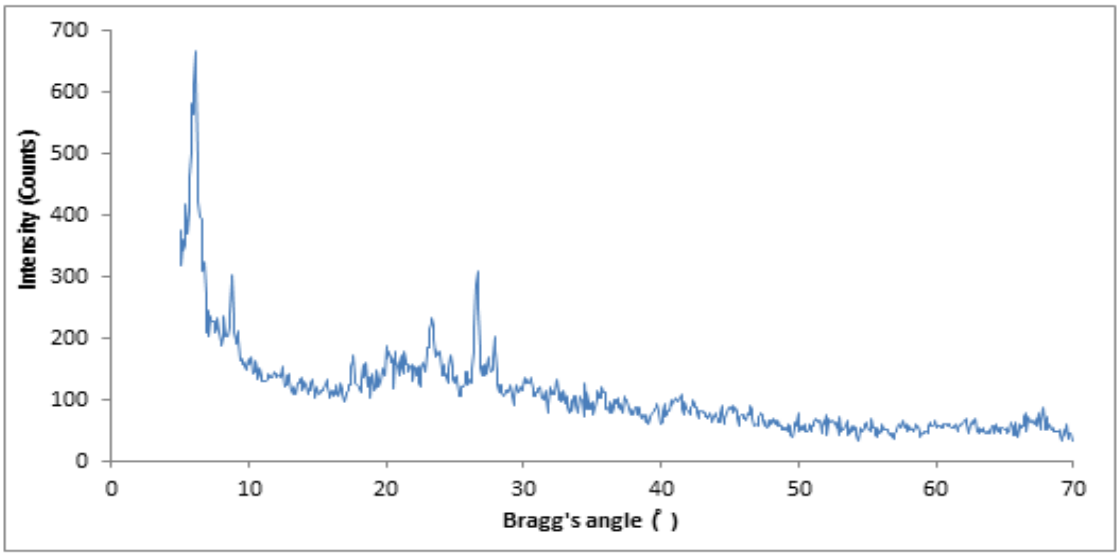


Figure 4.64: XRD pattern of Catalyst Y; using Zeo-BY: RE Y plus metakaolin and alumina support

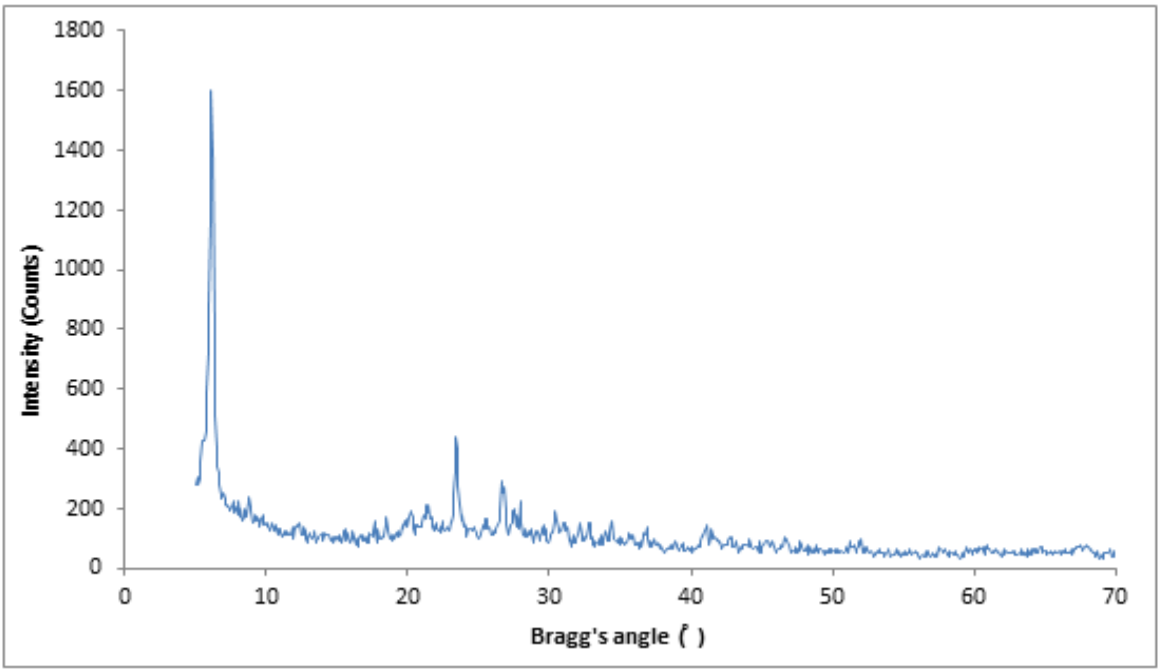


Figure 4.65: XRD pattern of Catalyst Y; using Zeo-HPC: RE Y plus metakaolin and alumina support

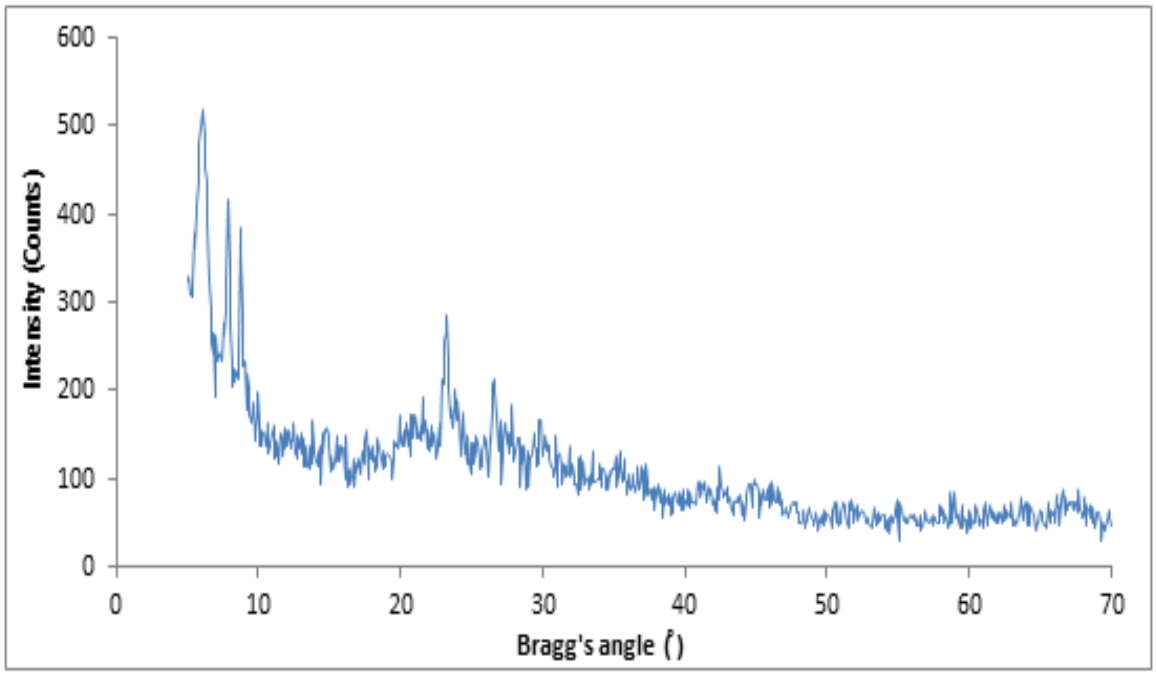


Figure 4.66: XRD pattern of Catalyst Y + ZSM; using Zeo-BY: RE Y+ ZSM5 plus metakaolin and alumina support

4.5.6.2 BET properties of the formulated catalysts

Table 4.19 presents the BET results of the surface area and pore sizes determination of the various catalysts prepared and the commercial zeolite Y catalyst. It could be observed that the specific surface areas of the Zeo-AY: Cat. Y, Zeo-BY: Cat. Y, Zeo- HPC: Cat. Y and Commercial Cat. Y were 193.4, 160.4, 280.7 and 306.0 m^2/g respectively. Each of the formulated catalysts had high surface compared to the surface area reported for zeolite Y catalyst by Ng *et al*., (2006); Ding *et al*., (2007); Li *et al*., (2007) although the commercial catalyst Y had even higher surface area value which was 58%, 90% and 9% higher than than Zeo-AY: Cat. Y, Zeo-BY: Cat. Y, Zeo- HPC respectively. Similarly the pore volume followed similar pattern while the pore diameter were relatively similar, hence, each of the catalysts remained microporous. It would be observed the incorporation of ZSM5 in the zeolite Y for the composite catalyst improved the surface area and the pore volume of the zeolite each by around 4% while the pore diameter remained relatively the same.

Table 4.19: BET surface area and pore sizes of the various catalyst Y zeolite formulated

Sample	Specific Surface Area (m^2/g)	Pore Volume (cm^3/g)	Pore Diameter (Å)
Zeo-AY: Catalyst Y	193.4	0.06483	13.41
Zeo-BY: Catalyst Y	160.4	0.0558	ND
Zeo- HPC: Catalyst Y	280.7	0.0963	13.72
Zeo-AY: Cat. Y + ZSM5	201.8	0.06798	13.47
Literature Value (Jia *et al*., 2013)	192.5	0.331	NA
Commercial Catalyst Y	306.0	0.1057	13.81

ND: Not determined

NA: Not available

More zeolite Y and zeolite Y + ZSM5 catalysts were formulated maintaining the content of alumina and silica sol as 20% each as described in Section 3.2.5 but metakaolin and zeolite contents were varied one at the expense of the other. Table 4.20 presents the BET results of the surface area and pore sizes determination of the various catalysts prepared using variable zeolite content. The specific surface areas of the Zeo-AY: Cat. Y containing 30%, 40% and 50% zeolite Y were 193.4, 202.7 and 223 m^2/g respectively. It could be observed that the surface area of the 30% zeolite content sample was very close to the literature value (Jia *et al*., 2013); the catalyst formation in the sited literature used 31 wt% zeolite content in the formulation. It would be observed that the surface area of the catalyst increased by 5% and 15% when the zeolite content became 40% and 50% respectively. The pore volume also increased by 9% and 21% respectively. The specific surface areas of the Zeo-AY: Cat. Y containing 30, and 50 zeolite Y + ZSM5 were 201.8 and 222 m^2/g respectively. It could be observed that the surface area of the 30% zeolite content sample increased by 10% when the zeolite content became 50%. It could be observed that the more the percentage zeolite content, the higher the surface area of the catalyst.

Table 4.20: BET results of the various catalyst Y formulated using variable zeolite content

Sample	Specific Surface Area (m^2/g)	Pore Volume (cm^3/g)	Pore Diameter (Å)
30% Zeo-AY: Cat. Y	193.4	0.06483	13.41
40% Zeo-AY: Cat. Y	202.7	0.0706	ND
50% Zeo-AY: Cat. Y	223	0.0786	ND
30% Zeo-AY: Cat. Y + ZSM5	201.8	0.06798	13.47
50% Zeo-AY: Cat. Y + ZSM5	222	0.07902	ND

Hence, by extension it implies the less the metakaolin content of the zeolite formulation the higher the surface area of the catalyst. This simply shows that the zeolite has much higher surface area than the metakaolin.

4.5.6.3 FTIR spectra of formulated catalysts

Figures 4.67 – 4.70 show the FTIR spectra of the various synthesized zeolite NaY, zeoite RE Y, catalyst Y zeolite and catalyst Y zeolite + ZSM5 respectively. It could be observed that the FTIR spectra of samples in each of the figures were similar to each other. It could be observed that the FTIR spectra of the zeolite NaY and RE Y possessed IR transmittance bands at wavelength of around 480, 550, 600, 715, 790, 1025, 1660 and 3500 cm^{-1}. Prior studies reported that the characteristic FTIR bands for zeolitic lattice are in the wavelength range of 460–1200 cm^{-1} (Modi *et al*., 2012) and the bands in these range of wavelength indicate the crystallinity of the material (Shen *et al*., 2014). Particularly the characteristic FTIR bands for zeolite Y are located around 1025, 790 and 715 cm^{-1} (Zhang *et al*., 2008). The band at 480 cm^{-1} was attributed to Si–O tetrahedral deformation. The band at 550 cm^{-1} was attributed to Si–O–Al octahedral stretching. The band at 715 cm^{-1} was attributed to Si–O–Al in-plane bending. The band at 790 cm^{-1} was attributed to Si–O–Al out-of-plane bending. The broad band stretching between 950 – 1020 cm^{-1} was attributed to Al–OH vibration and Si–O tetrahedral stretching vibration (in plane). The band at 1660 cm^{-1} was attributed to vibration of water molecule. The band at 3500 cm^{-1} was attributed to O–H bond stretching vibration (Percival *et al*., 1974; Kloprogge *et al*., 1999; Steudel *et al*.,2009; Benincasa *et al*., 2001; 2009; Pal *et al*., 2013). It would be observed that the band at 480, 550, 600 and 715 cm^{-1} were not well pronounced in the catalyst Y zeolite and catalyst Y zeolite + ZSM5 spectra this was due to the relative suppression of the crystallinity of the

catalysts due to incorporation of support material. It would be noted that some strange shoulder bands were present in the commercial zeolite HY at wavelength of 620, 830 and 840 cm^{-1} and in the commercial catalyst Y at wavelength of 970, 1410, 3670 and 3700 cm^{-1}; these were likely due to impurities present in the materials. It is also worth noting that some strange shoulder bands were present in the Zeo-BY: catalyst Y zeolite at wavelength of 2920 and 2970 cm^{-1}; this was likely due to impurities resulting from the material handling, the impurity did not result from the synthesis of the material as these bands were not present in the FTIR spectra of the Zeo-BY: NaY and RE Y shown in Figures 4.67 and 4.68 respectively.

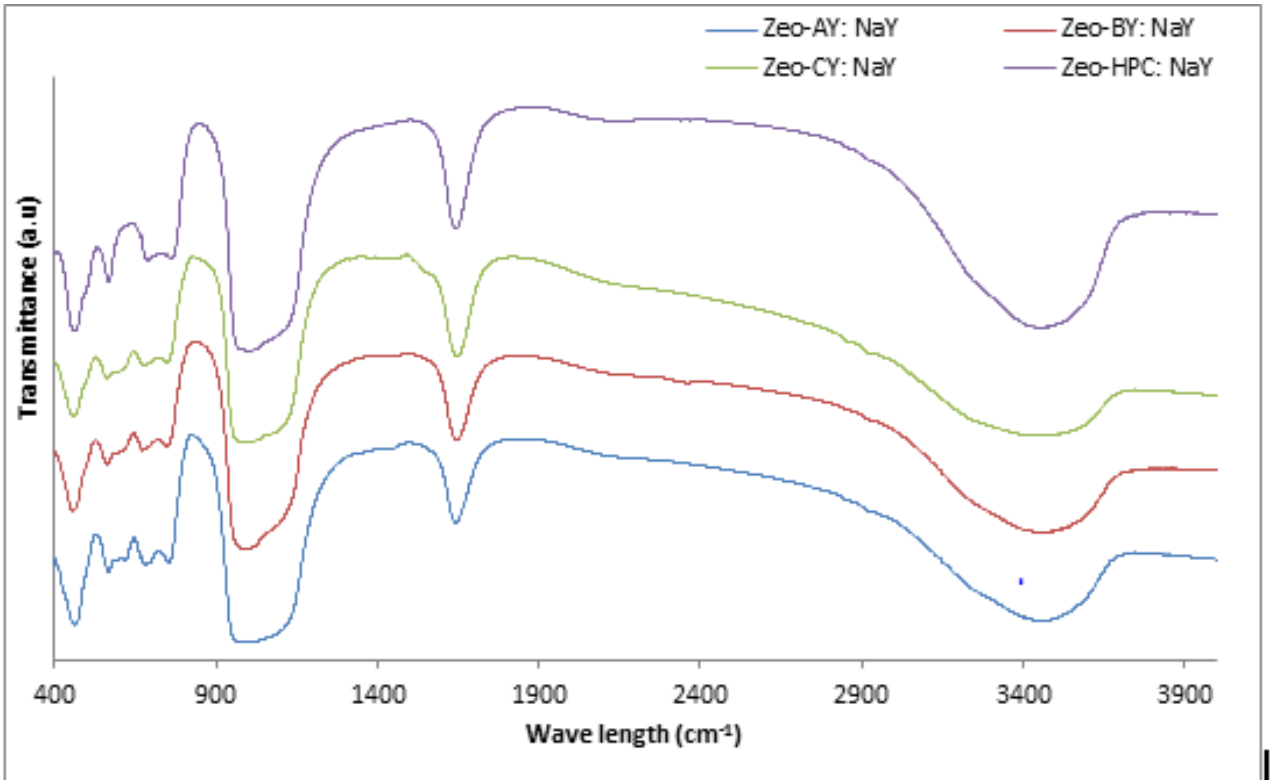


Figure 4.67: FTIR spectra of the various synthesized zeolite NaY

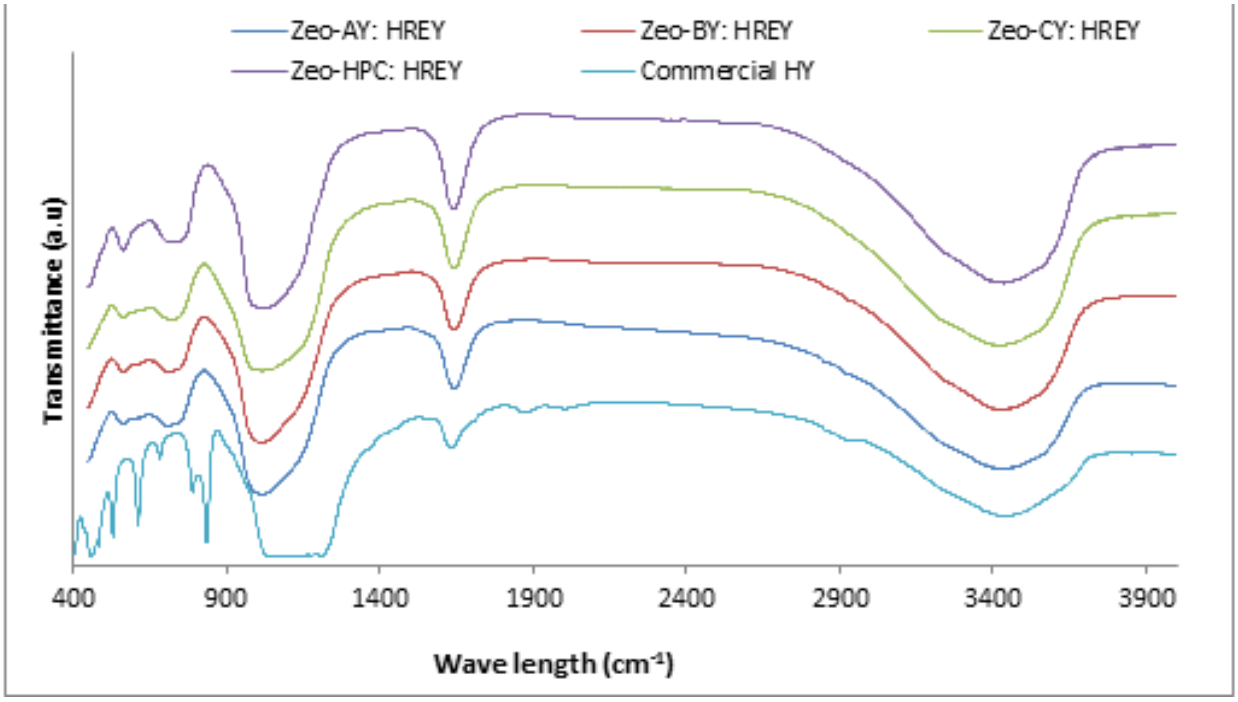


Figure 4.68: FTIR spectra of commercial and the various synthesized zeolite HY

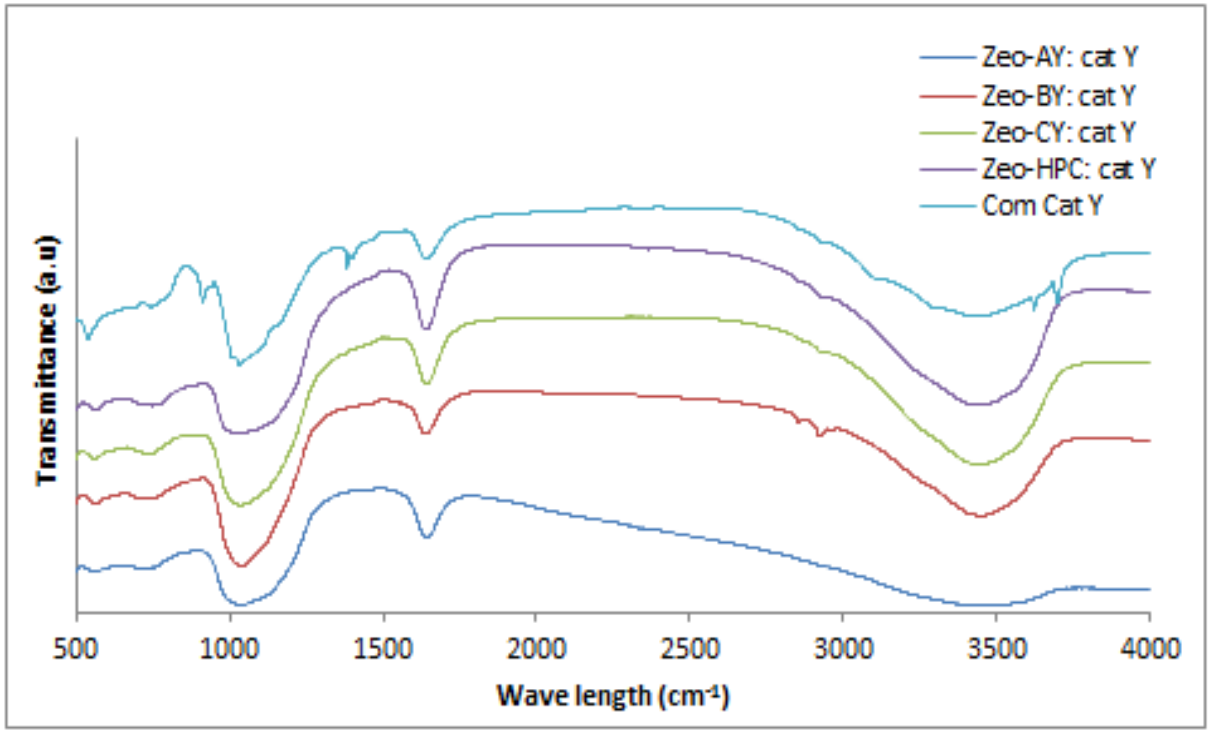


Figure 4.69: FTIR spectra of commercial and the various synthesized zeolite Y catalysts

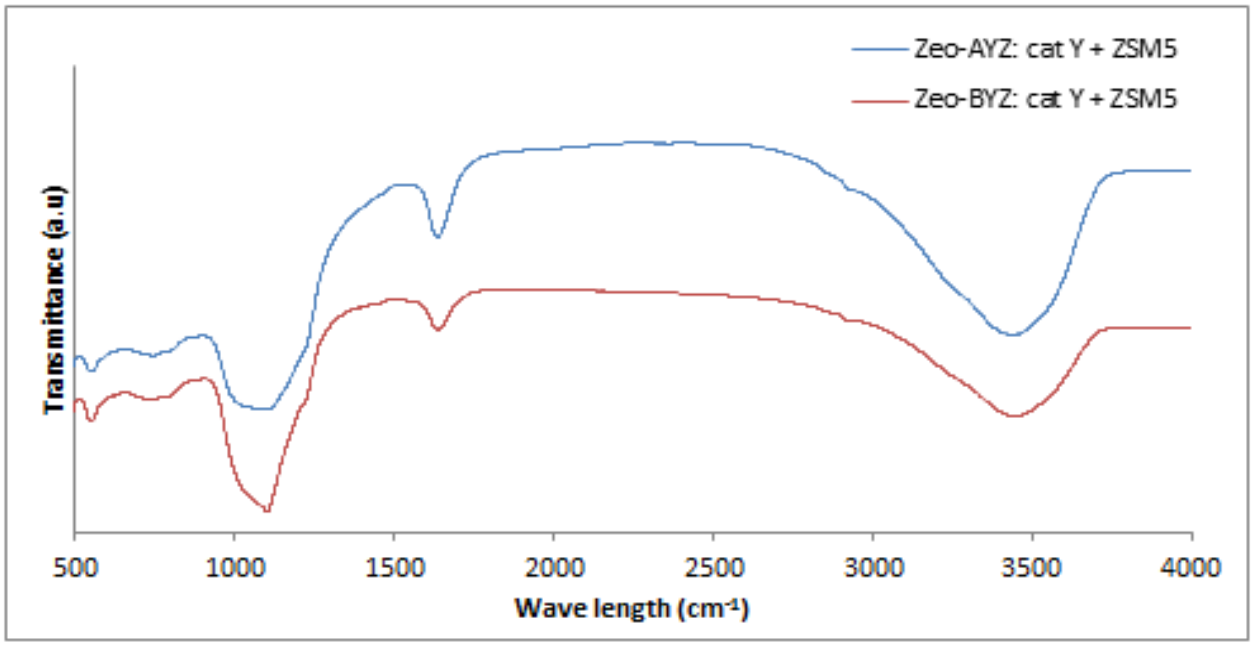


Figure 4.70: FTIR spectra of synthesized zeolite Y + ZSM5 catalysts

4.5.6.4 SEM micrographs of the formulated catalysts

Plates XXIX – XXXII show the SEM images of the various formulated zeolite catalyst Y scanned at variable magnifications. Plates XXIX A, B, C and D show the SEM micrographs of the Zeo-AY: catalyst Y scanned at magnifications of 8000, 20000, 45000 and 80000 respectively. It could be observed that each of the micrographs showed heterogeneous morphology depicting the active ingredients anchored on the support matrix. Two sizes of particles could be noted; one bigger and the other smaller. Plates XXX A, B, and C show the SEM micrographs of the Zeo-BY: catalyst Y scanned at magnifications of 14000, 23000, and 37000 respectively. Similarly heterogeneous morphology of variable sizes of agglomerated particles could be noted. Two sizes of particles could be distinguished; the bigger ones possessing irregular shape were attributed to the metakaolin and the alumina particles, average particle sizes of metakaolin and alumina were each estimated as 2.5 µm in Sections 4.1.4 and

4.2.4 respectively. Plates XXXI A, B, C and D show the SEM micrographs of the Zeo-CY: catalyst Y scanned at magnifications of 8000, 15000, 30000 and 80000 respectively. Plates XXXII A, B, C and D show the SEM micrographs of the Zeo-HPC: catalyst Y scanned at magnifications of 8000, 10000, 15000 and 20000 respectively. Each of the micrographs showed heterogeneous morphology of variable sizes of agglomerated particles. The differences in the particle sizes were more obvious in these images, sizes of particles could be distinguished; the bigger ones possessing irregular shape were attributed to the metakaolin and the alumina particles each having average particle size of 2.5 µm as discussed earlier. It could be noted that the smaller particles possessed an euhedral morphology having regularly shaped boundaries, these particles were attributed to be the zeolite Y particles, their average particle size was estimated as 200 nm in Section 4.5.5.6. Plates XXXIII A, B, C and D show the SEM micrographs of the commercial catalyst Y scanned at magnifications of 100, 10000, 27000 and 45000 respectively. It would be observed that at the least magnification the micrograph showed spherical particle morphology, this suggested that the catalyst was likely formulated using spray drying method; Sanden, (2003) reported that catalysts formulated by this method possess spherical shape. However, at the higher magnifications the porous morphology of the catalyst particles was obvious. Plates XXXIV – XXXVII show the SEM images of the various composite catalyst Y zeolite + ZSM5 at various magnifications. Like in the catalyst Y zeolite micrographs, each of the micrographs of the composite catalyst Y zeolite + ZSM5 showed heterogeneous morphology of variable sizes of agglomerated particles. However in addition to the two distinct sizes of particles observed in the catalyst Y an additional intermediate sized particles could be observed in the composite catalyst Y zeolite + ZSM5. The intermediate sized particles possessed

a spherical euhedral morphology and the average particle size was estimated as 1 µm, these particles were likely the ZSM5 added to the zeolite Y catalyst blend.

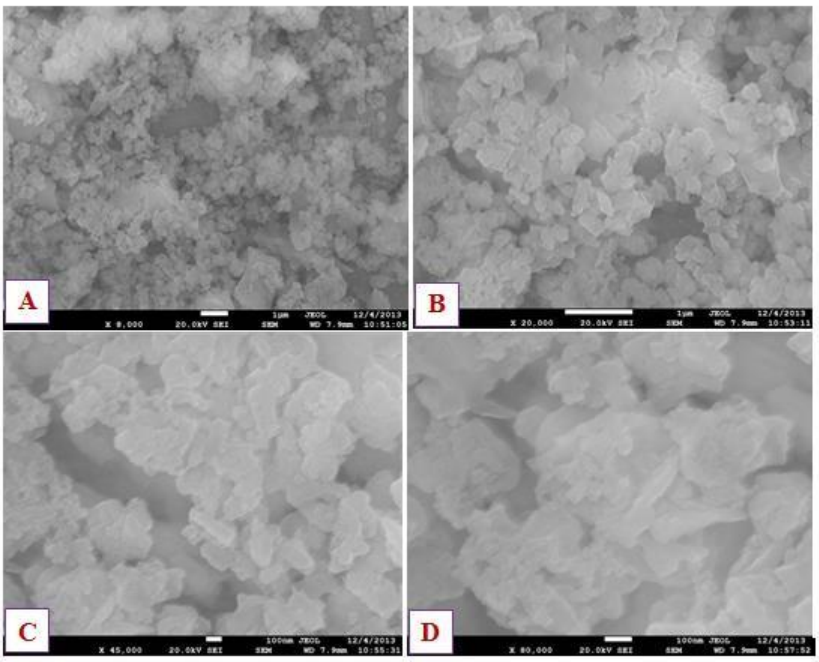


Plate XXIX: SEM images of Zeo-AY: catalyst Y at magnifications of (A) 8000 (B) 20000 (C) 45000 (D) 80000

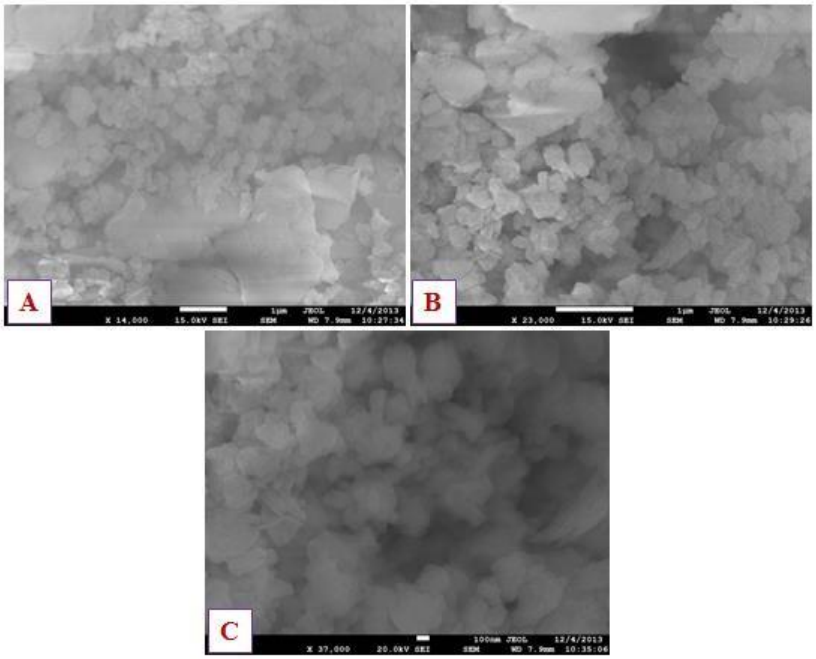


Plate XXX: SEM images of Zeo-BY: catalyst Y at magnifications of (A) 14000 (B) 23000 (C) 37000

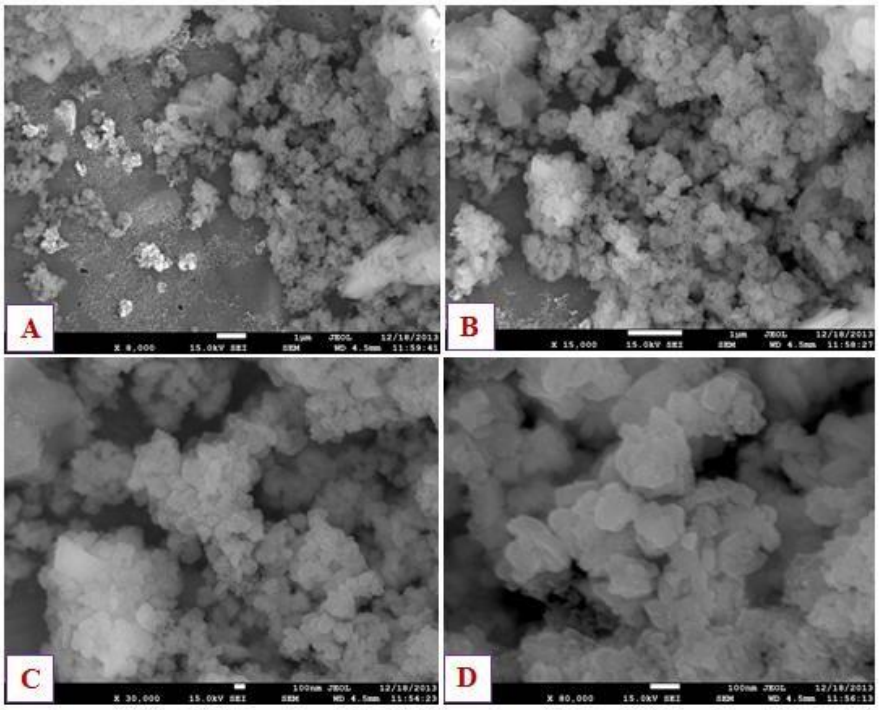


Plate XXXI: SEM images of Zeo-CY: catalyst Y at magnifications of (A) 8000 (B) 15000 (C) 30000 (D) 80000

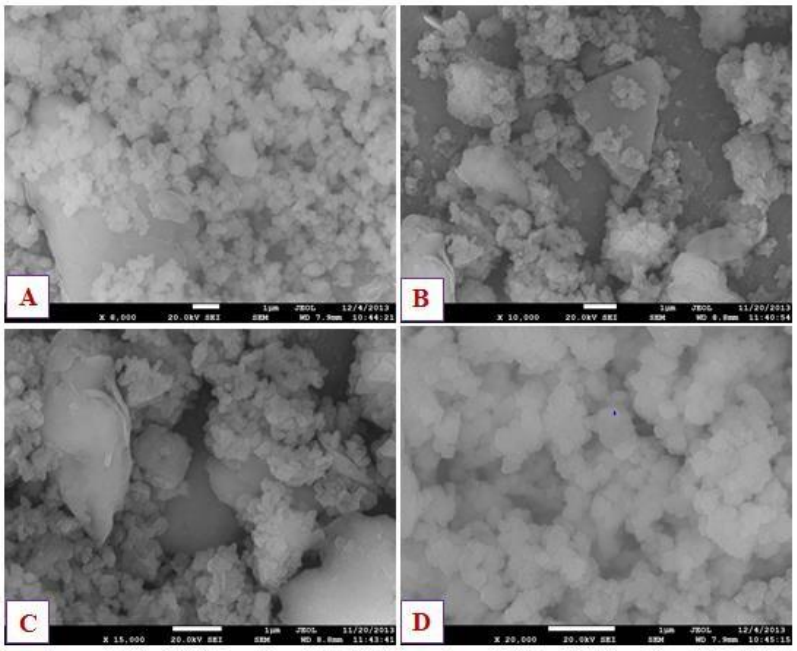


Plate XXXII: SEM images of Zeo-HPC: catalyst Y at magnifications of (A) 8000 (B) 10000 (C) 15000 (D) 20000

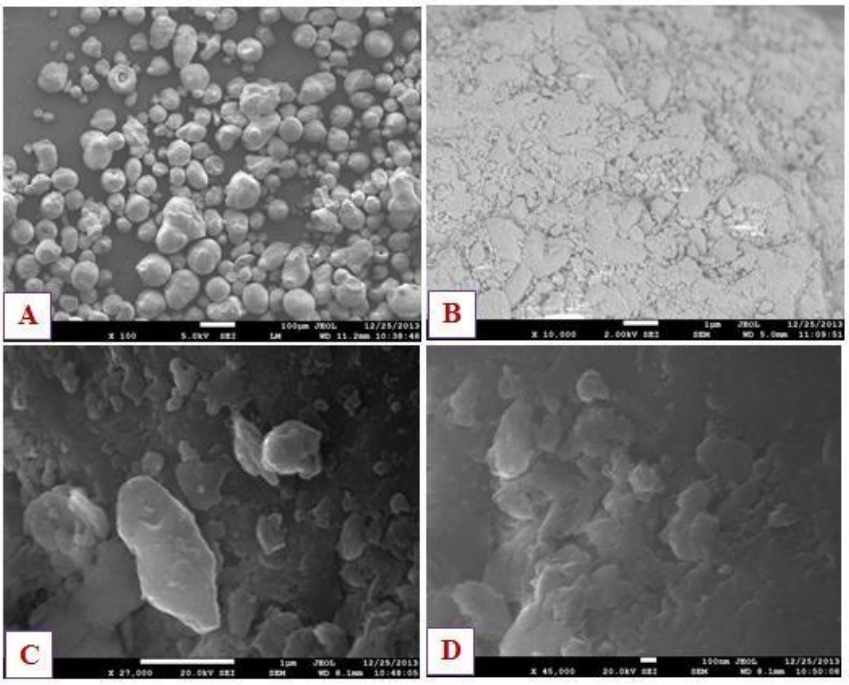


Plate XXXIII: SEM images of commercial catalyst Y at magnifications of (A) 100 (B) 10000 (C) 27000 (D) 45000

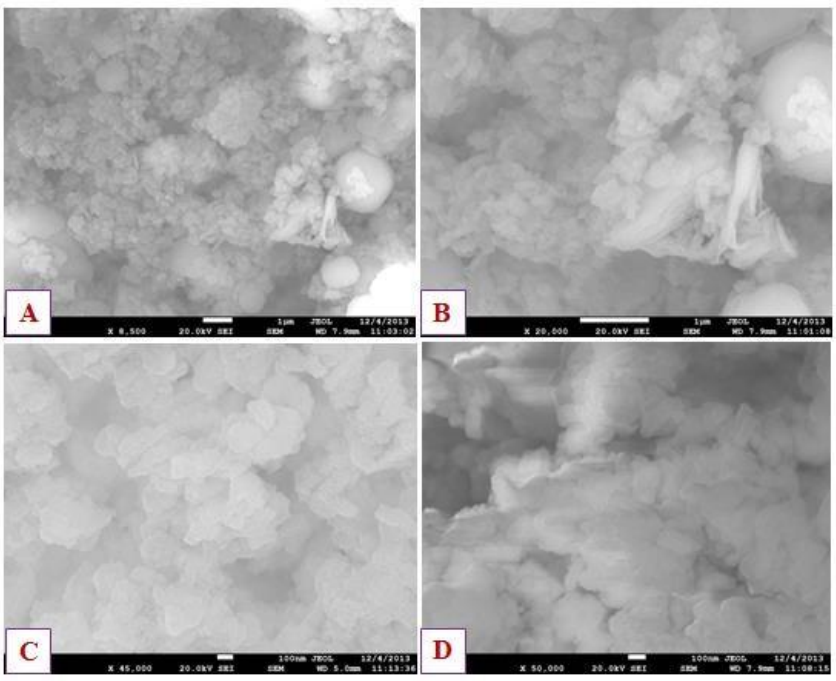


Plate XXXIV: SEM images of Zeo-AY: catalyst Y + ZSM5 at magnifications of (A) 8500 (B) 20000 (C) 45000 (D) 50000

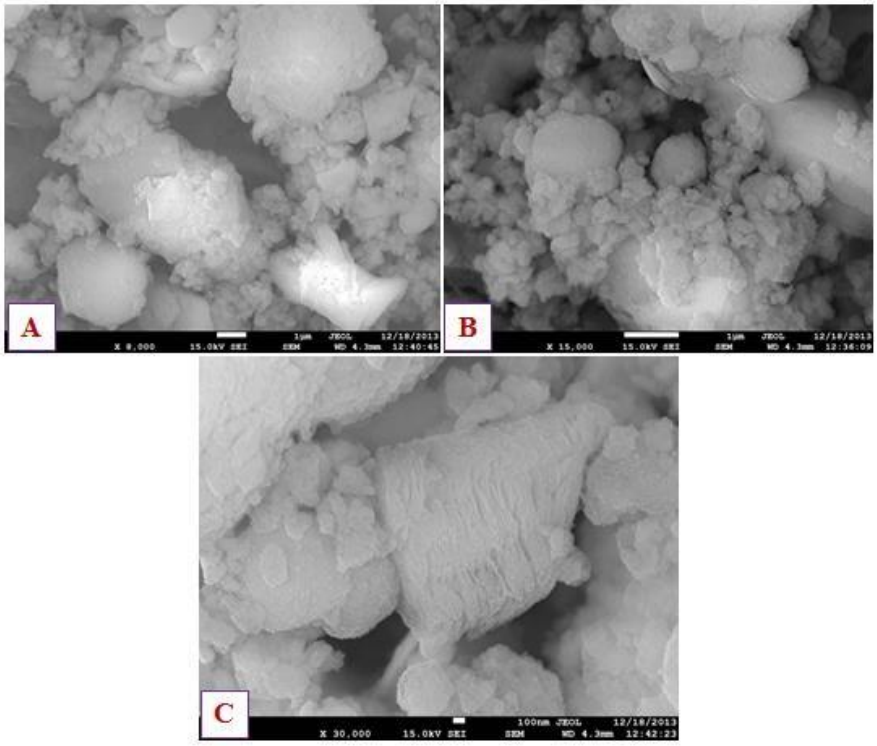


Plate XXXV: SEM images of Zeo-BY: catalyst Y + ZSM5 at magnifications of (A) 8500 (B) 15000 (C) 30000

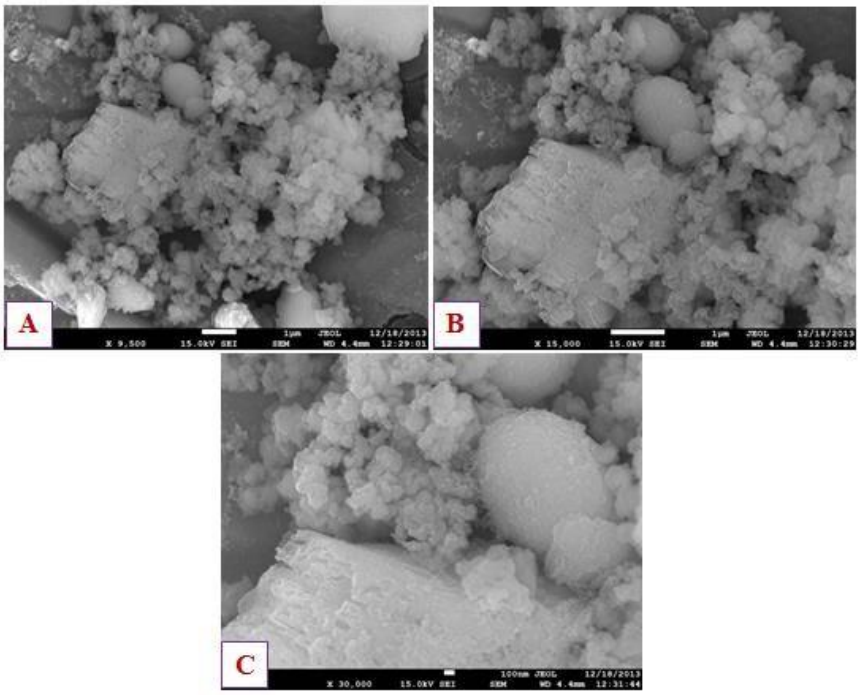


Plate XXXVI: SEM images of Zeo-CY: catalyst Y + ZSM5 at magnifications of (A) 9500 (B) 15000 (C) 30000

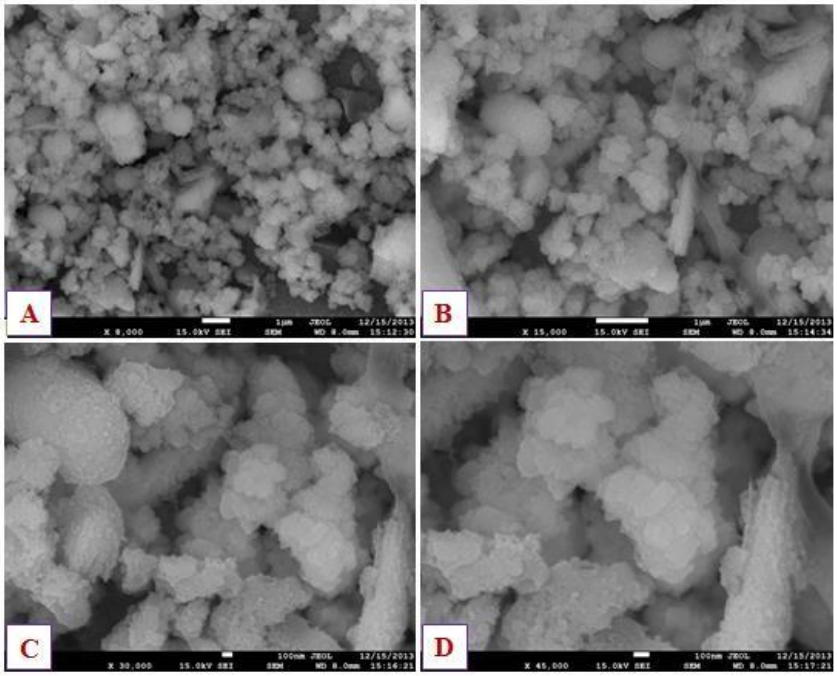


Plate XXXVII: SEM images of Zeo-HPC: catalyst Y + ZSM5 at magnifications of (A) 8400 (B) 15000 (C) 30000 (D) 45000

4.5.6.5 TEM images of the formulated catalysts

Plates XXXVIII A, B, C and D show the TEM images of the Zeo-AY: catalyst Y at magnifications of 100000, 200000, 300000 and 400000 respectively. At each magnification a clear heterogeneous crystal distributions having variable sizes could be observed. The small crystals possessed no definite shape, these crystals were likely the alumina crystals, the average crystal size was estimated as 10 nm in Section 4.2.5. A section of the bigger crystals was observed to possess definite shapes as could be seen from its clearly defined boundaries, this was likely the zeolite crystals, its average crystal size was estimated as 200 nm in Section 4.5.5.7. The other section of the bigger crystals was observed to possess no definite shapes this was likely the metakaolin unit particle, its average size was estimated as 150 nm in Section 4.1.5. Plates XXXIX A, B, C and D show the TEM images of the Zeo-AY: catalyst Y zeolite + ZSM5 at magnifications of 100000, 200000, 400000 and 600000 respectively.

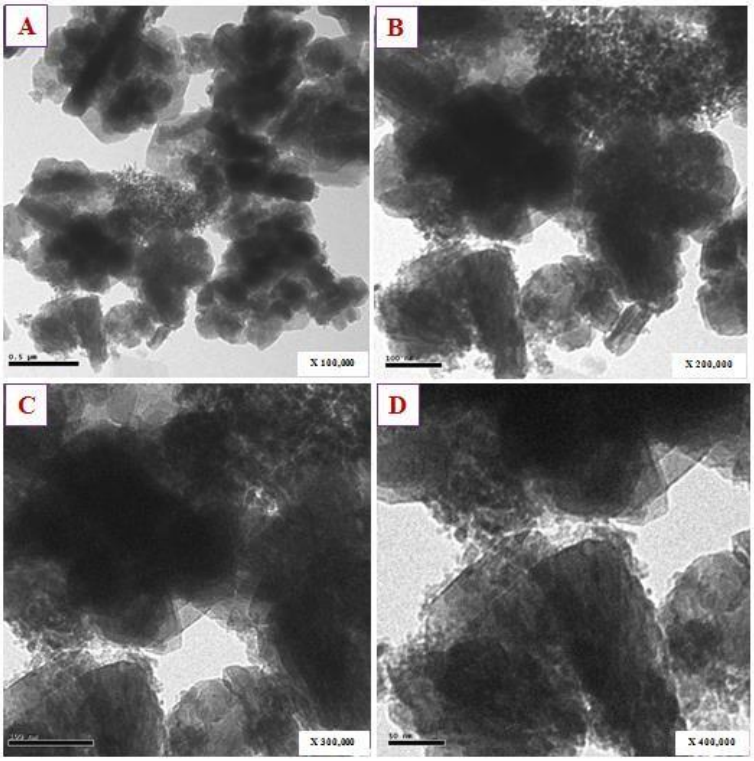


Plate XXXVIII: TEM images of Zeo-AY: catalyst Y at magnifications of (A) 100000 (B) 200000 (C) 300000 (D) 400000

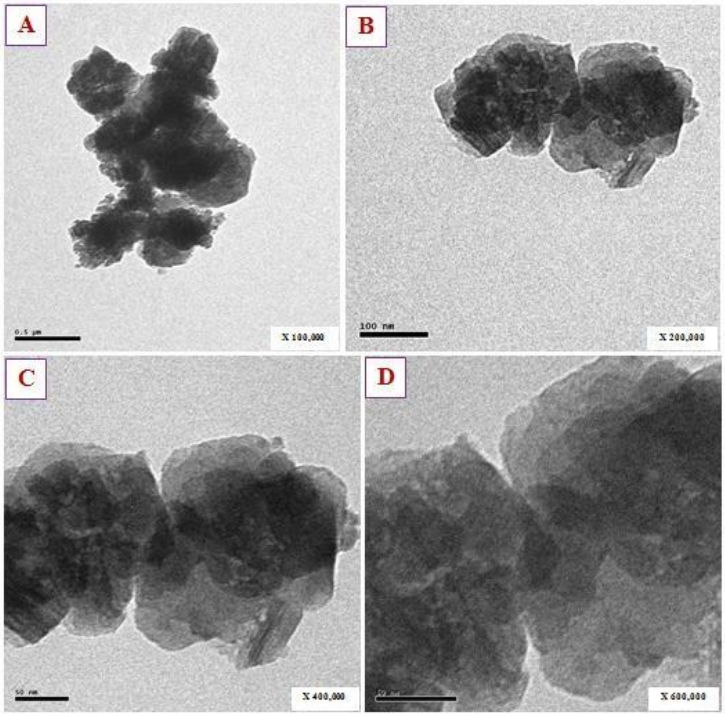


Plate XXXIX: TEM images of Zeo-AY: catalyst Y + ZSM5 at magnifications of (A) 100000 (B) 200000 (C) 400000 (D) 600000

At the least magnification a heterogeneous crystal distributions having variable sizes could be observed. However, irrespective of the magnification the images were not clear enough to reveal details of the shapes of the crystals due to overlapping effect of the crystals.

4.5.6.6 Thermogravimetric properties of the formulated catalysts

Figures 4.71 – 4.74 show the TGA/DTG thermal scan curves within temperature range of 30 - 750˚C for the various catalyst Y formulated. It could be observed that the total mass depletions of the formulated catalyst Y zeolite, as shown by the TGA curves were relatively the same for the various catalyst Y having average value of 10 wt%. The DTG curves of the various formulated catalyst Y zeolite suggested that the actual temperature responsible for the loss was about 120˚C, hence, the mass loss was likely due to effect of dehydration of the physically absorbed water molecules. Figure 4.75 shows the TGA/DTG thermal scan curves within temperature range of 30 - 750˚C for the commercial catalyst Y. It could be observed that the total mass depletion of the commercial catalyst Y zeolite, as shown by the TGA curves was about 18 wt%. The DTG curve suggested that the actual temperatures responsible for the loss were about 120 and 530˚C. The mass loss at 120˚C was likely due to effect of dehydration of the physically absorbed water molecules while that at 530˚C was likely due to deformation of the catalyst material due to the tendency of the catalyst losing its thermal stability at that temperature. Therefore, it could be observed that the commercial sample tends to lose its thermal stability at temperature higher than 530˚C. Figures 4.76 – 4.78 show the TGA/DTG thermal scan curves within temperature range of 30 - 750˚C for the various composite catalyst Y zeolite + ZSM5 formulated. It could be observed that the total mass depletions of the various composite catalysts Y zeolite + ZSM5, as shown by the TGA curves were relatively the same having average value

of 9 wt%. The DTG curves for the various composite catalysts Y zeolite + ZSM5 suggested that the actual temperature responsible for the loss was about 120˚C, hence, the mass loss was likely due to effect of dehydration of the physically absorbed water molecules. Hence, it would be noted that the incorporation of ZSM5 in the composite catalyst had not changed the thermal behaviour of the catalyst.

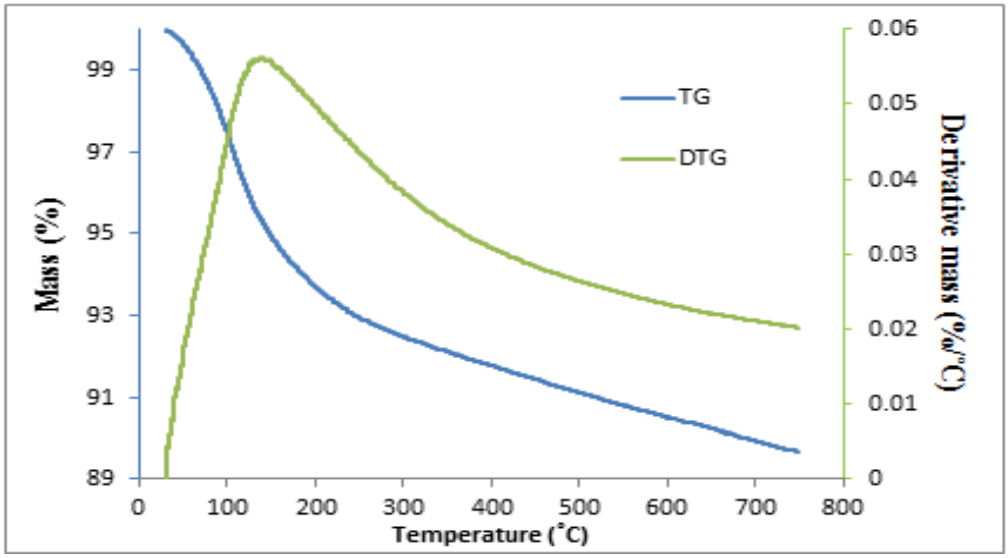


Figure 4.71: TGA/DTG curves of Zeo-AY: catalyst Y

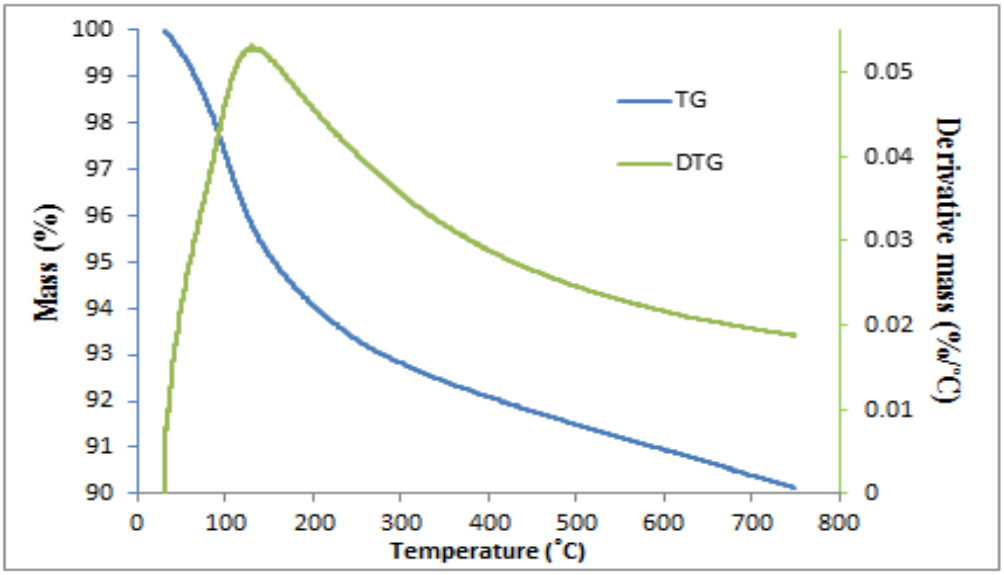


Figure 4.72: TGA/DTG curves of Zeo-BY: catalyst Y

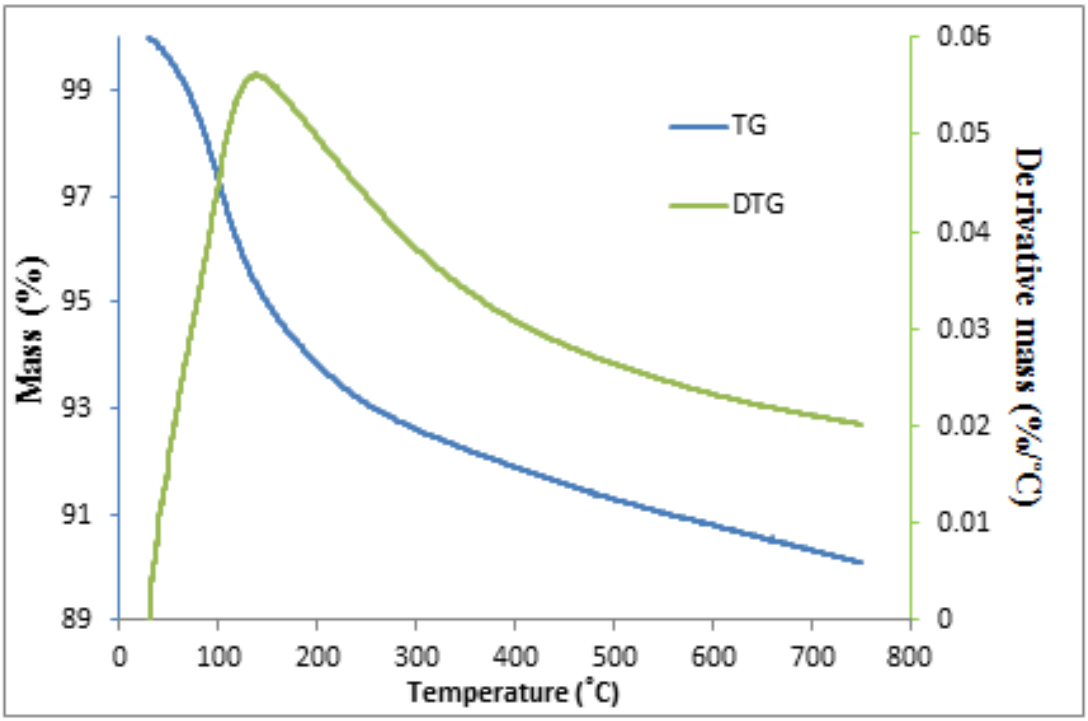


Figure 4.73: TGA/DTG curves of Zeo-CY: catalyst Y

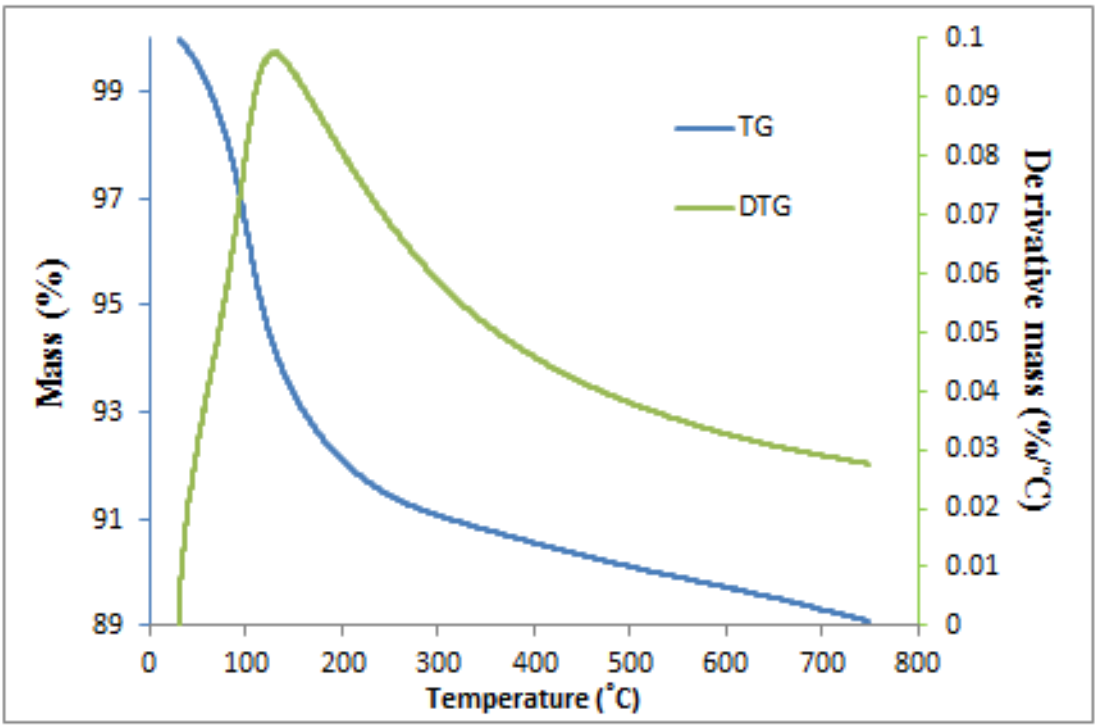


Figure 4.74: TGA/DTG curves of Zeo-HPC: catalyst Y

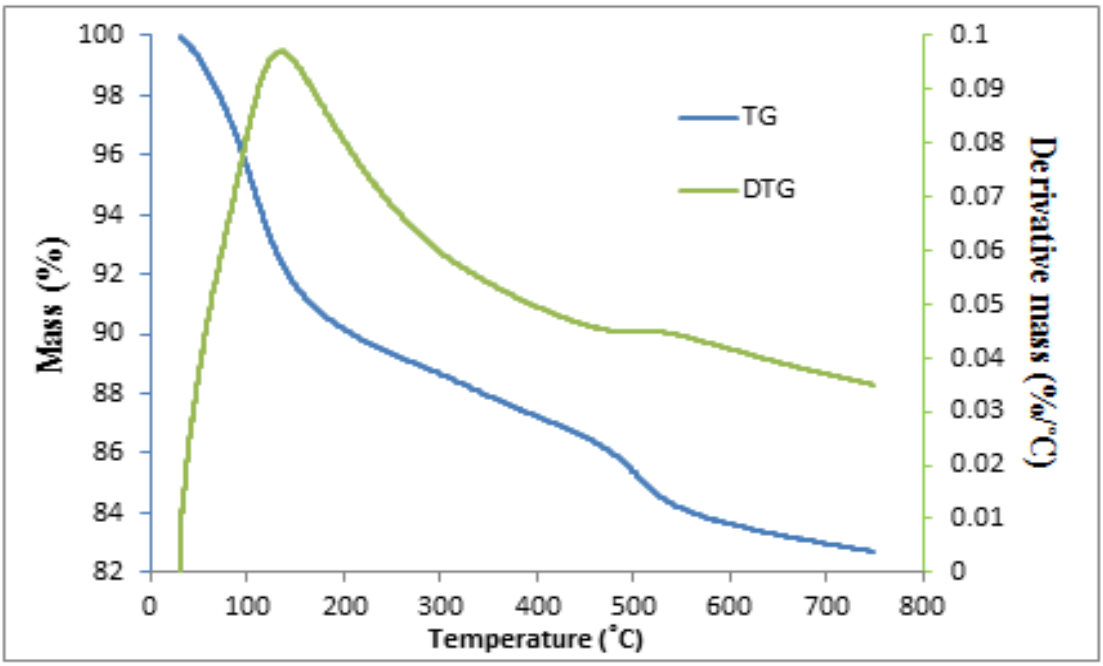


Figure 4.75: TGA/DTG curves of commercial catalyst Y

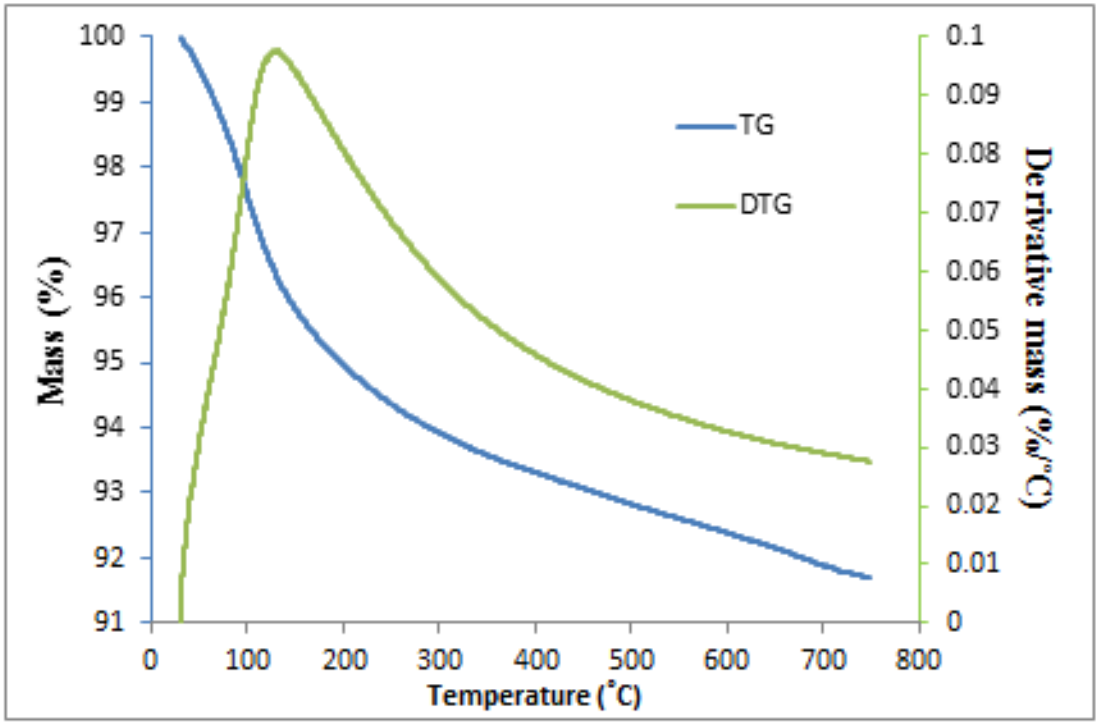


Figure 4.76: TGA/DTG curves of Zeo-BY: catalyst Y+ ZSM5

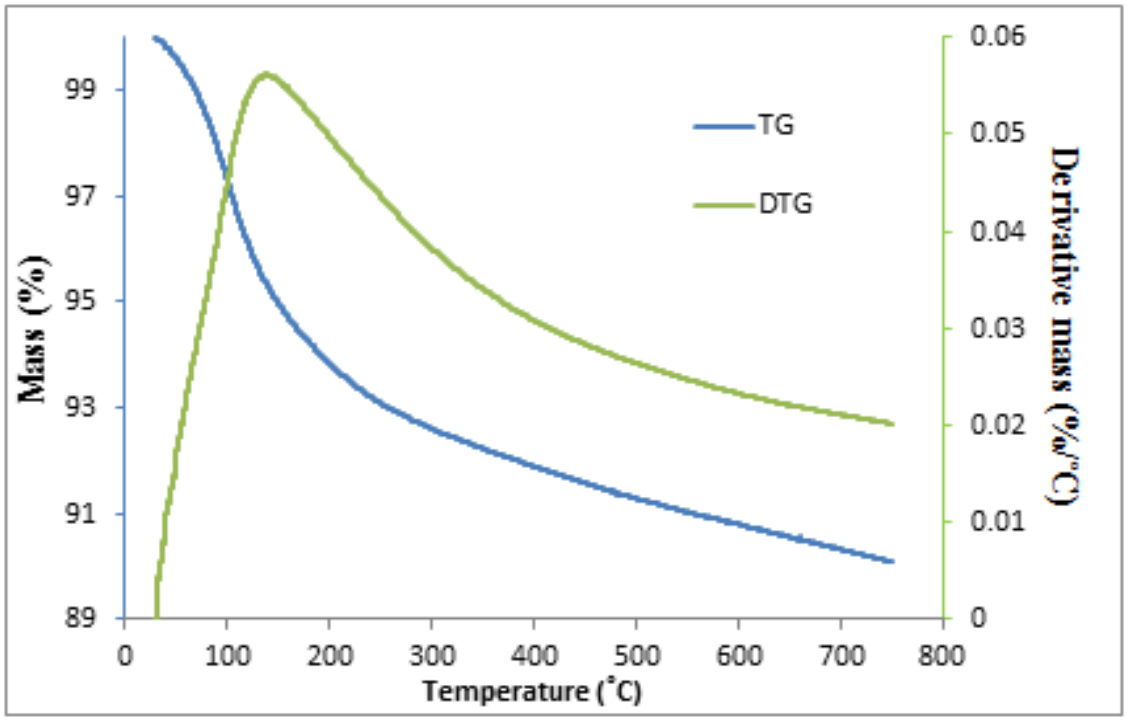


Figure 4.77: TGA/DTG curves of Zeo-CY: catalyst Y+ ZSM5

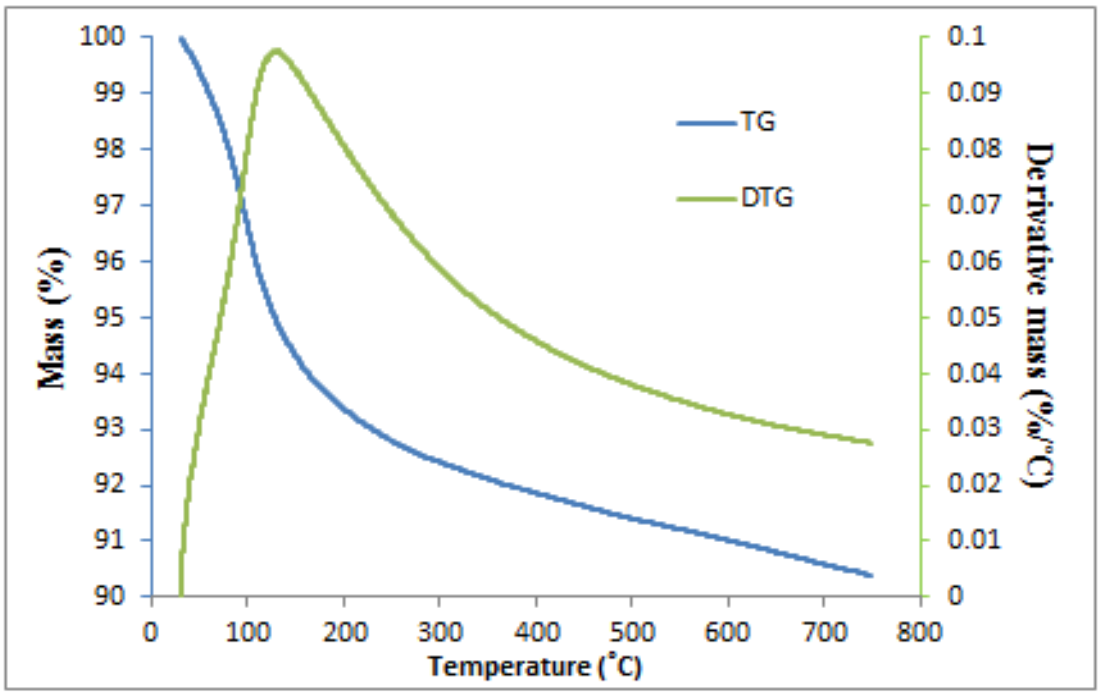


Figure 4.78: TGA/DTG curves of Zeo-HPC: catalyst Y+ ZSM5

Figures 4.79 and 4.80 show the isothermal scan of the various catalyst Y and the catalyst Y + ZSM5 respectively carried out at 750˚C for 1 hr. It would be observed that all the catalyst showed a relatively flat TGA curve implying no mass depletion during the isothermal scan, and this in extension indicate the thermal stability of the various catalyst at 750˚C for the duration of the heat soaking.

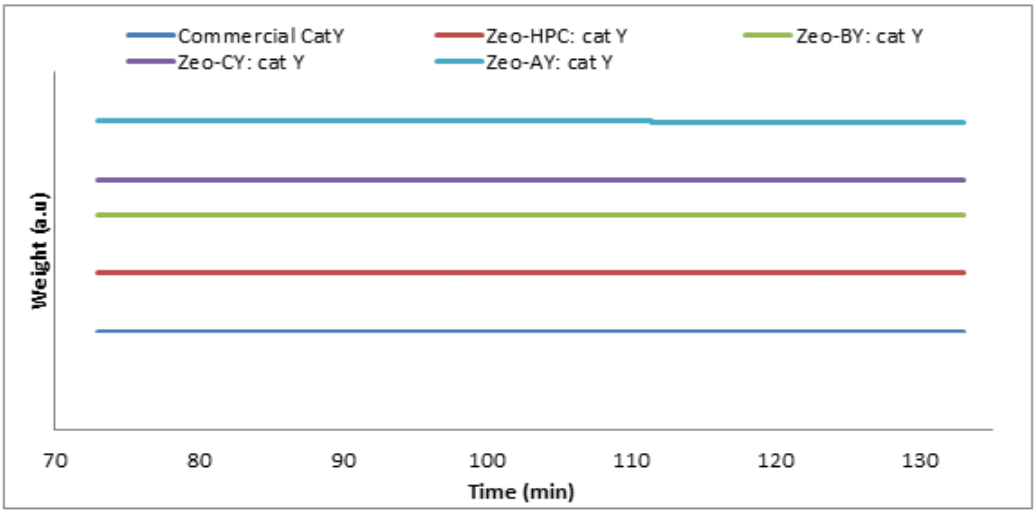


Figure 4.79: Isothermal scan of the various catalyst Y zeolite samples at 750˚C for 1 h

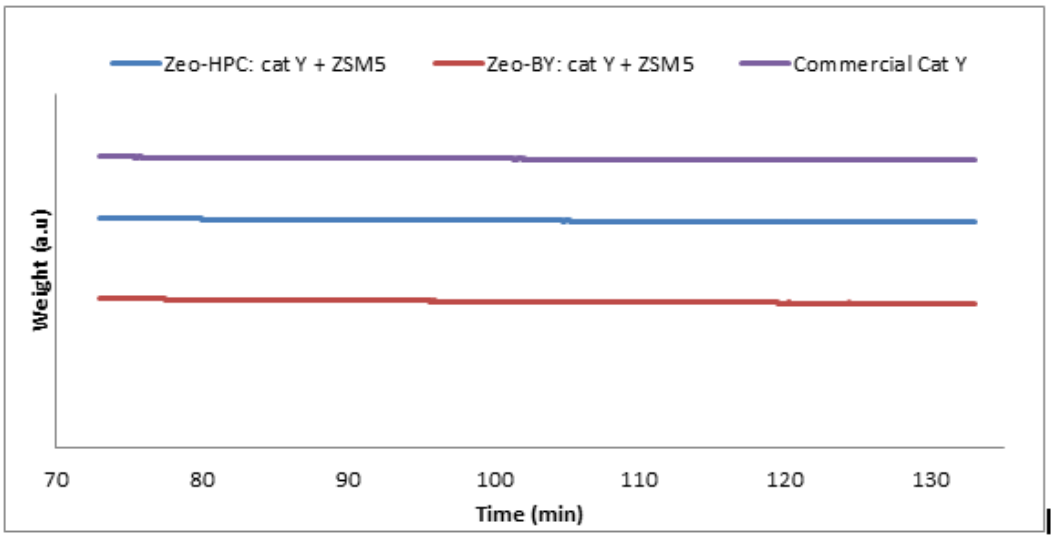


Figure 4.80: Isothermal scan of the various catalyst Y zeolite + ZSM5 blend at 750˚C for 1 h

4.5.7 Catalytic cracking of model petroleum oil using the formulated catalysts

The catalytic cracking performance of the formulated catalysts is presented in this sub-section.

4.5.7.1 Product distribution of the catalysts

Catalytic performance was tested by carrying out catalytic cracking using a fixed bed reactor, hexadecane as model heavy oil and reaction conditions of 300 - 550^0C, 2 bar, weight hourly space velocity (WHSV); 3 h^{-1}, N_2 gas flow; 50 l/hr. Figures 4.81 – 4.86 show the product distribution charts of the various formulated catalysts and the commercial catalyst at variable reaction temperatures. Figure 4.81 shows the bar chart of the product distribution of the various catalyst Y at reaction condition of 400˚C and keeping all other conditions unchanged, it could be observed that the commercial catalyst Y had relatively low products yield and relatively high unconverted feed. The gasoline and gaseous products yields of the commercial catalyst were 3.77% and 8.9% respectively. The unconverted feed was 86.2%. The gasoline yields of the other zeolite Y catalysts were 17.3%, 9.71%, 16.1% and 21.37% for the Zeo-AY, Zeo-BY, Zeo-CY and Zeo-HPC respectively. The gaseous products yields were 8.6%, 5.5%, 31.5% and 11.9% respectively. The unconverted feeds were 73.54%, 84.65%, 51.48% and 66.19% respectively, for the Zeo-AY, Zeo-BY, Zeo-CY and Zeo-HPC respectively. Figure 4.82 shows the bar chart of the product distribution of the commercial catalyst Y and the composite catalyst Y + ZSM5 of Zeo-AY and Zeo-CY at reaction condition of 400˚C and keeping all other condition unchanged, it could be observed that the gasoline yield of the Zeo-AY composite catalyst reduced slightly by 3% while the gaseous products yield increased enormously by 172% whereas the gasoline yield of the Zeo-CY composite catalyst increased by 151% and the gaseous products yield reduced by 70%.

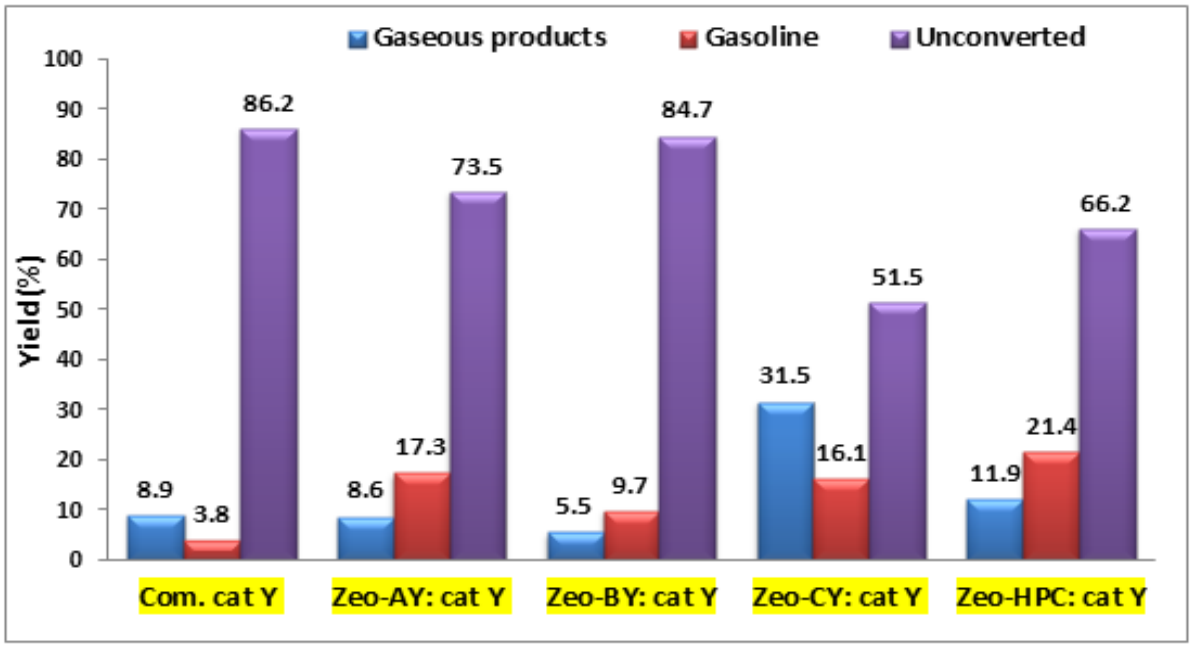


Figure 4.81: Product distribution of the various catalyst Y zeolite samples at 400˚C

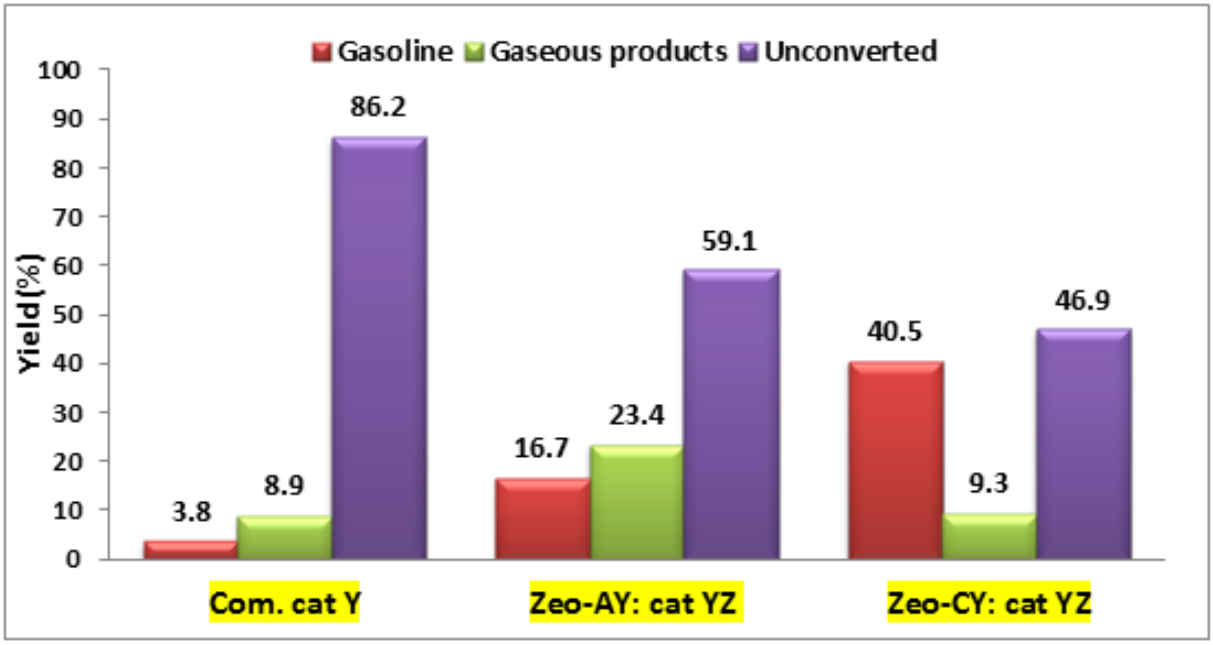


Figure 4.82: Product distribution of the various catalyst Y zeolite + ZSM5 blend at 400˚C

Hence, it could be observed that incorporation of ZSM5 had improved gasoline yield of the Zeo-CY composite catalyst and reduced its gaseous products at reaction temperature of 400˚C

whereas the opposite trend was observed for the Zeo-AY composite catalyst at the same reaction conditions.

Figure 4.83 shows the bar chart of the product distribution of the various catalyst Y zeolite samples at reaction condition of 500˚C and keeping all other conditions unchanged. It could be observed that the gasoline and gaseous products yields of the commercial catalyst were 18% and 14% respectively. The unconverted feed was 67%. The gasoline yield of the other zeolite Y catalysts were 25.6%, 12.86%, 17.92% and 34.38% for the Zeo-AY, Zeo-BY, Zeo-CY and Zeo-HPC respectively. The gaseous products yields were 10.8%, 23.6%, 51.6% and 20.0% respectively. The unconverted feeds were 62.91%, 62.39%, 29.11% and 44.85% respectively. Figure 4.84 shows the bar chart of the product distribution of the commercial catalyst Y and the composite catalyst Y + ZSM5 of Zeo-AY and Zeo-CY at reaction condition of 500˚C and keeping all other conditions unchanged.

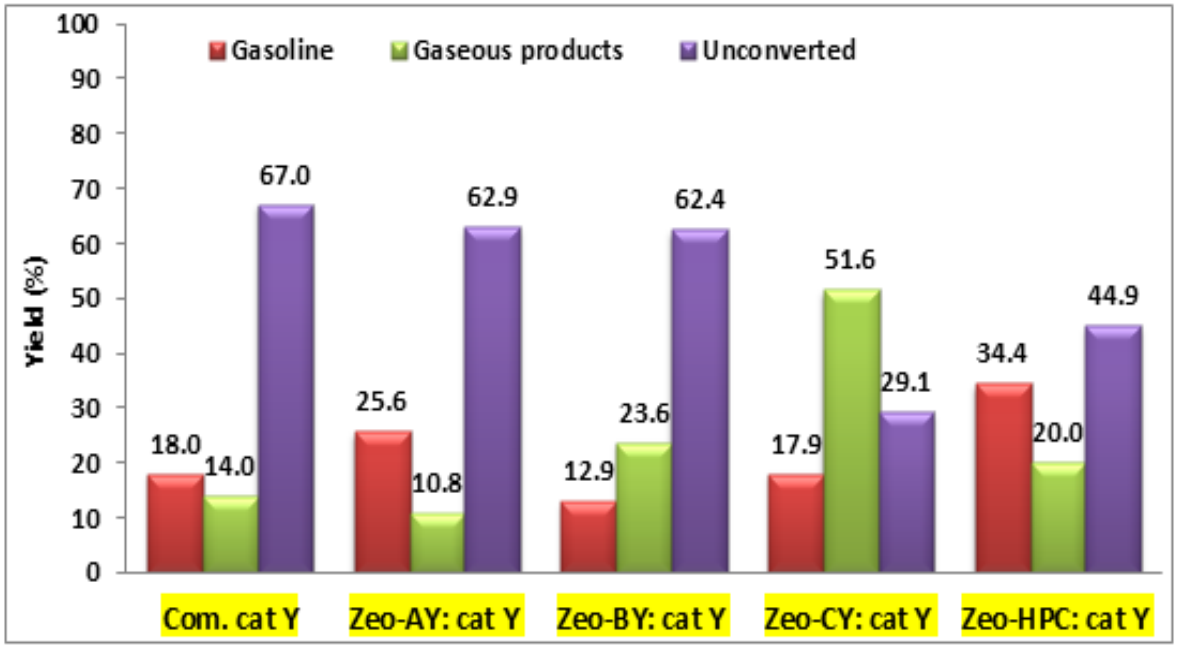


Figure 4.83: Product distribution of the various catalyst Y zeolite samples at 500˚C

It could be observed that the gasoline yield of the Zeo-AY composite catalyst reduced by 20% while the gaseous products yield increased by enormously by 176% whereas the gasoline yield of the Zeo-CY composite catalyst increased by 231% and the gaseous products yield reduced by 77%. It could be observed that the trend of product distribution behaviour of the Zeo-AY and Zeo-CY remained relatively the same for reaction temperature conditions of 400 and 500˚C. It could also be noted that the percentage unconverted feed became generally lower from 400 to 500˚C reaction temperatures.

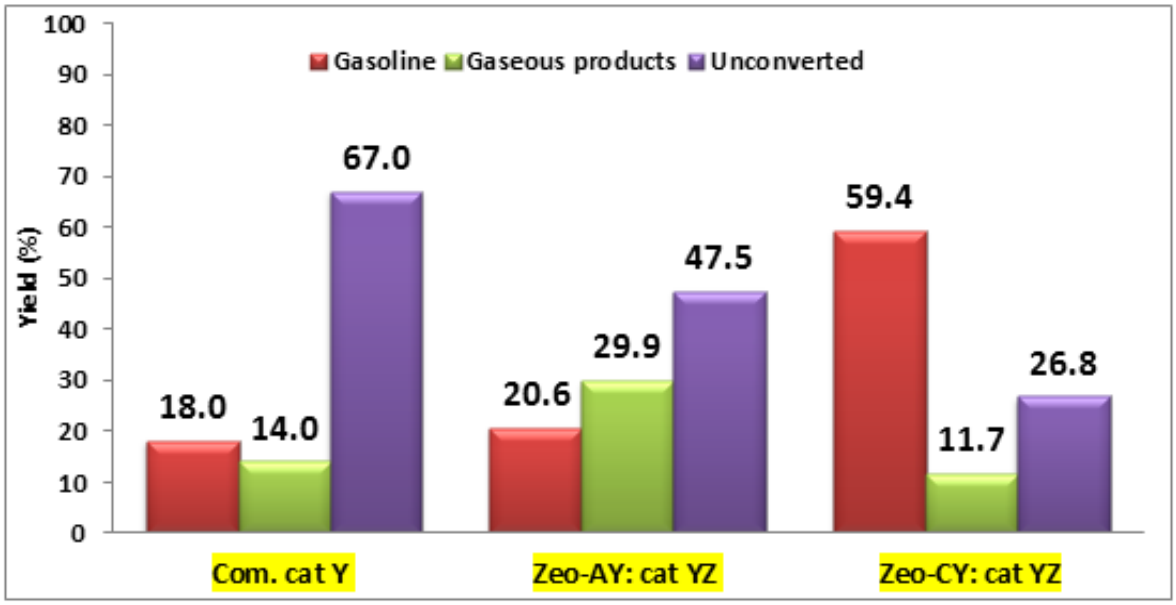


Figure 4.84: Product distribution of the various catalyst Y zeolite + ZSM5 blends at 500˚C

Figure 4.85 shows the bar chart of the product distribution of the various catalyst Y zeolite samples at reaction condition of 550˚C and keeping all other conditions unchanged. It could be observed that the gasoline yields of the Zeo-BY, Zeo-CY and Zeo-HPC catalysts were 17.33%, 39.11% and 33% respectively. The gaseous products yields were 27.8%, 23.5% and 29.4% respectively. The unconverted feeds were 51.75%, 34.65% and 36.34% respectively. Figure 4.86 shows the bar chart of the product distribution of the composite catalyst Y zeolite + ZSM5 of

Zeo-BY, Zeo-CY and Zeo-HPC at reaction condition of 550˚C; keeping all other conditions unchanged.

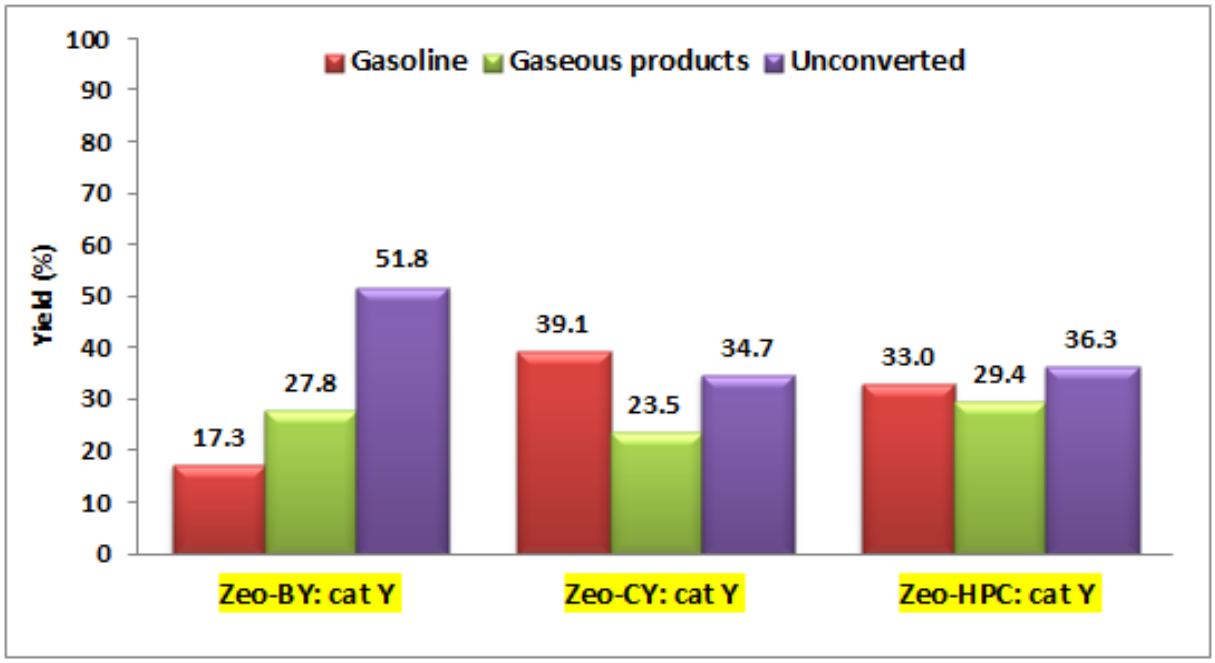


Figure 4.85: Product distribution of the various catalyst Y zeolite samples at 550˚C

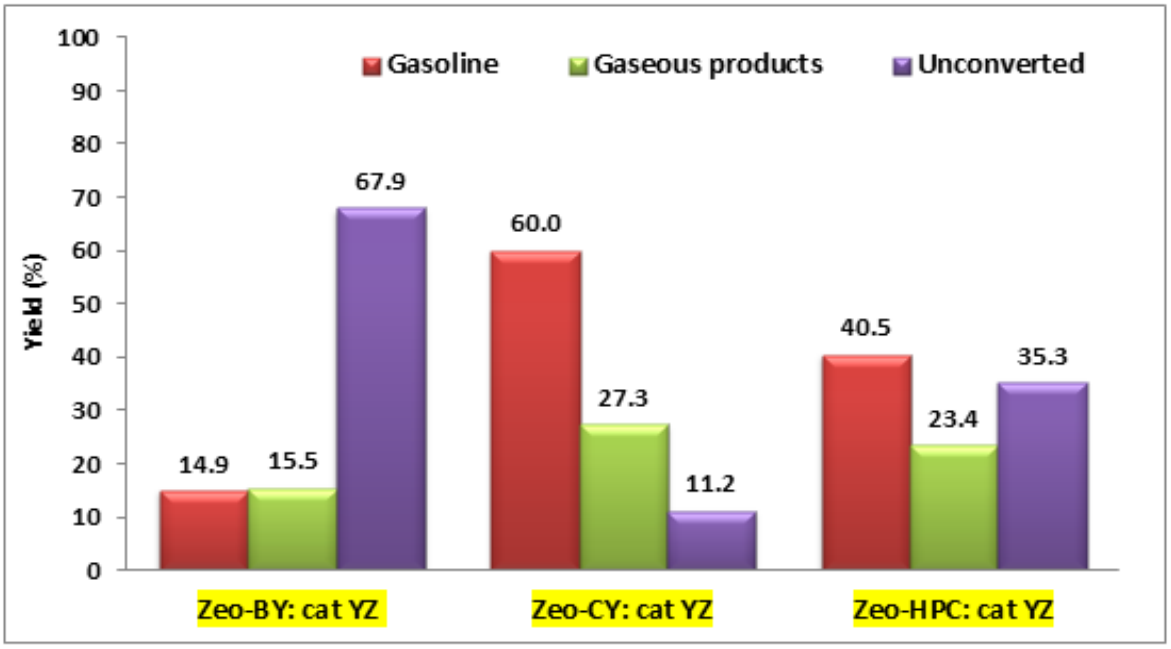


Figure 4.86: Product distribution of the various catalyst Y zeolite + ZSM5 blends at 550˚C

It could be observed that the gasoline and gaseous products yields of the Zeo-BY composite catalyst reduced by 14% and 44% respectively, whereas the gasoline and gaseous products yields of the Zeo-CY composite catalyst increased by 53% and 16% respectively. Hence, it could be observed that incorporation of ZSM5 had increased the gasoline, and gaseous products yield for Zeo-CY whereas the trend was the reverse in case of the Zeo-BY for reaction temperature 550˚C.

4.5.7.2 Comparison of gasoline distribution of the various catalysts

Figure 4.87 shows the comparison of gasoline yields of the various catalysts at reaction temperatures of 400 and 500˚C. It could be observed that at both temperatures the order of gasoline yields was Zeo-HPC > Zeo-AY > Zeo-CY. However, at 400˚C Zeo-BY was the fourth and the commercial catalyst was the last, whereas at 500˚C the reverse was the case. Figure 4.88 shows the comparison of gasoline yields of the various composite catalysts Y + ZSM5 at reaction temperatures of 400 and 500˚C. It could be observed that the Zeo-CY gave the highest gasoline yield at both the reaction temperatures of 400 and 500˚C. At 500˚C it could be observed that the relative difference in the gasoline yield among the other catalysts was very little, hence the other three composite catalysts gave relatively the same gasoline yield with the percentage mean difference being 5%. Although at 400˚C the Zeo-AY could be seen to give the second highest gasoline yield being slightly higher than the gasoline yields of Zeo-BY and Zeo-CY whereas the percentage mean difference between the gasoline yield for the Zeo-BY and Zeo-CY not much being only 8%. The best gasoline yield of 59.38% obtained for the composite catalyst Zeo-CY was higher than the value obtained by many researchers who worked in this area (Ng *et al*., 2006; Ding *et al*., 2007; Li *et al*., 2007).

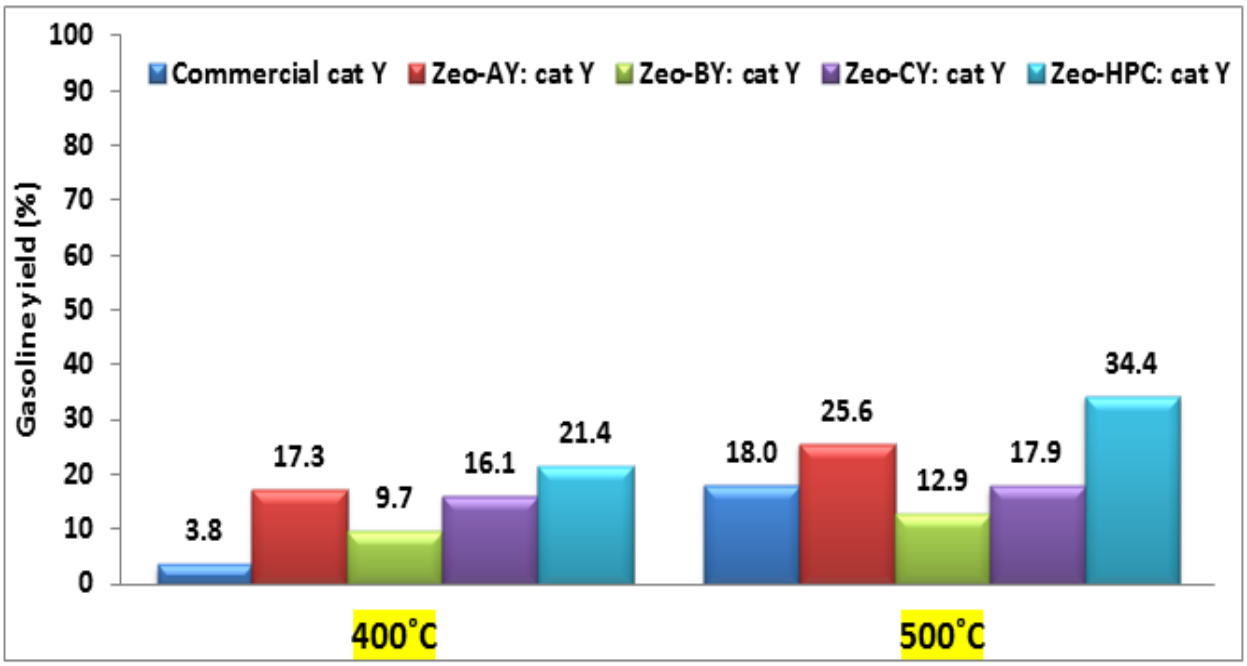


Figure 4.87: Comparison of the gasoline yield of the various Y catalysts at 400 and 500˚C

Having observed that incorporation of ZSM to Zeo-AY improved the gasoline yield of the catalyst, Figure 4.89 shows the comparison of gasoline yields of the catalyst Y and the composite catalyst Y + ZSM5 formulated from Zeo-AY using higher weight per cent zeolite content in the catalyst: 50 wt% at variable reaction temperatures. It could be observed that unlike in the earlier situation shown in Figures 4.83 and 4.84 where 30 wt% of zeolite was used, at higher zeolite content of 50 wt% the gasoline yields of the two types of catalysts were relatively at a competing range. The difference in the gasoline yield of the catalyst Y and the composite catalyst Y + ZSM5 was not much, it could be observed that the yield of the catalyst Y was rather higher at 400 and 550˚C which was opposite of the general trend observed at the 30 wt% zeolite content.

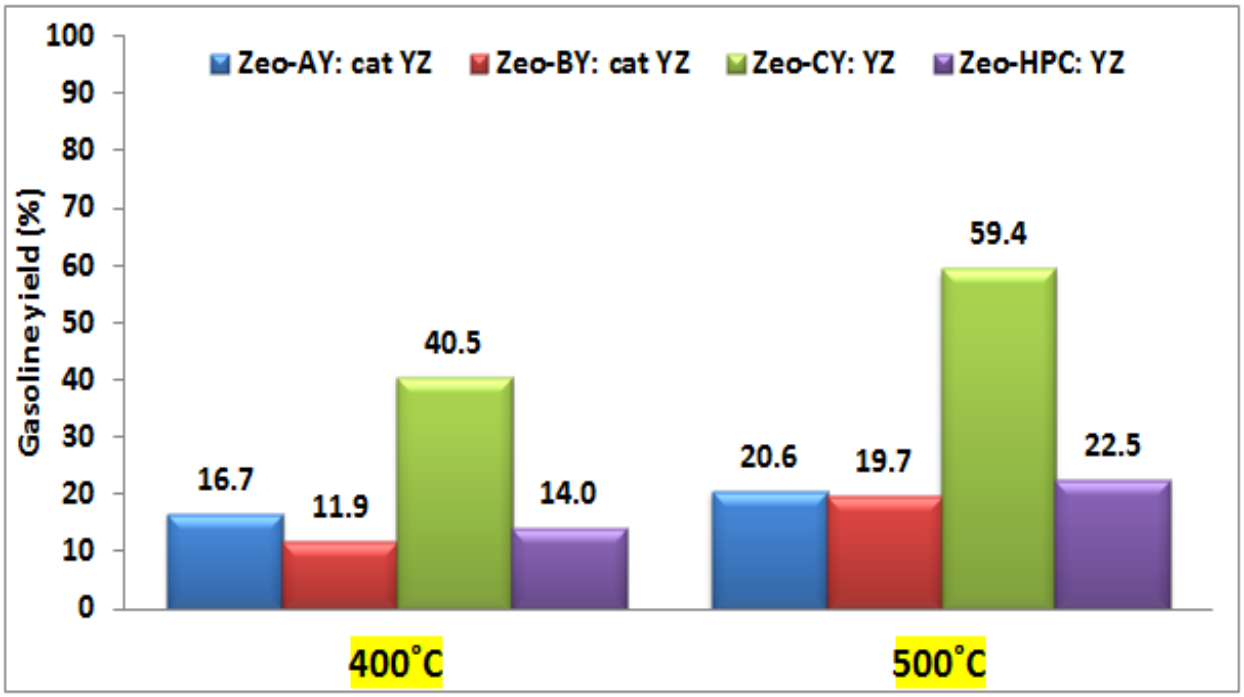


Figure 4.88: Comparison of the gasoline yield of the various Y+ ZSM5 catalysts at 400 and 500˚C

Figure 4.90 shows the comparison of gasoline yields of the composite catalyst Y + ZSM5 formulated from Zeo-AY using variable weight per cent zeolite content in the catalyst: 30 wt% and 50 wt% at variable reaction temperatures. It could be observed that at higher zeolite content the gasoline yields increased by 78% and 92% at 400 and 500˚C respectively. The gasoline yields obtained for the formulated catalysts were within the range reported in the literature (Ng *et al*., 2006; Ding *et al*., 2007; Li *et al*., 2007; Nam *et al*., 2011; Al-Shammari *et al*., 2014). The increase in gasoline yield observed for the composite catalysts was likely due to the fact that zeolite Y suffers chemical deactivation when used for cracking reaction as result of formation of products which do not freely diffuse out of the zeolite pores. Such products tend to block the pores and results into chemical deactivation of the catalyst. However, when the catalyst is made of zeolite Y and ZSM5 composite, ZSM5 tends to eliminate the chemical deactivation problem

of such products by the advantage of its high selectivity for easy outward diffusion of such products.

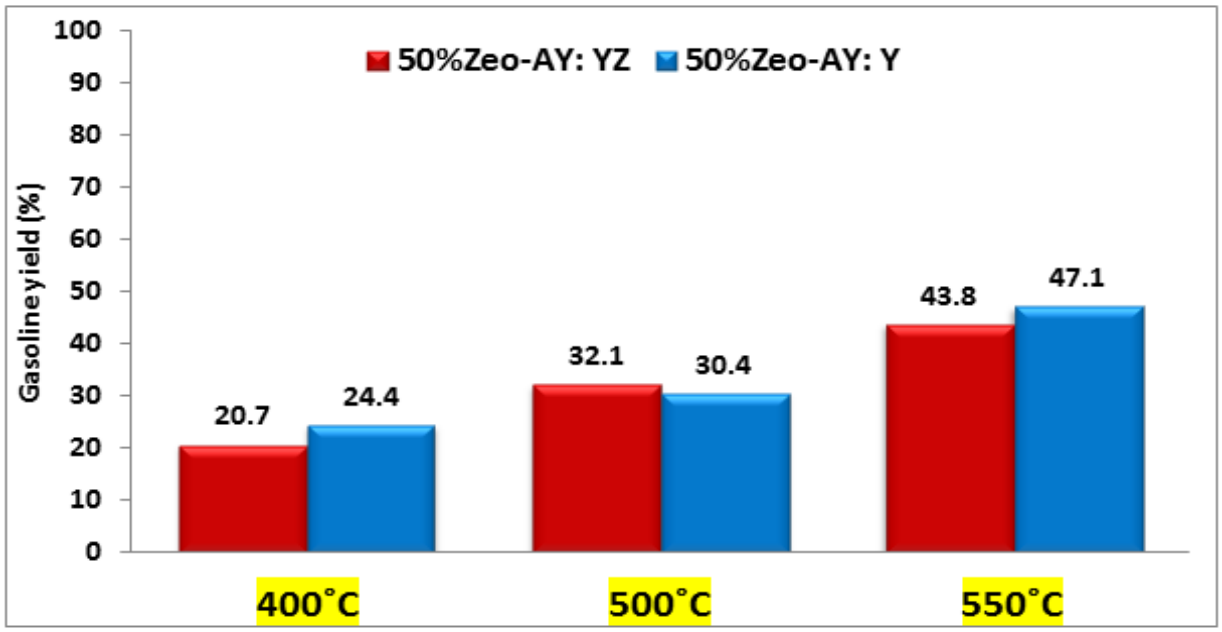


Figure 4.89: Comparison of the gasoline yield of the various Zeo-AY catalysts using variable zeolite percentage contents at variable reaction temperatures

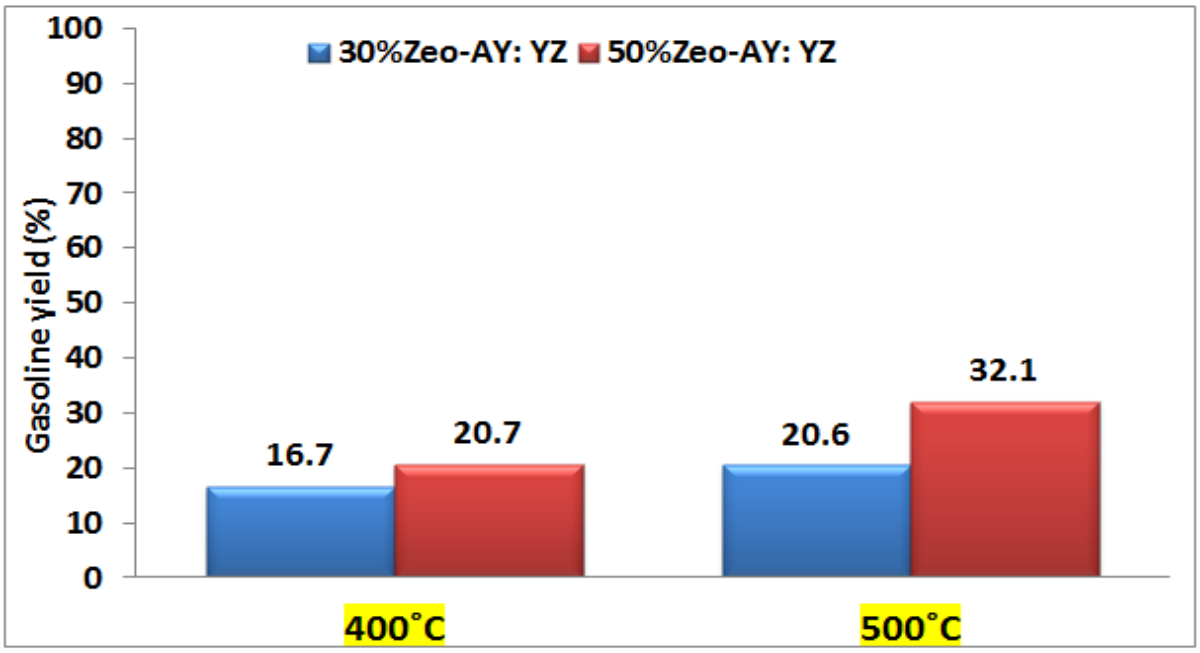


Figure 4.90: Comparison of the gasoline yield of Y+ ZSM5 catalysts having variable zeolite percentage contents at 400 and 500˚C

4.5.7.3 Analysis of the conversion of the various catalysts

Figure 4.91 shows the reaction conversion of the various Zeo-AY catalysts at variable reaction temperatures. It could be observed that incorporation of ZSM5 generally increased the activity of the catalyst; the increases in conversion were 890%, 55% and 42% at reaction temperatures of 300, 400 and 500˚C respectively. Similarly Figure 4.93 shows the reaction conversion of the various Zeo-CY catalysts at variable reaction temperatures. It could be observed that incorporation of ZSM5 also increased the activity of the catalysts generally; the increases in conversion were 9%, 3% and 36% at reaction temperatures of 400, 500 and 550˚C respectively. However, Zeo-BY and Zeo-HPC showed an opposite behaviour, as could be seen from their conversion charts; Figures 4.92 and 4.94, incorporation of ZSM5 rather suppressed the activity of the catalysts. Although in the case of Zeo-BY catalyst, at 400˚C deviation was observed; the activity of the catalyst was almost the same with and without the incorporation of ZSM5.

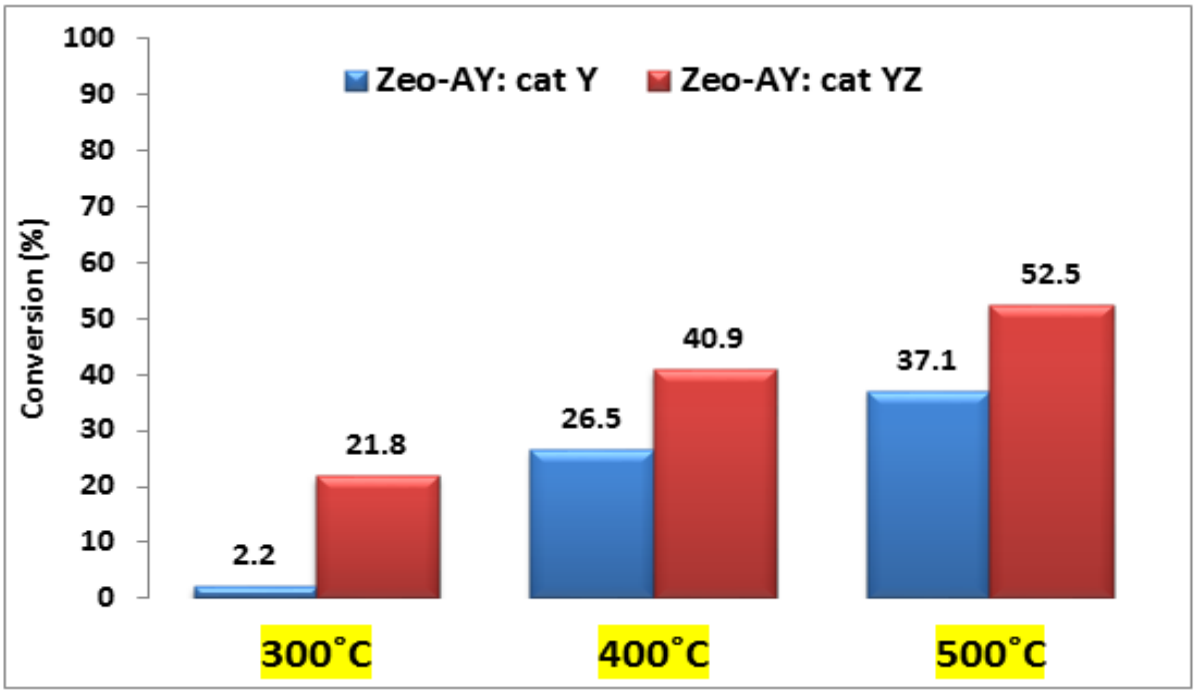


Figure 4.91: Reaction conversion of Zeo-AY catalysts at the various temperatures

Also in the case of the Zeo-HPC catalyst similar deviation was observed at 550˚C. The reduction in activity of the Zeo-BY catalyst was 33% conversion at both 500 and 550˚C. While the reductions in conversion of the Zeo-HPC catalyst were 49% and 32% at reaction temperatures of 400 and 500˚C respectively, whereas at 550˚C the conversion of the catalyst was relatively the same with and without ZSM5 incorporation.

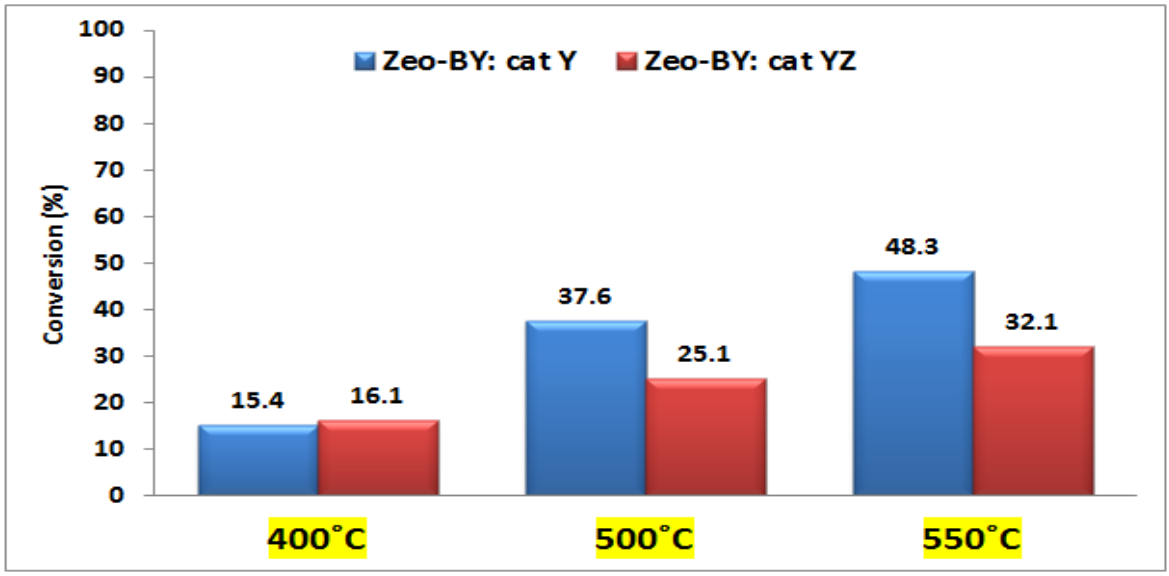


Figure 4.92: Reaction conversion of Zeo-BY catalysts at the various temperatures

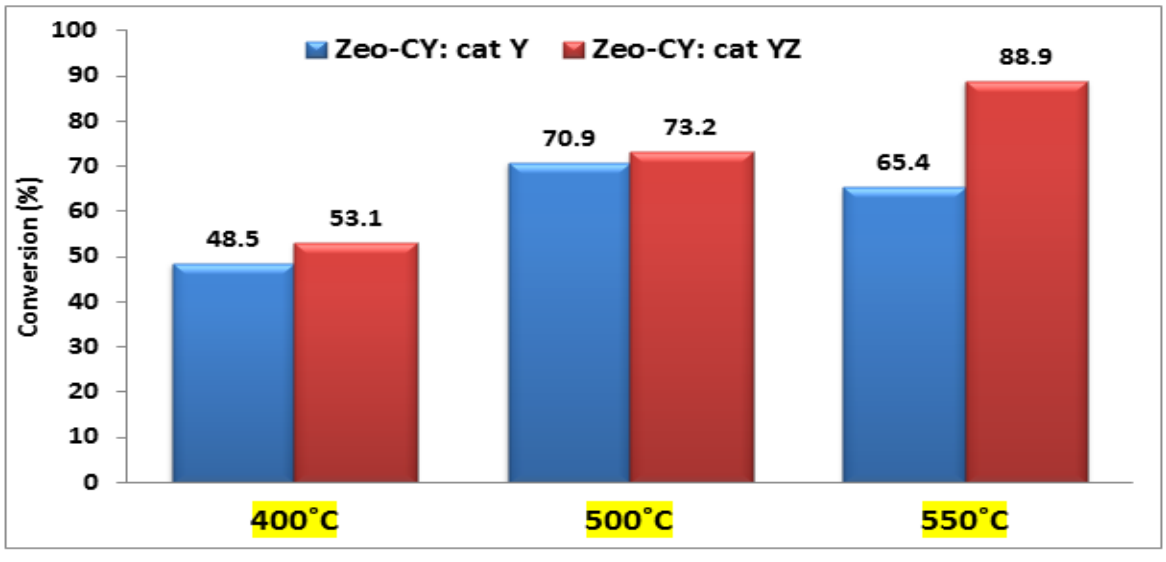


Figure 4.93: Reaction conversion of Zeo-CY catalysts at the various temperatures

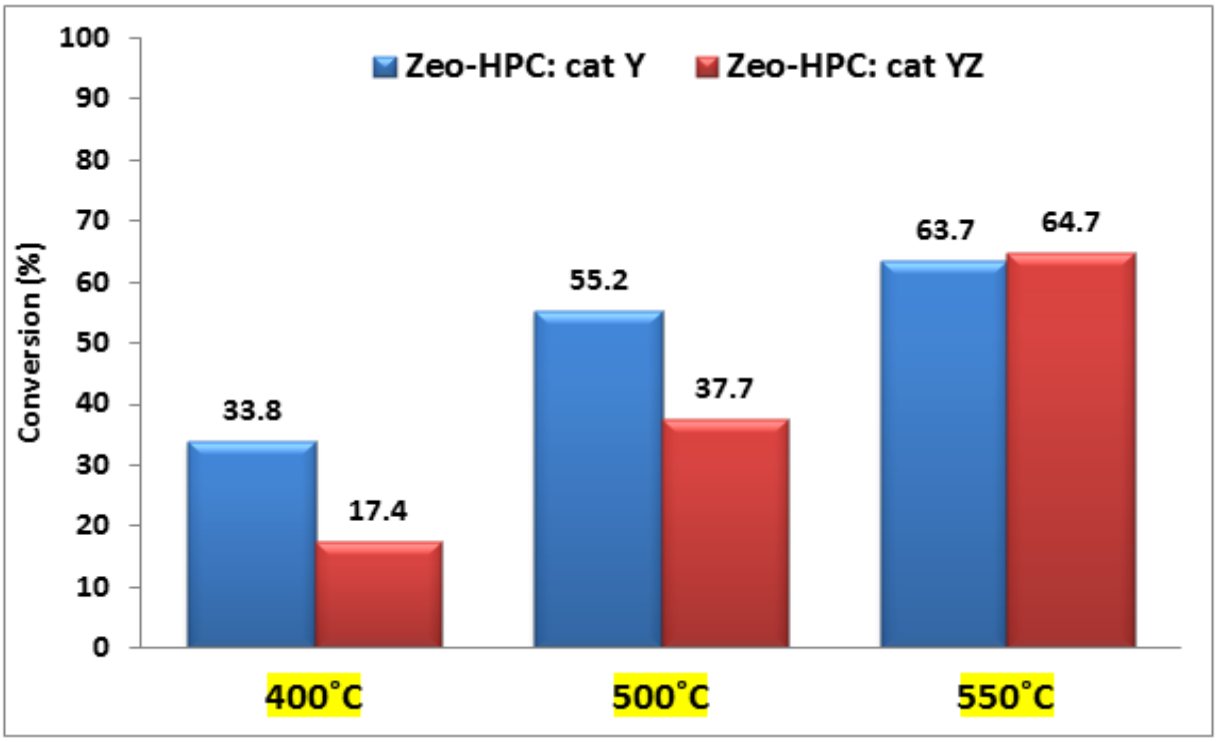


Figure 4.94: Reaction conversion of Zeo-HPC catalysts at the various temperatures

Figure 4.95 shows the comparison chart of the reaction conversion of the various catalyst Y at reaction temperatures of 400 and 500˚C. It could be observed that the order of the magnitude of reaction conversion among the catalysts was Zeo-CY > Zeo-HPC > Zeo-AY > Zeo-BY > Commercial catalyst Y for both temperaturtes considered, although at 500˚C Zeo-AY and Zeo-BY had relatively the same conversion. Figures 4.96 shows the comparison chart of the reaction conversion of the various composite catalyst Y + ZSM5 at reaction temperatures of 400 and 500˚C. It could be observed that the order of the magnitude of reaction conversion among the catalysts was Zeo-CY > Zeo-AY > Zeo-HPC > Zeo-BY for both temperatures considered. The conversions attained by the formulated catalysts fall within the range of conversions reported by other workers (Ding *et al*., 2007; Al-Shammari *et al*., 2014).

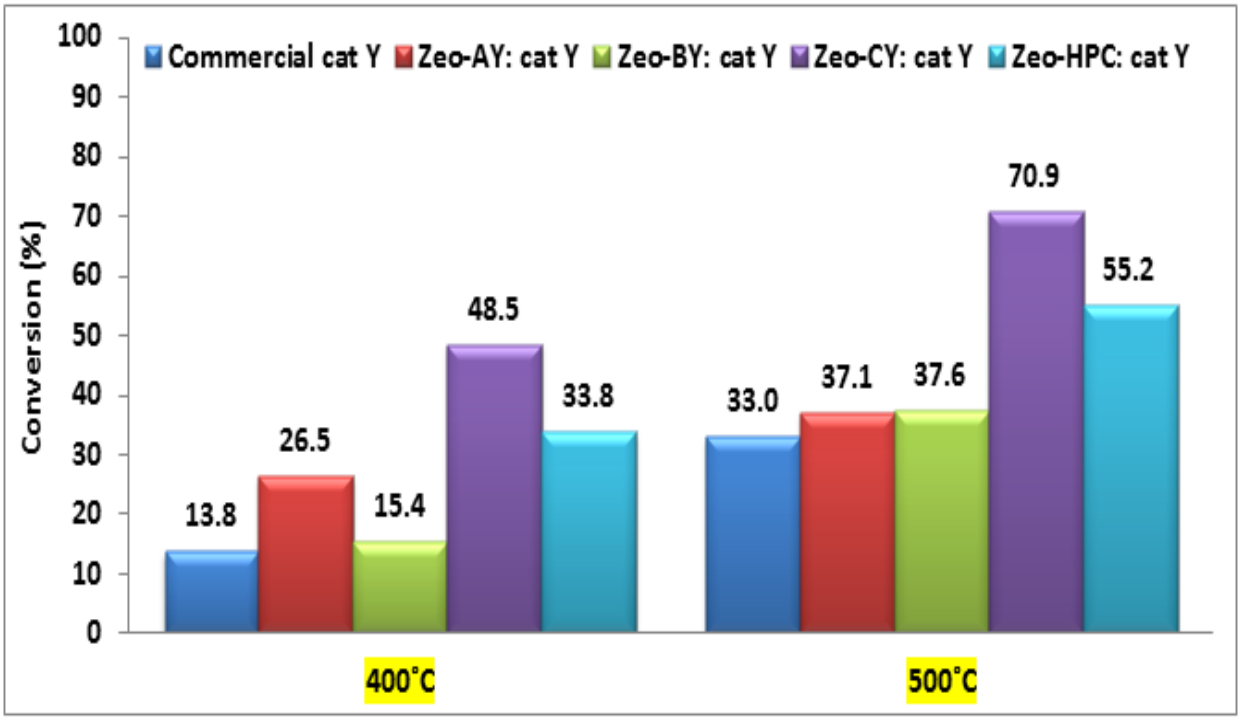


Figure 4.95: Comparison of the conversion of the various Y zeolite catalysts at 400 and 500˚C

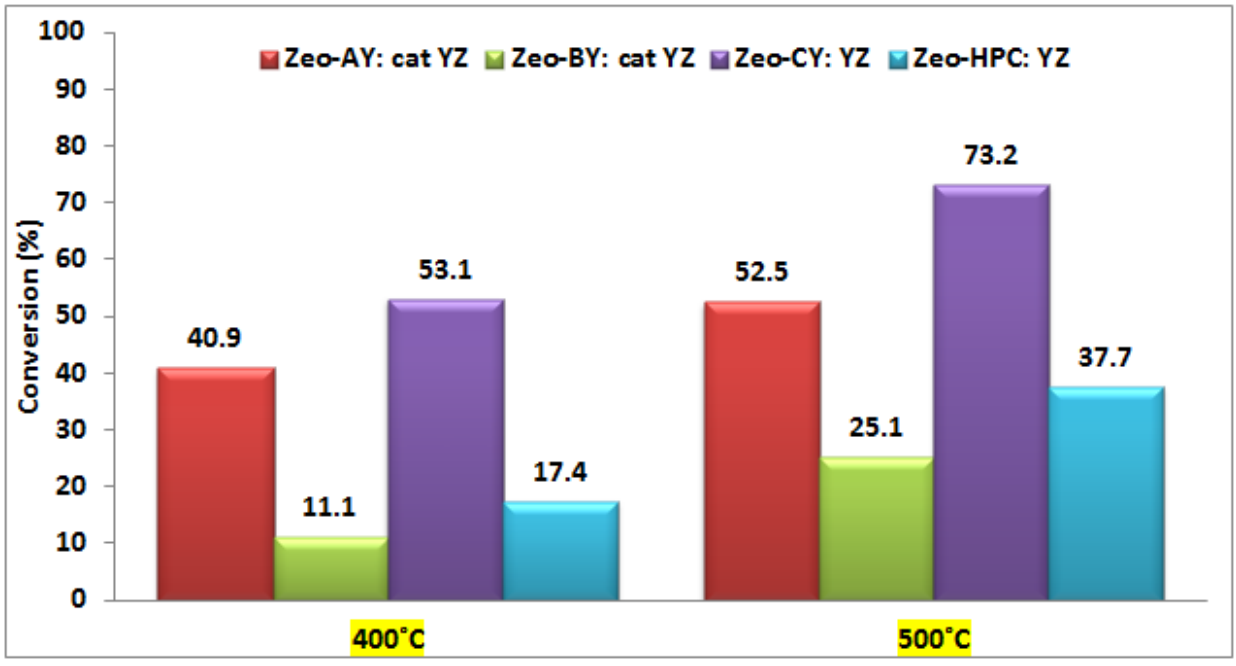


Figure 4.96: Comparison of the conversion of the various Y zeolite + ZSM5 catalysts at 400 and 500˚C

4.5.7.4 Product selectivity of the various catalysts

Figures 4.97 – 4.101 show the products selectivity of the commercial catalyst Y and for each of the various catalysts formulated at variable reaction temperatures. Figure 4.97 shows the product selectivity of the commercial catalyst Y at variable reaction temperatures. The selectivity was calculated using Equation (2.10). It could be observed that at low temperature of 300˚C selectivity for gasoline and gaseous products were relatively the same. However, at about 400 - 480˚C the catalyst developed higher selectivity for gaseous products whereas at 500˚C the catalyst favours relatively much higher selectivity of gasoline; the selectivity of gasoline at 500˚C was 29% higher than that of gaseous products. Figure 4.98 shows the product selectivity of the various Zeo-AY catalysts at variable reaction temperatures. It could be observed that at all the temperatures the catalyst Y zeolite gave higher gasoline selectivity, while the gaseous products selectivity was relatively very low. The gasoline selectivity values were 310%, 101% and 136% more than the gaseous products selectivity values at 300, 400, 500˚C respectively. It could also be noted that the gaseous products selectivity of the Zeo-AY: catalyst Y + ZSM5 was higher than the gasoline selectivity at higher temperatures, but the trend was reversed at 300˚C and lower temperatures. Figure 4.99 shows the product selectivity of the various Zeo-BY catalysts at variable reaction temperatures. It could be observed that the gaseous products had higher selectivity than the gasoline at reaction temperatures of 500 and 550˚C while at 400˚C it was the reverse. It could also be observed that incorporation of ZSM5 resulted to higher gasoline selectivity at temperatures of 400 and 500˚C. However, at 550˚C the selectivity of gasoline and gaseous products were relatively the same. Figure 4.100 shows the product selectivity of the various Zeo-CY catalysts at variable reaction temperatures. It could be observed that the gaseous products had higher selectivity than the gasoline at reaction temperatures of 400 and 500˚C while

at 550˚C the trend reversed. However, it could also be observed that incorporation of ZSM5 resulted to higher gasoline selectivity at all temperatures.

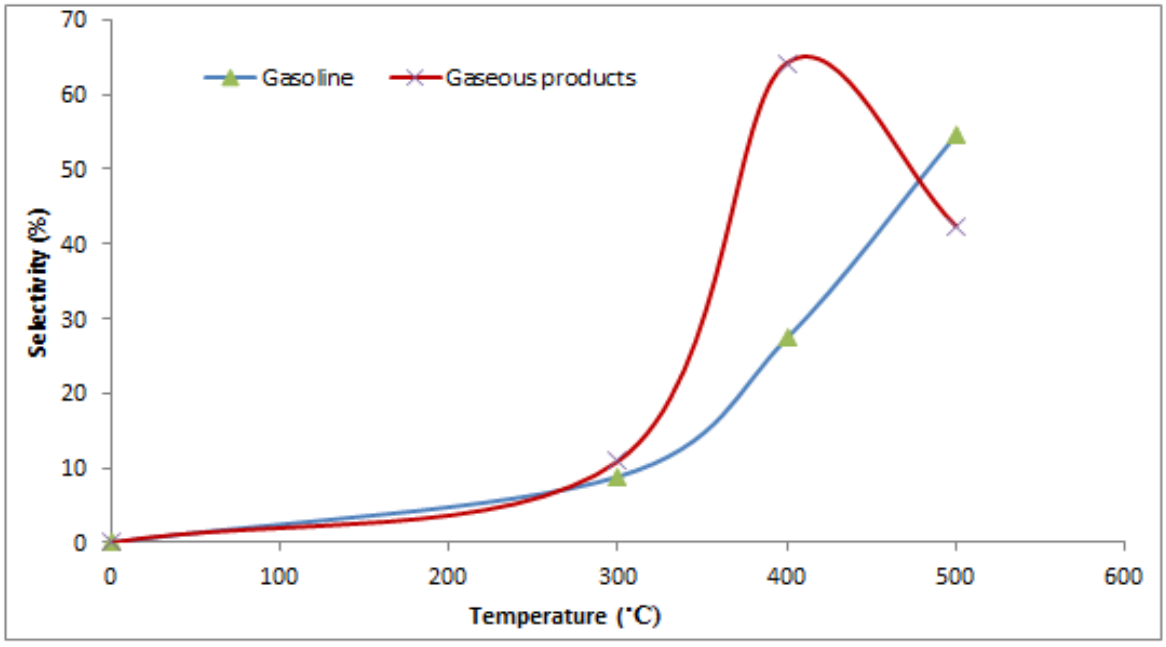


Figure 4.97: Product selectivity of the commercial catalyst at variable reaction temperatures

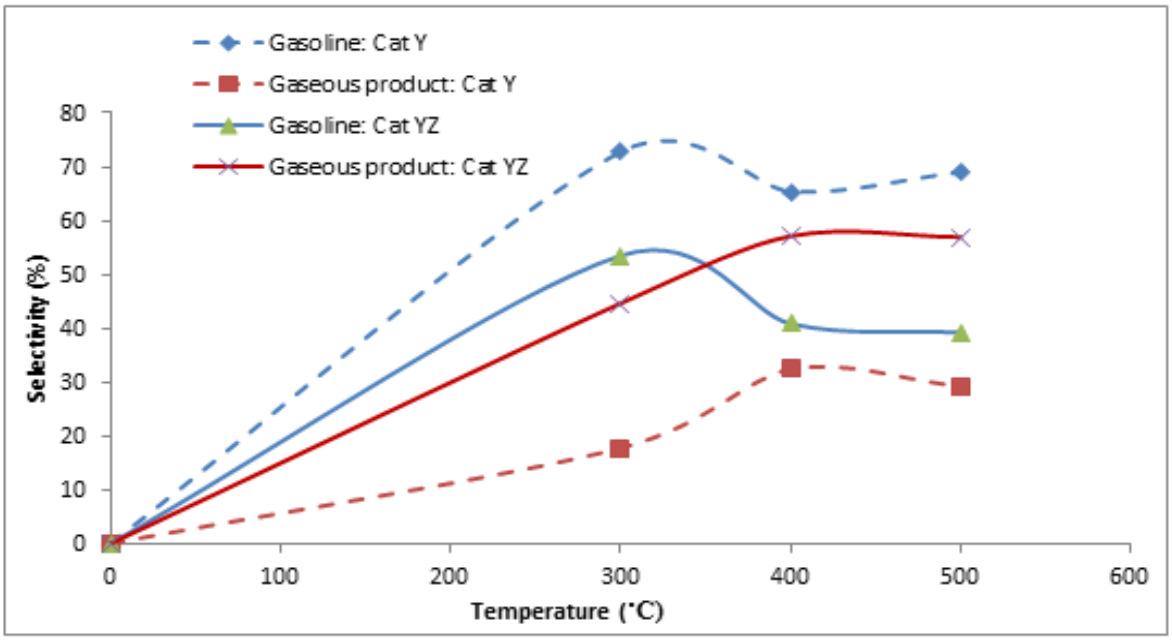


Figure 4.98: Product selectivity of Zeo-AY catalysts at variable reaction temperatures

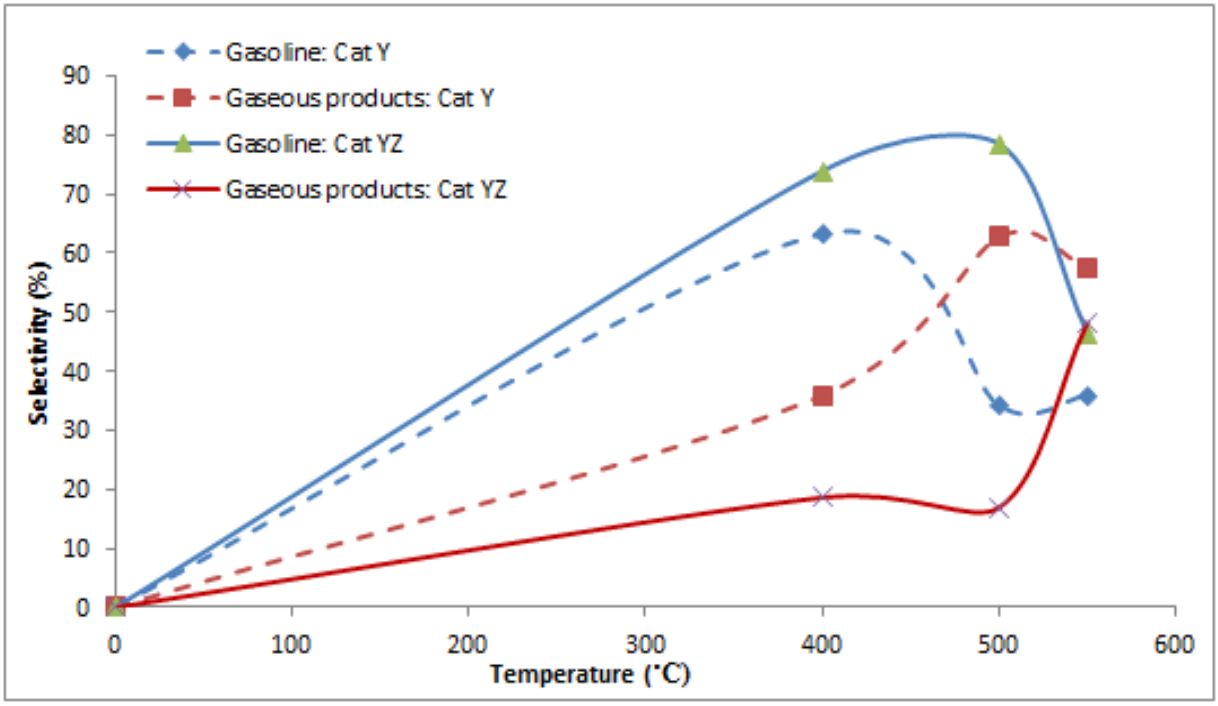


Figure 4.99: Product selectivity of Zeo-BY catalysts at variable reaction temperatures

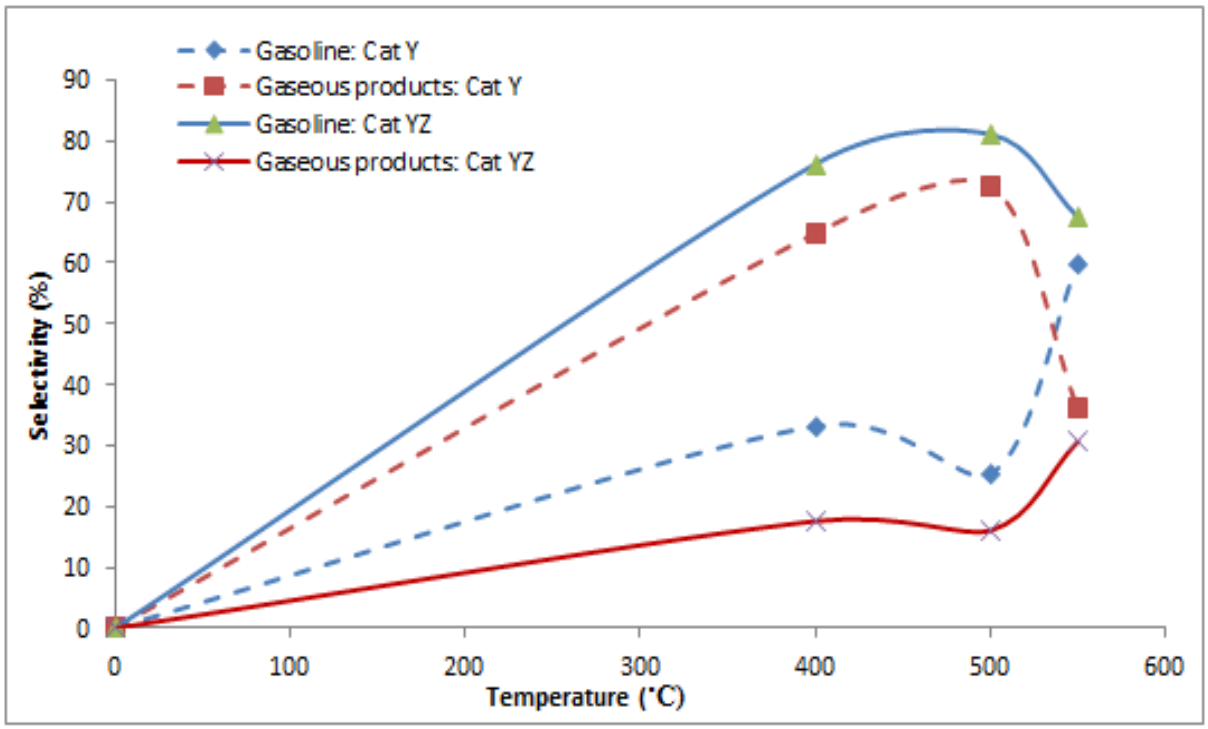


Figure 4.100: Product selectivity of Zeo-CY catalysts at variable reaction temperatures

Figure 4.101 shows the product selectivity of the various Zeo-HPC catalysts at variable reaction temperatures. It could be observed that the gasoline had distinctively higher selectivity than the gaseous products for both the catalyst Y and the composite catalyst Y zeolite + ZSM5 at all the reaction temperatures considered.

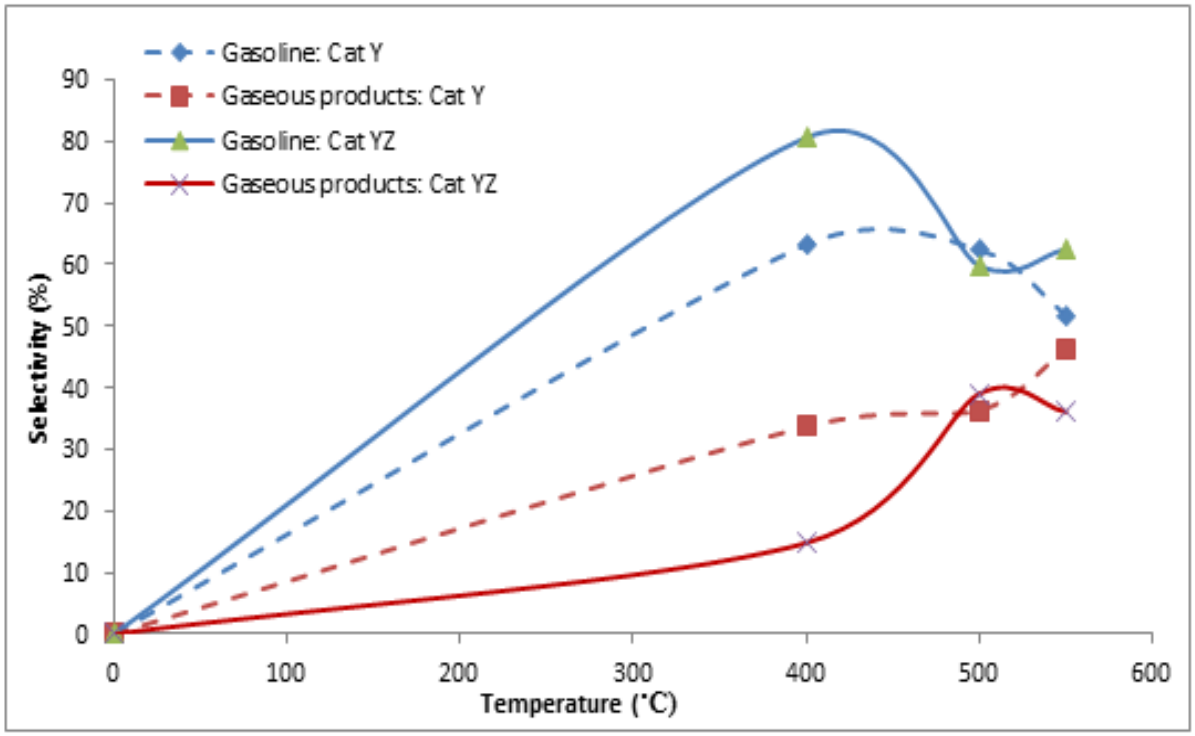


Figure 4.101: Product selectivity of Zeo-HPC catalysts at variable reaction temperatures

CHAPTER 5

5.0 CONCLUSIONS AND RECOMMENDATIONS

5.1 Conclusions

From the results of the investigation into the development of zeolite Y and ZSM5 composite catalyst from Kankara kaolin, the following conclusions were drawn:

I. Crystalline, microporous zeolite Y was successfully synthesized from Kankara kaolin using a novel split method.

II. Great improvement was achieved in the properties and purity of the synthesized zeolite Y using the novel split method when compared with the product obtained by the conventional method. The crystallinity of the zeolite Y synthesized using the novel split method was 72.5% whereas the crystallinity of the sample reported by some previous workers using the conventional method was 29.2%.

III. The physicochemical properties of the zeolite synthesized from Kankara kaolin was comparable with that of a commercial zeolite Y sample obtained from KRPC. The crystallinity was 72.5% that of the commercial zeolite Y, and the BET surface area and pore volume values were 38% and 18% respectively higher than that of the commercial zeolite Y.

IV. Thermally stable, crystalline and catalytically active catalyst Y zeolite and composite catalyst Y zeolite + ZSM5 were successfully formulated from the synthesized zeolite Y.

V. The synthesized zeolite showed highly promising prospect for adsorptive desulfurization performance when applied as a catalyst for desulfurization of a model petroleum fuel.

VI. The catalysts formulated showed a higher catalytic performance than the commercial catalyst Y when applied for cracking of model heavy oil. The gasoline yield, conversion and gasoline selectivity of the formulated catalysts were 42%, 12% and 25% respectively higher than that of the commercial catalyst.

VII. Among the various batches of the as-synthesized zeolite Y using the novel split method, the batch synthesized using analar grade acid and analar grade base (Zeo-CY) gave the best physicochemical properties. Then followed by the batch synthesized using industrial grade acid and analar grade base (Zeo-AY). The BET surface areas of the Zeo-CY and Zeo-AY were 830.0 and 732.0 m^2/g respectively. Their pore volumes were 0.2951 and 0.2611 cm^3/g respectively. Their pore diameters were 1.425 and 1.426 nm respectively. Their molar Si/Al ratios were 4.26 and 3.65 respectively. Their XRD characteristic peak intensities were 1765 and 1550 counts respectively, and their average particle size was 200 nm each.

VIII. The formulated catalyst Y using the synthesized zeolite Y prepared from Kankara kaolin via the novel split method showed high catalytic performances. The conversion and gasoline yield of Zeo-CY: catalyst Y at reaction temperature of 500˚C were 70.89% and 17.92% respectively while those of Zeo-AY: catalyst Y were 37.09% and 25.60% respectively. The gasoline selectivity values of Zeo-CY: catalyst Y and Zeo-CY: catalyst Y at 500˚C were 25% and 69% respectively.

IX. The formulated composite catalyst Y + ZSM5 samples using the zeolite Y synthesized from Kankara kaolin via the novel split method showed higher catalytic performances than their counterpart catalyst Y samples. For instance considering Zeo-CY and reaction condition of 500˚C: The conversion and gasoline yield of the catalyst Y + ZSM5 were 73.17% and 59.38% respectively, while those of the catalyst Y were 70.9% and 17.9% respectively. The gasoline selectivity values of the catalyst Y + ZSM5 and the catalyst Y were 81.2% and 25.3% respectively.

X. At higher weight composition of the zeolite content (> 30 wt%) in the catalyst formulation the boosting effect of ZSM5 for gasoline yield diminished. for a 50 wt% zeolite content the increase in gasoline yield due to addition of ZSM5 at reaction temperature of 500˚C was only 5.7% whereas for 30 wt% zeolite it was 24%.

5.2 Recommendations

From the foregoing the following recommendations may be made.

I. Pilot plant study of the production of zeolite Y and ZSM5 composite catalyst should be carried out using the bench-scale parameters generated from this work.

II. Further investigation should be carried out using catalyst formulated from ZSM5 only without inclusion of zeolite Y.

III. The Nigerian government and relevant stake holders should invest in the further development of the findings of this research work towards the commercialization of the process.

CONTRIBUTIONS TO KNOWLEDGE

I. Novel method of synthesis of zeolite Y from kaolin was developed.

II. Methods of processing high grade aluminum hydroxide from kaolin suitable for the synthesis of zeolite Y was developed.

III. Method of producing zeolite synthesis grade sodium silicate from kaolin was developed.

IV. Method of producing alumina from kaolin for use as support in FCC catalyst was developed.

V. The catalytic performance of zeolite Y and Y + ZSM5 blend prepared from kaolin as FCC catalyst was determined.

PUBLICATIONS

1. Journals:

i. **Salahudeen**, **N.,** Ahmed, A. S., Al-Muhtaseb, A. H., Dauda, M., Waziri, S. M., Jibril, B. Y. (2014), Synthesis of Gamma Alumina from Kankara Kaolin Using a Novel Technique. *Applied Clay Science*, 105-106: 170-177.

ii. **Salahudeen**, **N.,** Ahmed, A. S., Dauda, M., Waziri, S. M., Jibril, B. Y., Al-Muhtaseb, A. H. (2014), Study of the Thermal Stability Effect of Impregnation of Lanthanum Metal on FCC Catalyst. *Australian Journal of Industry Research*, 1 (2): 10-15.

iii. **N. Salahudeen**, A. S. Ahmed, A. H. Al-Muhtaseb, M. Dauda, S. M. Waziri, B. Y. Jibril, (2014), Synthesis and Characterization of Micro-Sized Silica from Kankara Kaolin. *Journal of Engineering Research*, 19 (1): 27-32

iv. **N. Salahudeen**, A. Nasiru, A. S. Ahmed, M. Dauda, S. M. Waziri, P. C. Okonkwo and M. T. Isa, (2015), Chemical and Physical Comparative Study of the Effect of Wet and Dry Beneficiation of Kankara Kaolin. *Nigerian Journal of Technology*, 34 (2): in press.

2. Conferences:

i. **Salahudeen, N.**, Ahmed, A. S., Dauda, M., Waziri, S. M., Jibril, B. Y., Al-Muhtaseb, A. H. (2014), Study of Thermal Stability of Synthesized FCC Catalyst. Book of Abstract of the 6th Federation of European Zeolite Association (FEZA) Conference, held on 8 – 11th September, at Universitat Leipzig, Germany. p 800.

ii. **Salahudeen, N.**, Ahmed, A. S., Dauda, M., Waziri, S. M., Jibril, B. Y., Al-Muhtaseb, A. H., Al-Sabahi, J. (2014), Microwave Assisted Adsorptive Desulfurization of Model Diesel Using Synthesized Microporous Zeolite HREY. Book of Extended Abstract of the 1st Nigeria International Conference on Zeolite (NICZ), held on 10th – 11th December, at NICON Luxury, Abuja. p 37-41.

iii. **Salahudeen, N.**, Ahmed, A. S., Dauda, M., Waziri, S. M., Jibril, B. Y., Al-Muhtaseb, A. H., Al-Sabahi, J. (2014), Adsorption Study of Microporous Activated Alumina Synthesized from Kaolin Using Phenol Solution as Absorbate. Book of Extended Abstract of the 1st Nigeria International Conference on Zeolite (NICZ), held on 10th – 11th December, at NICON Luxury, Abuja. p 68-72.

iv. **Salahudeen, N.**, Ahmed, A. S., Dauda, M., Waziri, S. M., Jibril, B. Y., Al-Muhtaseb, A. H., Al-Sabahi, J. (2014), Synthesis of microporous activated alumina from Kankara kaolin. Proceedings of the Nigerian Engineering Conference, held on 15th – 18th September, at Ahmadu Bello University, Zaria. p. 66.

v. Yusuf, O. A., Ahmed, A. S., **Salahudeen**, **N.,** Dauda, M., Yawas, D. S. (2014), Mechanical Characterization of FCC Catalyst Prepared from Synthesized Zeolite Y. Proceedings of the Nigerian Engineering Conference, held on 15th – 18th September, at Ahmadu Bello University, Zaria. p 67.

3. Patent:

i. Ahmed, A. S., **Salahudeen, N.**, Bawa, S. G., Waziri, S. M. and Dauda, M. (2014), (To PTDF and ABU), Development of Zeolite Y from Kaolin Using Novel Processing Method, Nig. Pat RP: NG/PT/NC/2013/3

REFERENCES

Abo-El-Enein, S. A., Heikal, M., Amin, M. S. and Negm, H. H. (2013), Reactivity of dealuminated kaolin and burnt kaolin using cement kiln dust or hydrated lime as activators. *Construction and Building Materials,* 47: 1451–1460.

Ahmed, A. S. (2008), Properties of Kaolin and Methods of Beneficiation: Proceedings of the First Nigerian Conference on Zeolite, Organized by PTDF Professorial Chair in Chemical Engineering, Ahmadu Bello University, Zaria, Held at Institute of Development Research, ABU, Zaria, 1: 1 – 17.

Ajayi, A. O. (2012), Development of Large Pore Zeolite from Kankara and Elefun Kaolinite. Unpublished Ph. D Dissertation, Department of Chemical Engineering, Ahmadu Bello University, Zaria.

Ajayi, A. O., Atta, A. Y., Aderemi, B. O. and Adefila, S. S. (2010*),* Novel Method of Metakaolin Dealumination Preliminary Investigation. *Journal of Applied Sciences Research*, 6(10): 1539-1546.

Akcay, M. (2005), The Surface Acidity and Characterization of Fe-montmorillonite Probed by in Situ FT-IR Spectroscopy of Adsorbed Pyridine. *Applied Catalysis A: General,* 294: 156–160.

Al-Khattaf, S., (2003), The Influence of Alumina on the Performance of FCC Catalysts during Hydrotreated VGO Catalytic Cracking. *Energy & Fuels*, 17: 62-68.

Al-Shammari, A. A., Ali, S. A., Al-Yassir, N., Aitani, A. M., Ogunronbi, K. E., Al-Majnouni, K. A. and Al-Khattaf, S. S. (2014), Catalytic Cracking of Heavy Naphtha-Range Hydrocarbons Over Different Zeolites Structures. *Fuel Processing Technology,* 122: 12 – 22.

American Public Health Association: APHA, (1996), "Standard Methods for the Examination of Water and Wastewater". Published by the American Water Works Association, Water Environment Federation, USA.

Anderson, J. R., Foger, K., Mole, T., Rajadhyaksha, R. A. and Saunders, J. V. (1979), Reactions on ZSM5-Type Zeolite Catalysts. *Journal of Catalysis,* 58: 114-130.

Andrejkovicova, S. (2012), Air Lime Mortars with Incorporation of Sepiolite and Synthetic Zeolite Pellets. *Acta Geodynamica et Geomaterialia,* 9: 79–91.

Atta, A. Y., Jibril, B. Y., Aderemi, B. O. and Adefila., S. S. (2012), Preparation of Analcime from Local kaolin and Rice Husk Ash. *Applied Clay Scienc*e, 61: 8–13.

Atta, A. Y., Ajayi, O. A. and Adefila, S. S. (2007), Synthesis of Faujasite Zeolites from Kankara Kaolin Clay. *Journal of Applied Sciences Research,* 3(10): 1017-1021.

Auerbach, S. M., Carrado, K. A., and Dutta, P. K. (2003), "Handbook of zeolite science and technology", 2nd edition, 8 -36, New York, USA, Marcel Dekker Inc.

Baerlocher, C., Meier, W. H. and Olson, D. H. (2007). "Atlas of Zeolite Framework Types", 6th edition, Amsterdam, Netherlands, Elsevier.

Baerlocher, C. and McCusker, L. B. Database of Zeolite Structures, http://www.izastructure.org/databases. Retrieved on 23/07/2014.

Bansiwal, A., Pillewan, P., Biniwale, R. B. and Rayalu, S. S. (2010), Copper Oxide Incorporated Mesoporous Alumina for Defluoridation of Drinking Water. *Microporous and Mesoporous*, 129: 54–61.

Barth-Wirshing, U., Holler, H., Klammer, D. and Konrad, B. (1993), Synthetic Zeolites Formed from Expanded Perlite: Type Formation Conditions and Properties. *Mineral Petroleum,* 48: 275–294.

Barzetti, T. Selli, E. Moscotti D. and Forni, L. (1996), Pyridine and Ammonia as Probes for FTIR Analysis of Solid Acid Catalysts. *J. Chem. Soc., Faraday Trans.*, 92: 1401-1407

Bebon, C., Colson, D., Marrot, B., Klein, J. P., Renzo, F. D. (2002), Synthesis of Zeolites: Study and Applications of a New Process of Homogeneous Shaking out of the Medium to Minimize the Shear Rate during the Crystallization. *Microporous and Mesoporous Materials*, 53 13-20.

Benincasa, E., Brigatti, M. F., Medici, L. and Poppi, L. (2001), K-rich Rectorite from Kaolinized Micaschist of the Sesia-Lanzo Zone. *Italy Clay Mineral*, 36: 421–433.

Bergaya, F. and Lagaly, G. (2013), "Handbook of clay science". 2nd edition, 18-295, Amsterdam, Netherlands, Elsevier.

Bhatia, S. (1990), "Zeolite Catalysis: Principles and Applications". Boca Raton, Florida, CRC Press Inc.

Borade, R., Sayari, A., Adnot, A. and Kaliaguine, S. (1990), Characterization of Acidity in ZSM5 Zeolites: An X-ray Photoelectron and IR Spectroscopy Study. *Journal of Physical Chemistry*, 94: 5989-5994.

Bose, S. D., Saha, R. K. and Gupta, P. S. (2007), FCC Riser Hydrodynamics: Effect of some Operating Variables. *Indian Journal of Chemical Technology,* 14: 473– 480.

Cejka, J. Corma, A. and Zone, S. (2010), Zeolites and Catalysis, Synthesis, Reactions and Applications. WILEY-VCH Verlag GmbH & Co. KGaA, Weinheim.

Chen, P. (1977), "Tables of Key Lines in X – ray Powder Diffraction Patterns of Minerals in Clays and Associated Rocks". Indiana, Bloomington.

Christidis, G. E. and Papantoni, H. (2008), Synthesis of FAU Type Zeolite Y from Natural Raw Materials: Hydrothermal SiO2-Sinter and Perlite Glass. *The Open Mineralogy Journal*, 2: 1-5

David, T. W. (2007), Zeolites- Earliest Solid State Acids. *AU Journal of Tchnology*, 11(1): 36-41.

Ding, F., Ng, S. H., Xu, C. and Yui, S. (2007), Reduction of Light Cycle Oil in Catalytic Cracking of Bitumen-Derived Crude HGOs though Catalyst Selection. *Fuel Processing Technology*, 88: 833–845.

Du, X., Wang, Y., Su, X. and Li, J. (2009), Influences of pH Value on the Microstructure and Phase Transformation of Aluminium Hydroxide. *Powder Technology*, 192: 40–46.

Du, X., Zhang, H., Li, X., Tan, Z., Liu, H. and Gao, X. (2013), Cation Location and Migration in Lanthanum-Exchanged NaY zeolite. *Chinese Journal of Catalysis* 34: 1599–1607.

Dyer, A. (1988), "Introduction to Zeolite Molecular Sieves". 1: 65-80, England, John Wiley & Sons.

Edomwonyi-Otu, L. C. (2008), Effect of Salting Agent on the Production of Alum from Kankara Kaolin. Unpublished MSc. Thesis, Department of Chemical Engineering, Ahmadu Bello University, Zaria.

Edomwonyi-Otu, L. C., Aderemi, B. O., Ahmed, A. S., Coville, N. J. and Maaza, M. (2013), Influence of Thermal Treatment on Kankara Kaolinite. *Opticon1826*, 15(5): 1-5

El-Naggar, A. Y. (2013), Characterization of Modified and Polymer Coated Alumina Surfaces by Infrared Spectroscopy. *Journal of Spectroscopy*, 1: 1-5.

Erikh, V. N., Rasina, M. G. and Rudin, M. G. (1988), "The Chemistry and Technology of Petroleum and Gas". Moscow, Mir Publishers.

Fukushima, Y. (1980), Effect of Zeolite Additives in Feed on the Physiological Condition of Cows. *Chikusan no Kenkyu*, 33: 1393-1395.

Gao, X., Qin, Z., Wang, B., Zhao, X., Li, J., Zhao, H., Liu, H. and Shen, B. (2012), High silica REHY Zeolite with Low Rare Earth Loading as High Performance Catalyst for Oil Conversion. *Applied Catalysis A: General*, 413: 254–260.

Gary, J. H., and Handwerk, G. E. (2001), "Petroleum Refining: Technology and Economics". 4th edition, Florida, CRC Press. Boca Raton.

Ginter, D. M., Bell, A. T. and Radke, C. J. (1992), "Synthesis of Microporous Materials, Molecular Sieves". New York, Van Nostrand Reinhold.

Guglielmo, V. and Lara, R. (2007), "The Art of Cryogenics; Low-Temperature Experimental Technique". 1st edition, Burlington, USA, Elsevier.

Guisnet, M. and Ribeiro, F. R. (2002), Deactivation and Regeneration of Zeolite Catalyst. *Catalyst Science Series*, 9: 12-17

Hatakeyama, T. and Quinn, F. X. (1999), "Thermal Analysis Fundamentals and Applications to Polymer Science". 1: 25-40. England, John Wiley & Sons.

Htay, M. M. and Oo, M. M. (2008), Preparation of Zeolite Y Catalyst for Petroleum Cracking. *World Academy of Science, Engineering and Technology*, 24: 114-120

Iyoki, K. Itabashi, K. and Okubo, T. (2014), Progress in Seed-Assisted Synthesis of Zeolites Without Using Organic Structure-Directing Agents. *Microporous and Mesoporous Materials*, 189: 22–30.

Jia, L., Sun, X., Ye, X., Zou, C., Gu, H., Huang, Y., Niu, G. and Zhao, D. (2013). Core–Shell Composites of USY/Mesosilica: Synthesis and Application in Cracking Heavy Molecules with High Liquid Yield. *Microporous and Mesoporous Materials*, 176: 16–24.

Jiang, J., Duanmu, C., Yang, Y., Gu, X. and Chen, J. (2014), Synthesis and Characterization of High Siliceous ZSM5 Zeolite from Acid-Treated Palygorskite. *Powder Technology* ,251: 9–14.

Kemball, C., Dowden, D. A., Acres, G. J. K., Bird, A. J., Jenkins, J. W. and King, F. (1981), The Design and Preparation of Supported Catalysts. *Catalysis*, 4: 1-30.

Khabuanchalad, S., Prayoonpokarach, K. P. and Wittayakun, P. (2008), Transformation of Zeolite NaY Synthesized from Rice Husk Silica to NaP During Hydrothermal Synthesis. *Journal of Science and Technology*, 15(3): 225-231.

Kloprogge, J. T., Frost, R. L. and Hickey, L. (1999), "Infrared Absorption and Emission Study of Synthetic Mica–Montmorillonite in Comparison to Rectorite, Beidellite and Paragonite". *Journal of Materials Science Letters*, 18: 1921-1923.

Konwar, R. J. and De, M. (2013), Effects of Synthesis Parameters on Zeolite Templated Carbon for Hydrogen Storage Application. *Microporous and Mesoporous Materials*, 175: 16–24.

Lee, S. O., Jung, K. H., Oh, C. J., Lee, Y. H., Tran, T. and Kim, M. J. (2009), Precipitation of Fine Aluminium Hydroxide from Bayer Liquors. *Hydrometallurgy*, 98: 156–161.

Lee, J. S., Kim, H. S., Park, N., Lee, T. J. and Kang, M. (2013), Low Temperature Synthesis of α-Alumina from Aluminium Hydroxide Hydrothermally Synthesized using $[Al(C_2O_4)_x(OH)_y]$ Complexes. *Chemical Engineering Journal*, 230: 351–360.

Li, X., Li, C., Zhang, J., Yang, C. and Shan, H. (2007), Effects of Temperature and Catalyst to Oil Weight Ratio on the Catalytic Conversion of Heavy Oil to Propylene Using ZSM5 and USY Catalysts. *Journal of Natural Gas Chemistry*, 16: 92–99.

Ma, C. and Eggleton, R. A. (1999), Surface Layer Types of Kaolinite; a High Resolution Transmission Electron Microscope Study. *Clays and Clay Minerals*, 47: 181–191.

Ma, Y., Yan, C., Alshameri, A., Qiu, X., Zhou, C. and li, D. (2014), Synthesis and Characterization of 13X Zeolite from Low-Grade Natural Kaolin. *Advanced Powder Technology,* 25: 495–499

Mezni, M., Hamzaoui, A., Hamdi, N. and Srasra, E. (2011), Synthesis of Zeolites from the Low-Grade Tunisian natural Illite by Two Different Methods. *Applied Clay Science,* 52: 209–218

Modi, C. K. and Trivedi, P. M. (2012), Zeolite-Y Based Nanohybrid Materials: Synthesis, Characterization and Catalytic Aspects. *Microporous and Mesoporous Materials,* 155: 227–232.

Mravec, D. Hudec, J. and Janotka, H. (2005), Some Possibilities of Catalytic and Noncatalytic Utilization of Zeolites. *Chemistry Paper,* 59(1): 62 – 69.

Nam, L. T. H., Vinh, T. Q., Loan, N. T. T., Tho, V. D. S., Yang, X. and Su, S. (2011), Preparation of Bio-Fuels by Catalytic Cracking Reaction of Vegetable Oil Sludge. *Fuel,* 90: 1069–1075.

New York Times; Asia Pacific, (2011). Level of Radioactive Materials Rise Near Japanese Plant. By the Associated Press. New York, Published on April 16.

Ng, S. H., Zhu, Y., Humphies, A., Nakajima, N., Tsai, T. Y. R., Ding, F., Ling, H. and Yui, S. (2006), Key Observations from a Comprehensive FCC Study on Canadian Heavy Gas Oils from Various Origins: Yield Profiles in Batch Reactors. *Fuel Processing Technology,* 87: 475 – 485.

Oliver, R. W. (2000), The Coming Biotech Age: The Business of Bio-Materials. New York, McGraw Hill.

Pal, P., Das, J. K., Das, N. and Bandyopadhyay, S. (2013), Synthesis of NaP Zeolite at Room Temperature and Short Crystallization Time by Sonochemical Method. *Ultrasonics Sonochemistry,* 20: 314–321.

Panda, A. K., Misha, B. G., Misha, D. K. and Singh, R. K. (2010), Effect of Sulfuric Acid Treatment on the Physico-Chemical Characteristics of Kaolin Clay. *Colloids and Surfaces A: Physicochem. Eng. Aspects*, 363: 98–104.

Percival, H. J., Duncan, J. F. and Foster, P. K. (1974), Interpretation of the Kaolinite–Mullite Reaction Sequence from Infrared Absorption Spectra. *Journal of American Ceramic Society,* 57: 57–61.

Rahman, M. M., Hasnida, N. and Wan, N, W. B. (2009), Preparation of Zeolite Y Using Local Raw Material Rice Husk as a Silica Source. *Journal of Scientific Research*, 1(2): 285-291.

Reusch, W. (2013). Infrared Spectroscopy: http://www.chemistry.msu.edu/faculty/reusch. Retrieved on 07/01/2015.

Robson, H. (2001), "Verified Synthesis of Zeolitic Materials" 2nd edition. Published on behalf of the Synthesis Commission of the International Zeolite Association, Amsterdam, Netherlands, Elsevier.

Ruren, X. Gao, Z. Chen, J. and Wenfu, Y. (2007), "From Zeolites to Porous MOF Materials". 1: 168-414. Amsterdam, Netherlands, Elsevier.

Saceda, J. F., Rintramee, K., Khabuanchalad, S., Prayoonpokarach, S., De, R. L. and Wittayakun, J. (2012), Properties of Zeolite Y in Various Forms and Utilization as Catalyst or Supports for Cerium Oxide in Ethanol Oxidation. *Journal of Industrial and Engineering Chemistry*, 18(1): 420-424.

Sandeep, K., Saxena, M. K. and Nagabhatla, V. (2013), Studies on Textural Properties of Lanthanum-Exchanged Y Zeolites as Promising Materials for Value Upgradation of Jatropha Oil. *Journal of Material Science,* 48:7949–7959.

Sanden, S. C. T. (2003), "A Fundamental Study of Spray Drying Fluid Catalytic Cracking Catalyst". Universiteitsdrukkerij, Technische Universiteit, Eindhoven.

Santi D., Tobias H. T., Calemma V. and Weitkamp, J. (2013), High-Performance Ring-Opening Catalysts Based on Iridium-Containing Zeolite Beta in the Hydroconversion of Decalin. *Applied Catalysis A: General,* 455: 46– 57.

Serrano, D. P., Escola, J. M. and Pizarro, P. (2013), Synthesis Strategies in the Search for Hierarchical Zeolites. *Chemistry Society Review,* 42: 4004-4035.

Shen, Y., Zhao, P. and Shao, Q. (2014), Porous Silica and Carbon Derived Materials from Rice Husk Pyrolysis Char. *Microporous and Mesoporous Materials,* 188: 46–76.

Smith, J. V. (1988), Topochemistry of Zeolites and Related Materials: Topology and Chemistry. *Chemistry Review,* 88: 149-182.

Song, H., Wan, X., Dai, M., Zhang, J., Li, F. and Song, H. (2013), Deep Desulfurization of Model Gasoline by Selective Adsorption over Cu–Ce Bimetal Ion-Exchanged Y Zeolite. *Fuel Processing Technology*, 116: 52–62.

Speight, J. G. (1999), "The Chemistry and Technology of Petroleum". New York, Marcel Dekker Inc.

Steudel, A., Batenburg, L. F., Fischer, H. R., Weidler, P. G. and Emmerich, K. (2009), Alteration of Swelling Clay Minerals by Acid Activation. *Applied Clay Science,* 44: 105–115.

Tatrai, E., Bacsy, E., Kárpáti, J. and Ungvary, G. (1992), On the Examination of the Pulmonary Toxicity of Mordenite in Rats. *Polish Journal of Occupational Medical Environmental Health*, 5: 237–243.

Taufiqurrahmi, N., Mohamed, A. R. and Bhatia, S. (2010), Deactivation and Coke Combustion Studies of Nanocrystalline Zeolite Beta in Catalytic Cracking of Used Palm Oil. *Chemical Engineering Journal*, 163: 413–421.

Treacy, M. M. J. and Higgins, J. B. (2001), "Collection of Simulated XRD Powders for Zeolites". Published on behalf of the Synthesis Commission of the International Zeolite Association, Amsterdam, Netherlands, Elsevier.

Uddin, J. (2012). Macro To Nano Spectroscopy. Rijeka, Croatia, InTech Publication ISBN: 978-953-51-0664-7.

Valtchev, V., Majano, G., Mintova, S., and Perez-Ramirez, J. (2013), Tailored Crystalline Microporous Materials by Post-Synthesis Modification. *Chemistry Society Review*, 42: 263–290.

Vermeiren, W., and Gilson, J. P. (2009), Impact of Zeolites on the Petroleum and Petrochemical Industry. *Topics in Catalysis*, *52*: 1131–1161.

Virta, L. R. (2012), "Zeolites: Mineral Commodity Summaries". A report by United States Geological Survey, USA.

Wajima, T., Hagaa, M., Kuzawa, K., Ishimoto, H.,Tamadaa, O., Ito, K., Nishiyama, T., Downs, R. T. and Rakovan, J. F. (2006), Zeolite Synthesis from Paper Sludge Ash at Low Temperature (90˚C) With Addition of Diatomite. *Journal of Hazardous Materials*, B132 : 244–252

Wilson, J. W. (1997), "Fluid Catalytic Cracking Technology and Operation". Tulsa, PennWell Books.

Xu, R., Pang, W., Yu, J., Huo, Q. and Chen, J. (2007), "Chemistry of Zeolites and Related Porous Materials: Synthesis and Structure". John Wiley & Sons (Asia) Pte Ltd, Singapore.

Zhang, Y., Liu, Y. and Li, Y. (2008), Synthesis and Characteristics of Y-Zeolite/MCM-48 Biporous Molecular Sieve. *Applied Catalysis A: General*, 345: 73–79.

APPENDIX A

Detail Calculations for the Dealumination of Metakaolin

Generally dealumination reaction of kaolin using sulphuric acid can be expressed as in Equation (A1).

$$Al_2O_3 \bullet 2SiO_2 + 3H_2SO_4 \longrightarrow Al_2(SO_4)_3 + 2SiO_2 + 3H_2O \qquad (A1)$$

During the dealumination process only the alumina component of the metakaolin takes place in the reaction with sulphuric acid, the silica component is inert. Therefore, the actual reactive component of the dealumination reaction can be expressed as in Equation (A2).

$$Al_2O_3 + 3H_2SO_4 \longrightarrow Al_2(SO_4)_3 + 2SiO_2 + 3H_2O \qquad (A2)$$

Stoichiometric Mass: 102g 294g

Using the XRF result of 32.94 wt% of Al_2O_3 in the metakaolin.

Taking a 50 g metakaolin basis for each batch of dealumination.

Calculations:

Amount of Al_2O_3 the 50 g metakaolin = 0.3294 x 50

= 16.47g Al_2O_3

Weight of acid needed (assuming 100% concentration H_2SO_4) = 16.47 g x 294/102 = 47.47 g

However, the concentration of the H_2SO_4 used was 98%. Therefore the weight of 98% Conc acid needed = 100/98 x 47.47 g = 48.44 g

Density of the acid ρ, was given as 1.84 g/cm^3. Hence, the volume of acid needed for each batch of dealumination V, was calculated as;

$$V = m/\rho \qquad (A3)$$

$$= 47.47/ 1.84 = 25.80 \text{ cm}^3$$

The dealumination reaction was carried out in stoichiometric excess acid ratio. Therefore, the amount of acid depends on the acid excess ratio intended. The ratios considered in this work

were 1:2, 1:3, 1:4 and 1:5 stoichiometric ratio of alumina – acid. These ratio were referred to in this work as 1, 2, 3, 4 and 5 folds respectively. These also mean 100, 200, 300, 400 and 500% stoichiometric excess acid.

Therefore, in order to establish a generalized formula for the dealumination. Assuming F to be the number of fold of a batch dealumination of 50 g metakaolin, it follows that;

$$\text{Volume of acid needed } V = 25.80\ F\ cm^3 \quad \text{(A4)}$$

The dealumination was carried out using 60 wt% concentration of acid as reported by Edomwonyi-Otu, (2008).

To prepare a 60 wt% acid it follows that;

$$M_1C_1 = M_2C_2 \quad \text{(A5)}$$

Where M_1 and M_2 were the mass of the acid-water mixture at concentration C_1 and C_2 respectively.

$$M_{98\%}\ C_{98\%} = M_{60\%}\ C_{60\%} \quad \text{(A6)}$$

From Equation (A3) it follows that $M = V\ \rho$

Hence,

$$(V_1\ \rho_1) \times 98\% = (V_2\ \rho_2) \times 60\% \quad \text{(A7)}$$

The density of the 60 wt% acid was determined as 1.51 g/cm^3 (Edomwonyi-Otu, 2008)

Substituting these into Equation (A7) we have;

$$V_{60\%} = (1.84 \times (25.80\ F) \times 60\%)/\ 1.51 \times 60$$

$$= 51.3494\ F\ cm^3$$

Since the amount of the 98 wt% acid needed was 25.80 F cm^3

And the of the acid-water mixture was calculated as 51.3494 F cm^3

Therefore, the amount of water used was obtained as follows;

$$M_{mix} = M_w + M_{acid\ (98\%)} \quad \text{(A8)}$$

$$M_w = M_{mix} - M_{acid\ (98\%)}$$

It implies; $V_w \rho_w = V_{mix} \rho_{mix} - V_{acid\ (98\%)} \rho_{acid\ (98\%)}$

Taking ρ_w as 1 g/cm^3

$V_w = 1.51 \times 51.3494\ F - 1.84 \times 25.80\ F$

$= 30.08\ F\ cm^3$

Therefore, the dealumination parameter can be summarized as follows;

Amount of netakaolin per batch: 50 g

Volume of acid (98% Concentrated sulphuric acid): 25.80 F C

Volume of distilled water: 30.08 F cm^3

Further summary of the dealumination parameter are presented in Table A1.

Table A1. Summary of dealumination parameters.

Dealumination Fold	**Volume of 98% Conc. Acid (cm^3)**	**Volume of distilled water (cm^3)**
2	51.6	60.16
3	77.4	90.24
4	103.2	120.32
5	129	150.4

APPENDIX B

GCMS Online-Gas and Liquid Analyses Data Obtained for the Cracking of Hexadecane

The cracking results obtained based on the online GCMS analyses of the gaseous and the liquid products collected.

Gas analysis

The data presented here are the raw data obtained from the analysis of the GCMS results and was based on the wt% of the feed model oil.

Yield of the gaseous stream

The Yield of the gaseous stream was interpreted as presented in the data below

Sum of the (CO_2 + CO + C_1 to C_4) wt% was interpreted as the yield of the gaseous product.

Yield of the liquid stream

The yield of the liquid stream was calculated as follows;

Y_l = ——

Where G = Sum total of the yield of products in the gaseous stream,

D = sum of the yield of products in the liquid stream. For Gasoline fraction; D = $C_4 – C_{12}$

All yields were calculated with respect to the mass of the feed.

The conversion was calculated as; X = 100 - ——

Table B1. GCMS gas analysis for Commercial Catalyst Y at 300˚C

Components	Wt%
CO_2	0.01
CO	0.10
C_1	0.01
C_2	-
C_2^1	0.02
C_3	0.02
C_3^1	0.06
iC_4	0.06
C_4	0.01
C_4^1	0.08
iC_5	0.01
C_5	0.01
C_5^1	0.01
C_6	0.04

Table B2. GCMS liquid analysis for Commercial Catalyst Y at 300˚C

Saturates				Unsaturates		Aromatics	Unknown	Total
Carbon Number	**Cyclic**	**Iso**	**Normal**	**Cyclic**	**Normal + Iso**			
1								
2								
3								
4								
5								
6								
7		0.08						**0.08**
8		0.11						**0.11**
9								
10		0.02						**0.02**
11						0.02		**0.02**
12								
13								
14							0.05	**0.05**
15			0.11				0.27	**0.38**
16			96.68				0.37	**97.05**
17			0.38				1.81	**2.19**
18							0.07	**0.07**
19							0.02	**0.02**
20							-	
Total		**0.21**	**97.17**			**0.02**	**2.60**	**100.0**

Table B3. GCMS gas analysis for Commercial Catalyst Y at 400˚C

Components	Wt%
CO_2	4.25
CO	0.0
C_1	0.04
C_2	0.04
C_2^1	0.26
C_3	0.47
C_3^1	1.89
iC_4	0.09
C_4	0.62
C_4^1	1.19
iC_5	0.02
C_5	0.02
C_5^1	0.08
C_6	0.06

Table B4. GCMS liquid analysis for Commercial Catalyst Y at 400˚C

Saturates				Unsaturates		Aromatics	Unknown	Total
Carbon Number	**Cyclic**	**Iso**	**Normal**	**Cyclic**	**Normal + Iso**			
1								
2								
3								
4			0.01		0.04			**0.05**
5		0.01	0.04		0.25		0.02	**0.32**
6	0.01	0.02	0.11	0.11	0.18			**0.43**
7		0.05	0.27		0.07	0.02		**0.41**
8		0.01	0.47				0.03	**0.51**
9			0.53					**0.53**
10		0.03	0.54					**0.57**
11			0.57			0.01		**0.58**
12			0.54					**0.54**
13			0.41					**0.41**
14			0.10				0.02	**0.12**
15			0.09				0.45	**0.54**
16			94.12				0.47	**94.59**
17			0.30					**0.30**
18								
19								
20							0.10	**0.11**
TOTAL	**0.01**	**0.12**	**98.10**	**0.11**	**0.54**	**0.03**	**1.09**	**100.00**

Table B5. GCMS gas analysis for Commercial Catalyst Y at 500˚C

Components	Wt%
CO_2	5.28
CO	0.3
C_1	0.04
C_2	0.04
C_2^1	0.26
C_3	1.28
C_3^1	2.60
iC_4	0.89
C_4	1.02
C_4^1	2.29
iC_5	0.8
C_5	0.6
C_5^1	1.20
C_6	0.06

Table B6. GCMS liquid analysis for Commercial Catalyst Y at 500˚C

Saturates				Unsaturates		Aromatics	Unknown	Total
Carbon	**Cyclic**	**Iso**	**Normal**	**Cyclic**	**Normal + Iso**			
1								
2								
3								
4	0.02	0.80	1.20		0.04			**2.06**
5	0.01	0.12	0.80	0.62	1.25		0.01	**2.81**
6	0.01	0.16	0.21	0.11	2.18	1.40		**4.07**
7	0.62	0.18	0.47	0.62	1.07	0.78		**3.74**
8	0.32	0.01	0.47	0.40	0.86	0.60	0.01	**2.67**
9			0.73		0.42	0.20		**1.35**
10		0.03	0.54					**0.57**
11			0.57			0.01		**0.58**
12			0.54					**0.54**
13			0.41					**0.41**
14			0.10				0.02	**0.12**
15			0.09				0.32	**0.41**
16			80.10				0.27	**80.37**
17			0.30					**0.30**
18								
19								
20								
TOTAL	**0.98**	**1.30**	**86.53**	**1.75**	**5.82**	**2.99**	**0.63**	**100.0**

Table B7. GCMS gas analysis for Zeo-AY Cat Y at 300˚C

Components	Wt%
CO_2	0.0
CO	0.0
C_1	0.03
C_2	0.0
C_2^1	0.04
C_3	0.07
C_3^1	0.07
iC_4	0.03
C_4	0.03
C_4^1	0.12
iC_5	0.0
C_5	0.01
C_5^1	0.0
C_6	0.1

Table B8. GCMS liquid analysis for Zeo-AY Cat Y at 300˚C

Saturates				Unsaturates		Aromatics	Unknown	Total
Carbon Number	**Cyclic**	**Iso**	**Normal**	**Cyclic**	**Normal + Iso**			
1								
2								
3								
4			0.01		0.02			**0.03**
5		0.03	0.05		0.15		0.02	**0.25**
6		0.05	0.12	0.10	0.12			**0.39**
7		0.07	0.11		0.23			**0.41**
8		0.08	0.07					**0.15**
9	0.01							**0.01**
10			0.03					**0.03**
11			0.02				0.21	**0.23**
12								
13							0.01	**0.01**
14								
15			0.09				0.13	**0.22**
16			97.98				0.30	**98.28**
17								
18								
19								
TOTAL	**0.01**	**0.23**	**98.48**	**0.10**	**0.52**		**0.67**	**100.01**

Table B9. GCMS gas analysis for Zeo-AY Cat Y at 400˚C

Components	Wt%
CO_2	1.68
CO	0.00
C_1	0.08
C_2	0.05
C_2^1	0.48
C_3	1.68
C_3^1	1.88
iC_4	0.42
C_4	0.42
C_4^1	1.88
iC_5	0.02
C_5	0.11
C_5^1	0.14
C_6	0.14

Table B10. GCMS liquid analysis for Zeo-AY Cat Y at 400˚C

Saturates				Unsaturates		Aromatics	Unknown	Total
Carbon Number	**Cyclic**	**Iso**	**Normal**	**Cyclic**	**Normal + Iso**			
1								
2			0.07					**0.07**
3			0.10					**0.10**
4		0.12	0.28		0.97			**1.37**
5	0.02	0.26	1.03	0.04	2.15		0.01	**3.51**
6	0.34	0.37	1.24	0.22	2.14		0.02	**4.33**
7	0.20	0.98	1.02		1.70	0.82	0.08	**4.80**
8	0.08	0.24	0.63		1.17	0.72	0.01	**2.85**
9	0.04	0.06	0.20		0.08	0.22		**0.60**
10	0.06	0.27	0.18			0.25		**0.76**
11			0.18			0.04		**0.22**
12			0.12					**0.12**
13			0.08					**0.08**
14							0.02	**0.02**
15			0.15				0.18	**0.33**
16			80.02				0.78	**80.80**
17								
18							0.04	**0.04**
19								
20								
TOTAL	**0.74**	**2.30**	**85.30**	**0.26**	**8.21**	**2.05**	**1.14**	**100.0**

Table B11. GCMS gas analysis for Zeo-AY Cat Y at 500˚C

Components	Wt%
CO_2	2.41
CO	0.00
C_1	0.10
C_2	0.07
C_2^1	0.60
C_3	2.21
C_3^1	2.13
iC_4	0.56
C_4	0.44
C_4^1	2.31
iC_5	0.05
C_5	0.11
C_5^1	0.18
C_6	0.16

Table B12. GCMS liquid analysis for Zeo-AY Cat Y at 500˚C

Saturates				Unsaturates		Aromatics	Unknown	Total
Carbon Number	**Cyclic**	**Iso**	**Normal**	**Cyclic**	**Normal + Iso**			
1								
2			0.07					**0.07**
3			0.10					**0.10**
4		0.18	0.48		0.97			**1.64**
5	0.04	0.46	1.13	0.04	3.45		0.08	**5.21**
6	0.33	0.67	1.56	0.87	3.12		0.10	**6.64**
7	0.30	1.28	1.18		2.93	0.82	0.28	**6.78**
8	0.72	0.34	0.83		1.27	1.46	0.41	**5.04**
9	0.08	0.16	0.44		0.08	0.72		**1.48**
10	0.08	0.47	0.29			0.25		**1.09**
11			0.23			0.04		**0.26**
12			0.16					**0.16**
13			0.08					**0.08**
14							0.02	**0.02**
15			0.15				0.28	**0.43**
16			70.02				0.93	**70.95**
17								
18							0.04	**0.04**
19								
20								
TOTAL	**1.56**	**3.56**	**76.73**	**0.91**	**11.83**	**3.28**	**2.14**	**100.0**

Table B13. GCMS gas analysis for Zeo-AY Cat Y + ZSM5 at 300˚C

Components	Wt%
CO_2	0.29
CO	1.58
C_1	0.03
C_2	0.2
C_2^1	0.07
C_3	1.60
C_3^1	2.04
iC_4	0.45
C_4	0.53
C_4^1	2.94
iC_5	0.07
C_5	0.21
C_5^1	0.16
C_6	0.17

Table B14. GCMS liquid analysis for Zeo-AY Cat Y + ZSM5 at 300˚C

Saturates				Unsaturates		Aromatics	Unknown	Total
Carbon Number	**Cyclic**	**Iso**	**Normal**	**Cyclic**	**Normal + Iso**			
1								
2								
3			0.03					**0.03**
4		0.07	0.28		0.55			**0.90**
5		0.20	0.86	0.02	2.06			**3.14**
6	0.04	0.39	1.13	0.82	1.30	0.04		**3.72**
7		0.79	0.71		1.58		0.06	**3.14**
8	0.05	0.11	0.32		0.49			**0.97**
9		0.03	0.14		0.04			**0.21**
10		0.02	0.10					**0.12**
11		0.03	0.06					**0.09**
12			0.03					**0.03**
13			0.02					**0.02**
14		0.02	0.02					**0.04**
15			0.09					**0.09**
16			87.23		0.02			**87.25**
17			0.25					**0.25**
18								
TOTAL	**0.09**	**1.66**	**91.27**	**0.84**	**6.04**	**0.04**	**0.06**	**100.0**

Table B15. GCMS gas analysis for Zeo-AY Cat Y + ZSM5 at 400˚C

Components	Wt%
CO_2	0.11
CO	2.28
C_1	0.33
C_2	0.20
C_2^1	3.41
C_3	3.87
C_3^1	8.32
iC_4	0.57
C_4	0.44
C_4^1	3.83
iC_5	0.04
C_5	0.07
C_5^1	0.05
C_6	0.07

Table B16. GCMS liquid analysis for Zeo-AY Cat Y + ZSM5 at 400˚C

Saturates				Unsaturates		Aromatics	Unknown	Total
Carbon Number	**Cyclic**	**Iso**	**Normal**	**Cyclic**	**Normal + Iso**			
1								
2			0.09					**0.09**
3			0.06					**0.06**
4		0.08	0.26		0.81			**1.15**
5	0.09	0.18	0.53	0.02	2.03		0.05	**2.90**
6	0.31	0.16	0.93	0.35	1.03	0.19	0.16	**3.13**
7	0.13	0.16	1.63		0.34	1.44	0.09	**3.79**
8	0.03	0.02	1.95		0.15	2.27		**4.42**
9			1.67			0.77		**2.44**
10		0.06	1.36			0.09		**1.51**
11			1.23					**1.23**
12		0.02	0.96					**0.98**
13			0.55					**0.55**
14			0.09					**0.09**
15			0.08					**0.08**
16			77.34					**77.34**
17			0.23					**0.23**
18			0.01					**0.1**
TOTAL	**0.56**	**0.68**	**88.97**	**0.37**	**4.36**	**4.76**	**0.30**	**100.0**

Table B17. GCMS gas analysis for Zeo-AY Cat Y + ZSM5 at 500˚C

Components	Wt%
CO_2	0.17
CO	3.28
C_1	0.43
C_2	0.28
C_2^1	4.02
C_3	4.68
C_3^1	9.88
iC_4	0.87
C_4	0.42
C_4^1	5.86
iC_5	0.06
C_5	0.09
C_5^1	0.25
C_6	0.04

Table B18. GCMS liquid analysis for Zeo-AY Cat Y + ZSM5 at 500˚C

Saturates				Unsaturates		Aromatics	Unknown	Total
Carbon Number	**Cyclic**	**Iso**	**Normal**	**Cyclic**	**Normal + Iso**			
1								
2			0.06					**0.06**
3			0.08					**0.08**
4		0.12	0.32		0.41			**0.85**
5	0.09	0.26	0.76	0.01	2.83		0.02	**3.97**
6	0.44	0.21	1.24	0.30	2.46	0.19	0.12	**4.96**
7	0.22	0.24	2.46	0.02	0.32	2.58	0.07	**5.91**
8	0.03	0.06	0.48	0.10	0.10	3.20	0.01	**3.98**
9		0.02	2.48			2.64	0.02	**5.16**
10		0.06	1.86	0.01		0.09		**2.02**
11		0.01	1.73		0.01	0.02		**1.77**
12		0.02	0.24		0.02	0.01		**0.29**
13		0.08	0.72					**0.80**
14		0.02	0.11		0.10			**0.23**
15		0.77	0.08	0.10				**0.95**
16		0.08	67.87	0.01	0.20			**68.16**
17	0.02	0.48	0.28				0.02	**0.80**
18			0.01					**0.01**
TOTAL	**0.80**	**2.43**	**80.78**	**0.55**	**6.45**	**8.73**	**0.26**	**100.0**

Table B19. GCMS gas analysis for Zeo-CY Cat Y at 400˚C

Components	Wt%
CO_2	0.01
CO	2.38
C_1	3.58
C_2	3.86
C_2^1	5.89
C_3	5.23
C_3^1	7.86
iC_4	0.32
C_4	0.26
C_4^1	2.08
iC_5	0.03
C_5	0.02
C_5^1	0.10
C_6	0.12

Table B20. GCMS liquid analysis for Zeo-CY Cat Y at 400˚C

Saturates				Unsaturates		Aromatics	Unknown	Total
Carbon Number	**Cyclic**	**Iso**	**Normal**	**Cyclic**	**Normal + Iso**			
1								
2								
3			0.08					**0.08**
4		0.01	0.12		0.31		0.20	**0.64**
5	0.80	0.12	0.24	0.05	1.08		0.84	**3.13**
6	0.28	0.12	0.38	0.32	1.62	0.89	0.34	**3.95**
7	0.16	0.18	0.48		0.98	2.98	0.64	**5.42**
8	0.22	0.21	0.47	0.01	0.21	3.45	1.02	**5.59**
9	0.16	0.04	0.34		0.16	1.23	0.20	**2.13**
10	0.22	0.01	0.28	0.01	0.08	0.38	0.01	**0.99**
11		0.10	0.16		0.16	0.01	0.01	**0.44**
12		0.01	0.18	0.02	0.11	0.04	0.46	**0.82**
13		0.01	0.14		0.10		0.02	**0.27**
14			0.02	0.01			0.62	**0.65**
15		0.01	0.11		0.26		0.04	**0.42**
16			75.42					**75.42**
17			0.01				0.02	**0.03**
18			0.01					**0.01**
19			0.01					**0.01**
TOTAL	**1.84**	**0.82**	**78.45**	**0.42**	**5.07**	**8.98**	**4.42**	**100.00**

Table B21. GCMS gas analysis for Zeo-CY Cat Y at 500˚C

Components	Wt%
CO_2	0.05
CO	5.64
C_1	6.23
C_2	5.81
C_2^1	12.19
C_3	7.14
C_3^1	10.23
iC_4	0.26
C_4	0.47
C_4^1	3.55
iC_5	0.03
C_5	0.07
C_5^1	0.17
C_6	0.14

Table B22. GCMS liquid analysis for Zeo-CY Cat Y at 500˚C

Saturates				Unsaturates		Aromatics	Unknown	Total
Carbon Number	**Cyclic**	**Iso**	**Normal**	**Cyclic**	**Normal + Iso**			
1								
2								
3			0.17					**0.17**
4		0.06	0.26		0.70			**1.02**
5	0.13	0.16	0.47	0.05	2.56		0.38	**3.75**
6	0.41	0.04	0.56	0.71	2.40	1.55	0.46	**6.13**
7	0.39	0.24	0.79		1.98	4.98	0.39	**8.77**
8	0.39	0.33	0.65		0.44	6.52	0.15	**8.48**
9	0.32	0.14	0.48		0.34	2.34	0.14	**3.76**
10	0.41	0.11	0.41		0.24	0.64	0.09	**1.90**
11		0.10	0.38		0.25		0.28	**1.01**
12		0.11	0.32		0.13	0.19	0.72	**1.47**
13			0.25		0.13		0.57	**0.95**
14			0.09				0.47	**0.56**
15			0.12		0.53		0.22	**0.87**
16			60.42				0.20	**60.62**
17			0.01					**0.01**
18							0.45	**0.45**
19			0.03				0.05	**0.08**
TOTAL	**2.05**	**1.29**	**65.41**	**0.76**	**9.70**	**16.22**	**4.57**	**100.0**

Table B23. GCMS gas analysis for Zeo-CY Cat Y at 550˚C

Components	Wt%
CO_2	0.04
CO	0.00
C_1	1.36
C_2	1.82
C_2^1	2.79
C_3	4.55
C_3^1	4.96
iC_4	3.68
C_4	1.71
C_4^1	2.62
iC_5	0.24
C_5	0.15
C_5^1	0.33
C_6	0.11

Table B24. GCMS liquid analysis for Zeo-CY Cat Y at 550˚C

Saturates				Unsaturates		Aromatics	Unknown	Total
Carbon Number	**Cyclic**	**Iso**	**Normal**	**Cyclic**	**Normal + Iso**			
1								
2								
3								
4								
5			0.02				0.01	**0.03**
6	0.12	0.12	0.13	0.08	0.12	0.36	0.04	**0.97**
7	0.37	0.32	0.40		0.64	6.34	0.25	**8.32**
8	0.44	0.41	0.49		0.14	16.00	0.23	**17.71**
9	0.23	0.17	0.38		0.24	8.94	0.55	**10.51**
10	0.21	0.94	0.33		0.01	2.31	0.79	**4.59**
11		1.21	0.36			0.57	2.42	**4.56**
12		0.68	0.40			0.23	2.61	**3.92**
13		0.04	0.22		0.01		1.01	**1.28**
14			0.07		0.30		1.17	**1.54**
15					0.02		0.73	**0.75**
16			45.77				0.03	**45.80**
17	0.01		0.01					**0.02**
18								
TOTAL	**1.38**	**3.89**	**48.58**	**0.08**	**1.48**	**34.75**	**9.84**	**100.0**

Table B25. GCMS gas analysis for Zeo-BY Cat Y at 400˚C

Components	Wt%
CO_2	0.08
CO	0.11
C_1	0.07
C_2	0.03
C_2^1	0.16
C_3	1.04
C_3^1	1.43
iC_4	0.38
C_4	0.32
C_4^1	1.89
iC_5	0.07
C_5	0.12
C_5^1	0.06
C_6	0.18

Table B26. GCMS liquid analysis for Zeo-BY Cat Y at 400˚C

Saturates				Unsaturates		Aromatics	Unknown	Total
Carbon Number	**Cyclic**	**Iso**	**Normal**	**Cyclic**	**Normal + Iso**			
1								
2								
3								
4		0.03	0.10		0.19			**0.32**
5		0.14	0.51	0.02	1.23			**1.90**
6	0.05	0.30	0.95	0.63	0.90	0.05	0.03	**2.91**
7		0.73	0.67		1.41	0.03	0.05	**2.89**
8	0.16	0.41	0.34		0.22	0.02	0.06	**1.21**
9	0.03	0.02	0.16		0.03	0.04		**0.28**
10	0.02	0.10	0.11					**0.23**
11		0.02	0.07					**0.09**
12			0.04					**0.04**
13			0.02					**0.02**
14							0.02	**0.02**
15			0.09					**0.09**
16			89.72		0.02		0.26	**90.00**
17								
18								
TOTAL	**0.26**	**1.75**	**92.78**	**0.65**	**4.00**	**0.14**	**0.42**	**100.00**

Table B27. GCMS gas analysis for Zeo-BY Cat Y at 500˚C

Components	Wt%
CO_2	5.70
CO	0.13
C_1	0.08
C_2	0.12
C_2^1	2.57
C_3	4.39
C_3^1	5.88
iC_4	0.97
C_4	0.60
C_4^1	3.16
iC_5	0.08
C_5	0.10
C_5^1	0.06
C_6	0.06

Table B28. GCMS liquid analysis for Zeo-BY Cat Y at 500˚C

Saturates				Unsaturates		Aromatics	Unknown	Total
Carbon Number	**Cyclic**	**Iso**	**Normal**	**Cyclic**	**Normal + Iso**			
1								
2								
3								
4					0.12			**0.12**
5			0.04		0.15		0.20	**0.39**
6	0.09	0.04		0.15	0.16	0.04	0.11	**0.59**
7		0.05	0.68		0.12	1.18	0.04	**2.07**
8		0.18	1.48		0.14	3.21	0.09	**5.10**
9		0.12	1.66			0.95	0.04	**2.77**
10	0.08	1.13	1.35		0.09	0.32	0.08	**3.05**
11			1.20		0.09			**1.29**
12		0.05	0.87		0.06		0.14	**1.12**
13			0.45		0.08		0.03	**0.56**
14			0.08		0.11		0.20	**0.39**
15			0.09		0.01		0.10	**0.20**
16		0.27	81.40				0.31	**81.98**
17			0.32				0.05	**0.37**
18								
TOTAL	**0.17**	**1.84**	**89.62**	**0.15**	**1.13**	**5.70**	**1.39**	**100.00**

Table B29. GCMS gas analysis for Zeo-BY Cat Y at 550˚C

Components	Wt%
CO_2	6.20
CO	0.18
C_1	0.12
C_2	0.17
C_2^1	2.89
C_3	5.12
C_3^1	6.24
iC_4	1.24
C_4	0.96
C_4^1	4.64
iC_5	0.18
C_5	0.19
C_5^1	0.12
C_6	0.12

Table B30. GCMS liquid analysis for Zeo-BY Cat Y at 500˚C

Saturates				Unsaturates		Aromatics	Unknown	Total
Carbon Number	**Cyclic**	**Iso**	**Normal**	**Cyclic**	**Normal + Iso**			
1								
2								
3								
4					0.08			**0.08**
5	0.62		0.08		0.16		0.01	**0.87**
6	0.12	0.08		0.11	0.12	0.08	0.02	**0.53**
7		0.12	0.79		0.15	1.46	0.01	**2.53**
8		0.24	2.42	0.01	0.11	4.26		**7.04**
9		0.21	2.68			1.32	0.01	**4.22**
10	0.16	2.10	1.45	0.02	0.11	0.16		**4.00**
11		0.30	1.68	0.06	0.12	0.20	0.02	**2.38**
12	0.13	0.08	1.24		0.09	0.12	0.03	**1.69**
13		1.26	0.97	0.14	0.12		0.01	**2.50**
14		0.82	0.16		0.16		0.03	**1.17**
15	0.24	0.01	0.15	0.11	0.03			**0.54**
16	0.45	0.34	71.44	0.01				**72.24**
17			0.21					**0.21**
18								
TOTAL	**1.72**	**5.56**	**83.27**	**0.46**	**1.25**	**7.60**	**0.14**	**100.00**

Table B31. GCMS gas analysis for Zeo-BY Cat Y + ZSMS at 400˚C

Components	Wt%
CO_2	0.0
CO	0.0
C_1	0.01
C_2	0.02
C_2^1	0.32
C_3	0.62
C_3^1	1.21
iC_4	0.12
C_4	0.08
C_4^1	0.62
iC_5	0.01
C_5	0.02
C_5^1	0.07
C_6	0.02

Table B32. GCMS gas analysis for Zeo-BY Cat Y + ZSMS at 400˚C

Saturates				Unsaturates		Aromatics	Unknown	Total
Carbon Number	**Cyclic**	**Iso**	**Normal**	**Cyclic**	**Normal + Iso**			
1								
2								
3			0.01					**0.01**
4		0.02	0.14	0.01	0.16		0.23	**0.56**
5	0.01		0.32	0.01	0.87		0.02	**1.23**
6	0.01	0.01	0.03	0.02	0.95	0.24	0.24	**1.50**
7	0.01	0.12	0.74		0.14	1.68	0.37	**3.06**
8	0.64	0.08	0.02	0.01	0.02	1.89	0.31	**2.97**
9		0.01	0.38	0.12	0.10	0.75	0.26	**1.62**
10	0.02	0.03	0.26	0.01		0.11		**0.43**
11	0.03	0.02	0.17	0.04	0.01		0.23	**0.50**
12	0.01	0.02	0.24	0.02		0.01		**0.30**
13			0.11	0.02	0.02		0.61	**0.76**
14		0.01	0.02	0.01			0.20	**0.24**
15			0.02		0.01	0.01	0.03	**0.07**
16			86.32	0.01			0.24	**86.57**
17		0.01	0.03		0.02	0.10		**0.16**
18			0.01				0.01	**0.02**
TOTAL	**0.73**	**0.33**	**88.82**	**0.28**	**2.30**	**4.79**	**2.75**	**100.00**

Table B33. GCMS gas analysis for Zeo-BY Cat Y + ZSMS at 500˚C

Components	Wt%
CO_2	0.0
CO	0.0
C_1	0.03
C_2	0.03
C_2^1	0.65
C_3	0.81
C_3^1	1.62
iC_4	0.17
C_4	0.12
C_4^1	0.80
iC_5	0.03
C_5	0.04
C_5^1	0.09
C_6	0.07

Table B34. GCMS liquid analysis for Zeo-BY Cat Y + ZSMS at 500˚C

Saturates				Unsaturates		Aromatics	Unknown	Total
Carbon Number	**Cyclic**	**Iso**	**Normal**	**Cyclic**	**Normal + Iso**			
1								
2								
3			0.03					**0.03**
4		0.09	0.26		0.44			**0.79**
5	0.10		0.70	0.03	1.96		0.50	**3.29**
6		0.03	0.08	0.25	2.38	0.44	0.66	**3.84**
7	0.03	0.38	0.81		0.40	2.47	0.27	**4.36**
8	0.85	0.20				3.54	0.06	**4.65**
9			0.57		0.14	1.37		**2.08**
10		0.05	0.43			0.21	0.05	**0.74**
11	0.03	0.05	0.39				0.10	**0.57**
12		0.01	0.31			0.03	0.09	**0.44**
13			0.16				0.05	**0.21**
14			0.04				0.04	**0.08**
15			0.04				0.21	**0.25**
16			78.45					**78.45**
17			0.03					**0.03**
18							0.19	**0.19**
TOTAL	**1.01**	**0.81**	**82.30**	**0.28**	**5.32**	**8.06**	**2.22**	**100.00**

Table B35. GCMS gas analysis for Zeo-BY Cat Y + ZSMS at 550˚C

Components	Wt%
CO_2	0.01
CO	0.00
C_1	0.41
C_2	0.43
C_2^1	3.20
C_3	3.25
C_3^1	5.95
iC_4	0.30
C_4	0.29
C_4^1	1.64
iC_5	0.04
C_5	0.00
C_5^1	0.03
C_6	0.05

Table B36. GCMS liquid analysis for Zeo-BY Cat Y + ZSMS at 550˚C

Saturates				Unsaturates		Aromatics	Unknown	Total
Carbon Number	**Cyclic**	**Iso**	**Normal**	**Cyclic**	**Normal + Iso**			
1								
2								
3			0.28				0.02	**0.30**
4		0.07	0.26		1.04			**1.37**
5	0.09	0.08	0.44	0.02	1.62		0.03	**2.28**
6	0.14	0.02	0.79	0.21	0.41	0.86	0.27	**2.70**
7		0.02	1.14		0.11	2.86	0.01	**4.14**
8			1.20			2.18		**3.38**
9			0.95			0.27		**1.22**
10			0.77			0.02		**0.79**
11			0.68			0.09		**0.77**
12			0.49			0.07		**0.56**
13			0.28					**0.28**
14			0.07					**0.07**
15			0.03				1.50	**1.53**
16			78.65				1.79	**80.44**
17								
18			0.17					**0.17**
TOTAL	**0.23**	**0.19**	**86.20**	**0.23**	**3.18**	**6.35**	**3.62**	**100.00**

Table B37. GCMS gas analysis for Zeo-CY Cat Y +ZSM at 400˚C

Components	Wt%
CO_2	0.01
CO	0.01
C_1	0.03
C_2	0.08
C_2^1	1.28
C_3	2.68
C_3^1	3.04
iC_4	0.64
C_4	0.32
C_4^1	1.24
iC_5	0.04
C_5	0.02
C_5^1	0.03
C_6	0.08

Table B38. GCMS liquid analysis for Zeo-CY Cat Y +ZSM at 400˚C

Saturates				Unsaturates		Aromatics	Unknown	Total
Carbon Number	**Cyclic**	**Iso**	**Normal**	**Cyclic**	**Normal + Iso**			
1								
2								
3			0.22					**0.22**
4		0.08	0.62		0.98			**1.68**
5	0.24	0.32	2.59	0.16	1.76			**5.07**
6	0.58	0.62	3.20	0.83	1.24	2.42	0.01	**8.90**
7	0.32	0.34	2.13	0.20	1.02	3.62	0.02	**7.65**
8	0.18	0.34	2.98	0.40	0.18	5.21	0.02	**9.31**
9	0.12	0.17	1.89	0.32	0.10	1.28	0.03	**3.91**
10	0.38	0.09	2.62	0.01	0.01	0.31	0.02	**3.44**
11	0.08	0.12	2.15	0.01		0.01	0.10	**2.47**
12	0.20	0.14	1.64		0.01	0.08	0.02	**2.09**
13	0.60	0.06	0.08			0.01	0.01	**0.76**
14	0.50	0.02	0.17		0.34			**1.03**
15	0.20	0.32	0.16				0.02	**0.70**
16	0.02		51.62	0.02			0.20	**51.86**
17		0.01	0.80					**0.81**
18			0.10					**0.10**
TOTAL	**3.42**	**2.63**	**72.97**	**1.95**	**5.64**	**12.94**	**0.45**	**100.00**

Table B39. GCMS gas analysis for Zeo-CY Cat Y +ZSM at 500˚C

Components	Wt%
CO_2	0.02
CO	0.00
C_1	0.07
C_2	0.11
C_2^1	1.69
C_3	3.37
C_3^1	3.48
iC_4	0.70
C_4	0.41
C_4^1	1.86
iC_5	0.06
C_5	0.07
C_5^1	0.06
C_6	0.06

Table B40. GCMS liquid analysis for Zeo-CY Cat Y +ZSM at 500˚C

Saturates				Unsaturates		Aromatics	Unknown	Total
Carbon Number	**Cyclic**	**Iso**	**Normal**	**Cyclic**	**Normal + Iso**			
1								
2								
3			0.14					**0.14**
4		0.18	0.55		1.22			**1.95**
5	0.33	0.60	1.59	0.20	3.05		0.10	**5.87**
6	0.73	0.85	2.57	0.43	1.13	3.56	0.69	**9.96**
7	0.43	0.50	3.10		1.14	13.72	0.22	**19.11**
8	0.27	0.48	3.06		0.26	13.91		**17.98**
9	0.09	0.07	2.43		0.12	3.07	0.05	**5.83**
10	0.25	0.13	1.86			0.47	0.03	**2.74**
11	0.05	0.16	1.55			0.03	0.19	**1.98**
12		0.11	1.09			0.15	0.39	**1.74**
13							0.52	**0.52**
14			0.17		0.62		0.11	**0.90**
15			0.16				0.55	**0.71**
16			30.24				0.23	**30.47**
17								
18			0.10					**0.10**
19								
TOTAL	**2.15**	**3.08**	**48.61**	**0.63**	**7.54**	**34.91**	**3.08**	**100.00**

Table B41. GCMS gas analysis for Zeo-CY Cat Y +ZSM at 550˚C

Components	Wt%
CO_2	0.02
CO	0.75
C_1	0.66
C_2	0.66
C_2^1	6.68
C_3	5.37
C_3^1	8.64
iC_4	0.70
C_4	0.55
C_4^1	3.23
iC_5	0.06
C_5	0.10
C_5^1	0.03
C_6	0.10

Table B42. GCMS liquid analysis for Zeo-CY Cat Y +ZSM at 550˚C

Saturates				Unsaturates		Aromatics	Unknown	Total
Carbon Number	**Cyclic**	**Iso**	**Normal**	**Cyclic**	**Normal + Iso**			
1								
2								
3								
4		0.19	0.40		0.42			**1.01**
5	0.26	0.92	1.39	0.03	2.37		0.01	**4.98**
6	1.26	1.55	2.07	0.78	1.59	2.10	0.41	**9.76**
7	1.26	1.20	2.14		1.82	11.39	0.54	**18.35**
8	1.04	1.83	1.83		1.09	19.53	0.13	**25.45**
9	0.51	0.96	1.36		0.16	3.63	0.29	**6.91**
10	0.03	5.79	1.10		0.03	2.09	0.33	**9.37**
11		0.94	0.97			0.29	1.40	**3.60**
12	0.10	0.48	0.76			0.12	1.44	**2.90**
13		0.03	0.40		0.02		0.67	**1.12**
14			0.10				0.40	**0.50**
15			0.08				0.48	**0.56**
16			15.32				0.07	**15.39**
17								
18							0.10	**0.10**
TOTAL	**4.46**	**13.89**	**27.92**	**0.81**	**7.50**	**39.15**	**6.27**	**100.00**

Table B43. GCMS gas analysis for HPC Cat Y at 400˚C

Components	Wt%
CO_2	0.00
CO	0.18
C_1	0.19
C_2	0.25
C_2^1	0.78
C_3	6.42
C_3^1	1.69
iC_4	0.94
C_4	0.36
C_4^1	1.12
iC_5	0.03
C_5	0.06
C_5^1	0.02
C_6	0.04

Table B44. GCMS liquid analysis for HPC Cat Y at 400˚C

Saturates				Unsaturates		Aromatics	Unknown	Total
Carbon Number	**Cyclic**	**Iso**	**Normal**	**Cyclic**	**Normal + Iso**			
1								
2								
3			0.30					**0.30**
4		0.68	1.12		0.98			**2.78**
5		1.64	1.87	0.01	2.47		0.02	**6.01**
6	0.24	1.02	1.62	0.08	0.98		0.01	**3.95**
7	0.32	0.89	0.85		1.89	1.45	0.03	**5.43**
8	0.42	0.34	0.01	0.02	0.24	1.41	0.01	**2.45**
9	0.02	0.08	0.12		0.88	1.08	0.02	**2.20**
10	0.08	0.05	0.06	0.01		0.25	0.01	**0.46**
11		0.03	0.14	0.01	0.01	0.01	0.04	**0.24**
12		0.02	0.01			0.02	0.26	**0.31**
13			0.02	0.03	0.01		0.01	**0.07**
14		0.01				0.01	0.01	**0.03**
15			0.01		0.16		0.30	**0.47**
16		0.01	75.12	0.04		0.01	0.11	**75.29**
17					0.01			**0.01**
18								
TOTAL	**1.08**	**4.77**	**81.25**	**0.20**	**7.63**	**4.24**	**0.83**	**100.00**

Table B45. GCMS gas analysis for HPC Cat Y at 500˚C

Components	Wt%
CO_2	0.00
CO	0.30
C_1	0.35
C_2	0.44
C_2^1	1.28
C_3	9.47
C_3^1	3.48
iC_4	1.73
C_4	0.87
C_4^1	2.08
iC_5	0.09
C_5	0.09
C_5^1	0.04
C_6	0.02

Table B46. GCMS liquid analysis for HPC Cat Y at 500˚C

Saturates				Unsaturates		Aromatics	Unknown	Total
Carbon Number	**Cyclic**	**Iso**	**Normal**	**Cyclic**	**Normal + Iso**			
1								
2								
3			0.90					**0.90**
4		1.02	2.13		1.96			**5.11**
5		1.93	2.93	0.11	4.54		0.38	**9.89**
6	0.49	2.02	2.24	1.26	1.74		0.59	**8.34**
7	0.47	1.43	1.09		2.19	2.71	0.07	**7.96**
8	0.74	0.83			0.44	2.36	0.07	**4.44**
9	0.05	0.12	0.23		1.82	2.01		**4.23**
10	0.16	0.12	0.16			0.45	0.03	**0.92**
11		0.07	0.11				0.11	**0.29**
12		0.07	0.08			0.09	0.49	**0.73**
13			0.04				0.03	**0.07**
14							0.01	**0.01**
15			0.03		0.26		0.59	**0.88**
16			56.12				0.11	**56.23**
17								
18								
TOTAL	**1.91**	**7.61**	**66.06**	**1.37**	**12.95**	**7.62**	**2.48**	**100.00**

Table B47. GCMS gas analysis for HPC Cat Y at 550˚C

Components	Wt%
CO_2	0.06
CO	2.10
C_1	2.23
C_2	1.51
C_2^1	4.62
C_3	7.75
C_3^1	5.97
iC_4	1.25
C_4	0.77
C_4^1	3.12
iC_5	0.11
C_5	0.12
C_5^1	0.08
C_6	0.11

Table B48. GCMS liquid analysis for HPC Cat Y at 550˚C

Saturates				Unsaturates		Aromatics	Unknown	Total
Carbon Number	**Cyclic**	**Iso**	**Normal**	**Cyclic**	**Normal + Iso**			
1								
2								
3			0.53					**0.53**
4		0.37	0.92		1.66			**2.95**
5		0.84	1.47	0.16	3.99		0.42	**6.88**
6	0.44	1.07	1.38	1.13	3.20	1.02	0.16	**8.40**
7	0.29	0.84	1.02		2.66	4.35	0.48	**9.64**
8	1.10	0.75	0.67		0.42	5.79	0.04	**8.77**
9	0.80	0.25	0.47		0.27	1.59	0.11	**3.49**
10	0.39	0.88	0.37		0.77	0.54	0.13	**3.08**
11		0.11	0.28		0.61	0.20	0.28	**1.48**
12		0.06	0.21		0.49	0.14	0.27	**1.17**
13			0.16		0.36		0.31	**0.83**
14			0.05		0.30		0.17	**0.52**
15			0.02		0.13		0.25	**0.40**
16			51.64		0.05		0.07	**51.76**
17								
18							0.10	**0.10**
TOTAL	**3.02**	**5.17**	**59.19**	**1.29**	**14.91**	**13.63**	**2.79**	**100.00**

Table B49. GCMS gas analysis for HPC Cat Y + ZSM5 at 400˚C

Components	Wt%
CO_2	0.04
CO	0.00
C_1	0.08
C_2	0.05
C_2^1	0.46
C_3	1.06
C_3^1	0.48
iC_4	0.20
C_4	0.05
C_4^1	0.15
iC_5	0.02
C_5	0.02
C_5^1	0.01
C_6	0.04

Table B50. GCMS liquid analysis for HPC Cat Y + ZSM5 at 400˚C

Saturates				Unsaturates		Aromatics	Unknown	Total
Carbon Number	**Cyclic**	**Iso**	**Normal**	**Cyclic**	**Normal + Iso**			
1								
2								
3								
4			0.03		0.03			**0.06**
5	0.05	0.09	0.19		0.55		0.05	**0.93**
6	0.23	0.10	0.54	0.28	0.36	0.23	0.41	**2.15**
7	0.10	0.13	0.98		0.47	1.66		**3.34**
8			1.11		0.07	2.65		**3.83**
9			0.91			0.53		**1.44**
10	0.05	0.43	0.70			0.08		**1.26**
11		0.05	0.64			0.03		**0.72**
12		0.04	0.51					**0.55**
13			0.27					**0.27**
14			0.07					**0.07**
15			0.05				0.12	**0.17**
16			84.91					**84.91**
17			0.04				0.03	**0.07**
18							0.23	**0.23**
TOTAL	**0.43**	**0.84**	**90.95**	**0.28**	**1.48**	**5.18**	**0.84**	**100.00**

Table B51. GCMS gas analysis for HPC Cat Y + ZSM5 at 500˚C

Components	Wt%
CO_2	0.01
CO	0.06
C_1	0.24
C_2	0.32
C_2^1	1.09
C_3	7.45
C_3^1	3.08
iC_4	0.89
C_4	0.46
C_4^1	1.1
iC_5	0.02
C_5	0.01
C_5^1	0.04
C_6	0.06

Table B52. GCMS liquid analysis for HPC Cat Y + ZSM5 at 500˚C

Saturates				Unsaturates		Aromatics	Unknown	Total
Carbon Number	**Cyclic**	**Iso**	**Normal**	**Cyclic**	**Normal + Iso**			
1								
2								
3			0.03					**0.03**
4		0.33	0.65		0.68			**1.66**
5	0.12	0.65	1.05	0.12	1.58		0.01	**3.53**
6	0.75	0.54	0.95	0.85	0.24	0.26	0.02	**3.61**
7	0.42	0.74	0.68	0.02	0.98	2.89	0.01	**5.74**
8	0.38	0.31	0.47	0.04	0.26	4.78		**6.24**
9	0.04	0.21	0.31	0.01	0.12	2.15	0.04	**2.88**
10	0.14	0.12	0.22			0.82	0.08	**1.38**
11	0.02	0.14	0.24		0.01	0.11	0.02	**0.54**
12	0.02	0.16	0.19	0.02	0.01	0.08	0.20	**0.68**
13			0.06				0.10	**0.16**
14			0.01		0.01		0.10	**0.12**
15			0.06	0.06			0.02	**0.14**
16			73.11	0.02	0.02		0.03	**73.18**
17			0.08				0.02	**0.10**
18				0.01				**0.01**
TOTAL	**1.89**	**3.20**	**78.11**	**1.15**	**3.91**	**11.09**	**0.65**	**100.0**

Table B53. GCMS gas analysis for HPC Cat Y + ZSM5 at 550˚C

Components	Wt%
CO_2	0.02
CO	0.11
C_1	0.33
C_2	0.45
C_2^1	3.36
C_3	9.50
C_3^1	5.49
iC_4	1.46
C_4	0.63
C_4^1	2.0
iC_5	0.06
C_5	0.04
C_5^1	0.01
C_6	0.02

Table B54. GCMS liquid analysis for HPC Cat Y + ZSM5 at 550˚C

Saturates				Unsaturates		Aromatics	Unknown	Total
Carbon Number	**Cyclic**	**Iso**	**Normal**	**Cyclic**	**Normal + Iso**			
1								
2								
3			0.09					**0.09**
4		0.63	1.35		1.37			**3.35**
5	0.25	1.74	2.02	0.12	3.79		0.16	**8.08**
6	0.96	1.32	1.36	0.85	1.59	0.99	0.56	**7.63**
7	0.67	0.89	1.11		1.71	5.76	0.23	**10.37**
8	0.56	0.64	0.90		0.50	9.59	0.12	**12.31**
9	0.09	0.28	0.63		0.23	4.51	0.07	**5.81**
10	0.29	0.33	0.49			1.07	0.08	**2.26**
11		0.25	0.46			0.14	0.57	**1.42**
12	0.05	0.24	0.36		0.01	0.18	0.55	**1.39**
13			0.19				0.28	**0.47**
14			0.07		0.01		0.38	**0.46**
15							0.17	**0.17**
16			46.11					**46.11**
17			0.02					**0.02**
18							0.06	**0.06**
TOTAL	**2.87**	**6.32**	**55.16**	**0.97**	**9.21**	**22.24**	**3.23**	**100.00**

Table B55. GCMS gas analysis for Zeo-AY(50% zeolite) Cat Y at 400˚C

Components	Wt%
CO_2	0.01
CO	0.03
C_1	0.01
C_2	0.14
C_2^1	0.39
C_3	0.56
C_3^1	1.20
iC_4	0.24
C_4	0.26
C_4^1	0.18
iC_5	0.02
C_5	0.06
C_5^1	0.94
C_6	0.08

Table B56. GCMS liquid analysis for Zeo-AY(50% zeolite) Cat Y at 400˚C

Saturates				Unsaturates		Aromatics	Unknown	Total
Carbon Number	**Cyclic**	**Iso**	**Normal**	**Cyclic**	**Normal + Iso**			
1								
2								
3			0.08					**0.08**
4		0.03	0.21	0.01	1.25			**1.50**
5	0.10	0.24	0.32	0.02	1.68		1.15	**3.51**
6	0.32	1.18	0.89	0.30	0.98	0.22	0.98	**4.87**
7	0.47	0.22	0.74		1.62	0.86	0.62	**4.53**
8	0.26	1.37	0.98	0.02	0.24	1.62	0.32	**4.81**
9	0.01	0.04	1.11		0.02	0.47	0.02	**1.67**
10	0.02	0.72	0.62			0.11	0.15	**1.62**
11	0.05	0.04	0.68	0.01	0.01	0.02	0.12	**0.93**
12	0.01	0.50	0.34			0.03	0.01	**0.89**
13	0.50		0.21				0.02	**0.73**
14	0.01		0.06	0.02			0.02	**0.11**
15			0.11	0.01				**0.12**
16			74.6					**74.6**
17			0.01					**0.01**
18			0.02					**0.02**
19								
TOTAL	**1.75**	**4.34**	**80.98**	**0.39**	**5.80**	**3.33**	**3.41**	**100.00**

Table B57. GCMS gas analysis for Zeo-AY(50% zeolite) Cat Y at 500˚C

Components	Wt%
CO_2	0.01
CO	0.05
C_1	0.00
C_2	0.23
C_2^1	0.59
C_3	0.86
C_3^1	1.39
iC_4	0.21
C_4	0.06
C_4^1	0.89
iC_5	0.05
C_5	0.04
C_5^1	0.73
C_6	0.04

Table B58. GCMS liquid analysis for Zeo-AY(50% zeolite) Cat Y at 500˚C

Saturates				Unsaturates		Aromatics	Unknown	Total
Carbon Number	**Cyclic**	**Iso**	**Normal**	**Cyclic**	**Normal + Iso**			
1								
2								
3			0.05					**0.05**
4		0.09	0.31		0.86			**1.26**
5	0.16	0.32	0.91		3.22		0.15	**4.76**
6	0.74	0.27	1.49	0.90	1.65	0.31	0.55	**5.91**
7	0.52	0.50	1.86		1.38	1.80	0.12	**6.18**
8	0.30	0.51	1.83		0.33	3.29	0.03	**6.29**
9	0.03	0.10	1.41		0.04	0.73	0.01	**2.32**
10	0.05	0.93	1.08			0.23	0.15	**2.44**
11		0.08	0.94			0.04	0.13	**1.19**
12			0.70			0.03	0.04	**0.77**
13			0.37				0.03	**0.40**
14			0.09				0.26	**0.35**
15			0.11				0.21	**0.32**
16			61.45				2.17	**63.62**
17							0.43	**0.43**
18							3.71	**3.71**
19								
TOTAL	**1.80**	**2.80**	**72.60**	**0.90**	**7.48**	**6.43**	**7.99**	**100.00**

Table B59. GCMS gas analysis for Zeo-AY(50% zeolite) Cat Y at 550˚C

Components	Wt%
CO_2	0.01
CO	0.90
C_1	0.33
C_2	0.33
C_2^1	3.40
C_3	1.79
C_3^1	0.14
iC_4	1.45
C_4	0.04
C_4^1	0.13
iC_5	0.04
C_5	0.01
C_5^1	0.17
C_6	0.07

Table B60. GCMS liquid analysis for Zeo-AY(50% zeolite) Cat Y at 550˚C

Saturates				Unsaturates		Aromatics	Unknown	Total
Carbon Number	**Cyclic**	**Iso**	**Normal**	**Cyclic**	**Normal + Iso**			
1								
2								
3			0.03					**0.03**
4		0.03			0.72			**0.75**
5	0.27	0.68	1.07		2.66		0.10	**4.78**
6	0.60	0.46	1.82	0.50	1.02	2.61	0.33	**7.34**
7	0.35	0.17	2.22		1.11	10.77	0.07	**14.69**
8	0.12	0.27	2.10		0.26	10.75	0.01	**13.51**
9		0.10	1.69		0.04	1.10	0.19	**3.12**
10	0.09	1.97	1.34		0.01	0.42	0.21	**4.04**
11		0.21	1.15		0.01	0.26	0.28	**1.91**
12	0.01		0.86			0.17	0.14	**1.18**
13			0.50		0.01		0.12	**0.63**
14			0.12				0.10	**0.22**
15			0.03				0.12	**0.15**
16			47.24				0.02	**47.26**
17		0.28					0.11	**0.39**
TOTAL	**1.44**	**4.17**	**60.17**	**0.50**	**5.84**	**26.08**	**1.80**	**100.00**

Table B61. GCMS gas analysis for Zeo-AY(50%zeolite) Y+ZSM at 400˚C

Components	Wt%
CO_2	0.08
CO	1.21
C_1	0.89
C_2	0.76
C_2^1	4.28
C_3	3.59
C_3^1	5.68
iC_4	0.24
C_4	0.27
C_4^1	1.87
iC_5	0.04
C_5	1.62
C_5^1	0.08
C_6	0.58

Table B62. GCMS liquid analysis for Zeo-AY(50%zeolite) Y+ZSM at 400˚C

Saturates				Unsaturates		Aromatics	Unknown	Total
Carbon Number	**Cyclic**	**Iso**	**Normal**	**Cyclic**	**Normal + Iso**			
1								
2								
3			0.08					**0.08**
4		0.01	0.21		0.02			**0.24**
5	0.20	0.01	0.74	0.01	0.02		0.02	**1.00**
6	0.30	0.02	0.87	0.01	0.01	0.87	0.04	**2.12**
7	0.16	0.01	2.14	0.01		3.52	0.05	**5.89**
8	0.08	0.01	1.62	0.50	0.01	4.28	0.20	**6.70**
9			0.87	0.06		1.68	0.16	**2.77**
10	0.46		0.02	0.02	0.02	0.48	0.20	**1.20**
11	0.02	0.02	0.72	0.01	0.02	0.01	0.36	**1.16**
12	0.42	0.30	0.22	0.60	0.03	0.20	0.44	**2.21**
13	0.02	0.20	0.11	0.55		0.02	0.21	**1.11**
14	0.08	0.01	0.01	0.01	0.01		0.20	**0.32**
15		0.01	0.08		0.01		0.06	**0.16**
16		0.01	74.28	0.02	0.09		0.01	**74.41**
17							0.02	**0.02**
18					0.20		0.40	**0.60**
19							0.01	**0.01**
TOTAL	**1.74**	**0.61**	**81.97**	**1.80**	**0.44**	**11.06**	**2.38**	**100.00**

Table B63. GCMS gas analysis for Zeo-AY(50%zeolite) Y+ZSM at 500˚C

Components	Wt%
CO_2	0.11
CO	1.19
C_1	1.06
C_2	0.93
C_2^1	6.64
C_3	5.22
C_3^1	7.48
iC_4	0.37
C_4	0.35
C_4^1	2.23
iC_5	0.02
C_5	0.06
C_5^1	0.04
C_6	0.10

Table B64. GCMS liquid analysis for Zeo-AY(50%zeolite) Y+ZSM at 500˚C

Saturates				Unsaturates		Aromatics	Unknown	Total
Carbon Number	**Cyclic**	**Iso**	**Normal**	**Cyclic**	**Normal + Iso**			
1								
2								
3			0.03					**0.03**
4		0.06	0.17		0.31			**0.54**
5	0.11	0.18	0.44	0.04	0.92		0.02	**1.71**
6	0.28	0.25	0.78	0.19	0.45	1.84	0.07	**3.86**
7	0.17	0.19	1.14		0.34	9.53	0.04	**11.41**
8	0.04	0.13	1.34		0.15	11.79	0.04	**13.49**
9		0.01	1.26			3.72		**4.99**
10	0.11	0.30	1.17			0.84	0.13	**2.55**
11	0.09	0.17	1.12		0.02	0.03	0.33	**1.76**
12	0.03	0.13	0.90			0.50	1.09	**2.65**
13			0.56				0.36	**0.92**
14			0.14				0.43	**0.57**
15			0.08				0.26	**0.34**
16			54.00				0.40	**54.40**
17							0.01	**0.01**
18							0.75	**0.75**
19							0.02	**0.02**
TOTAL	**0.83**	**1.42**	**63.13**	**0.23**	**2.19**	**28.25**	**3.95**	**100.00**

Table B65. GCMS gas analysis for Zeo-AY(50%zeolite) Y+ZSM at 550˚C

Components	Wt%
CO_2	0.01
CO	0.35
C_1	0.36
C_2	0.52
C_2^1	3.51
C_3	12.76
C_3^1	6.89
iC_4	2.14
C_4	1.28
C_4^1	3.83
iC_5	0.18
C_5	0.20
C_5^1	0.19
C_6	0.26

Table B66. GCMS liquid analysis for Zeo-AY(50%zeolite) Y+ZSM at 550˚C

Saturates				Unsaturates		Aromatics	Unknown	Total
Carbon Number	**Cyclic**	**Iso**	**Normal**	**Cyclic**	**Normal + Iso**			
1								
2								
3			0.04					**0.04**
4		0.28	0.68		0.91			**1.87**
5	0.27	0.90	1.38	0.12	2.86		0.02	**5.55**
6	0.97	1.05	1.42	0.71	1.43	2.52	0.43	**8.53**
7	0.68	0.74	1.43		1.25	11.45	0.50	**16.05**
8	0.42	1.00	1.18		0.20	15.86	0.18	**18.84**
9	0.05	0.03	0.87		0.25	5.83	0.07	**7.10**
10	0.19	0.35	0.64			0.94	0.33	**2.45**
11	0.12	0.25	0.53		0.03	0.04	0.54	**1.51**
12	0.06	0.24	0.40			0.20	0.82	**1.72**
13			0.19				0.34	**0.53**
14			0.05				3.64	**3.69**
15			0.08				0.19	**0.27**
16			30.15					**30.15**
17			0.58				0.02	**0.60**
18			1.09				0.01	**1.09**
TOTAL	**2.76**	**4.84**	**40.71**	**0.83**	**6.93**	**36.84**	**7.09**	**100.00**